

PSaclay.pdf

X2.pdf

THÈSE DE DOCTORAT  
DE  
L'UNIVERSITÉ PARIS-SACLAY  
PRÉPARÉE À  
L'ÉCOLE POLYTECHNIQUE

ÉCOLE DOCTORALE N°579  
Sciences mécaniques et énergétiques, matériaux et géosciences  
Spécialité de doctorat : Mécanique des solides

Par  
Monsieur Tianyi LI

**Gradient Damage Modeling of Dynamic Brittle Fracture  
Variational Principles and Numerical Simulations**

**Thèse présentée et soutenue à Palaiseau, le 6 octobre 2016**

**Composition du Jury :**

M. Gilles DAMAMME	Directeur de recherche, CEA/DAM	Président du Jury
M. Alain COMBESURE	Professeur émérite, INSA de Lyon	Rapporteur
M. Corrado MAURINI	Professeur, Université Pierre et Marie Curie	Rapporteur
Mme Laura DE LORENZIS	Prof. Dr.-Ing., TU Braunschweig	Examinatrice
M. Jean-Jacques MARIGO	Professeur, Ecole Polytechnique	Directeur de thèse
M. Daniel GUILBAUD	Ingénieur de recherche, CEA Saclay	Co-encadrant
M. Serguei POTAPOV	Ingénieur de recherche, EDF Lab Paris-Saclay	Co-encadrant



# Résumé en français

## Introduction

Une bonne tenue mécanique des structures du génie civil en béton armé sous chargements dynamiques sévères est primordiale pour la sécurité et nécessite une évaluation précise de leur comportement en présence de propagation de fissures dynamiques. Dans ce travail, on se focalise sur la modélisation constitutive du béton assimilé à un matériau élastique-fragile endommageable en tension seulement. La rupture fragile s'accompagne de très peu de déformations loin de fissures et d'une localisation du tenseur des déformations le long des fissures. La modélisation et l'analyse décrites dans cette étude s'appliquent aux matériaux fragiles vérifiant ces comportements à la rupture.

Une étude bibliographique sur la rupture dynamique fragile est proposée dans le chapitre 1. Plusieurs modèles physiques sont comparés quant à leur aptitude à modéliser la rupture fragile : la théorie classique de Griffith, l'approche variationnelle de la rupture et les modèles d'endommagement à gradient formulés initialement dans un cadre quasi statique. Plusieurs objectifs de cette présente étude sont classifiés en fonction de l'approche utilisée (théorique ou numérique) et en utilisant les sujets thématiques suivants

- Vers la dynamique,
- Établir un lien avec les approches « champ de phase »,
- Meilleure compréhension des modèles d'endommagement à gradient, et
- Validation expérimentale.

## Modèles d'endommagement à gradient en dynamique

Le chapitre 2 regroupe les contributions théoriques de cette these. On postule que l'évolution spatio-temporelle de la localisation des déformations dans un solide fragile est régie par un modèle d'endommagement à gradient. Il consiste à introduire un nouveau champ scalaire  $0 \leq \alpha_t \leq 1$  réalisant une description régularisée entre la partie saine de la structure  $\alpha_t = 0$  et la région fissurée  $\alpha_t = 1$ .

On propose une formulation variationnelle des modèles d'endommagement à gradient en dynamique à l'aide de trois principes physiques d'irréversibilité, de stabilité et de bilan d'énergie

1. **Irréversibilité** : l'endommagement  $t \mapsto \alpha_t$  est non-décroissant du temps.
2. **Stabilité d'ordre un** : la variation première de l'action est non-négative par rapport aux évolutions arbitraires et admissibles du couple déplacement-endommagement

$$\mathcal{A}'(\mathbf{u}, \alpha)(\mathbf{v} - \mathbf{u}, \beta - \alpha) \geq 0 \text{ for all } \mathbf{v} \in C(\mathbf{u}) \text{ and all } \beta \in \mathcal{D}(\alpha).$$

3. **Bilan d'énergie** : la dissipation d'énergie est uniquement due à l'endommagement

$$\begin{aligned} \mathcal{H}_t = \mathcal{H}_0 + \int_0^t \left( \int_{\Omega} (\boldsymbol{\sigma}_s \cdot \boldsymbol{\varepsilon}(\dot{\mathbf{U}}_s) - \rho \dot{\mathbf{u}}_s \cdot \ddot{\mathbf{U}}_s) \, d\mathbf{x} - \mathcal{W}_s(\dot{\mathbf{U}}_s) - \dot{\mathcal{W}}_s(\mathbf{u}_s) \right) ds \\ + \int_{\Omega} \rho(\dot{\mathbf{u}}_t \cdot \dot{\mathbf{U}}_t - \dot{\mathbf{u}}_0 \cdot \dot{\mathbf{U}}_0) \, d\mathbf{x} \end{aligned}$$

fiss3.pdf

où l'énergie totale est définie par

$$\mathcal{H}_t = \mathcal{E}(\mathbf{u}_t, \alpha_t) + \mathcal{S}(\alpha_t) + \mathcal{K}(\dot{\mathbf{u}}_t) - \mathcal{W}_t(\mathbf{u}_t).$$

Il s'agit d'une extension en dynamique du formalisme existant en statique via la variation de l'intégrale temporelle d'un lagrangien généralisé prenant en compte l'énergie cinétique  $\mathcal{K}$  et aussi l'énergie dissipée  $\mathcal{S}$  due au processus d'endommagement. Grâce au caractère variationnel de la formulation, ces modèles d'endommagement permettent de rendre compte de toute l'évolution de la fissuration avec des trajets et topologies complexes et non-présupposés d'un point de vue modélisation de l'évolution du défaut.

Pour modéliser le comportement asymétrique des matériaux fragiles en traction et en compression, plusieurs formulations basées sur la dépendance de l'énergie élastique vis-à-vis de l'endommagement sont revues et un cadre unificateur est proposé via un principe variationnel. Ces modèles sont vus comme un paramètre matériau en soi décrivant différents mécanismes d'endommagement déterminés par la microstructure. Une meilleure compréhension de leur comportement est obtenue via un essai de traction/compression unidimensionnel.

On s'intéresse ensuite à l'équation d'évolution de fissures régularisées par le champ d'endommagement durant la phase de propagation. On démontre que la pointe de la fissure dynamique est régie par un critère de Griffith faisant intervenir le taux de restitution d'énergie dynamique conventionnel

$$G_t^\alpha = \int_{\Omega \setminus \Gamma_t} \left( (\kappa(\dot{\mathbf{u}}_t) - \psi(\boldsymbol{\varepsilon}(\mathbf{u}_t), \alpha_t)) \operatorname{div} \boldsymbol{\theta}_t + \boldsymbol{\sigma}_t \cdot (\nabla \mathbf{u}_t \nabla \boldsymbol{\theta}_t) + \operatorname{div}(\mathbf{f}_t \otimes \boldsymbol{\theta}_t) \cdot \mathbf{u}_t + \rho \ddot{\mathbf{u}}_t \cdot \nabla \mathbf{u}_t \boldsymbol{\theta}_t + \rho \dot{\mathbf{u}}_t \cdot \nabla \dot{\mathbf{u}}_t \boldsymbol{\theta}_t \right) \mathrm{d}\mathbf{x},$$

et le taux de dissipation d'endommagement

$$\gamma_t = \frac{\partial}{\partial l_t} \mathcal{S}^*(\alpha_t^*, l_t) = \int_{\Omega \setminus \Gamma_t} (\zeta(\alpha_t, \nabla \alpha_t) \operatorname{div} \boldsymbol{\theta}_t - \mathbf{q}_t \cdot \nabla \boldsymbol{\theta}_t \nabla \alpha_t) \mathrm{d}\mathbf{x}.$$

La démonstration et la dérivation rigoureuse de ces concepts dans le modèle d'endommagement reposent sur les techniques de dérivation lagrangienne par rapport au domaine basée sur la configuration fissurée initiale et une séparation d'échelles lorsque la longueur interne est petite par rapport à la taille de la structure.

## Implémentation numérique

Le caractère variationnel de l'approche permet aussi une implémentation numérique directe et de manière consistante pour des problèmes bi et tri-dimensionnels, cf. le chapitre 3. Elle est basée sur

une discrétisation par éléments finis standards en espace et le schéma de  $\beta$ -Newmark en temps. Le problème d'endommagement qui détermine l'état de fissuration à l'instant actuel est résolu à l'échelle de la structure par la méthode du gradient conjugué projeté. L'architecture informatique est basée sur la librairie d'algèbre linéaire numérique PETSc qui assure une gestion uniforme des vecteurs et des matrices lors d'un calcul séquentiel ou parallèle. Dans le cas explicite, le modèle discrétisé résumé par l'algorithme suivant est implémenté dans le code de dynamique rapide EuroPlexus, cf. (CEA & EC, 2015)

- 1: **for** chaque pas de temps  $n \geq 0$  **do**
- 2:   M-à-j  $\underline{\dot{\mathbf{u}}}^{n+1/2} = \underline{\dot{\mathbf{u}}}^n + \frac{\Delta t}{2} \underline{\ddot{\mathbf{u}}}^n$ .
- 3:   M-à-j  $\underline{\mathbf{u}}^{n+1} = \underline{\mathbf{u}}^n + \Delta t \underline{\dot{\mathbf{u}}}^{n+1/2}$ .
- 4:   Obtenir  $\underline{\alpha}^{n+1}$  via la minimisation d'énergie.
- 5:   Obtenir  $\underline{\ddot{\mathbf{u}}}^{n+1}$  via l'équilibre dynamique.
- 6:   M-à-j  $\underline{\dot{\mathbf{u}}}^{n+1} = \underline{\dot{\mathbf{u}}}^{n+1/2} + \frac{\Delta t}{2} \underline{\ddot{\mathbf{u}}}^{n+1}$ .
- 7: **end for**

Une implémentation *open source* est aussi disponible dans le code d'éléments finis FEniCS, voir (Li, 2015).

## Simulations numériques

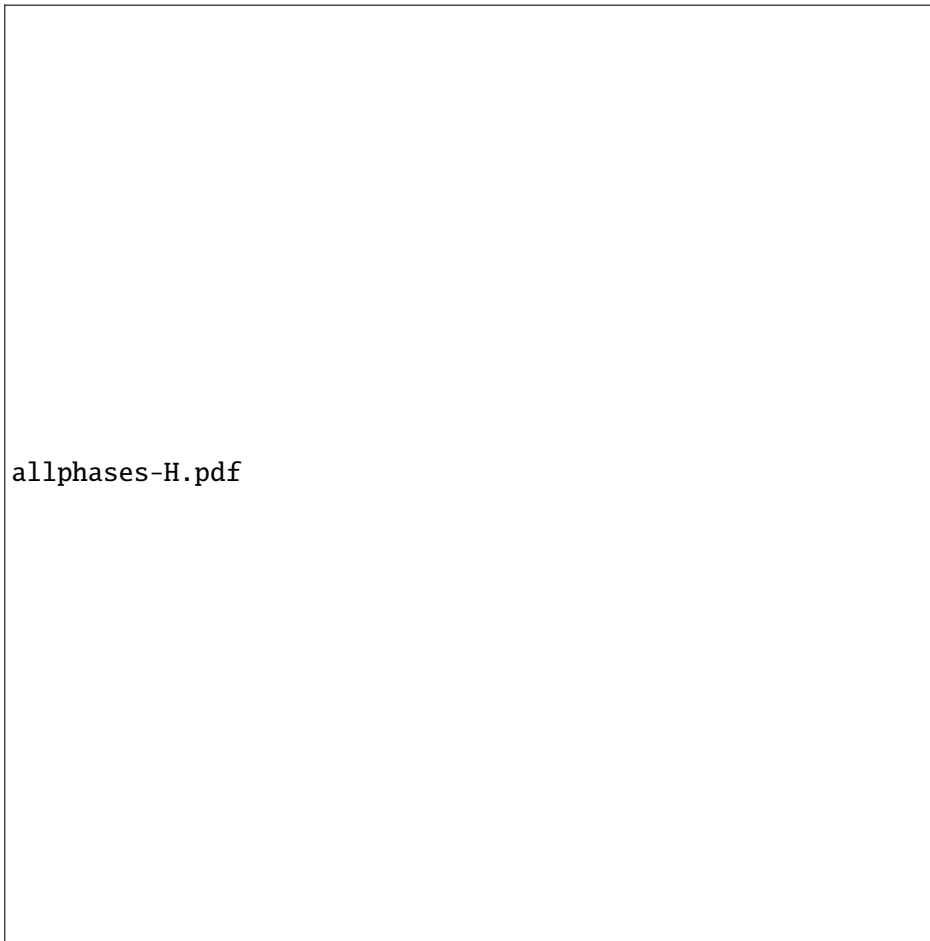
Les résultats de simulation obtenus issu des calculs parallèles sont alors discutés d'un point de vue numérique et physique dans le chapitre 4. L'efficacité du modèle numérique est démontrée via une analyse de scalabilité. On montre en particulier que la résolution du problème d'endommagement à l'échelle

plate\_scaling.pdf

de la structure n'est pas pénalisante pour un calcul explicite de fissuration fragile dynamique. Les lois constitutives d'endommagement et les formulations d'asymétrie en traction et en compression sont comparées quant à leur aptitude à modéliser la rupture fragile. On confirme que la loi d'endommagement intégrant une zone purement élastique est préférable aussi d'un point de vue numérique. Pour un comportement asymétrique en traction et en compression, le modèle basé sur la décomposition spectrale (contraintes/déformations principales) inscrit dans le cadre variationnel du chapitre 2 permettrait de mieux modéliser la rupture des matériaux fragiles. Cela permettrait un rapprochement avec les modèles « champ de phase » issue de la communauté mécanique numérique.

Pour mieux comprendre les approches d'endommagement à gradient en dynamique en tant qu'un modèle de rupture *per se*, on adopte une stratégie « divide ut regnes » et leurs propriétés spécifiques

sont analysées séparément pour différentes phases de l'évolution du défaut : nucléation, initiation, propagation, arrêt, branchement et bifurcation.



En particulier, la nucléation d'une fissure dans un solide sain est régie par un critère en contrainte accompagné des effets d'échelle introduits par la longueur interne. Cela est illustré par les simulations d'une barre sous choc et d'un essai brésilien sur un cylindre sous compression.

Via un calcul antiplan d'une plaque, on vérifie que la propagation de fissure satisfait la loi de Griffith démontrée dans le chapitre 2. Une analyse numérique de convergence vers le modèle quasi-statique y est aussi proposée.

Quelques observations numériques au tour d'un zoom spatio-temporel des phénomènes de branchement ou de bifurcation sont décrites et on propose une comparaison avec des critères classiques en mécanique de la rupture.

Des confrontations avec les résultats expérimentaux sont aussi réalisées afin d'évaluer le modèle et proposer des axes d'amélioration. En particulier, on envisage d'utiliser les lois d'endommagement plus sophistiquées pour pouvoir contrôler la bande d'endommagement pour le béton.

brazilian-size.pdf

crack\_speed.pdf





plate-micro-macro.pdf

# Avant-propos

## Research Background and Outline

From a modeling point of view, the present work concerns the *formulation* of mathematical models of the physical phenomenon in an industrial context. Due to the complexity of the problem, numerical simulation is also needed to provide an approximate solution of the previous theoretical models. To ensure the faithfulness of the numerically discretized computer model with respect to the theoretical one, the *verification* step should be first carried out in terms of numerical convergence properties. Finally, *validation* of the physical and the numerical models will be achieved via the comparison between simulation results and experimental observations. All these steps are covered in the present study.

In civil engineering, mechanical performance and integrity of the reinforced concrete structures are of paramount importance for safety. Severe transient dynamic loading conditions (such as impact or explosion) often lead to crack nucleation and its further space-time evolution in the most vulnerable area, which results in ultimate structural failure. A better understanding of the mechanics of defects would thus guide the civil engineers to optimize the dimensioning, the shape and the topology of the initial design. An accurate assessment of structural behaviors in the presence of dynamic crack propagation calls for more advanced physical models and their corresponding efficient computer implementations. In this aspect, the present work contributes thus to an improvement of the existing modeling of fracture in industrial structures, both from theoretical and numerical approaches.

Numerical simulation of reinforced concrete structures requires in general a separate modeling of the concrete, the reinforcement and the steel-concrete interaction. Due to the broadness of the subject, we will only focus here on the fracture behaviors of concrete itself. A coupling with the existing steel reinforcement models and in particular the phenomenon of interfacial fracture will be thoroughly investigated in the future. The mechanical behaviors of concrete fall into the category of brittle materials. Defect evolution in these materials with dynamical or inertia effects are commonly studied in the branch “dynamic fracture” of physics of solids. Very little deformation is present away from the fractured region and the strain tensor is essentially localized along the crack band. Without loss of generality, the methodology, modeling and analyses described in the present work should apply to a large class of materials that can be characterized by such constitutive and fracture behaviors.

Concretely, the mathematical modeling of dynamic brittle fracture will be performed in the framework of solid continuum mechanics with the usual Cauchy stress as the main stress measure. Adopting an engineering approach, we concentrate on a macroscopic phenomenological characterization of the constitutive behavior of brittle materials in the presence of fracture. In particular, the spatial and temporal evolution of strain localization in a brittle solid will be modeled by the gradient-damage approach that is gaining popularity in the recent years. It consists of introducing a new spatial scalar field  $\alpha_t$  that indicates and tracks the location of cracks. It can be considered as a damage variable since  $\alpha_t = 0$  refers to an intact material point whereas  $\alpha_t = 1$  stands for a totally damaged region, *i.e.* a crack or a strain-localization area. Compared to other existing approaches of dynamic fracture, the advantage of such gradient damage models lies in the crack path prediction with arbitrary crack topologies from a theoretic defect evolution modeling point of view. Its variational formulation also permits a direct and consistent numerical implementation both for two-dimensional and three-dimensional problems.

A brief bibliographical study of dynamic brittle fracture is provided in Chapter 1. We describe first the kinematics and physics of fracture in brittle materials with inertia, since the objective consists of faithfully and efficiently characterizing those phenomena. In order to motivate the present work and

to define a research scope, several currently used physical modeling approaches are compared with respect to their aptitude to approximate brittle fracture. This includes the classical Griffith's theory, the variational approach to fracture originated from the pioneer work of (Francfort & Marigo, 1998) and the current gradient damage model formulated in the quasi-static setting (Pham & Marigo, 2010b). Based on the literature investigation, the objectives of the present work can then be defined. They are classified depending on the methodology used (theoretical or numerical approach) and using the following four thematic subjects

- Going dynamical,
- Bridging the link with phase field approaches,
- Better understanding of gradient damage modeling of fracture, and
- Experimental validation.

To facilitate the presentation, the main novelty brought by the present study will be summarized at the beginning of each section by using the above classification.

Chapter 2 regroups the main theoretical contribution of this work. It concerns first a dynamic extension of the previous quasi-static gradient damage model in a variationally consistent framework. In quasi-statics, static equilibrium and the crack evolution of a solid corresponds to a minimum of the potential energy functional. In dynamics, this principle is generalized using an augmented space-time action integral and the temporal evolution of the coupled  $(\mathbf{u}, \alpha)$  field is governed by the stationarity of the former. As we shall see in the sequel, the benefits originating directly from the variational nature of the formulation are multi-fold. In explicit dynamics in the presence of violent loading conditions, finite rotations of fractured regions are often observed. We also propose a possible approach to incorporate geometrical nonlinearities through the introduction of the Hencky logarithmic strain. The concrete as well as other brittle materials are characterized by asymmetric behaviors in tension and in compression. Accounting for such effects is essential especially in dynamics due to wave reflections at the boundary. We then provide a systematic review of several existing approaches and carry out a theoretic study during a uniaxial traction/compression experiment. Finally we propose a theoretic exploration of the previous variational framework in the case when the damage band is localized along a spatially propagating path. A generalized Griffith criterion is obtained in the dynamic case that governs the temporal evolution of the gradient-damage crack tip. A separation of scales is then achieved by assuming that the internal length is small by comparison with the dimension of the body.

Then in Chapter 3, we present an efficient numerical implementation of the theoretic model described in the previous chapter. We follow a typical decoupling of the spatial and temporal discretization of the original continuous model and describe separately these two discretization procedures. Since the gradient damage approach consists of describing material constitutive behaviors inside the strain localization region, a relatively fine mesh is needed at least along the potential fracture path. In the present work, high computational needs will be overcome via parallel computing techniques. Efficiency of the numerical model is illustrated and demonstrated by a strong scaling analysis. In terms of final numerical implementation, we provide on the one hand an open-source Python implementation of dynamic gradient damage models based on the FEniCS Project, see (Li, 2015). On the other hand, the development is also conducted in the industrial explicit dynamics software EPX, cf. (CEA & EC, 2015).

Chapter 4 constitutes another main contribution of the present work through several well-chosen numerical experiments. These simulations are tailored to highlight specific properties of the dynamic gradient damage model during a complete defect evolution. A *divide and conquer* strategy is adopted and different temporal and spatial phases or events of dynamic fracture are investigated independently: nucleation, initiation, propagation, arrest, kinking, branching, . . . To facilitate the reading, the ordering of the chapter as well as the objectives of each experiment is first explained. The four thematic subjects initially devised are also used to classify these numerical simulations. Verification of the numerical discretized model is achieved through convergence studies and comparison with theoretical results. We also provide an experimental validation of the proposed model via correlations between numerical

and experimental observations. Limitations of the present model/parameters are also given toward improved modeling of dynamic fracture.

Finally some concluding remarks are given in Chapter 5. It consists of a general overview of the gradient damage approach to dynamic fracture both from a theoretical formulation/analysis and numerical implementation/investigation point of view. The presentation is classified using the four thematic subjects given in Chapter 1. Possible future work arising from the present study is also indicated.

## Notation Conventions

General notation conventions adopted in the present work are summarized as follows:

- Scalar-valued quantities will be denoted by italic Roman or Greek letters. It concerns not only the mathematical and physical constants such as the Young's modulus  $E$  but also the temporal and spatial dependence of such scalars. Several examples include a temporal evolution of the crack length  $l$ , a particular one-dimensional stress measure  $\sigma$  and the spatial damage field  $\alpha_t$ .
- Vectors and second-order tensors as well as their matrix representation will be represented by boldface letters. This concerns for example a particular material point in a three-dimensional body  $\mathbf{x}$ , the displacement field  $\mathbf{u}_t$ , the velocity field  $\dot{\mathbf{u}}_t$  and the stress tensor at that point  $\boldsymbol{\sigma}_t(\mathbf{x})$ .
- Higher order tensors will be indicated by sans-serif letters: the elasticity tensor  $\mathbf{A}$  for instance.
- Tensors are considered as linear operators and intrinsic notation is adopted. If the resulting quantity is not a scalar, the contraction operation will be written without dots, such as  $\boldsymbol{\sigma}_t = \mathbf{A}\boldsymbol{\varepsilon}_t = A_{ijkl}\boldsymbol{\varepsilon}_{kl}$  (the summation convention is assumed).
- Inner products between two tensors of the same order will be denoted with a dot, such as  $\mathbf{A}\boldsymbol{\varepsilon}_t \cdot \boldsymbol{\varepsilon}_t = A_{ijkl}\boldsymbol{\varepsilon}_{kl}\boldsymbol{\varepsilon}_{ij}$  (the summation convention is assumed).
- Time dependence of the involved quantity will be indicated by a subscript, like  $\mathbf{u} : (t, \mathbf{x}) \mapsto \mathbf{u}_t(\mathbf{x})$ . In particular, the notation  $\mathbf{u}_t$  is understood as the displacement field at a fixed time  $t$ , whereas  $\mathbf{u}$  refers to the time evolution of the displacement field.

## Publications and License Information

The present PhD work leads to the publication of the following journal papers. The author declare that only the personal contributions are used in this thesis.

- Li, T., Marigo, J.-J., Guilbaud, D., & Potapov, S. (2015). Variational Approach to Dynamic Brittle Fracture via Gradient Damage Models. *Applied Mechanics and Materials*, 784, 334–341. doi:[10.4028/www.scientific.net/AMM.784.334](https://doi.org/10.4028/www.scientific.net/AMM.784.334).
- Li, T., Marigo, J.-J., Guilbaud, D., & Potapov, S. (2016a). Gradient damage modeling of brittle fracture in an explicit dynamics context. *International Journal for Numerical Methods in Engineering*. doi:[10.1002/nme.5262](https://doi.org/10.1002/nme.5262).
- Li, T., & Marigo, J.-J. (2016). Crack Tip Equation of Motion in Dynamic Gradient Damage Models. *Journal of Elasticity*. doi:[10.1007/s10659-016-9595-0](https://doi.org/10.1007/s10659-016-9595-0).
- Li, T., Marigo, J.-J., Guilbaud, D., & Potapov, S. (2016b). Numerical investigation of dynamic brittle fracture via gradient damage models. *Advanced Modeling and Simulation in Engineering Sciences*, 3, 26. doi:[10.1186/s40323-016-0080-x](https://doi.org/10.1186/s40323-016-0080-x).

The present PhD thesis is written with  $\text{\LaTeX}$ . The source files are available in a public Bitbucket repository:

This work is licensed under a [Creative Commons “Attribution 4.0 International”](#) license.



Licensees may copy, distribute, display and perform the work and make derivative works and remixes based on it only if they give the author the credits (attribution). The following BibTeX code can be used to cite the current document:

```
@PhdThesis{Li:2016,  
  author = {Li, Tianyi},  
  title = {{G}radient-{{D}}amage {{M}}odeling of {{D}}ynamic {{B}}rITTLE {{F}}  
    racture: {{V}}ariational {{P}}rinciples and {{N}}umerical {{S}}imulations},  
  school = {Université Paris-Saclay},  
  year = {2016},  
  month = oct,  
}
```

Interested readers can freely use or adapt the document structure, the title page, etc., to their own needs.

## PhD Metadata

**Warning:** According to the dictionary, the word “metadata” refers to a set of data that describes and gives information about other data. This section provides information behind the present PhD work and has nothing to do with the rest of the document. Serious readers concerned with *la Patrie, les Sciences et la Gloire*<sup>1</sup> are sincerely invited to skip this section.

## Statistics

Several text-based work (Fortran/Python scripts, journal articles, public presentations) is stored and tracked in a private Bitbucket repository from the day I was introduced to the Mercurial version control system (approximately 2 months after the beginning of the thesis, *i.e.* in December 2013). Every *commit* to the repository represents some tasks done and can be used as a work unit. Of course, all commits are not born equal and some commits represent more important contributions than others (in terms of quantity and/or quality). However this effect is not taken into account here. *Future work could be devoted to a better quantification or discrimination of different commits.*

Up to August 10, 2016, a total of 636 commits are contributed to the present PhD thesis repository in the past 3 years minus 2 months. We are here interested in the distribution of these commits with respect to different temporal spans, see Figure 1.

- (a) **Per year:** The law of large numbers in probability theory seems to be verified: approximately an average of 250 commits are performed per year, according to the information for 2014 (total), 2015 (total) and 2016 (up to August). Thanks to the excellent working conditions in France, only  $\approx 215$  work days (excluding public holidays, weekends, and all vacations) are totalized per year. This means more than 1 commit is done per work day. Of course I do work also during holidays.
- (b) **Per month:** The most productive months are concentrated in the spring season, from March to June. I’m less productive during summer and autumn and least efficient when it’s cold. A quick literature search with Google doesn’t seem to confirm this finding.
- (c) **Per day:** Mysteriously the 15th of each month contributes least to the current PhD work.

---

<sup>1</sup>Motto of l’Ecole Polytechnique.

- (d) **Per weekday:** The first peak is arrived on Wednesday. A significant loss of efficiency is observed on Thursday for unknown reasons. Most commits are done on Friday, since some work is left for the weekend to come.
- (e) **Per hour:** Logically most commits are performed around 18 o'clock when I leave *work*, to make sure that I can still work after *work*: the second most commits are contributed around 22 o'clock.



Figure 1 – Distribution of commits up to August 10, 2016: (a) per year, (b) per month, (c) per day, (d) per weekday and (e) per hour

## Remerciements

Mes remerciements vont tout d'abord à Jean-Jacques, cher directeur de thèse. Je lui remercie d'avoir assuré la qualité scientifique dans ce travail et de m'avoir également confié les responsabilités de mes productions scientifiques. Je ne vais pas répéter ce qui a été dit le jour de la soutenance, mais grâce à lui j'ai pu découvrir le campus et le cercle Polytechniciens, un paysage autrefois méconnu et fort lointain.

J'aimerais ensuite remercier tous les membres du jury d'avoir bien examiné le travail. Je remercie Monsieur Damamme de s'être déplacé de Gramat afin de présider mon jury de thèse. J'adresse aussi mes remerciements à Madame de Lorenzis d'avoir participé physiquement au jury à une distance

d'environ 900 km de son lieu de travail. Merci aussi à Monsieur Francfort qui a accepté d'examiner cette thèse.

Je remercie également les deux rapporteurs : Monsieur Combescure de l'INSA de Lyon et Monsieur Maurini de Paris VI. Je les remercie d'avoir apprécié en général le manuscrit et d'avoir formulé les remarques scientifiques appropriées. J'en profite pour dire merci à Corrado ; sans lui je n'aurais probablement pas pu contribuer aussi au projet FEniCS et découvrir le cercle des chercheurs numériques HPC.

Je voudrais remercier ensuite mes deux co-encadrants industriels : Daniel (CEA Saclay) et Serguei (EDF Lab Clamart puis Paris-Saclay). Sans eux, cette thèse se serait déroutée vers une thèse purement académique. Merci à Serguei, Hariddh et Vincent pour leurs conseils et aides concernant EuroPlexus.

J'exprime aussi mes remerciements à Patrick, directeur de l'IMSIA (*presque* vrai), et Marie-Line, pour leur aide précieuse. J'ai pu ainsi participer à plusieurs et suffisamment de colloques et congrès nationaux et internationaux durant ces trois années de thèse.

J'aimerais remercier les co-occupants-de-bureau, les co-travailleurs, les co-FEniCSiens, les co-mangeurs (cantine comprise, couscous compris, pizza authentique faite maison comprise), les co-buveurs (café compris, et dont le vieillissement n'est pas forcément exceptionnellement prolongé), les co-fumeurs, les co-rigoleurs et co-blogueurs (Tokyo University), les co-voyageurs-d'AMA, les co-dormeurs-à-l'aéroport-de-Marseille, les co-randonneurs et co-promeneurs, le co-enquêteur-du-M (un truc RATP), les co-pongistes (joueur de ping-pong), les co-cinéphiles et peut-être aussi le co-cataphile. . . Sans vous ces trois années au LaMSID 8193 Clamart et à l'IMSIA 9219 Palaiseau seraient sans doute moins drôles.

Ô cher dsp0647318 (à tel point que je l'ai encore mémorisé jusqu'aujourd'hui, soit 5760 mn après la soutenance), un vieux Debian Squeeze, qui m'a accompagné dans le froid du R013 et qui a dû beaucoup souffrir grâce à FEniCS (cancer de disques RAID). Tu t'es libéré un mois avant l'échéance mais je te remercie quand même pour ta loyauté. Monsieur Hérisson à œil unique, ne m'en veuille pas si je t'ai lassé sur mon bureau O2C.10A. Avant de se jeter dans la poubelle de Saclay, dis merci à quiconque qui voudra prendre quelques articles sur la mécanique des milieux continus, la rupture. . .



chinese.pdf

Merci à ma famille, et surtout à ma mère, mon père et Sa Majesté le caniche Laffi le Gros pour leur soutien et encouragement.

Enfin, j'aimerais remercier tous ceux et celles que j'ai côtoyés et auxquels je n'ai pas eu de chance de dire merci.

# Contents

<b>Résumé en français</b>	<b>iii</b>
<b>Avant-propos</b>	<b>ix</b>
<b>1 Introduction</b>	<b>1</b>
1.1 Dynamic Brittle Fracture in a Nutshell . . . . .	2
1.2 Griffith's Theory of Dynamic Fracture . . . . .	6
1.3 Variational Approach to Fracture . . . . .	12
1.4 Gradient Damage Modeling of Fracture . . . . .	17
1.5 Research Scope and Objectives . . . . .	21
<b>2 Dynamic Gradient Damage Models</b>	<b>25</b>
2.1 Variational Framework Based on Physical Principles . . . . .	25
2.2 Tension-Compression Asymmetry . . . . .	38
2.3 Griffith's Law in Gradient Damage Models . . . . .	47
<b>3 Numerical Implementation</b>	<b>67</b>
3.1 Spatial Discretization . . . . .	67
3.2 Temporal Discretization . . . . .	70
3.3 Implementation . . . . .	74
<b>4 Simulation Results</b>	<b>79</b>
4.1 Crack Nucleation in a Bar Under Impact . . . . .	80
4.2 Antiplane Tearing . . . . .	93
4.3 Plane Crack Kinking . . . . .	107
4.4 Dynamic Crack Branching . . . . .	111
4.5 Edge-Cracked Plate Under Shearing Impact . . . . .	122
4.6 Crack Arrest Due to the Presence of a Hole . . . . .	130
4.7 Brazilian Splitting Test on Concrete Cylinders . . . . .	132
4.8 Dynamic Fracture of L-Shaped Concrete Specimen . . . . .	138
4.9 CEA Impact Test on Beams . . . . .	144
<b>5 Conclusion and Future Work</b>	<b>153</b>
5.1 Going Dynamical . . . . .	153
5.2 Link with Phase-Field Approaches . . . . .	156
5.3 Better Understanding of Gradient Damage Modeling . . . . .	157
5.4 Experimental Validation . . . . .	159
<b>A Griffith Revisited</b>	<b>161</b>
<b>B Detailed Calculations</b>	<b>167</b>





# 1

## Introduction

### Contents

---

<b>1.1</b>	<b>Dynamic Brittle Fracture in a Nutshell</b>	<b>2</b>
1.1.1	Kinematics and physics	2
1.1.2	Classification of different modeling approaches	5
<b>1.2</b>	<b>Griffith's Theory of Dynamic Fracture</b>	<b>6</b>
1.2.1	Boundary-value evolution problem	7
1.2.2	Theoretical and experimental critiques	9
1.2.3	Numerical aspects	11
<b>1.3</b>	<b>Variational Approach to Fracture</b>	<b>12</b>
1.3.1	Crack evolution as an energy minimization movement	12
1.3.2	Elliptic regularization	14
1.3.3	Extension to dynamics	16
<b>1.4</b>	<b>Gradient Damage Modeling of Fracture</b>	<b>17</b>
1.4.1	Variational formulation and its justification	17
1.4.2	Two different interpretations of the damage gradient	18
1.4.3	Modeling of tension-compression asymmetry	20
<b>1.5</b>	<b>Research Scope and Objectives</b>	<b>21</b>

---

This chapter exposes the reader to the general physical context and outlines the motivation and objectives of the present work. The fundamental background of dynamic brittle fracture is first recalled in Section 1.1, where a classification of different modeling approaches is also given. Some representative models are then discussed with respect to their aptitude to approximate dynamic brittle fracture phenomena both from a physical and numerical point of view. The Griffith's theory is first recalled in Section 1.2. It constitutes the most classical approach to fracture mechanics and provides a reference model for comparisons with other formulations. With the help of modern tools of the Calculus of Variations, its main idea based on energetic competition is formalized and extended to a general setting within the variational approach to fracture, of which an introductory presentation is given in Section 1.3. Finally we turn to the main objective of this present work and provide a general presentation and physical motivations of the gradient damage model in Section 1.4. Finally the scope and objectives of the present contribution is summarized in Section 1.5.

## 1.1 Dynamic Brittle Fracture in a Nutshell

### 1.1.1 Kinematics and physics

The concept of cracks constitutes the *raison d'être* of fracture mechanics. Specifically, fracture mechanics focuses on the evolution of cracks as well as their impact on the structural behaviors. The objective of fracture mechanics is to better understand different crack evolution phases by providing their corresponding governing physical criteria. They can then be used by civil engineers and material scientists to optimize the structural dimensioning and design, and to readjust the chemical composition to ensure integrity of the composite for instance. From a kinematic point of view, cracks  $\Gamma_t$  are naturally defined in the reference configuration as a moving interface in the uncracked configuration  $\Omega$ , see Figure 1.1. Due to external loading conditions, the deformed configuration  $\varphi_t(\Omega \setminus \Gamma_t)$  of the cracked body may be described by the usual displacement vector  $\mathbf{u}_t$ . The presence of cracks often leads to separation of the body into two or more pieces, where the displacement vector defined in the reference configuration becomes discontinuous across them. This constitutes a major difficulty when modeling cracks and their evolutions in a continuum mechanics framework, since displacements are in general considered to be at least continuous inside the body.



Figure 1.1 – Current cracked reference configuration  $\Omega \setminus \Gamma_t$  and its deformation defined by the displacement vector  $\mathbf{u}_t$

Cracks can be regarded as a macroscopic manifestation of material defects at a microscopic scale. Hence different materials are in general associated with a different failure mechanism. In the present work only brittle fracture phenomenon is considered, as opposed to ductile fracture.

- Generally speaking brittle fracture occurs without significant deformation of the material. Structural failure with such materials is accompanied by little energy dissipation. Quasi-brittle materials, by definition, satisfy these characteristics. It concerns ceramics, glass, rock, concrete and some polymers such as polymethyl-methacrylate (PMMA). Metals may as well observe a brittle behavior at low temperatures.
- Ductile fracture, on the contrary, is accompanied by moderate plastic (inelastic) deformation which takes place before the ultimate failure. It concerns mostly metals at room or higher temperatures. The ductile-to-brittle transition depends on the temperature, on the composition, but also on the strain rate the material is subject to, see for example (Kalthoff, 2000).

- To discriminate between brittle and ductile fracture, near-tip behaviors of the mechanical fields can be analyzed, see Figure 1.2. Brittle fracture can be characterized by a globally nearly elastic behavior, possibly except inside a small region, called fracture process zone, where non-elastic effects (plasticity, damage, . . . ) take place. It is called the small-scale yielding condition where the elasticity dominates the structural behavior and the crack evolution. However, in ductile fracture, plasticity plays an essential role since a significant plastic zone surrounds the crack tip. Inelastic material behaviors must be taken into account in order to predict the evolution of the cracked body.



Figure 1.2 – Comparison between brittle fracture (a) and ductile fracture (b) in terms of near-tip behaviors of the mechanical fields

In this work inertial effects are taken into account in the structural analysis of cracked bodies. This is the object of dynamic fracture. As opposed to the traditional quasi-static approach, the framework of dynamic fracture focuses on some specific problem settings and may present some theoretic advantages.

- The introduction of kinetic energy brings a physical time scale to the fracture problem. Inertial effects could not be ignored if one wants to analyze the transient behavior of structures due to external dynamic loadings such as impact or the interactions between stress waves and the crack (Ravi-Chandar & Knauss, 1984d).
- Even though the structure is subject to slowly applied loads such that the quasi-static hypothesis is verified, the crack itself may still propagate at a speed comparable to that of the mechanical waves. In the classical fracture mechanics theory, such situations refer to an *unstable propagation* since crack evolution is no longer controllable through external hard or soft devices applied to the body. A complete theoretic framework for analyzing such unstable propagations necessarily includes dynamics.

Dynamic fracture is not only reserved for industrial civil structures. It also concerns daily objects whenever they are subject to extreme loading conditions. A broken screen of a smartphone due to impact is illustrated in Figure 1.3. The screen is made of glass and the failure can be characterized as

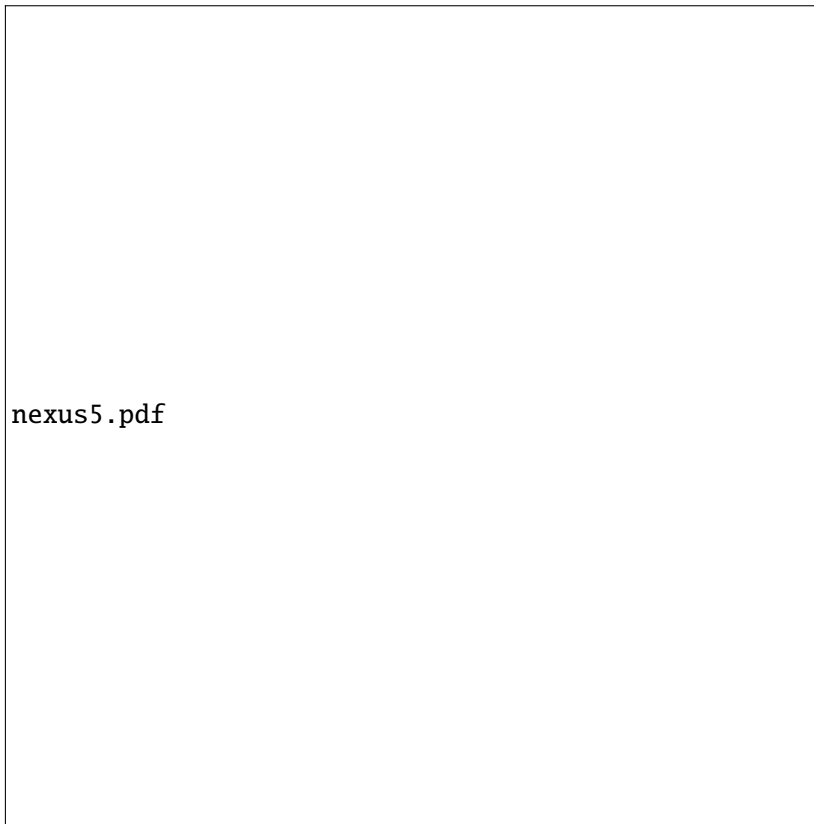


Figure 1.3 – Several (dynamic) fracture mechanics phenomena displayed by the *post-mortem* crack patterns on the broken screen of a Google Nexus 5 phone obtained after an unintentional drop test

brittle fracture. The temporal and spatial evolution of cracks can be characterized by several stages or events which are summarized as follows. The temporal evolution focuses on *when* cracks propagate:

- **Nucleation and/or initiation** concerns the appearance of a propagating crack inside a body (or on its boundary) due to external loading. On the one hand, *nucleation* refers to the formation of cracks from a perfectly flawless configuration. From a material point of view, the nucleation event should be considered as a macroscopic modeling simplification since micro cracks or flaws may be present at a lower scale and may eventually evolve into macro-cracks under the influence of external loading. These material or structural imperfections are in general not accounted for in a continuum mechanics approach and we consider that a body is initially sound when stress singularity is absent from an elastic modeling viewpoint. On the other hand, crack *initiation* refers to the time at which the existing macro-crack or the defect begins to propagate in the structure.
- **Propagation**, being stable or not, is the most dangerous part of defect evolution for industrial structures as it constitutes a threat to structural integrity. Crack propagation is systematically accompanied by an energy consumption characterized by the fracture toughness of the material. It measures the energy required to open a crack of unit surface. This energy consumption is balanced by a release of the total mechanical energy. This energy balance concept is the cornerstone of several theoretical models of fracture mechanics (Griffith, 1921; Mott, 1947). According to experiments performed on brittle materials (Ravi-Chandar & Knauss, 1984c), there exists a terminal velocity for crack propagation depending on the solicitation modes.
- **Arrest** refers to a propagating crack that becomes stationary in a continuous or abrupt fashion.

In the latter case, arrest can no longer be considered as a time reversal of the crack initiation process (Ravi-Chandar & Knauss, 1984a).

Meanwhile, the spatial evolution refers to the path along which the crack propagates, *i.e.* how cracks propagate. In a two-dimensional setting, the crack path can be characterized by the following concepts:

- **Curving and kinking** concerns curvature evolution of the crack path. When idealizing the crack as a mathematical curve  $l \mapsto \gamma(l)$ , crack curving refers to a tangent that varies continuously along the path, as opposed to kinking where a discontinuous change of crack propagation direction takes place, see Figure 1.4. This last can be considered as a theoretic modeling of a crack that suddenly deviates from its initial propagation direction.

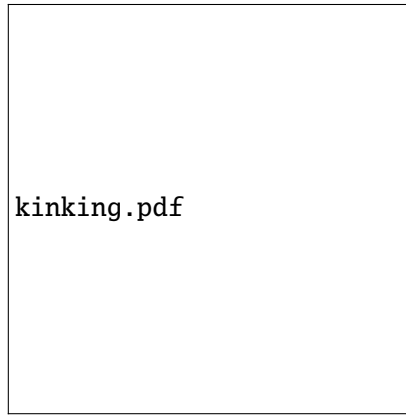


Figure 1.4 – Curved crack path versus kinked crack path

- **Branching** refers to the splitting of a primary propagating crack into two or several branches. From a macroscopic modeling viewpoint, it involves a topology change of the crack set, since additional crack tips are created after such a process. This point of view of crack branching is experimentally recorded by (Schardin, 1959). Meanwhile, by investigating the microstructure of fracture process zone, it is observed in (Ravi-Chandar & Knauss, 1984b, 1984c; Sharon & Fineberg, 1996; Sharon, Gross, & Fineberg, 1995) that such macro-branching phenomenon is always preceded by the so-called micro-branching attempts. It corresponds to a dynamic instability reviewed in (Fineberg & Marder, 1999) where micro cracks develop and interact with the primary single crack when propagating above a critical velocity. More energy is dissipated along the main crack (see (Sharon, Gross, & Fineberg, 1996)), which provides a physical interpretation of using an apparent velocity-dependent fracture toughness for the primary crack.

Remark that other more complex topology changes could affect the spatial path of the crack set, which include coalescence (merging) of several cracks for instance.

### 1.1.2 Classification of different modeling approaches

A non-exhaustive review of mainstream physical and computational models of fracture mechanics is given here. The discussion is intentionally limited to approaches formulated within the Continuum Mechanics framework where the body occupies a connected subset  $\Omega$  of the Euclidean space as its reference configuration. The kinematics and forces that the body experiences can be described by material fields defined on  $\Omega$ . A finer description at a lower scale, such as molecular dynamics models (Abraham, Brodbeck, Rafey, & Rudge, 1994), lattice dynamics calculations (Marder & Gross, 1995) and the discrete elements method (Hentz, Donzé, & Daudeville, 2004), is not considered here.

Based on the kinematic description of cracks in the continuum body, different fracture mechanics models can be classified into the following three categories:

1. **Discrete modeling approach** where the crack is considered as an explicit sharp interface in the body across which the displacement vector is discontinuous. The advantage of the sharp-interface description of cracks lies in the explicit definition of a crack surface in the body, which leads to an unambiguous and quantifiable evolution of the crack front. It includes but is not limited to the classical Griffith's theory of fracture mechanics (Freund, 1990), the variational approach to fracture (Bourdin, Francfort, & Marigo, 2008; Francfort & Marigo, 1998; Larsen, 2010) and the cohesive zone models (Barenblatt, 1962).
2. **Smeared modeling approach** where strong discontinuities are regularized by strain localizations within a finite and thin band. The smeared description of cracks no longer refers to a certain topology of the crack as compared to the discrete modeling approach. Precisely, it provides an approximation of the crack topology which may become particularly complex due to branching and coalescence phenomena. The gradient damage model (Pham, Amor, Marigo, & Maurini, 2011; Pham & Marigo, 2010b) formulated in the rate-independent evolution framework in the sense of (Mielke, 2005) falls into this category. It admits other physics-based formulations such as (Comi, 1999) or variational formulations like (Lorentz & Andrieux, 1999). The phase-field models originated from the mechanical community (Borden, Verhoosel, Scott, Hughes, & Landis, 2012; Hofacker & Miehe, 2012; Miehe, Welschinger, & Hofacker, 2010) and the physical community (Hakim & Karma, 2009; Karma, Kessler, & Levine, 2001) are also similar in essence to gradient damage approaches. We observe that the gradient of the damage field or the phase field is introduced in these models. It can be considered as a non-local regularization of conventional mathematically ill-posed local damage models reviewed in (Lorentz & Andrieux, 2003; Peerlings, Geers, de Borst, & Brekelmans, 2001). The peridynamic approach is also gaining popularity in the last years (see (Silling & Lehoucq, 2010) for a review on its theory and applications). It can be regarded as a generalized non-local continuum mechanics model.
3. A combination of the previous two approaches where a **transition** between a smeared description and a discrete description of cracks is achieved. The “element deletion method” reviewed in (Song, Wang, & Belytschko, 2008) could be considered as the simplest method in this category. The work of (Cazes, Coret, Combescure, & Gravouil, 2009; Cuvilliez, Feyel, Lorentz, & Michel-Ponnelle, 2012; de Borst, Remmers, Needleman, & Abellan, 2004) concerns a transition between non-local damage models and the cohesive zone model. The Thick Level Set approach introduced in (Moës, Stolz, Bernard, & Chevaugeon, 2011; Moreau, Moës, Picart, & Stainier, 2015) provides another unified framework incorporating a discontinuous crack description surrounded by continuous strain-softening regions.

## 1.2 Griffith's Theory of Dynamic Fracture

Several formulations of the Griffith's theory of dynamic fracture mechanics exist. The Newtonian approach (Freund, 1990) is the most classical one and is herein summarized. The Eshelbian point of view (Eshelby, 1975) exploits the symmetry possessed by a generalized action integral but the derived so-called energy-momentum tensor still needs to be combined with local momentum and energy balance conditions to produce the crack equation of motion (Adda-Bedia, Arias, Amar, & Lund, 1999; Maugin, 1994).

The fundamental assumption underlying the Griffith's theory of fracture concerns the energy dissipation of a propagating crack  $\Gamma_t$ . It is modeled as a sharp-interface surface in the bulk  $\Omega$ . Griffith postulates in his pioneering work (Griffith, 1921) that the creation of a crack calls for an energy consumption that is proportional to its total area  $|\Gamma_t|$  which characterizes the amount of energy needed to break the atomic bonds on the crack surface at a microscopic scale. The crack surface can thus be regarded to possess a surface energy which reads

$$S_t = G_c \cdot |\Gamma_t| \quad (1.1)$$

where  $G_c$  is called the fracture toughness, *i.e.* the energy required to create a crack of unit surface in the body  $\Omega$ . Griffith assumes that  $G_c$  is a material constant that characterizes the resistance of the material to crack formation.

### 1.2.1 Boundary-value evolution problem

The boundary-value evolution problem is obtained by considering local momentum equilibrium in the uncracked bulk and an energy flux integral entering into the crack tip which balances the energy dissipated due to crack propagation (Cherepanov, 1989; Nakamura, Shih, & Freund, 1985). Consider a two-dimensional homogeneous and isotropic cracked body as illustrated in Figure 1.1. In this case the crack can be parametrized by its current arc-length denoted by  $l_t$ . We often place ourselves under the small displacement hypothesis for brittle materials, which leads to the definition of the linearized strain tensor  $\varepsilon_t = \varepsilon(\mathbf{u}_t) = \frac{1}{2}(\nabla \mathbf{u}_t + \nabla^T \mathbf{u}_t)$ . Hence, the Griffith's theory of fracture is usually referred as the linear elastic fracture mechanics (LEFM) theory in the literature. Away from the crack, the classical elastodynamic equation governs the kinematics of the body, which in the absence of body forces reads

$$\begin{aligned} \rho \ddot{\mathbf{u}}_t &= \operatorname{div} \boldsymbol{\sigma}_t \quad \text{in } \Omega \setminus \Gamma_t \\ \boldsymbol{\sigma}_t \mathbf{n} &= \mathbf{F}_t \quad \text{on } \partial\Omega_F \end{aligned} \quad (1.2)$$

where  $\rho$  refers to the material density and  $\mathbf{F}_t$  denotes the surface traction density applied on the subset  $\partial\Omega_F$  of the boundary. The stress tensor  $\boldsymbol{\sigma}_t = \mathbf{A}\varepsilon_t$  admits an explicit expression via the use of Lamé coefficients

$$\boldsymbol{\sigma}_t = \lambda \operatorname{tr}(\varepsilon_t) \mathbb{I} + 2\mu \varepsilon_t$$

with  $\mathbb{I}$  the identity tensor of rank 2. Plugging this expression into the dynamic equilibrium equation in the bulk gives the Navier's equations of motion

$$\rho \ddot{\mathbf{u}}_t = (\lambda + \mu) \nabla(\operatorname{div} \mathbf{u}_t) + \mu \operatorname{div}(\nabla \mathbf{u}_t) \quad (1.3)$$

where  $\operatorname{div}(\nabla \mathbf{u}_t)$  denotes the vectorial Laplacian of  $\mathbf{u}_t$ . On the one hand, if we suppose that the displacement is irrotational  $\operatorname{rot} \mathbf{u}_t = \mathbf{0}$ , then (1.3) reduces to

$$\ddot{\mathbf{u}}_t = c_d^2 \operatorname{div}(\nabla \mathbf{u}_t)$$

where  $c_d = \sqrt{(\lambda + 2\mu)/\rho}$  is the dilatational wave speed. On the other hand, considering equivoluminal waves that satisfy  $\operatorname{div} \mathbf{u}_t = \mathbf{0}$  in (1.3), we obtain

$$\ddot{\mathbf{u}}_t = c_s^2 \operatorname{div}(\nabla \mathbf{u}_t)$$

with  $c_s = \sqrt{\mu/\rho}$  denoting the shear wave speed. For a general wave evolution, it can be partitioned into a purely dilatational component and a purely shearing component, see for example (Sternberg, 1960). Suppose that the crack evolution  $t \mapsto \Gamma_t$  is known, the displacement time evolution problem can then be completed by the Dirichlet boundary conditions of  $\mathbf{u}_t$  prescribed on a subset  $\partial\Omega_U$  of the boundary, as well as a set of initial conditions  $(\mathbf{u}_0, \dot{\mathbf{u}}_0)$  defined on the initial cracked configuration  $\Omega \setminus \Gamma_0$ .

In the presence of the crack  $\Gamma_t$ , the displacement and stress present a well-known  $O(r^{1/2})$  and  $O(r^{-1/2})$  asymptotic behaviors at the crack tip when the elastodynamic equation (1.3) is solved in the bulk of  $\Omega \setminus \Gamma_t$ . In the case of an in-plane fracture problem, these two fields admit the following near-tip form

$$\begin{aligned} \mathbf{u}_t(r, \theta) &\approx \frac{K_I(t)\sqrt{r}}{\sqrt{2\pi\mu}} \boldsymbol{\Theta}_I(\theta, \dot{l}_t) + \frac{K_{II}(t)\sqrt{r}}{\sqrt{2\pi\mu}} \boldsymbol{\Theta}_{II}(\theta, \dot{l}_t) + \dots \\ \boldsymbol{\sigma}_t(r, \theta) &\approx \frac{K_I(t)}{\sqrt{2\pi r}} \boldsymbol{\Sigma}_I(\theta, \dot{l}_t) + \frac{K_{II}(t)}{\sqrt{2\pi r}} \boldsymbol{\Sigma}_{II}(\theta, \dot{l}_t) \end{aligned} \quad (1.4)$$

where the  $K$ 's are the stress intensity factors. Compared to the quasi-static regime, the angular functions  $\boldsymbol{\Theta}$ 's and  $\boldsymbol{\Sigma}$ 's depend on the current crack speed. When the crack propagates  $\dot{l}_t > 0$ , the near tip behaviors for the velocity and the acceleration fields develop the following steady state form

$$\dot{\mathbf{u}}_t(\mathbf{x}) \approx -i \nabla \mathbf{u}_t \tau_t = O(r^{-1/2}) \quad \text{and} \quad \ddot{\mathbf{u}}_t(\mathbf{x}) \approx -i \nabla \dot{\mathbf{u}}_t \tau_t = O(r^{-3/2}), \quad (1.5)$$



where  $\boldsymbol{\tau}_t$  denotes the current propagation direction. The asymptotic expansion of the velocity reads

$$\dot{\mathbf{u}}_t(r, \theta) \approx \frac{\dot{l}_t K_I(t)}{\sqrt{2\pi r \mu}} \mathbf{V}_I(\theta, \dot{l}_t) + \frac{\dot{l}_t K_{II}(t)}{\sqrt{2\pi r \mu}} \mathbf{V}_{II}(\theta, \dot{l}_t). \quad (1.6)$$

We now turn to the governing equation of the crack growth in the Griffith's theory. Based on the thermodynamic energy balance law, the rate of energy that flows into the crack region delimited by an arbitrary contour  $C$  encircling the crack tip (see Figure 1.1) can be evaluated by the following energy flux

$$F_t = \int_C \left( (\boldsymbol{\sigma}_t \mathbf{n}) \cdot \dot{\mathbf{u}}_t + (\psi(\boldsymbol{\varepsilon}_t) + \kappa(\dot{\mathbf{u}}_t)) \dot{l}_t (\mathbf{n} \cdot \boldsymbol{\tau}_t) \right) ds. \quad (1.7)$$

where  $\psi$  and  $\kappa$  denote respectively the elastic energy density and the kinetic energy density and  $\mathbf{n}$  is the normal vector pointing out of the contour  $C$ . The thickness of the body  $\Omega$  is neglected and quantities are defined per unit thickness as usual for plane problems. The first term in (1.7) stands for the rate of work applied to the crack region inside  $C$  while the second term corresponds to the energy transport due to crack propagation. A detailed derivation of (1.7) can be found for example in (Freund, 1972; Nakamura et al., 1985). From this energy flux, a dynamic energy release rate  $G_t$  that corresponds to the amount of energy released per unit crack extension can be defined by dividing (1.7) by the current crack velocity  $\dot{l}_t$  and taking a contour that shrinks onto the crack tip. It is physically meaningful since the energy flux is indeed path-independent due to the steady state condition (1.5) near the crack tip. If  $r$  denotes the maximum distance of  $C$  to the crack tip, we have

$$G_t = J_t = \lim_{r \rightarrow 0} \int_{C_r} \mathbf{J}_t \mathbf{n} \cdot \boldsymbol{\tau}_t ds \quad \text{with} \quad \mathbf{J} = \left( \psi(\boldsymbol{\varepsilon}(\mathbf{u}_t)) + \kappa(\dot{\mathbf{u}}_t) \right) \mathbb{I} - \nabla \mathbf{u}_t^T \boldsymbol{\sigma}_t. \quad (1.8)$$

It can be regarded as the dynamic extension of the classical  $J$ -integral in the sense of (Cherepanov, 1967; Rice, 1968). By using the asymptotic near-tip behavior of the fields (1.4) and (1.6), the dynamic energy release rate can be related to the stress intensity factors via the following equation

$$G_t = \frac{1}{\bar{E}} \left( A_I(\dot{l}_t) K_I(t)^2 + A_{II}(\dot{l}_t) K_{II}(t)^2 \right) \quad (1.9)$$

where  $\bar{E} = E/(1 - \nu^2)$  for plane strain problems,  $\bar{E} = E$  for plane stress problems and  $A$ 's are two universal material-dependent functions (Freund, 1990, p. 234). This is the generalization of the Irwin's formula (Irwin, 1957) since when the crack is stationary  $\dot{l}_t \rightarrow 0$ , these two functions converge to 1.

Due to the fundamental assumption of a Griffith crack (1.1), the amount of energy consumed per unit crack advance in the case of a sharp-interface surface is simply  $G_c$ , a material constant. The stress-free condition  $\boldsymbol{\sigma}_t \mathbf{n} = \mathbf{0}$  is found on the crack lip. Owing to the energy balance of the cracked body, the following Griffith criterion holds

$$\dot{l}_t \geq 0, \quad G_t \leq G_c \quad \text{and} \quad (G_t - G_c) \dot{l}_t = 0. \quad (1.10)$$

The Griffith's criterion provides an equation of motion of the crack tip. Several consequence of (1.10) derived in (Freund, 1990) include but are not limited to

- The limiting speed for an in-plane crack is the Rayleigh wave speed  $c_R$  which depends only on the Poisson's ratio. It is defined as the root of the following Rayleigh equation

$$R(c) = 4\alpha_d \alpha_s - (1 + \alpha_s^2)^2 = 0 \quad (1.11)$$

where  $\alpha_d = \sqrt{1 - c^2/c_d^2}$  and  $\alpha_s = \sqrt{1 - c^2/c_s^2}$ . Approximation methods exist to give an explicit expression of the Rayleigh wave speed, see for example (Royer & Clorennec, 2007). Its evolution as a function of  $\nu$  is provided in Figure 1.5.

- The limiting speed for a mode-III crack is the shear wave speed  $c_s$ .

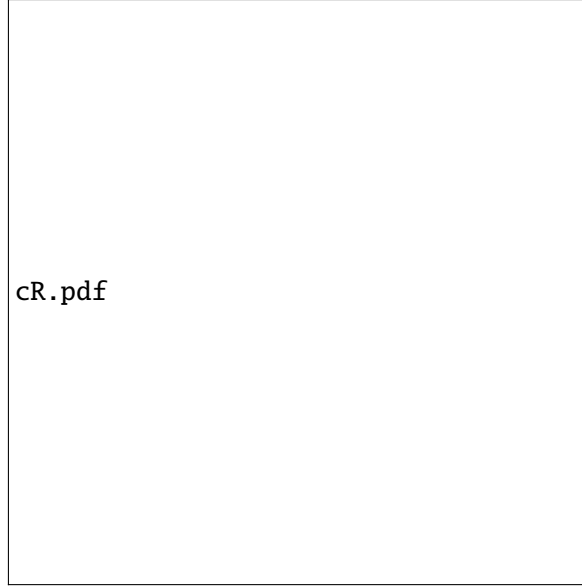


Figure 1.5 – Rayleigh wave speed as a function of the Poisson's ratio. Comparison between the exact solution of (1.11) and the approximation provided in (Royer & Clorennec, 2007)

*Remark* (Prediction of the crack speed in inplane cases). According to stress singularity analyses, see for example (Freund, 1990), the dynamic stress intensity factors admit the following form

$$K_I(t, l_t, \dot{l}_t) = k(\dot{l}_t) K_I(t, l_t, 0),$$

where  $K_I(t, l_t, 0)$  corresponds to the intensity factor of a *stationary* crack under the same geometry and loading conditions. This quantity can be evaluated using interaction integrals (Réthoré, Gravouil, & Combescure, 2005). Assuming a constant fracture toughness  $G_c$ , then according to Griffith's law (1.10), during propagation we have

$$G_t = \frac{1}{E} A_I(\dot{l}_t) k(\dot{l}_t)^2 K_I(t, l_t, 0)^2 = G_c. \quad (1.12)$$

It is found that the universal function  $g(v) = A_I(v)k(v)^2$  can be approximated by a linear function

$$g(v) = A_I(v)k(v)^2 \approx 1 - \frac{v}{c_R}.$$

From (1.12), an approximate crack velocity can thus be explicitly deduced. This method is frequently referred to the Kanninen's formula (Kanninen & Popelar, 1985) in the computational fracture mechanics community, see for example (Haboussa, Grégoire, Elguedj, Maigre, & Combescure, 2011).

### 1.2.2 Theoretical and experimental critiques

From the physical point of view, the main drawbacks of the Griffith's theory as a modeling approach to dynamic brittle fracture concerns crack nucleation and crack path prediction, see (Francfort & Marigo, 1998) for a discussion on these points for the quasi-static Griffith's theory which applies also in the dynamic case. Remark however that through the introduction of inertia effects, the Griffith's theory accompanied with the dynamic energy release rate (1.8) is able to account for the classically termed “brutal” or “unstable propagation” cases where cracks propagate at a velocity comparable to the material sound speed such that the quasi-static hypothesis no longer holds. On the contrary, such propagations which may involve “temporal” discontinuities can not be considered by the quasi-static Griffith's theory, see (Francfort & Marigo, 1998).

**Nucleation** The Griffith criterion (1.10) based on the competition between the energy release rate and the material fracture toughness fails to predict crack nucleation from a body that lacks enough stress singularities, see (Marigo, 2010). Moreover, it is known that the remote tensile stress  $\sigma$  needed to initiate a pre-existing crack of length  $l$  inside an infinite domain scales with  $1/\sqrt{l}$ . When  $l$  is large this size effect is validated experimentally (Griffith, 1921), however for small cracks  $\sigma$  tends to infinity and it is surely not the correct behavior for real materials which possess a maximal stress.

To circumvent the crack nucleation deficiency present in the classical Griffith's theory, several possibilities can be considered.

1. The first one concerns the introduction of a *strength* criterion which bounds the maximal stress magnitude in the body. Still adopting a sharp-interface description of cracks, the cohesive zone model (Barenblatt, 1962; Elices, Guinea, Gómez, & Planas, 2002) falls into this category. It revisits the Griffith's modeling of cracks (1.1) by providing a new description of the crack surface energy

$$S_t = \int_{\Gamma_t} \phi(\llbracket \mathbf{u}_t \rrbracket) ds \quad (1.13)$$

where the potential  $\phi$  characterizes the local material toughness that corresponds to a displacement jump  $\llbracket \mathbf{u}_t \rrbracket$  on the crack lip. The derivative of  $\phi$  gives then the traction acting on the crack lips. It regularizes the initial Griffith theory by introducing a critical/maximal stress  $\sigma_c = \|\phi'(\mathbf{0})\|$  that the material can support. When the displacement jump becomes sufficiently big, the potential  $\phi$  converges to the Griffith fracture toughness  $G_c$ , corresponding to a completely open crack portion free of stress traction.

2. Crack nucleation with the Griffith's surface energy (1.1) can be predicted in the variational approach to fracture through the use of global minimizations. It will be discussed in Section 1.3.
3. Finally thanks to an evolution criterion of the damage or phase field variable, crack nucleation is also possible in the smeared modeling approaches which will be discussed in Section 1.4.

**Path** We observe that the Griffith criterion (1.10) is just a scalar equation governing the temporal evolution of the crack arc length. It is due to the fundamental assumption of the Griffith's theory concerning the crack topology: a single crack surface that propagates along an arbitrary but given path without branching or other topology changes. Path prediction itself is not part of the Griffith's theory and must be determined by additional physics-motivated criteria.

- Concerning crack kinking, several models compete with each other: the Principle of Local Symmetry (Gol'Dstein & Salganik, 1974), the  $G$ -max criterion (Hussain, Pu, & Underwood, 1974) and the  $\sigma_{\theta\theta}$ -max criterion (Erdogan & Sih, 1963), for instance. Although they predict numerically close in-plane kinking angles from isotropic materials, they indeed give incompatible results from a theoretic point of view, see for example (Chambolle, Francfort, & Marigo, 2009) for a comparison between the PLS and the  $G$ -max criterion. Furthermore, kinking prediction in the presence of a mode-III component becomes even more tedious (Pham & Ravi-Chandar, 2016). These criteria were developed initially for quasi-static crack kinking problems, however they are also frequently used in dynamic situations (Grégoire, Maigre, Réthoré, & Combescure, 2007; Haboussa et al., 2011). A fully dynamic criterion that predicts crack kinking is still an on-going research subject (Adda-Bedia & Arias, 2003).
- As far as the crack branching is concerned, currently there exists only necessary indications or conditions for the macro or micro-branching phenomena within the framework of Griffith's theory (1.10), see (Katzav, Adda-Bedia, & Arias, 2007; Ravi-Chandar & Knauss, 1984c). In (Yoffe, 1951), Yoffe analyzes the stress distribution ahead of the crack tip in mode-I situations and finds that when the crack velocity exceeds approximately 60% of the Rayleigh wave speed, the maximum  $\sigma_{\theta\theta}$  stress is no longer situated in front of the crack tip, see Figure 1.6. This could be regarded as a necessary condition which reflects a redistribution of the stress tensor after

branching. However the critical speed found is strictly larger than the experimentally found one, where  $v_c \approx 0.4c_R$ , see (Fineberg & Marder, 1999).

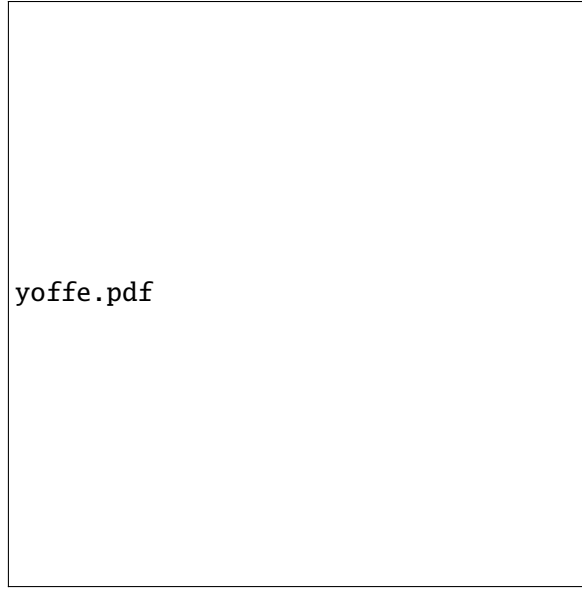


Figure 1.6 – The hoop stress variation as a function of the angle with the propagation direction, for several velocities. The Poisson's ratio is taken to be 0.2

Another approach is based on the Eshelby's energetic approach. According to (Eshelby, 1970), crack branching is possible only if the crack has acquired enough energy so that after branching the Griffith criterion (1.10) still holds for branched cracks. A limiting critical branching speed implies hence a vanishing velocity of the branches. Based on this concept as well as the Principle of Local Symmetry (Gol'Dstein & Salganik, 1974), authors of (Katzav et al., 2007) derive a necessary condition of crack branching and predict a critical velocity  $v_c \approx 0.46c_R$ . This provides hence a better approximation of the experimentally found critical speed. Nevertheless crack branching phenomena contain microscopic effects (Ravi-Chandar & Knauss, 1984b) and are of 3-d nature (Fineberg & Marder, 1999). Better understanding this dynamic instability is still an active on-going research subject, see (Bouchbinder, Goldman, & Fineberg, 2014; Fineberg & Bouchbinder, 2015).

**Propagation** The limiting crack speed (the Rayleigh wave speed for in-plane crack propagation, for example) is hardly observed in experiments, see (Ravi-Chandar & Knauss, 1984c) where the terminal velocity is found to be only half of  $c_R$ . It could be explained by the micro-branching phenomena described in Section 1.1. When this dynamic instability phenomenon is suppressed, the Griffith criterion (1.10) predicts a crack evolution conforming to the experiment where the crack speed reaches indeed the theoretic limiting speed, see (Fineberg & Bouchbinder, 2015; Sharon & Fineberg, 1999). Otherwise, either we should no longer consider the crack surface as a sharp-interface but as an ensemble of micro-voids or micro-cracks along the main crack, *i.e.* a smeared description of cracks, either the fracture toughness  $G_c$  used in the Griffith criterion (1.10) should become velocity-dependent to account for more energy dissipation when the main crack propagates (Sharon et al., 1996).

### 1.2.3 Numerical aspects

Numerically we need to account for displacement discontinuities across a sharp-interface crack in a finite element setting. Traditionally the crack can only be positioned along the element edges and remeshing is needed when the crack geometry evolves since it involves a topology change of the initial mesh. The accurate evaluation of local singularities is also a major issue with the classical  $C^0$  finite element method, since the convergence rate is significantly bounded by these singularities. Since the

advent of the eXtended-Finite Element Method (Moës, Dolbow, & Belytschko, 1999) coupled with the level-set geometrical tracking framework (Stolarska, Chopp, Moës, & Belytschko, 2001), cracks can now be freely incorporated into the numerical model based on a fixed mesh. Discontinuities and crack tip singularities can be taken into account in the local interpolation functions and the convergence rate is considerably improved. Nevertheless, it should be noted that the inherent limitations of the physical model as outlined above are still present.

### 1.3 Variational Approach to Fracture

The objective of the variational approach to fracture is to settle down a complete and unified brittle fracture theory within the Continuum Mechanics framework, which is capable of predicting the onset and the space-time evolution of sharp-interface cracks with possible complex topologies which the previous sharp-interface fracture theories fail to deliver.

While the pioneering paper (Francfort & Marigo, 1998) formalizes the mathematical ideas of the variational approach to fracture, another paper (Bourdin, Francfort, & Marigo, 2000) indicates some possible directions concerning its effective numerical implementation in a finite element context. A comprehensive review paper (Bourdin et al., 2008) summarizes the characteristics of crack evolution predicted by the variational model, both for the Griffith's surface energy model (1.1) and the cohesive description of cracks (1.13). These papers have also raised continuous interests in the mathematics communities toward a better mathematical precision and understanding of the model, see (Negri, 2010) for a review on different yet similar variational approaches to fracture.

The theory is initially proposed in a quasi-static setting. A formulation of a sharp-interface dynamic fracture model constitutes still an on-going research subject within the mathematics community, see (Larsen, 2010).

#### 1.3.1 Crack evolution as an energy minimization movement

Griffith's theory is essentially based on an energetic competition between a structural energy release rate defined as the derivative of the potential energy with respect to the crack length, and a fracture toughness as a material constant characterizing macroscopic toughness. It can be readily transformed to an equivalent criterion based on energy minimization concepts, by using the total energy of the cracked body. However we recognize that the main drawbacks of the Griffith's theory (and other previous sharp-interface fracture model such as the cohesive zone model) lie in an *a priori* assumption of the crack topology upon which the concept of energy release rates relies. It's the constraint that the variational approach to fracture pioneered by (Francfort & Marigo, 1998) aims to overcome.

A mere retranslation of Griffith's original idea, the variational formulation focuses on global energetic quantities of the cracked body where cracks  $\Gamma$  are now considered to be an arbitrary closed subdomain of the body  $\Omega$  in a dim-dimensional configuration. Two energies can then be defined.

The first one concerns the surface energy

$$S(\Gamma_t) = \int_{\Gamma_t} G_c d\mathcal{H}^{\dim-1}, \quad (1.14)$$

where  $\mathcal{H}^{\dim-1}$  denotes the dim – 1 dimensional Hausdorff measure, which yields a non-zero finite value when  $\Omega$  is a sharp-interface surface or curve for 3-d or 2-d problems. It can be considered as a generalization of the Griffith's surface energy (1.1) for a large class of crack topologies. Remark that cohesive effects can be as well accounted for, by replacing the  $G_c$  constant by the potential  $\phi$  in (1.13).

The second energy is the elastic stored energy of the body at equilibrium corresponding to the crack state  $\Gamma_t$ . It reads

$$\mathcal{E}(\Gamma_t) = \inf_{\mathbf{u} \in C} \int_{\Omega \setminus \Gamma_t} \psi(\boldsymbol{\varepsilon}(\mathbf{u})) d\mathbf{x}, \quad (1.15)$$

where  $C$  is an appropriate function space that takes into account the Dirichlet boundary conditions prescribed on a portion of the boundary. Unilateral effects, see for example (Amor, Marigo, & Maurini,

2009; Francfort & Marigo, 1998), may be as well considered. The total potential energy of the cracked body is the sum of the previous two energetic quantities in the absence of body forces and surface tractions, which leads to

$$\mathcal{P}(\Gamma_t) = \mathcal{E}(\Gamma_t) + \mathcal{S}(\Gamma_t). \quad (1.16)$$

The variational approach to fracture sees the crack evolution as a minimization movement of the total energy under an irreversibility condition to prevent self-healing of cracks. Formally, with an arbitrary temporal discretization  $t^n$  with  $1 \leq n \leq N$ , the governing equations are given by

$$\Gamma^{n-1} \subset \Gamma^n, \quad \mathcal{P}(\Gamma^n) \leq \mathcal{P}(\Gamma) \text{ for all } \Gamma \supset \Gamma^{n-1}, \quad (1.17)$$

where  $\Gamma^0$  denotes an initial given crack set. As a mathematical modeling of fracture, (1.17) provides a unified and systematic approach to predict arbitrary crack evolution. In particular, crack nucleation from an initially perfectly sound structure is now possible even with the Griffith's surface energy (1.1), by comparing the elastic energy of the uncracked body and the total energy of a test cracked configuration. Concerning the crack path, the variational approach retrieves exactly the Griffith's criterion (1.10) when the crack topology is constrained along a certain predefined surface. However its scope is even further and is fully capable of delivering a crack path of complex topologies without *a priori* presuppositions, see (Bourdin et al., 2008).

The attentive readers can not fail to realize the precise minimization structure underlying (1.17): that of global minimization. As a mathematical model of brittle fracture, it is indeed a convenient postulate to fulfill the objectives of predicting crack nucleation and path in a unified framework. Nevertheless, as is already indicated by the same authors in (Chambolle et al., 2009; Francfort & Marigo, 1998), global minimization remains far from being a physics-based principle. The major concerns refer to the presence of possible energy barriers in the dependence of the total potential energy  $\mathcal{P}$  with respect to the crack set  $\Gamma$ , see for example the point  $B$  in Figure 1.7. Suppose that

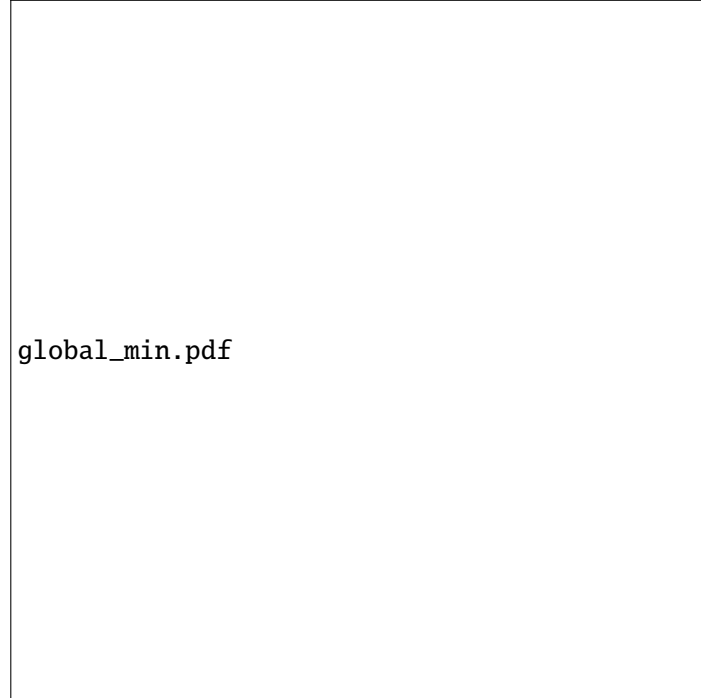


Figure 1.7 – Variational approach to fracture mechanics: global or local minimization?

the crack at the previous time step is described by  $\Gamma^{n-1}$ . Due to the loading increment at the current time step  $t^n$ , the crack will evolve into a new configuration. Assume the behavior of the potential energy described in Figure 1.7, according to global minimization (1.17), the crack will *instantaneously* propagate through the body  $\Omega$  described by the crack set  $\Gamma_{\text{glo}}^n$ , even though by doing so it must pass across an energy barrier  $B$  corresponding to an intermediate crack state which costs more energy than



the previous time step, while actually attaining *continuously* the final state  $\Gamma_{\text{glo}}^n$ . The contradiction lies in the fact that while the crack tests every configuration possible to minimize the total potential energy, it does not know if there exists a physically feasible *path* in the configuration space to arrive at that global minimum. In the same situation, a more intuitive solution will be to occupy the configuration  $\Gamma_{\text{loc}}^n$  which corresponds to a local minimum in the potential energy curve. This meta-stability concept is widely invoked in solid mechanics, see for example (Nguyen, 2000). However as compared to global minimization postulate where crack path prediction is completely topology-free, local minimization calls for a precise definition of a *distance* between two arbitrary crack states, *i.e.* defining a certain metric or topology to the crack admissible space. If the topology is too trivial, no improvement can be made compared to the Griffith's theory. If it is too rich, mathematical difficulties may arise. The variational approach to fracture based on local minimization is still an active on-going research topic, see for example (Chambolle et al., 2009; Charlotte, Francfort, Marigo, & Truskinovsky, 2000; Marigo, 2010; Negri, 2010) for a discussion on this point.

### 1.3.2 Elliptic regularization

Stated in the form of (1.17), the variational approach to fracture can be regarded as a Free Discontinuity Problem where the unknown crack set introduces displacement discontinuities somewhere in the body, see (Braides, 1998) for a mathematical treatment on this topic. The total potential energy (1.16) which we minimize in the fracture mechanics context resembles the Mumford-Shah functional (Mumford & Shah, 1989) defined in the image segmentation context. This latter energy functional admits the so-called Ambrosio-Tortorelli regularization (Ambrosio & Tortorelli, 1990) which can be regarded as an elliptic approximation converging to the initial model in a certain sense. Based on these two observations, authors of (Bourdin et al., 2000) introduce a mathematically-sound  $\ell$ -parametrized two-field functional approximation of (1.16). As we shall see in Section 1.4, this lays down a theoretic foundation of the latter gradient damage approaches (Pham, Amor, et al., 2011) and phase-field models (Miehe, Hofacker, & Welschinger, 2010).

Their method consists of introducing an auxiliary continuous scalar field defined on  $\Omega_t$ , which we note here  $\alpha_t \in [0, 1]$  anticipating its interpretation as a damage variable, which represents the unknown location of cracks  $\Gamma_t$ . We adopt the convention that  $\alpha_t(\mathbf{x}) = 1$  when  $\mathbf{x} \in \Gamma$  and  $\alpha_t(\mathbf{x}) = 0$  otherwise. The approximation of the discrete crack by a continuous field is parametrized by a small numerical parameter  $\ell$ , see Figure 1.8. As  $\ell \rightarrow 0$ , the  $\alpha$ -field should collapse into a sharp-interface description of  $\Gamma_t$ . Remark that the introduction of such fields constitutes exactly a smeared description of cracks, cf. Section 1.1.2. However here it is mainly motivated by a numerical implementation of the initial sharp-interface variational model (1.17).

The regularized energy functional of (1.16) reads

$$\mathcal{P}_\ell(\mathbf{u}_t, \alpha_t) = \mathcal{E}_\ell(\mathbf{u}_t, \alpha_t) + \mathcal{S}_\ell(\alpha_t) = \int_{\Omega} (1 - \alpha_t)^2 \psi(\boldsymbol{\varepsilon}(\mathbf{u}_t)) \, d\mathbf{x} + \int_{\Omega} G_c \left( \frac{\alpha_t^2}{4\ell} + \ell \nabla \alpha_t \cdot \nabla \alpha_t \right) \, d\mathbf{x} \quad (1.18)$$

from which we readily recognize  $\mathcal{E}_\ell$  as a regularized version of the elastic energy (1.15) when using  $\mathbf{u}_t$  at equilibrium at a fixed crack state  $\alpha_t$ . The second part of (1.18), *i.e.*  $\mathcal{S}_\ell(\alpha_t)$ , corresponds to an approximation of the Griffith crack surface energy (1.14) of the Ambrosio-Tortorelli type. Note however that an extension to the cohesive surface energy (1.13) is also possible, see (Conti, Focardi, & Iurlano, 2015). The evolutions of the  $(\mathbf{u}, \alpha)$  couple inherits from the original sharp-interface model (1.17): at every time step  $t^n$ , they achieve a global minimum of the total regularized potential functional  $\mathcal{P}_\ell$ , under the condition that the evolution of  $\alpha$  is irreversible, *i.e.*  $\dot{\alpha}_t \geq 0$ .

The convergence of this regularized model toward the initial model is made in a special setting involving  $\Gamma$ -convergence theories (Braides, 2002). Specifically, one can prove that the global minimum attained in the regularized model (1.18) converges to that of the original sharp-interface model (1.16), when  $\ell \rightarrow 0$ . Using this fundamental result, the real crack evolution governed by the global minimization principle can thus be predicted through a  $\ell$ -parametrized approximation functional. In particular, Griffith crack surface energy (1.14) can be approximated by the regularized crack surface

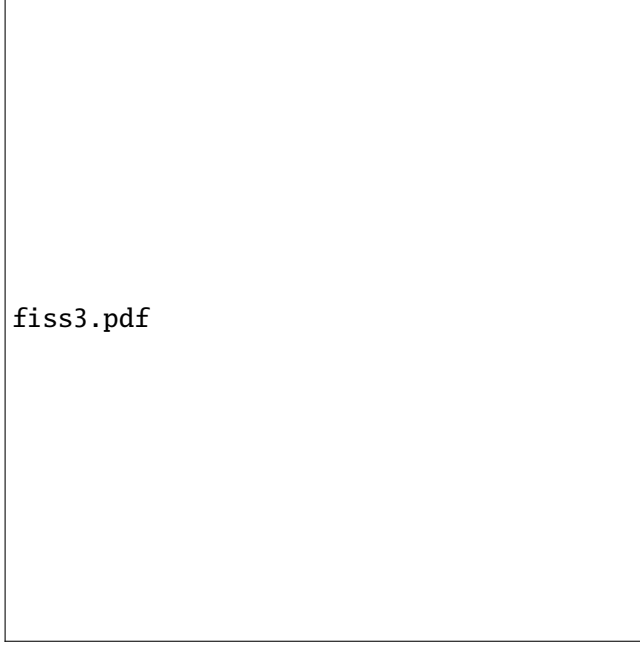


Figure 1.8 – Approximation of the discrete crack  $\Gamma_t$  by a continuous field  $\alpha_t$  parametrized by  $\ell$

energy  $\mathcal{S}_\ell(\alpha_t)$  in (1.18). In the classical two-dimensional Griffith setting for a single crack of length  $l_t$ , we have thus

$$\mathcal{S}_\ell(\alpha_t) \approx G_c \cdot l_t. \quad (1.19)$$

This equation can be used to deduce the current crack length from the knowledge of the regularized crack surface energy  $\mathcal{S}_\ell(\alpha_t)$ .

Classical  $C^0$  finite element methods can therefore be used to discretize in space the displacement  $\mathbf{u}_t$  and the newly introduced scalar field  $\alpha_t$ . Thanks to the variational approach, direct numerical implementation based on mathematical optimization methods can be applied. We observe from (1.18) that  $\mathcal{P}_\ell$  is not convex in the couple  $(\mathbf{u}_t, \alpha_t)$ , due to the crossed term in the elastic energy. It is not a surprising result since the prediction of crack nucleation or further evolution essentially lies in its non-convexity. We remark however that the regularized functional  $\mathcal{P}_\ell$  is separately convex in both variables. From a numerical point of view, this leads intuitively to the use of an alternate minimization procedure proposed in (Bourdin et al., 2000).

At every time step, it consists of alternately minimizing  $\mathcal{P}_\ell$  at fixed  $\alpha_t$  and then at fixed  $\mathbf{u}_t$  until numerical convergence upon an appropriate error norm and a tolerance. A detailed numerical analysis of the discretized model is performed in (Bourdin et al., 2008). The converged solution couple  $(\mathbf{u}_t, \alpha_t)$  can only be guaranteed to be a stationary point or at best a local minimum of the regularized energy (1.18). Numerically global minimization remains far beyond the scope of traditional gradient-based numerical algorithms and constitutes one of the difficulties of the variational approach to fracture in the sense of (1.17), see (Bourdin et al., 2008). For a triangulation with a typical mesh size  $h$ , a linear convergence  $\mathcal{O}(h)$  can be observed for the approximation  $\mathcal{S}_\ell(\alpha_t)$  of the Griffith crack surface energy (1.14). Hence the estimation (1.19) reads specifically

$$\mathcal{S}_\ell(\alpha_t) \approx \left(1 + c \frac{h}{\ell}\right) G_c \cdot l_t. \quad (1.20)$$

Note that the convergence rate is independent of the local finite element interpolation order, while the coefficient  $c$  depends on it. Another interpretation of (1.20) is given in (Bourdin et al., 2008). At a fixed  $h/\ell$ , it identifies an apparent amplified fracture toughness in the regularized fracture model (1.18). Indeed, the energy consumed per unit length of crack now reads

$$(G_c)_{\text{eff}} = \left(1 + c \frac{h}{\ell}\right) G_c, \quad (1.21)$$



where  $(G_c)_{\text{eff}}$  is the numerical amplified fracture toughness due to spatial discretization.

Besides global minimization, another numerical difficulty of the regularized fracture model concerns the parameter  $\ell$ . On the one hand it should be as small as possible to guarantee  $\Gamma$ -convergence to the sharp-interface model. On the other hand it implies an extremely computationally demanding finite-element simulation since the mesh size should be itself smaller than  $\ell$  according to (1.20).

### 1.3.3 Extension to dynamics

Formulating a variational model to dynamic fracture in the same spirit of the Francfort-Marigo model (1.17) is still an active on-going research and has not reached a relatively mature state. Let us just note that a naive adaptation of the (global) energy minimization principle (1.17) by including the kinetic energy into the total potential energy (1.16) is doomed in dynamics, due to the hyperbolic nature of the dynamic wave equation. According to (Larsen, 2010), a reasonable variational dynamic fracture model that frees itself with an *a priori* crack topology, *i.e.* the Griffith's theory (1.10), should verify the following conditions:

1. The displacement  $\mathbf{u}_t$  satisfies the elastodynamic equation (1.2) in the uncracked bulk  $\Omega \setminus \Gamma_t$  just like the Griffith case.
2. If the crack surface energy (1.14) is taken into account, then the system ensures an energy balance such that the rate of change of the total energy is equal to external power applied to the body via hard or soft devices.
3. Since a stationary crack state (accompanied by a corresponding displacement evolution) always verifies the previous two conditions, we should add an additional crack evolution criterion enforcing the crack to propagate if it is able to.

It is exactly the third item that raises mathematical and mechanical modeling difficulties. Observe again that at an arbitrary time step a separate minimization of the total energy with respect to the crack does not make sense in such dynamic setting, since the elastic energy (and the kinetic energy) is determined by the displacement (and the velocity) field defined by the current crack state and is not affected by a virtual testing crack variation. Several examples of the third item are given in (Larsen, 2010). A particular crack evolution law that merits mentioning is the following Maximal Dissipation (MD) condition

3. If a testing crack evolution  $t \mapsto K_t$  accompanied with its corresponding displacement evolution verifies 1. and 2., and if  $K_t \supset \Gamma_t$  for all  $t$ , then the real crack evolution is given by  $\Gamma_t = K_t$  for all  $t$ .

It can be seen that (MD) furnishes the worst crack scenario possible with respect to set inclusion, which resembles global minimization. However existence theories of such evolutions from a mathematical point of view are still absent and call for on-going researches.

On the contrary, an extension to the dynamic setting is indeed possible for the regularized fracture model (1.18). A separate minimization of the total energy is possible due to the fact that the elastic energy depends explicitly on the scalar field  $\alpha$ . Based on this observation, authors of (Bourdin, Larsen, & Richardson, 2011) propose the following dynamic regularized fracture model:

1.  $\mathbf{u}_t$  satisfies the wave equation in the bulk  $\Omega$  with an elastic energy indicated by (1.18), *i.e.* with a stress tensor modulated by  $(1 - \alpha)^2$ .
2.  $\alpha_t$  realizes a separate minimization of the regularized functional  $\alpha \mapsto \mathcal{P}_\ell(\mathbf{u}, \alpha)$  under the condition that  $\alpha_t$  is a non-decreasing function of time.

From a formulational point of view, these two equations can be embedded into a generalized action integral  $\mathcal{A}_\ell(\mathbf{u}, \alpha)$  of which the precise definition will be given in Section 2.1. At a certain given parameter  $\ell$ , this model produces satisfactory crack nucleation, propagation and branching phenomena

and seems to have a certain link with the Griffith's theory (1.10). Recall that the regularized functional (1.18) is obtained in a *top-down* approach since it is considered as an approximation of the sharp-interface functional (1.16). The  $\ell$  parameter is of purely numerical nature and should be chosen as small as possible. On the contrary, the dynamic regularized fracture model (Bourdin et al., 2011) here symbolized by  $\mathcal{A}_\ell$  is directly obtained by adapting the original regularized one  $\mathcal{P}_\ell$ . On the one hand, the role played by this internal length  $\ell$  is not yet clear. On the other hand, the sharp-interface model in the limit  $\ell \rightarrow 0$  of  $\mathcal{A}_\ell$  is neither obvious, see (Bourdin et al., 2011). The dynamic extension of the original variational approach to fracture (Bourdin et al., 2008) can be summarized in Figure 1.9.

$$\begin{array}{ccc}
 \mathcal{P}(\Gamma_t) & \xrightarrow{\text{dynamics}} & ? \\
 \downarrow \ell\text{-regul.} & & \uparrow \ell \rightarrow 0 \\
 \mathcal{P}_\ell(\mathbf{u}_t, \alpha_t) & \xrightarrow{\text{dynamics}} & \mathcal{A}_\ell(\mathbf{u}, \alpha)
 \end{array}$$

Figure 1.9 – In the quasi-static setting the regularized two-field fracture model  $\mathcal{P}_\ell(\mathbf{u}_t, \alpha_t)$  in (1.18) is regarded as an approximation of the sharp-interface Francfort-Marigo model  $\mathcal{P}(\Gamma_t)$  of (1.17) and convergence is achieved when  $\ell \rightarrow 0$ . In the dynamic case, we merely know how to add inertial effects into  $\mathcal{P}_\ell(\mathbf{u}_t, \alpha_t)$  to obtain a dynamic regularized model  $\mathcal{A}_\ell(\mathbf{u}, \alpha)$ . Formulating a precise sharp-interface dynamic fracture model or investigating the limit of  $\mathcal{A}_\ell(\mathbf{u}, \alpha)$  as  $\ell \rightarrow 0$  are at present a formidable challenge both from the mechanics and mathematics point of view

## 1.4 Gradient Damage Modeling of Fracture

In this section we propose to give an overview of the gradient damage approaches as a particular smeared modeling of fracture behavior. Although it admits a close link with the variational approach to fracture, the construction of the model itself is completely independent. Its use as a genuine physical model for brittle fracture starts from the pioneering work of (Pham, Amor, et al., 2011) where the properties and behaviors of the model are analyzed with respect to its aptitude to approximate fracture phenomena. In this section we indicate some justifications of the variational nature of the formulation and then give motivations of introducing the damage gradient into the model. Finally we discuss an extension of original gradient damage models to take into account tension-compression asymmetry effects.

### 1.4.1 Variational formulation and its justification

The current formulation of the gradient damage model in the rate-independent evolution framework in the sense of (Mielke, 2005) is achieved in (Pham & Marigo, 2010a, 2010b). We refer the readers to (Pham, Amor, et al., 2011) and references therein for a thorough review of its variational and constitutive ingredients as well its properties especially when applied to brittle fracture. Details of the formulation is omitted and we will mainly motivate the construction of such damage models.

The scalar field  $\alpha_t$  introduced in the elliptic regularization (see Section 1.3.2) of the variational approach to fracture is now interpreted as a damage variable ranging from 0 (intact material) to 1 (totally damaged material). It constitutes a genuine smeared description of cracks and is no longer regarded as a numerical artifact during the  $\ell$ -regularization.

The elastic-damage evolution is governed by several physics-motivated principles based on the definition of a potential energy  $\mathcal{P}(\mathbf{u}_t, \alpha_t)$  of the body  $\Omega$ . Adopting the notation used in a review paper (Pham, Amor, et al., 2011) of gradient damage models, in the absence of external work potential, the potential energy  $\mathcal{P}(\mathbf{u}_t, \alpha_t)$  reads

$$\mathcal{P}(\mathbf{u}_t, \alpha_t) = \int_{\Omega} \left( a(\alpha_t) \psi(\boldsymbol{\varepsilon}(\mathbf{u}_t)) + w(\alpha_t) + \frac{1}{2} w_1 \ell^2 \nabla \alpha_t \cdot \nabla \alpha_t \right) \mathrm{d}\mathbf{x} \quad (1.22)$$

where  $\alpha \mapsto a(\alpha)$  and  $\alpha \mapsto w(\alpha)$  denote two damage constitutive functions and  $w_1 = w(1)$ . An appropriate choice of these functions calls for a systematic study of the material and structural behaviors of a gradient damage body, see for example (Pham, Amor, et al., 2011; Pham & Marigo, 2013; Pham, Marigo, & Maurini, 2011). The two-field  $(\mathbf{u}, \alpha)$  evolution is then governed by the following

**Definition 1.1** (Quasi-Static Gradient Damage Evolution Law).

1. **Irreversibility:** the damage  $t \mapsto \alpha_t$  is a non-decreasing function of time.
2. **Meta-stability:** the current state  $(\mathbf{u}_t, \alpha_t)$  must be stable in the sense that for all  $\mathbf{v} \in C_t$  and all  $\beta \in \mathcal{D}(\alpha_t)$ , there exists a  $\bar{h} > 0$  such that for all  $h \in [0, \bar{h}]$  we have

$$\mathcal{P}(\mathbf{u}_t + h(\mathbf{v} - \mathbf{u}_t), \alpha_t + h(\beta - \alpha_t)) \geq \mathcal{P}_t(\mathbf{u}_t, \alpha_t). \quad (1.23)$$

The spaces  $C_t$  and  $\mathcal{D}(\alpha_t)$  denote respectively the kinematically admissible space taking into account the Dirichlet boundary conditions and the admissible space for damage evolution reinforcing in particular the irreversibility condition, see (Pham, Amor, et al., 2011).

3. **Energy balance:** the only energy dissipation is due to damage such that we have the following energy balance

$$\mathcal{P}(\mathbf{u}_t, \alpha_t) = \mathcal{P}(\mathbf{u}_0, \alpha_0) + \int_0^t \left( \int_{\Omega} \sigma_s \cdot \varepsilon(\dot{\mathbf{U}}_s) \, d\mathbf{x} \right) ds. \quad (1.24)$$

The formulation embodied by Definition 1.1 is variational in essence, which guarantees generality of the approach in which specific material constitutive behaviors can be taken into account, see (Pham & Marigo, 2013; Pham, Marigo, & Maurini, 2011). Similar to the variational approach to fracture, the complex crack evolution, including initiation, nucleation, propagation and branching, can be predicted within a unified framework. Several properties of the gradient damage model also rely on the fundamental variational principles on which the gradient damage model is based, see for example (Sicsic & Marigo, 2013; Sicsic, Marigo, & Maurini, 2014). It also permits a direct numerical implementation based on mathematical optimization methods similar for the regularized fracture problem, for example in (Amor et al., 2009; Pham, Amor, et al., 2011). The variational nature of damage models can be justified via the following two approaches:

1. On the one hand, thanks to the Drucker-Ilyushin postulate (Marigo, 2002), one shows that the strain work of a local elastic-damage material is necessarily a state function independent of the strain path undertaken, see for example (Pham & Marigo, 2010a). The state function is the sum of the elastic energy density  $\psi$  and the damage dissipation potential  $w$  in (1.22). The evolution laws for the  $(\mathbf{u}, \alpha)$  can thus be deduced by considering variations of the local potential energy  $\mathcal{P}_0(\mathbf{u}_t, \alpha_t)$  obtained by setting  $\ell = 0$  in the non-local counterpart  $\mathcal{P}(\mathbf{u}_t, \alpha_t)$  in (1.22).
2. On the other hand, the gradient damage evolution laws can also be interpreted as a Generalized Standard Material (with an extension of the classical point-wise normality rule to the structural scale) in the sense of (Halphen & Nguyen, 1975) which is automatically variational in nature, see the work of (Lorentz & Andrieux, 1999; Lorentz & Benallal, 2005).

## 1.4.2 Two different interpretations of the damage gradient

The presence of the damage gradient  $\nabla \alpha_t$  in the potential energy (1.22) highlights the non-locality of the material constitutive model. Two independent interpretations can be given to motivate the construction of the gradient damage models and are summarized as follows.

1. **Regularization of conventional damage models:** As the name indicates, gradient damage models belong to the general theory of continuum damage mechanics initiated by the pioneer work of (Kachanov, 1958) and then formalized in the thermodynamic framework through the work of (Lemaitre & Chaboche, 1978) and others. The damage variable  $\alpha_t$  can be regarded as a

macroscopic characterization of the effective area of the cross-section where defect takes place at a microscopic scale. Compared to these conventional damage models, the gradient damage approach (1.22) consists of introducing an additional damage gradient which *regularizes* the conventional mathematically and mechanically ill-posed local strain-softening mechanism. Either in the quasi-static setting (Benallal, Billardon, & Geymonat, 1993) or in the dynamic setting (Bazant & Belytschko, 1985), local models could produce extreme strain/damage localization within a vanishing band. Hence material failure can occur without any energy dissipation. This implies a spurious mesh dependence of the finite-element results, since the mesh size determines the localization band and the energy dissipated during such strain localization. An additional characteristic length must be introduced through the use of some non-local operators in the material constitutive behavior or in the damage criterion, see (de Vree, Brekelmans, & van Gils, 1995; Jirasek, 1998; Lorentz & Andrieux, 2003; Peerlings et al., 2001) for a thorough review of several approaches. Different non-local damage models for example presented in (Comi, 1999, 2001; de Borst et al., 2004; Lorentz & Andrieux, 2003; Peerlings, de Borst, Brekelmans, & Geers, 1998; Peerlings, de Borst, Brekelmans, & de Vree, 1996; Peerlings et al., 2001) can all be considered as a smeared approach to fracture. The peridynamic approach as reviewed in (Silling & Lehoucq, 2010) regularizes both the strain and the damage variables and also falls into this category.

According to (Lorentz & Andrieux, 2003), the gradient penalty operator which consists of introducing the gradient of the concerned variable into the total energy of the body is favored compared to the integral-type convolution operator. The question remains as to whether the strain gradient (Peerlings et al., 1996) or the damage gradient (Lorentz & Benallal, 2005; Pham, Amor, et al., 2011) is to be introduced. A tangible answer is provided in the work of (Le, Maurini, Marigo, & Vidoli, 2015), where it is shown that the damage-regularized model should be preferred to the strain-regularized model. Indeed, in the latter case the damage variable may continue developing into a diffuse region surrounding the strain localization. Energy dissipation in such process is not physics-based from a fracture modeling point of view. On the contrary, in gradient damage models strain localization is accompanied by a stationary damage profile corresponding to a finite and definite energy dissipation due to crack nucleation, which can be interpreted as the material toughness.

2. **Improvement of the variational approach to fracture:** One can not fail to realize the similarity between the gradient damage potential energy (1.22) and that of the regularized fracture model (1.18) initially proposed in (Bourdin et al., 2000) for Griffith's surface energy (1.1). The presence of the damage gradient can thus be considered as a *hint* through such regularization process. The major difference resides in the fact that in the variational approach to fracture the  $\ell$ -regularized potential (1.18) is considered as a purely numerical artifact invented to solve the real minimization problem (1.17), while here the gradient damage approach is considered to be a genuine physical model *per se*. Indeed, the  $\ell$  parameter is considered here as a material parameter and hence possesses a finite value, contrary to the regularized fracture model where  $\ell$  is purely numerical in nature and should be chosen as small as possible. Geometrically  $\ell$  determines the *band* of the damaged region as can be seen in Figure 1.8. The potential energy (1.22) captures the Ambrosio-Tortorelli regularization via a particular choice of the constitutive functions. Based on rigorous  $\Gamma$ -convergence results in (Braides, 2002), a rigorous link can be established between the gradient damage model and its underlying sharp-interface model as  $\ell \rightarrow 0$  in a  $\Gamma$ -convergence sense for a general class of these constitutive functions. However here the sharp-interface model is merely considered as a limit behavior of the gradient damage model while the latter is regarded as an improvement of the variational approach to fracture. This interpretation is mainly motivated by the following facts:

- Recall that the minimization structure behind the variational approach to fracture is based on global minimization (cf. Section 1.3.1). In solid mechanics, a meta-stability principle is a more physically grounded approach and provides a selection criterion of a multitude

of *equilibrium* states in damage mechanics, see the work of (Benallal & Marigo, 2007; Nguyen, 2000). As far as numerical implementation is concerned, local minimization is also more accessible from traditional gradient-based algorithms. The meta-stability principle (1.23) as used in the quasi-static gradient damage model compares thus only a variation of the current state within a neighborhood, and brutal jumps across energy barriers are prevented. In this improved variational framework based on local minimization, authors of (Sicsic & Marigo, 2013) establish a rigorous link between the gradient damage evolution and the Griffith's theory of dynamic fracture. The damage band evolution is governed by an asymptotic Griffith's law based on the energy release rate of the outer problem and the dissipated energy inside the damage band. The internal length receives here a physical interpretation since it achieves a separation of scales between the classic linear elastic fracture mechanics (LEFM) and the damage process zone undergoing a strain softening behavior. Furthermore, the gradient damage model remains capable of accounting for nucleation and complex crack evolutions, see for example (Bourdin, Marigo, Maurini, & Sicsic, 2014; León Baldelli, Babadjian, Bourdin, Henao, & Maurini, 2014; Maurini, Bourdin, Gauthier, & Lazarus, 2013; Mesgarnejad, Bourdin, & Khonsari, 2013; Sicsic et al., 2014).

- Through analytical investigations (Pham & Marigo, 2013; Pham, Marigo, & Maurini, 2011) and numerical simulations (Amor et al., 2009; Pham, Amor, et al., 2011) of gradient damage models, the  $\ell$  parameter, or the internal length, admits a genuine material parameter interpretation. Compared to the Griffith's theory, the introduction of such a length scale introduces additional physical size effects especially when the crack length is small. Furthermore, the maximum stress  $\sigma_m$  that the material can sustain is directly related to this parameter. For certain damage constitutive models, we have  $\sigma_m \rightarrow \infty$  when  $\ell \rightarrow 0$  and hence damage initiation becomes no longer possible with the meta-stability principle (1.23). It is an expected result due to the deficiency of the Griffith's theory and  $\Gamma$ -convergence results. The internal length parameter  $\ell$  contributes to the macroscopic material and structural behavior of such models. Its calibration should be performed based on experimental facts. This interpretation is acknowledged for example in (Freddi & Royer-Carfagni, 2010; Lancioni & Royer-Carfagni, 2009; Pham, Amor, et al., 2011).

These two interpretations are schematized in Figure 1.10. Following the above discussions, we now regard the gradient damage approach as an improved physical and material constitutive modeling of brittle fracture.

$$\begin{array}{ccc} \mathcal{P}_0(\mathbf{u}_t, \alpha_t) & \xrightarrow{+\nabla\alpha} & \mathcal{P}(\mathbf{u}_t, \alpha_t) \\ & & \downarrow \ell \rightarrow 0 \\ & & \mathcal{P}(\Gamma_t) \end{array}$$

Figure 1.10 – The gradient damage model represented by the potential energy  $\mathcal{P}$  admits two different interpretations: on the one hand, it can be considered as a regularization of local damage models denoted by  $\mathcal{P}_0$  (by setting  $\ell = 0$  in  $\mathcal{P}(\mathbf{u}_t, \alpha_t)$ ); on the other hand, the sharp-interface Francfort-Marigo variational model  $\mathcal{P}(\Gamma_t)$  defined in (1.17) can be regarded as a limit behavior of gradient damage models in terms of rigorous  $\Gamma$ -convergence theories (Braides, 2002)

### 1.4.3 Modeling of tension-compression asymmetry

Due to their specific microstructural damage mechanisms, brittle materials such as concrete are characterized by different macroscopic failure behaviors in tension and in compression, see for instance



(Kupfer & Gerstle, 1973; Lee, Song, & Han, 2004) for experimental illustrations. This aspect is particularly important in dynamic calculations due to reflection of waves at the body boundary, see for example (Moreau et al., 2015). The original gradient damage approach displays an identical behavior under tensile and compressive loading conditions. Accounting for tension-compression asymmetry in the potential energy (1.22) has already been considered in (Amor et al., 2009; Freddi & Royer-Carfagni, 2010; Piero, Lancioni, & March, 2007). It consists mainly of redevising the elastic behaviors of the gradient damage material through the stored elastic energy density  $\psi$ . The newly obtained potential functional is here denoted by  $\widehat{\mathcal{P}}(\mathbf{u}_t, \alpha_t)$ .

It turns out that this tension-compression asymmetry is closely related to the modeling of the unilateral contact condition in fracture mechanics, see (Amor et al., 2009). With a sharp-interface description of cracks, in a small displacement theory this condition reads

$$[[\mathbf{u}_t]] \cdot \mathbf{n} \geq 0 \text{ on } \Gamma,$$

where  $[[\mathbf{u}_t]]$  denotes the displacement jump on the crack lip. It can be interpreted as an injectivity constraint prescribed on the displacement field, see (Ciarlet & Nečas, 1987). This constraint can be readily included into the minimization procedure (1.17) in the variational approach to fracture through an adaptation of the kinematic admissible space  $\mathcal{C}$  for the displacement problem (1.15), and hence leads to a new definition of the potential energy (1.16) denoted here by  $\widehat{\mathcal{P}}(\Gamma_t)$ . Mathematical analysis of the variational problem accounting for non-interpenetration in the sense of (Ciarlet & Nečas, 1987) is performed for example in (Maso & Lazzaroni, 2010).

After having taken into account the tension-compression asymmetry effects in the gradient damage model and the unilateral condition in the variational fracture model, we would like to consider the link between  $\widehat{\mathcal{P}}(\Gamma_t)$  and the limit behavior of  $\widehat{\mathcal{P}}(\mathbf{u}_t, \alpha_t)$  when  $\ell \rightarrow 0$ . Unfortunately an answer to this question seems to remain out of reach in the two directions. On the one hand, an elliptic regularization of the sharp-interface model with non-interpenetration seems lacking at present. On the other hand, the  $\Gamma$ -convergence result for the limit  $\ell \rightarrow 0$  is still unclear, see (Amor et al., 2009; Freddi & Royer-Carfagni, 2010). This point is illustrated in Figure 1.11. We believe this constitutes a difficulty for correctly modeling crack opening and closure effects when using the gradient damage model as a phase-field approach to fracture.

$$\begin{array}{ccc} \mathcal{P}(\Gamma_t) & \xrightarrow{\text{unilateral effects}} & \widehat{\mathcal{P}}(\Gamma_t) \\ \downarrow \ell\text{-regul.} & & \uparrow \ell \rightarrow 0? \\ \mathcal{P}(\mathbf{u}_t, \alpha_t) & \xrightarrow{\text{T-C asymmetry}} & \widehat{\mathcal{P}}(\mathbf{u}_t, \alpha_t) \end{array}$$

Figure 1.11 – The link between the sharp-interface model with non-interpenetration  $\widehat{\mathcal{P}}(\Gamma_t)$  and the gradient-damage model with tension-compression asymmetry effects  $\widehat{\mathcal{P}}(\mathbf{u}_t, \alpha_t)$  remains unclear

## 1.5 Research Scope and Objectives

Based on the previous literature study, in this section the scope and objectives of the present work are defined. The work is divided into several thematic topics and is both theoretical and numerical in nature.

**Going dynamical** The first objective of the present work is to propose a formulation of gradient damage models in a dynamic setting. Due to the link between the variational approach to fracture and the gradient damage model indicated in Sections 1.3 and 1.4, this will be achieved by embedding the dynamic extension of the  $\ell$ -regularized fracture model proposed in (Bourdin et al., 2011), which is based on the Ambrosio-Tortorelli regularization, into the variational framework of (Pham & Marigo,

2010b) in terms of several physical properties. The dynamic behavior of gradient damage models can thus be investigated theoretically or numerically with respect to a general class of damage constitutive functions  $\alpha \mapsto a(\alpha)$  and  $\alpha \mapsto w(\alpha)$ .

We also propose an extension of the dynamic gradient damage model to large displacement situations. Initially, gradient damage models are formulated under small displacement hypothesis (small strain and rotation), however for dynamic fracture problems large displacement or even finite strain theories should be preferred given the violence of impact-type loading conditions. Indeed, not only the material is experiencing strain localization inside the damage process zone, but also fast propagation of cracks of length comparable to that of the structure could result in the finite rotations of some fractured zones (like in dynamic fragmentation situations).

Numerical implementation of the model constitutes the next main objective of this work. The spatial discretization is based on the standard  $C^0$  finite element method. It is based on the pioneering work of (Bourdin et al., 2000) for  $\ell$ -regularized fracture model and the work of (Pham, Amor, et al., 2011) for quasi-static gradient damage models. In large displacement situations, it should be noted that the discretization domain is different for the displacement problem and the damage problem. We use a second-order time-stepping scheme for temporal discretization of the coupled problem. Both explicit and implicit methods are considered even though the efforts are concentrated on the former one. The numerical solving of the discretized damage problem, *i.e.* minimization of the potential energy (1.22) with respect to the damage variable, is based on a specialized numerical linear algebra library PETSc for data structure and for well optimized optimization algorithms, see (Balay et al., 2015). The efficiency of the numerical implementation will be illustrated by several simulations results in a parallel computing framework.

Dynamic extension of previous theoretic analyses or results in the quasi-static setting also falls into this category. It concerns in particular the link between gradient damage models and Griffith's theory established in a quasi-static setting by (Sicsic & Marigo, 2013).

**Bridging the link with phase field approaches ( $\alpha \leftrightarrow \phi$ )** In this work another objective is to strengthen the bridge between the phase-field and the gradient-damage communities in order to achieve a better modeling of brittle dynamic fracture. Phase-field modeling of fracture is gaining popularity over the last few years within the computational mechanics community pioneered by the work of (Miehe, Hofacker, & Welschinger, 2010; Miehe, Welschinger, & Hofacker, 2010). Meanwhile, the phase-field model originated from the physics community constitutes another continuum mechanics approach for studying fracture problems, see for example (Hakim & Karma, 2009; Karma et al., 2001) and a review paper (Spatscheck, Brener, & Karma, 2011). Following the classification given in Section 1.1.2, they both also adopt a smeared description of cracks.

The author provides a review of the existing particular approaches in both communities to account for the tension-compression asymmetry of fracture behavior of materials in the framework discussed in Section 1.4.3. A better understanding and comparison of these physical models is provided through analytical studies of a uniaxial traction experiment and their applications to real fracture problems via numerical simulations. The difficulty in modeling the real non-interpenetration condition via these tension-compression asymmetry formulations is also illustrated.

The widely used regularized surface density function in the phase-field description of cracks is recognized as a special choice of the damage constitutive laws: that corresponding to the Ambrosio-Tortorelli regularization. Through concrete numerical simulations of dynamic fracture problems, different damage constitutive laws are compared in terms of their aptitude to approximate fracture, both from the computational and physical point of view.

**Better understanding of gradient damage modeling of fracture ( $\nabla\alpha \rightarrow \Gamma$ )** In this part the author aims to highlight specific properties of gradient damage approaches when regarded as a genuine physical model of fracture. This will be achieved by mainly comparing the defect evolution obtained in the gradient damage model and other damage or fracture models. Thanks to the variational principles, gradient damage or phase-field approaches settle down a unified and coherent computational framework

covering the onset and the space-time propagation of cracks with possible complex topologies. They have been successfully applied to study various real-world dynamic fracture problems, see for example (Borden et al., 2012; Dally & Weinberg, 2015; Hofacker & Miehe, 2012; Schlüter, Willenbücher, Kuhn, & Müller, 2014). The objective here is to better understand these variational principles and to provide further physical insights into the gradient damage model, through theoretical analysis and some representative simulation examples. It can be regarded as a justification of gradient damage approaches.

In the quasi-static setting, the work of (Lorentz, Cuvilliez, & Kazymyrenko, 2011; Lorentz, Cuvilliez, & Kazymyrenko, 2012) performs a theoretical and numerical investigation on the similar behaviors between the gradient damage model and the cohesive zone model. In (Hossain, Hsueh, Bourdin, & Bhattacharya, 2014; Klinsmann, Rosato, Kamlah, & McMeeking, 2015; Sicsic & Marigo, 2013), importance is given to the defect propagation phase, and a comparison with the Griffith's linear elastic theory is conducted. In dynamics, more well-designed numerical experiments should be performed to carry out such verification, see (Schlüter, Kuhn, Müller, & Gross, 2016) for instance for an investigation of the phase-field crack speeds for plane problems. In this contribution, the specific properties of the dynamic gradient damage model will be investigated independently for several phases of the defect temporal and spatial evolution. According to Section 1.1.1, the present work concerns thus a careful analysis of the gradient-damage modeling of crack nucleation, initiation, propagation, arrest, kinking and branching. A *divide and conquer* strategy is thus adopted to understand the behaviors of the gradient damage model during a complex crack evolution such as that observed in Figure 1.3.

**Experimental validation** Here the numerical results obtained with the dynamic gradient damage model are compared with some experimental facts. It can be considered as a continued work of (Mesgarnejad, Bourdin, & Khonsari, 2015) but in the dynamic setting. The validation is based on qualitative or quantitative behaviors of the temporal or spatial evolution that the smeared crack follows. Validation is conducted for brittle materials including PMMA and concrete.

## Summary of this Chapter

In this chapter we provide a selected literature study on fracture and damage after a brief description of some representative dynamic fracture mechanics phenomena in Section 1.1. The three theoretic approaches presented here, *i.e.* the Griffith's theory of fracture (Section 1.2), the variational approach to fracture (Section 1.3.1) and the gradient damage model (Section 1.4), are not completely independent from each other. On the contrary, they can be regarded as a progressive sophistication toward a better modeling of fracture behaviors previously discussed. Based on the merits, gaps and drawbacks of each model, the scope and objectives of the present research work are then exposed in Section 1.5. It is summarized in Table 1.1 which will be used, whenever it is appropriate, at the beginning of each section from the next chapter to situate the content that follows.

Table 1.1 – Thematic subjects covered by the present research on dynamic gradient damage models tackled by theoretical or numerical approaches. This table will be used, whenever it is appropriate, at the beginning of each section from the next chapter to situate the content that follows. For that, a or several 👍 symbol(s) will be placed in the corresponding line and column

	Going dynamical	$\alpha \leftrightarrow \phi$	$\nabla \alpha \rightarrow \Gamma$	Experimental validation
Theoretics	👍	👍	👍	
Numerics	👍	👍	👍	👍





# 2

## Dynamic Gradient Damage Models

### Contents

<b>2.1</b>	<b>Variational Framework Based on Physical Principles</b>	<b>25</b>
2.1.1	Variational ingredients	26
2.1.2	Dynamic evolution laws	30
2.1.3	Equivalent local interpretations	33
2.1.4	Comparison with phase-field approaches	35
2.1.5	Extension to large displacement situations	37
<b>2.2</b>	<b>Tension-Compression Asymmetry</b>	<b>38</b>
2.2.1	Review of existing models	39
2.2.2	Uniaxial traction and compression experiment	43
2.2.3	How to choose among different models	45
<b>2.3</b>	<b>Griffith's Law in Gradient Damage Models</b>	<b>47</b>
2.3.1	Lagrangian description in the initial cracked configuration	47
2.3.2	Generalized Griffith criterion for a propagating damage band	50
2.3.3	Separation of scales	58

In this chapter the author first proposes a variational framework of the gradient damage models in the dynamic setting. Its ingredients and physical principles are presented in Section 2.1. The author then reviews and analyzes in Section 2.2 several approaches in an attempt to account for the tension-compression asymmetry of damage behavior of materials. In Section 2.3 the dynamic gradient damage evolution is theoretically compared with the Griffith's theory of fracture. It is found that the crack evolution is governed by an asymptotic Griffith's law as long as the internal length is small compared to the dimension of the body.

### 2.1 Variational Framework Based on Physical Principles

In this section the author extends the original quasi-static gradient damage models as formulated in (Pham & Marigo, 2010b) to the dynamic setting. A variationally consistent framework for dynamic gradient damage models thanks to the definition of a generalized space-time action integral is obtained. A comparison with other phase-field approaches is then carried out. An extension to large-displacement situations is also discussed. The thematic subjects covered are summarized in Table 2.1.

Table 2.1 – Thematic subjects covered in this section

	Going dynamical	$\alpha \leftrightarrow \phi$	$\nabla \alpha \rightarrow \Gamma$	Experimental validation
Theoretics	👍	👍		
Numerics				

### 2.1.1 Variational ingredients

For the sake of simplicity, let us consider first a homogeneous and isotropic body  $\Omega$  under the small strain hypothesis. Anisotropy is not the object of the present study and we assume that the local elastic material behavior can be characterized by two constants: the Young's modulus  $E$  and the Poisson's ratio  $\nu$  for instance. A discussion on an extension to large displacement situations is provided at the end of this section, since they should not influence the variational formulation proposed here.

The construction of the dynamic model is based on that of the quasi-static gradient damage model (Pham, Amor, et al., 2011; Pham & Marigo, 2010b). Its physical background and motivation has been discussed in Section 1.4 and are not reproduced here. An element in the phase space of the dynamic gradient damage model regarded as a dynamical system corresponds to a state tuple  $(\mathbf{u}_t, \dot{\mathbf{u}}_t, \alpha_t)$  consisting of the displacement field  $\mathbf{u}_t$ , the velocity field  $\dot{\mathbf{u}}_t$  and the damage field  $\alpha_t$ . They are scalar or vector fields defined on the body  $\Omega$ , *i.e.* a snapshot of the dynamic evolution at a certain time  $t$ . The modeling parameters are embedded into several energetic quantities that are defined as follows. The elastic energy as well as the damage dissipation energy retain their quasi-static definitions, since they are unaffected by dynamics.

- **Elastic energy** characterizes the elastic behavior of the material. It is given by

$$\mathcal{E}(\mathbf{u}_t, \alpha_t) = \int_{\Omega} \psi(\boldsymbol{\varepsilon}(\mathbf{u}_t), \alpha_t) \, d\mathbf{x} = \int_{\Omega} \frac{1}{2} \mathbf{A}(\alpha_t) \boldsymbol{\varepsilon}(\mathbf{u}_t) \cdot \boldsymbol{\varepsilon}(\mathbf{u}_t) \, d\mathbf{x}, \quad (2.1)$$

where  $\boldsymbol{\varepsilon}(\mathbf{u}_t) = \frac{1}{2}(\nabla \mathbf{u}_t + \nabla^T \mathbf{u}_t)$  denotes the linearized strain and  $\mathbf{A}(\alpha)$  is the isotropic Hooke's elasticity tensor at a given damage state. We assume that the Poisson's ratio is unaffected by the damage variable, which leads to

$$\mathbf{A}(\alpha) = \mathbf{a}(\alpha) \mathbf{A}_0,$$

where  $\alpha \mapsto \mathbf{a}(\alpha)$  is an adimensional function of damage characterizing stiffness degradation in the bulk from an initial undamaged state  $\mathbf{A}_0 = \mathbf{A}(0)$ . The *damage-dependent* stress tensor conjugate to the strain variable is thus given by

$$\boldsymbol{\sigma}_t = \mathbf{A}(\alpha_t) \boldsymbol{\varepsilon}(\mathbf{u}_t). \quad (2.2)$$

It can be observed that here the damage acts symmetrically on the undamaged elastic energy density  $\psi_0(\boldsymbol{\varepsilon}(\mathbf{u}_t)) = \psi(\boldsymbol{\varepsilon}(\mathbf{u}_t), 0)$  such that

$$\psi(\boldsymbol{\varepsilon}(\mathbf{u}_t), \alpha_t) = \psi(-\boldsymbol{\varepsilon}(\mathbf{u}_t), \alpha_t) = \mathbf{a}(\alpha_t) \psi_0(\boldsymbol{\varepsilon}(\mathbf{u}_t)). \quad (2.3)$$

An extension to tension-compression asymmetry will be discussed in Section 2.2.

- **Kinetic energy** is defined as usual by

$$\mathcal{K}(\dot{\mathbf{u}}_t) = \int_{\Omega} \kappa(\dot{\mathbf{u}}_t) \, d\mathbf{x} = \int_{\Omega} \frac{1}{2} \rho \dot{\mathbf{u}}_t \cdot \dot{\mathbf{u}}_t \, d\mathbf{x}. \quad (2.4)$$

The material density  $\rho$  is independent of the damage, which implies total mass conservation. Furthermore, it assumes that the local damage behavior is not affected by inertia.

- **Damage dissipation energy** quantifies the amount of energy consumed in a damage process. For theoretic analyses of gradient damage models, for example in (Pham, Amor, et al., 2011; Sicsic & Marigo, 2013), one often uses the following definition

$$\mathcal{S}(\alpha_t) = \int_{\Omega} \varsigma(\alpha_t, \nabla \alpha_t) \, d\mathbf{x} = \int_{\Omega} \left( w(\alpha_t) + \frac{1}{2} w_1 \ell^2 \nabla \alpha_t \cdot \nabla \alpha_t \right) \, d\mathbf{x}, \quad (2.5)$$

where  $\alpha \mapsto w(\alpha)$  describes local damage dissipation during a homogeneous damage evolution and its maximal value  $w(1) = w_1$  is the energy completely dissipated during such process when damage attains 1. For numerical implementation purposes, see (Bourdin et al., 2014; Mesgarnejad et al., 2015), a non-essential rescaling of the internal length  $\ell = \sqrt{2}\eta$  is usually performed and (2.5) is rewritten as follows

$$\mathcal{S}(\alpha_t) = \int_{\Omega} \varsigma(\alpha_t, \nabla \alpha_t) \, d\mathbf{x} = \int_{\Omega} \frac{G_c}{c_w} \left( \frac{w(\alpha_t)}{\eta} + \eta \nabla \alpha_t \cdot \nabla \alpha_t \right) \, d\mathbf{x}. \quad (2.5')$$

To ensure equivalence between these two definitions, we have necessarily  $w(\alpha) = w_1 \tilde{w}(\alpha)$  and  $G_c = c_w w_1 \eta$ , where  $\alpha \mapsto \tilde{w}(\alpha)$  denotes the adimensional damage dissipation function. Note that

In the sequel, both  $\ell$  and  $\eta$  denote the material internal length.

**Damage constitutive functions** We assume that the stiffness degradation function  $\alpha \mapsto a(\alpha)$  along with the damage dissipation function  $\alpha \mapsto w(\alpha)$  verify certain constitutive properties which characterize the behavior of a *strongly brittle material* for the underlying local damage model, cf. (Pham & Marigo, 2013; Pham, Marigo, & Maurini, 2011; Sicsic & Marigo, 2013). In particular, we have

- Energy completely dissipated during a homogeneous damage evolution is finite:  $0 < w_1 < \infty$ . This condition justifies the use of a damage variable the value of which is between 0 and 1.
- Strain-softening, which ensures that the elastic domain in the stress space is a decreasing function of damage in the sense of set inclusion. Using the variational nature of the elastic-damage evolution (Marigo, 2002), it implies that the function  $\alpha \mapsto s'(\alpha)/w'(\alpha)$  must be increasing, where  $s = a^{-1}$ . This property should be verified for all  $\alpha \in [0, 1]$ , or at least in a neighborhood of  $\alpha = 1$ . During a homogeneous uniaxial traction experiment, it leads to the definition of the critical stress  $\sigma_c$  beyond which damage grows and the maximal stress that the material can sustain:

$$\sigma_c = \sqrt{\frac{2E w'(0)}{s'(0)}}, \quad \sigma_m = \max_{\beta \in [0, 1]} \sqrt{\frac{2E w'(\beta)}{s'(\beta)}}. \quad (2.6)$$

Depending on the specific damage constitutive laws  $\alpha \mapsto a(\alpha)$  and  $\alpha \mapsto w(\alpha)$  used, the material and structural behaviors could be quantitatively or even qualitatively different. An abundant literature is devoted to a theoretic or numerical analysis of these damage constitutive laws. The interested readers are referred to (Lorentz et al., 2012; Pham, Amor, et al., 2011; Pham & Marigo, 2013; Pham, Marigo, & Maurini, 2011) and references therein for a discussion on this point. In the numerical simulation part of this work, two particular damage constitutive laws will be considered. They both involve only polynomial functions of the damage up to degree 2, thus the elastic energy  $\mathcal{E}$  as well as the damage dissipation energy  $\mathcal{S}$  are *quadratic* with respect to damage, a rather interesting property from a computational cost point of view since the Hessian matrix is constant.

- The Pham, Amor, Marigo and Maurini model initially introduced in (Pham, Amor, et al., 2011) and named after their initials:

$$a(\alpha) = (1 - \alpha)^2, \quad w(\alpha) = \alpha. \quad (\text{PAMM})$$

Damage does not evolve as long as a non-zero critical stress is not reached, a rather appreciated property when modeling brittle fracture. Then a strain-softening behavior is observed as damage

grows for  $\alpha \in (0, 1)$ , which implies that the critical stress coincides with the maximal stress. According to (2.6), we have

$$\sigma_c = \sigma_m = \sqrt{w_1 E}.$$

- The original Ambrosio and Tortorelli regularization model introduced in (Bourdin et al., 2000):

$$a(\alpha) = (1 - \alpha)^2, \quad w(\alpha) = \alpha^2. \quad (\text{AT})$$

In this model a purely elastic domain is absent  $\sigma_c = 0$  and the strain-softening property is satisfied only for  $\alpha \in (\frac{1}{4}, 1)$ . At  $\alpha = \frac{1}{4}$  the stress reaches its maximal value and is given by

$$\sigma_m = \frac{3\sqrt{6}}{16} \sqrt{w_1 E}.$$

Their constitutive behaviors are illustrated in the Figure 2.1 during a homogeneous uniaxial traction experiment. Their respective maximal stress  $\sigma_m$  as well as the corresponding strain  $\varepsilon_m$  are used for normalization.



Figure 2.1 – Constitutive behaviors for the (PAMM) model (a) and the (AT) model (b) during a homogeneous uniaxial traction experiment

**Links between damage and fracture** As outlined in Sections 1.3 and 1.4, the link between damage and fracture can be established in terms of the  $\Gamma$ -convergence theory. The damage dissipation energy

(2.5) can be regarded as an equivalent Griffith crack surface functional in the phase-field model. An effective fracture toughness  $G_c$ , *i.e.* the energy required to create a unit Griffith-like crack surface, can be identified as the energy dissipated during the optimal damage profile creation in a uniaxial traction experiment, see (Pham, Amor, et al., 2011) for a detailed discussion on this point. The optimal damage profile  $\alpha_*$  can be considered as the theoretic cross-section perpendicular to a gradient-damage crack. If  $x$  refers to the transverse coordinate axis centered at the crack where  $\alpha_*(x) = 1$ , the optimal damage profile for the (PAMM) model is given by

$$\alpha_*(x) = \begin{cases} \left(1 - \frac{|x|}{2\eta}\right)^2 & \text{if } |x| < 2\eta, \\ 0 & \text{else.} \end{cases} \quad (2.7)$$

While for the damage constitutive model (AT), one derives

$$\alpha_*(x) = \exp\left(-\frac{|x|}{\eta}\right). \quad (2.8)$$

These two damage profiles are illustrated in Figure 2.2. It can be observed that (2.8) does not possess a finite support from a theoretic point of view. With such optimal damage profiles, the corresponding

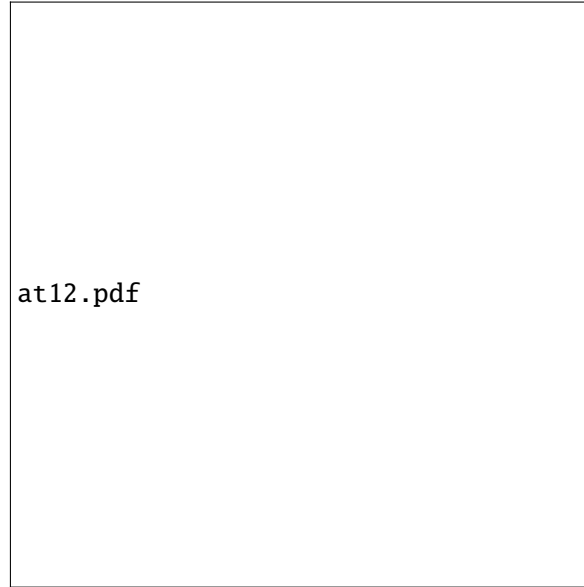


Figure 2.2 – Optimal damage profiles for the (PAMM) and (AT) damage constitutive models

dissipated energy can be consequently computed by injecting  $\alpha_*$  into (2.5) or (2.5'). For the damage dissipation energy written in the form of (2.5), we have

$$G_c = 2\sqrt{2}\ell \int_0^1 \sqrt{w_1 w(\beta)} d\beta. \quad (2.9)$$

This equation prescribes a relation between the fracture toughness  $G_c$ , the maximal damage dissipation  $w_1$  and the internal length  $\ell$ .

When the damage dissipation energy is written in the form of (2.5'), one anticipates the fact that the gradient damage model can be regarded as a genuine model of fracture. The link between damage and fracture is hidden in the definition of the normalization coefficient  $c_w$ . According to (2.9), it leads to

$$c_w = 4 \int_0^1 \sqrt{w(\beta)} d\beta. \quad (2.10)$$

A direct calculation gives  $c_w = \frac{8}{3}$  for the (PAMM) model and  $c_w = 2$  for the (AT) one.

**Modeling parameters** The modeling parameters of the dynamic gradient damage model can thus be summarized in Table 2.2. The elastodynamic parameters corresponds to the material density as well as two elastic constants. The fracture behavior can be characterized by a maximal stress defined by (2.6) and a fracture toughness  $G_c$ , thanks to the identification (2.9) or to the definition of the normalization coefficient in (2.10). The internal length  $\ell$  can be regarded as a parameter that achieves a link between damage and fracture. It can be considered as a dependent or independent modeling parameter depending on the choice of damage constitutive functions.

Table 2.2 – Modeling parameters of the dynamic gradient damage model regarded as a genuine model of fracture

	Elastodynamics	Fracture	Damage $\leftrightarrow$ fracture	Constitutive functions
Parameters	$\rho, E$ and $\nu$	$G_c$ and $\sigma_m$	$\ell$	$a(\alpha)$ and $w(\alpha)$

The damage constitutive functions  $a(\alpha)$  and  $w(\alpha)$  contribute to the quantitative behaviors of gradient damage models used to approximate brittle fracture. Remark that no additional parameters are introduced in the (PAMM) and the (AT) models. In particular, the internal length  $\ell$  is determined as long as the two fracture parameters  $G_c$  and  $\sigma_m$  as known. More modeling parameters can be introduced via the use of more sophisticated constitutive functions such as that defined in (Alessi, Marigo, & Vidoli, 2015; Lorentz et al., 2012). For instance, in (Alessi et al., 2015) the following damage constitutive laws are proposed

$$a(\alpha) = \frac{1 - w(\alpha)}{1 + (k - 1)w(\alpha)}, \quad w(\alpha) = 1 - (1 - \alpha)^2.$$

Its homogeneous damage behavior is characterized by a linear softening curve parametrized by the  $k$ -parameter as illustrated in Figure 2.3. According to (2.6) and (2.9), the following relationships between the material parameters hold

$$G_c = \pi w_1 \eta, \quad \sigma_c^2 = \frac{2G_c E}{\pi k \eta}.$$

In particular, the introduction of the  $k$ -parameters permits one to interpret  $\ell$  as a genuine independent parameter. In that case, the  $k$ -parameter is fixed as long as other material parameters are

$$k = \frac{2G_c E}{\pi \eta \sigma_c^2}.$$

Future work could be devoted to a thorough theoretic and numerical analysis of these kind of models in the dynamic setting.

### 2.1.2 Dynamic evolution laws

In this work we propose to formulate the variational dynamic evolution problem using an extension of Hamilton's principle, cf. (Hamilton, 1834). In the quasi-static case the meta-stability condition (1.23) is a physically feasible principle due to the minimization structure of static equilibrium. In dynamics however, we merely have a *stationary* action integral, since the temporal minimality is not always guaranteed, see (Gray & Taylor, 2007). From a mathematical modeling point of view, Hamilton's principle applies to temporal *boundary value problems* defined in an interval  $[0, T]$ , since the state at both time ends is fixed during arbitrary variations of the action. More sophisticated variational principles can be designed to take into account only the initial displacement  $\mathbf{u}_0$  and the initial velocity  $\dot{\mathbf{u}}_0$  conditions, see for example (Gurtin, 1964). We admit that the use of Hamilton's principle may not be an optimal one from a formulation point of view. Nevertheless it is not the object of the present work. Here Hamilton's principle is mainly used to derive the equations to solve the physical *initial value problem*.



Figure 2.3 – Constitutive behaviors for the constitutive functions proposed in (Alessi, Marigo, & Vidoli, 2015) during a homogeneous uniaxial traction experiment: (a) stress-strain behavior and (b) damage evolution



The loading conditions and the admissible function spaces are now specified. Body forces  $\mathbf{f}_t$  and surface tractions  $\mathbf{F}_t$  applied to the body through a subset  $\partial\Omega_F$  of the boundary are characterized by an external work potential  $\mathcal{W}_t$  given by

$$\mathcal{W}_t(\mathbf{u}_t) = \int_{\Omega} \mathbf{f}_t \cdot \mathbf{u}_t \, dx + \int_{\partial\Omega_F} \mathbf{F}_t \cdot \mathbf{u}_t \, ds. \quad (2.11)$$

On a subset  $\partial\Omega_U$  of the boundary the body is subject to a prescribed displacement  $t \mapsto \mathbf{U}_t$  which is built into the definition of the admissible displacement space  $C_t$ . We suppose that the admissible displacement space is an affine space of form  $C_t = C_0 + \mathbf{U}_t$  where the associated vector space  $C_0$  is given by

$$C_0 = \{ \mathbf{u}_t : \Omega \rightarrow \mathbb{R}^{\dim} \mid \mathbf{u}_t = \mathbf{0} \text{ on } \partial\Omega_U \}. \quad (2.12)$$

*Remark* (Dirichlet boundary condition). The field  $\mathbf{U}_t \in C_t$  should be understood as a *lifting* of the Dirichlet boundary condition classically defined only on  $\partial\Omega_U$ .

Damage is here modeled as an irreversible defect evolution. Its admissible space will be built from a current damage state  $0 \leq \alpha_t \leq 1$  and it is defined by

$$D(\alpha_t) = \{ \beta_t : \Omega \rightarrow [0, 1] \mid 0 \leq \alpha_t \leq \beta_t \leq 1 \}. \quad (2.13)$$

It can be seen that a virtual damage field  $\beta_t$  is admissible, if and only if it is accessible from the current damage state  $\alpha_t$  verifying the irreversibility condition, *i.e.* the damage only grows. In order to use Hamilton's principle, we consider an arbitrary interval of time  $I = [0, T]$  and fix the values of  $(\mathbf{u}, \alpha)$  at both time ends denoted by  $\mathbf{u}_{\partial I} = (\mathbf{u}_0, \mathbf{u}_T)$  and  $\alpha_{\partial I} = (\alpha_0, \alpha_T)$ . Hence, the admissible displacement and damage evolution spaces read

$$C(\mathbf{u}) = \{ \mathbf{v} : I \times \Omega \rightarrow \mathbb{R}^{\dim} \mid \mathbf{v}_t \in C_t \text{ for all } t \in I \text{ and } \mathbf{v}_{\partial I} = \mathbf{u}_{\partial I} \}, \quad (2.14)$$

$$\mathcal{D}(\alpha) = \{ \beta : I \times \Omega \rightarrow [0, 1] \mid \beta_t \in D(\alpha_t) \text{ for all } t \in I \text{ and } \beta_{\partial I} = \alpha_{\partial I} \}. \quad (2.15)$$

*Remark* (Spatial and temporal regularity of  $\mathbf{u}$  and  $\alpha$ ). Informally, we assume that the displacement  $\mathbf{u}$  and the damage  $\alpha$  are sufficiently regular in time and in space such that all the energetic quantities defined in Section 2.1.1 make sense. Before the onset of fracture when the damage attains 1 somewhere in the body  $\text{ess sup } \alpha_t < 1$ , the elastic energy density (2.3) is strictly positive almost everywhere, hence a natural functional framework for the displacement would be  $H^1(\Omega, \mathbb{R}^{\dim})$ . Since the temporal derivative of the damage is not involved in the variational formulation, for every  $t \in I$  the damage  $\alpha_t$  belongs at least to  $H^1(\Omega) \cap L^\infty(\Omega)$ . Due to the kinetic energy (2.4), the current velocity  $\dot{\mathbf{u}}_t$ , regarded as the temporal derivative of the displacement in the distributional sense, should be an element of  $L^2(\Omega, \mathbb{R}^{\dim})$ . A precise statement of the function spaces in the most general case remains beyond the scope of this work.

With all the variational ingredients set, we are now in a position to introduce the following space-time action integral associated with an admissible pair of displacement and damage evolutions  $(\mathbf{u}, \alpha) \in C(\mathbf{u}) \times \mathcal{D}(\alpha)$ , which involves an augmented Lagrangian

$$\mathcal{A}(\mathbf{u}, \alpha) = \int_I \mathcal{L}_t(\mathbf{u}_t, \dot{\mathbf{u}}_t, \alpha_t) \, dt = \int_I (\mathcal{E}(\mathbf{u}_t, \alpha_t) + \mathcal{S}(\alpha_t) - \mathcal{K}(\dot{\mathbf{u}}_t) - \mathcal{W}_t(\mathbf{u}_t)) \, dt. \quad (2.16)$$

The coupled two-field time-continuous dynamic gradient damage problem can then be formulated by the following

**Definition 2.1** (Dynamic Gradient Damage Evolution Law).

1. **Irreversibility**: the damage  $t \mapsto \alpha_t$  is a non-decreasing function of time.
2. **First-order stability**: the first-order action variation is non-negative with respect to arbitrary admissible displacement and damage evolutions

$$\mathcal{A}'(\mathbf{u}, \alpha)(\mathbf{v} - \mathbf{u}, \beta - \alpha) \geq 0 \text{ for all } \mathbf{v} \in C(\mathbf{u}) \text{ and all } \beta \in \mathcal{D}(\alpha). \quad (2.17)$$

3. **Energy balance:** the only energy dissipation is due to damage

$$\begin{aligned} \mathcal{H}_t = \mathcal{H}_0 + \int_0^t \left( \int_{\Omega} (\sigma_s \cdot \varepsilon(\dot{\mathbf{U}}_s) - \rho \dot{\mathbf{u}}_s \cdot \ddot{\mathbf{U}}_s) \, d\mathbf{x} - \mathcal{W}_s(\dot{\mathbf{U}}_s) - \mathcal{W}_s(\mathbf{u}_s) \right) ds \\ + \int_{\Omega} \rho(\dot{\mathbf{u}}_t \cdot \dot{\mathbf{U}}_t - \dot{\mathbf{u}}_0 \cdot \dot{\mathbf{U}}_0) \, d\mathbf{x} \end{aligned} \quad (2.18)$$

where the total energy is defined by

$$\mathcal{H}_t = \mathcal{E}(\mathbf{u}_t, \alpha_t) + \mathcal{S}(\alpha_t) + \mathcal{K}(\dot{\mathbf{u}}_t) - \mathcal{W}_t(\mathbf{u}_t).$$

In the first-order stability condition (2.17), we evaluate the directional (Gâteaux) derivative of the action integral at  $(\mathbf{u}, \alpha)$ , a possible solution to the dynamic evolution problem, in the direction  $(\mathbf{v} - \mathbf{u}, \beta - \alpha)$  which corresponds to a perturbation. Formally, using the Lagrangian  $\mathcal{L}_t$ , we have

$$\mathcal{A}'(\mathbf{u}, \alpha)(\mathbf{w}, \beta - \alpha) = \int_I \left( \frac{\partial \mathcal{L}_t}{\partial \mathbf{u}_t}(\mathbf{s}_t)(\mathbf{w}_t) + \frac{\partial \mathcal{L}_t}{\partial \dot{\mathbf{u}}_t}(\mathbf{s}_t)(\dot{\mathbf{w}}_t) + \frac{\partial \mathcal{L}_t}{\partial \alpha_t}(\mathbf{s}_t)(\beta_t - \alpha_t) \right) dt,$$

where  $\mathbf{w} = \mathbf{v} - \mathbf{u}$  denotes a displacement evolution variation and  $\mathbf{s}_t = (\mathbf{u}_t, \dot{\mathbf{u}}_t, \alpha_t)$  corresponds to a state of the dynamical system. Remark that (2.17) is written as a variational inequality to take into account the unilateral effects introduced by the irreversibility condition in the definition of the damage admissible space (2.13). It can be regarded as an extension of Hamilton's principle applied to systems with irreversible dissipation.

The energy balance condition (2.18) characterizes the energy flow into the system: the external work is balanced by the mechanical energy variation of the system consisting of the elastic energy (2.1) and the kinetic energy (2.4), and the energy dissipated in the process of crack production (2.5). The energy balance condition (2.18) complements the first-order stability condition (2.17) which ensures that energy could only be dissipated through damage (or gradient-damage like fracture). Observe that (2.18) also applies to non-smooth evolutions in the presence of possible velocity shocks, since no higher spatial or temporal derivatives of the displacement and the damage are involved other than that needed for the definition of the Lagrangian density. With the help of integration by parts, the regularity is transferred to the boundary conditions  $t \mapsto \mathbf{U}_t$  and the external work potential  $t \mapsto \mathcal{W}_t$ . If in particular the acceleration field  $\ddot{\mathbf{u}}_t$  is sufficiently regular, the energy balance condition admits an equivalent formulation which reads after an integration by parts in the time domain

$$\mathcal{H}_t = \mathcal{H}_0 + \int_0^t \left( \int_{\Omega} (\sigma_s \cdot \varepsilon(\dot{\mathbf{U}}_s) + \rho \ddot{\mathbf{u}}_s \cdot \dot{\mathbf{U}}_s) \, d\mathbf{x} - \mathcal{W}_s(\dot{\mathbf{U}}_s) - \mathcal{W}_s(\mathbf{u}_s) \right) ds. \quad (2.18')$$

### 2.1.3 Equivalent local interpretations

By developing the Gâteaux derivative of the action integral, further physical insights into the first-order stability condition (2.17) can be obtained if sufficient spatial and temporal regularities of the involved fields are assumed. Writing the variation  $\mathbf{v} - \mathbf{u}$  by  $\mathbf{w}$  and testing (2.17) with  $\beta = \alpha$ , we obtain after an integration by parts in the time domain

$$\mathcal{A}'(\mathbf{u}, \alpha)(\mathbf{w}, 0) = \int_I \left( \int_{\Omega} (\sigma_t \cdot \varepsilon(\mathbf{w}_t) + \rho \ddot{\mathbf{u}}_t \cdot \mathbf{w}_t) \, d\mathbf{x} - \mathcal{W}_t(\mathbf{w}_t) \right) dt = 0 \text{ for all } \mathbf{w}_t \in C_0 \quad (2.19)$$

where the equality  $\mathcal{A}'(\mathbf{u}, \alpha)(\mathbf{w}, 0) = 0$  follows given that the associated linear space  $C_0$  of  $C_t$  is a vector space. The arbitrariness of the temporal variation of  $\mathbf{w}$  leads thus to the weak elastic-damage dynamic wave equation

$$\int_{\Omega} (\sigma_t \cdot \varepsilon(\mathbf{w}_t) + \rho \ddot{\mathbf{u}}_t \cdot \mathbf{w}_t) \, d\mathbf{x} - \mathcal{W}_t(\mathbf{w}_t) = 0 \text{ for all } \mathbf{w}_t \in C_0. \quad (2.20)$$

If further spatial regularity is assumed, one deduces the strong form

$$\rho \ddot{\mathbf{u}}_t - \operatorname{div} \sigma_t = \mathbf{f}_t \quad \text{in } \Omega \quad \text{and} \quad \sigma_t \mathbf{n} = \mathbf{F}_t \quad \text{on } \partial\Omega_F \quad (2.21)$$

Compared to the classical elastodynamic equation, here the stress tensor  $\sigma_t$  is damage dependent through the elasticity tensor, see (2.2).

We now turn to the governing equation for damage evolution induced from the first-order stability condition (2.17). We observe that the admissible damage space  $D(\alpha_t)$  defined in (2.13) is convex. Due to the arbitrariness of the temporal variation of  $\beta$ , testing (2.17) now with  $\mathbf{v} = \mathbf{u}$  gives the Euler's inequality condition stating the partial minimality of the total energy with respect to the damage variable under the irreversible constraint for every  $t \in I$

$$\mathcal{E}(\mathbf{u}_t, \alpha_t) + \mathcal{S}(\alpha_t) \leq \mathcal{E}(\mathbf{u}_t, \beta_t) + \mathcal{S}(\beta_t) \text{ for all } \beta_t \in D(\alpha_t). \quad (2.22)$$

Although the same energy minimization principle (2.22) holds also for quasi-static gradient damage models (Pham, Amor, et al., 2011), here the displacement field  $\mathbf{u}_t$  is governed by the elastic-damage wave equation (2.21). Developing the Euler's inequality condition and performing an integration by parts of the damage gradient term yield a strong formulation of (2.22) which serves as the local damage criterion at a particular material point

$$Y_t + \operatorname{div} \mathbf{q}_t \leq 0 \quad \text{in } \Omega \setminus \Gamma_t \quad \text{and} \quad \mathbf{q}_t \cdot \mathbf{n} \geq 0 \quad \text{on } \partial\Omega \setminus \Gamma_t. \quad (2.23)$$

For notational simplicity, the following dual variables are defined

$$Y_t = -\frac{1}{2} \mathbf{A}'(\alpha_t) \boldsymbol{\varepsilon}(\mathbf{u}_t) \cdot \boldsymbol{\varepsilon}(\mathbf{u}_t) - w'(\alpha_t) \quad \text{and} \quad \mathbf{q}_t = w_1 \ell^2 \nabla \alpha_t \quad (2.24)$$

They can be interpreted as the energy release rate density with respect to damage and the damage flux vector, see (Sicsic & Marigo, 2013). In (2.23), the subset  $\Gamma_t = \{ \mathbf{x} \in \Omega \mid \alpha_t(\mathbf{x}) = 1 \}$  denotes the totally damaged region. We note that the local damage criterion holds only in the uncracked part of the body, since  $\beta_t = \alpha_t = 1$  on  $\Gamma_t$  because of the definition of the admissible damage space (2.13). Due to the presence of the damage gradient, the criterion is described by an elliptic type equation in space involving the Laplacian of the damage. Assuming that the considered fields are also sufficiently smooth in time, the global energy balance (2.18) leads to the following consistency condition

$$(Y_t + \operatorname{div} \mathbf{q}_t) \dot{\alpha}_t = 0 \quad \text{in } \Omega \setminus \Gamma_t \quad \text{and} \quad (\mathbf{q}_t \cdot \mathbf{n}) \dot{\alpha}_t = 0 \quad \text{on } \partial\Omega \setminus \Gamma_t. \quad (2.25)$$

Hence damage growth is possible until a certain non-local threshold is reached. Similarly here the local consistency condition holds only in the uncracked part of the body, since  $\dot{\alpha}_t = 0$  on  $\Gamma_t$  by definition. These local interpretations (2.23) and (2.25) are also formally the same with that derived in the quasi-static model (Pham & Marigo, 2010b; Sicsic & Marigo, 2013).

**Damage initiation in an initially sound region** If the body is initially undamaged inside a particular region (where the damage as well as the damage gradient are zero), then according to the consistency condition (2.25), damage could initiate as long as the following condition is satisfied

$$Y_t|_{\alpha_t=0} = 0 \implies -\frac{1}{2} \mathbf{a}'(0) \mathbf{A}_0 \boldsymbol{\varepsilon}(\mathbf{u}_t) \cdot \boldsymbol{\varepsilon}(\mathbf{u}_t) - w'(0) = 0. \quad (2.26)$$

This criterion can be equivalently written in the stress-space, which reads

$$-\frac{1}{2} \mathbf{a}'(0) \mathbf{S}_0 \sigma_t \cdot \sigma_t - w'(0) = 0, \quad (2.26')$$

where  $\mathbf{S}_0 = \mathbf{A}_0^{-1}$  denotes the compliance tensor.

**Construction of the optimal damage profile** As is noted in Section 2.1.1, the optimal damage profile  $\alpha_*$  (for example that given in (2.7) for the (PAMM) law) corresponds to the damage field at fracture during a uniaxial traction experiment of a bar centered at  $x = 0$ . Concretely, it consists of

applying the consistency condition (2.25) at the instant of fracture when the uniaxial stress vanishes  $\sigma = 0$ . The optimal damage profile is thus the solution to the following differential equation

$$w'(\alpha_*(x)) - w_1 \ell^2 \alpha_*''(x) = 0 \text{ for } x \in [-D, D] \quad (2.27)$$

where  $D$  measures the half-damage band or the support of the damage field where  $\alpha_t > 0$ . Hence we have  $D = 2\eta$  for the (PAMM) model and  $D = \infty$  for the (AT) model. One can easily solve this autonomous second order differential equation by using the boundary conditions  $\alpha_* = 0$  and  $\alpha_*' = 0$  at  $x = \pm D$ . Readers are referred to (Pham, Amor, et al., 2011) for a detailed derivation.

**Singular surfaces and jump conditions** Here we discuss the presence of a possible singular surface  $S_t \subset \Omega$  inside the reference configuration  $\Omega$  across which first derivatives of the fields involved in the variational ingredients could be discontinuous: the strain  $\boldsymbol{\varepsilon}(\mathbf{u}_t)$ , the velocity  $\dot{\mathbf{u}}_t$  or the damage gradient  $\nabla \alpha_t$ . The body is partitioned into two parts  $\Omega^+$  and  $\Omega^-$ , and we note  $\mathbf{n}$  as the normal vector of  $S_t$  pointing into  $\Omega^+$ . As usual we define the jump of a quantity  $q$  to be

$$[[q]](\mathbf{x}) = \lim_{\Omega^+ \ni \mathbf{y} \rightarrow \mathbf{x}} q(\mathbf{y}) - \lim_{\Omega^- \ni \mathbf{y} \rightarrow \mathbf{x}} q(\mathbf{y}).$$

Due to the presence of the damage gradient, the damage field remain continuous across such surfaces  $[[\alpha_t]] = 0$ . The same case takes place for the displacement vector  $[[\mathbf{u}_t]] = \mathbf{0}$  before the onset of fracture  $\sup \alpha_t < 1$ .

The variational approach outlined in Definition 2.1 permits also a systematic derivation of the jump conditions across such surfaces. We assume here that the space-time evolution  $t \mapsto S_t$  is known advance and its normal velocity in the reference configuration  $\Omega$  is denoted by  $V_t$ . A perturbation to the singular surface is considered in (Batra, Bedford, & Drumheller, 1986) however the formalism is similar to what will be described in Section 2.3. The presence of such surfaces can thus be included into the admissible spaces (2.12) and (2.13). The first-order stability condition (2.17) leads directly to the classical vectorial jump condition for the stress tensor

$$[[\rho \dot{\mathbf{u}}_t]] V_t + [[\boldsymbol{\sigma}_t]] \mathbf{n} = \mathbf{0}.$$

Compared to the classical stress jump condition, note that here the stress tensor  $\boldsymbol{\sigma}_t$  is modulated by the damage, see (2.2). Concerning the damage criterion, we have

$$[[\nabla \alpha_t]] \cdot \mathbf{n} \leq 0.$$

As can be seen from Figure 2.2, a discontinuity in the damage gradient often corresponds to the fracture point where  $\alpha_t = 1$ .

Similarly, the global energy balance condition (2.18) results in the following energy density jump condition

$$[[\psi(\boldsymbol{\varepsilon}(\mathbf{u}_t), \alpha_t) + \kappa(\dot{\mathbf{u}}_t) + \zeta(\alpha_t, \nabla \alpha_t)]] V_t + [[\boldsymbol{\sigma}_t \dot{\mathbf{u}}_t]] \cdot \mathbf{n} = 0.$$

In addition to the remark concerning the stress tensor, the dissipated energy density (2.5) is also included. When the damage evolves  $\dot{\alpha}_t > 0$ , the normal component of the damage gradient is continuous across these surfaces. We have

$$[[\nabla \alpha_t]] \cdot \dot{\alpha}_t \mathbf{n} = 0.$$

### 2.1.4 Comparison with phase-field approaches

Two essentially different phase-field models co-exist in the literature: one that originated from the mechanics community initiated by the work of (Miehe, Hofacker, & Welschinger, 2010; Miehe, Welschinger, & Hofacker, 2010), and the other independently proposed by the physicists via the work of (Hakim & Karma, 2009; Karma et al., 2001). They will be separately compared with the gradient damage approach outlined in Definition 2.1.

**Phase-field model originated from the mechanics community** The phase-field model in the sense of (Miehe, Hofacker, & Welschinger, 2010; Miehe, Welschinger, & Hofacker, 2010) is initially stated for rate-independent evolutions but has been quickly extended to the dynamic setting in (Hofacker & Miehe, 2013; Hofacker & Miehe, 2012). Since then, phase-field models have been used to study various real-world dynamic fracture problems, see for example the work of (Borden et al., 2012; Schlüter et al., 2014). The governing equations are similar to that derived from the variational principles for the gradient damage model. In particular, the evolution law of the phase-field lies in on the definition of a *regularized crack functional* which measures the Griffith's surface energy of the phase-field crack. It turns out that this functional can be regarded as a damage dissipation energy (2.5) in the gradient-damage terminology with a particular damage constitutive law: the (AT) model. Using (2.10), the damage dissipation energy associated with the (AT) model reads

$$\mathcal{S}(\alpha_t) = \int_{\Omega} \frac{G_c}{2} \left( \frac{\alpha_t^2}{\eta} + \eta \nabla \alpha_t \cdot \nabla \alpha_t \right) d\mathbf{x},$$

which agrees exactly with that used in (Hofacker & Miehe, 2013; Hofacker & Miehe, 2012; Klinsmann et al., 2015; Miehe, Hofacker, & Welschinger, 2010; Miehe, Welschinger, & Hofacker, 2010). In (Borden et al., 2012; May, Vignollet, & de Borst, 2015; Schlüter et al., 2014), a non-essential rescaling of the internal length  $\eta = 2\tilde{\eta}$  is performed. As stated in Section 2.1.1, this constitutive law originates from the Ambrosio and Tortorelli regularization model introduced in (Bourdin et al., 2000) and enjoys hence the desired  $\Gamma$ -convergence property. In this respect, these phase-field models correspond to a special case of gradient damage models.

Another difference between the gradient damage model and these phase-field approaches lies in the irreversibility condition (cf. a discussion on this point in (Amor et al., 2009)). In our approach the damage is assumed to be an irreversible evolution, *i.e.*  $\dot{\alpha}_t \geq 0$ . This condition is enforced during the energy minimization principle (2.22) as an optimization constraint prescribed in the damage admissible space (2.13). By doing so, (2.22) corresponds to a bound-constrained optimization problem which requires specially designed numerical algorithms. On the contrary, in these phase-field approaches the irreversibility condition is only weakly prescribed:

- In (Borden et al., 2012; Klinsmann et al., 2015; May et al., 2015; Miehe, Hofacker, & Welschinger, 2010; Miehe, Welschinger, & Hofacker, 2010) for instance, the irreversible constraint is dropped during energy minimization. The current phase-field corresponds to the solution of the following unconstrained optimization problem

$$\mathcal{E}(\mathbf{u}_t, \alpha_t) + \mathcal{S}(\alpha_t) \leq \mathcal{E}(\mathbf{u}_t, \beta_t) + \mathcal{S}(\beta_t) \text{ for all } \beta_t. \quad (2.28)$$

The irreversible behaviors of the phase-field is modeled via the introduction of a history field defined by

$$\mathcal{H}_t = \max_{s \leq t} \psi_0(\boldsymbol{\varepsilon}(\mathbf{u}_s)) \quad (2.29)$$

which records for every material point the maximal undamaged elastic energy density in the history. The growth criterion for the phase field adapted from (2.25) is then given by

$$-a'(\alpha_t)\mathcal{H}_t - w'(\alpha_t) + \operatorname{div} \mathbf{q}_t = 0, \quad (2.30)$$

where the history field  $\mathcal{H}_t$  is regarded as the driving force of damage. According to the analyses in (Amor, 2008), this method can only be applied to the (AT) model, since in that case the unconstrained solution  $\alpha_t$  to (2.22) or solved by (2.30) is necessarily bounded by the interval  $[0, 1]$ . When other sophisticated models are used such as the (PAMM) model, one has to introduce the bound constraints during the minimization procedure.

- In (Lancioni & Royer-Carfagni, 2009), one solves the same linear system (2.28) and then performs an *a posteriori* projection in the admissible space. It can be considered as a numerical approximation of the real irreversibility condition embedded in the bound-constrained minimization problem. Nevertheless this method is also only limited to the (AT) model.

- In (Bourdin et al., 2000; Schlüter et al., 2014), the same linear system (2.28) is solved and one prescribes irreversibility only for totally damaged material points, *i.e.* where  $\alpha_t(\mathbf{x}) = 1$ . According to (Amor et al., 2009), it can be regarded as a purely numerical approximation of the constrained minimization problem (2.22). On the other hand, this is also physics-motivated according to (Schlüter et al., 2014). Nevertheless, the physical motivation behind this weakly reinforced irreversibility originates from an undesired property of the (AT) model: that of strain-hardening in the phase-field interval  $[0, \frac{1}{4}]$ , see Figure 2.1. This property has already been illustrated theoretically in (Pham, Amor, et al., 2011) and numerically in (Borden et al., 2012) for instance. In this interval *damage* does not take place since the stress increases with the phase-field, and hence the material behavior should be reversible. However a more natural requirement, that the (PAMM) model satisfies, is the strain-softening behavior for every phase field in the interval  $\alpha \in (0, 1)$ . In this case the phase-field retrieves its physical meaning of *damage*, and one necessarily should introduce the irreversible condition and solve a constrained minimization problem (2.22).

**Phase-field model originated from the physics community** The phase-field model studied in (Hakim & Karma, 2009; Karma et al., 2001) constitutes another continuum and regularized approach for quasi-static and dynamic fracture problems. Compared to the gradient damage approach, in these models the phase field evolution is *viscous* in nature. The governing equations for the phase fields  $\phi$  can be obtained in a semi-variational way from a potential energy  $\mathcal{P}(\mathbf{u}_t, \phi_t)$  defined as the sum of the elastic energy similar to (2.1) and the dissipation energy similar to (2.5). Using the notations given in (Hakim & Karma, 2009), one has

$$\chi^{-1} \dot{\phi}_t = - \frac{\partial \mathcal{P}}{\partial \phi_t}(\mathbf{u}_t, \phi_t), \quad (2.31)$$

which corresponds to the standard Ginzburg-Landau equation with  $\chi > 0$  a kinetic or mobility (Kuhn & Müller, 2010) coefficient. This parameter controls an *additional* energy dissipation in the form of heat during the crack propagation, as can be seen by following (corrected) equation based on (13) in (Hakim & Karma, 2009)

$$\mathcal{H}_t = -\chi \left( \frac{\partial \mathcal{P}}{\partial \phi_t}(\mathbf{u}_t, \phi_t) \right)^2 \leq 0. \quad (2.32)$$

Recall that damage is the only dissipation mechanism in the gradient damage model since an energy balance condition (2.18) is added in the formulation.

A parallel consequence of the appearance of a kinetic coefficient  $0 < \chi < \infty$  in (2.31), as discussed in (Bourdin et al., 2011), is that an evolutionary parabolic equation (2.31) governing the phase field is coupled with the elliptic static equilibrium problem or the hyperbolic dynamic wave equation. Physically it means that the crack can evolve solely with a rate determined by  $\chi$ , even if the structure is in static equilibrium at  $t = T$  with all external loading frozen for all  $t > T$ . With a physical time being introduced into the model (the dimension of the kinetic coefficient is  $[\text{T}]^{-1}$ ), the coupled system isn't well suited for quasi-static computations, as numerically the static problem should be combined with a specific time-stepping scheme (the explicit Euler scheme in (Hakim & Karma, 2009)) to integrate the evolution problem for the phase field.

### 2.1.5 Extension to large displacement situations

We discuss a large-displacement extension of the original gradient damage model in an explicit dynamics case. The small displacement condition (small rotation and small strain) is a plausible hypothesis for brittle materials when finite rotations are also not expected in the body. Otherwise geometrical nonlinearities should be taken into account in the definition of the elastic energy (2.1) or more specifically the undamaged elastic energy density (2.3), through the introduction of a nonlinear strain measure.

In the literature, a Lagrangian strain measure based on the right Cauchy-Green tensor  $\mathbf{F}_t^T \mathbf{F}_t$  is used for the geometrically nonlinear or finite-strain extension of phase-field models, both in the quasi-static



case, see (Clayton & Knap, 2014; Miehe & Schänzel, 2014; Miehe, Schänzel, & Ulmer, 2015; Piero et al., 2007) and in the implicit dynamic case, cf. (Hesch & Weinberg, 2014; Miehe, Hofacker, Schänzel, & Aldakheel, 2015). It is a natural choice since the current configuration  $\Omega_t$  is not known in advance for implicit calculations and the momentum equilibrium is written either in the initial reference configuration  $\Omega = \Omega_0$  (total Lagrangian formulation) or in the last known reference configuration (updated Lagrangian formulation). In explicit dynamics however, dynamic momentum balance can be directly prescribed in the current known configuration  $\Omega_t = \varphi_t(\Omega)$  updated from the last iteration following the explicit temporal discretization scheme. For this reason here we will use the Eulerian Hencky logarithmic strain tensor (Xiao, Bruhns, & Meyers, 1997) defined by

$$\mathbf{h}_t = \mathbf{h}(\mathbf{u}_t) = \log \mathbf{V}_t = \sum_i (\log \lambda_i) \mathbf{n}_i \otimes \mathbf{n}_i \quad (2.33)$$

where  $\mathbf{V}_t$  is the left stretch tensor from the polar decomposition of the deformation gradient  $\mathbf{F}_t = \mathbb{I} + \nabla \mathbf{u}_t = \mathbf{V}_t \mathbf{R}_t$  and  $(\lambda_i, \mathbf{n}_i)$  denotes a pair of the principal stretch and the corresponding spatial principal directions. Based on this strain measure, a simple Hookean type hyperelastic model (Xiao & Chen, 2002) is adopted to account for geometric nonlinearities

$$\psi_0(\mathbf{h}_t) = \frac{1}{2} \lambda (\text{tr } \mathbf{h}_t)^2 + \mu \mathbf{h}_t \cdot \mathbf{h}_t. \quad (2.34)$$

We emphasize that the stress measure conjugate to the Hencky logarithmic strain is the Kirchhoff stress, which implies the following definition of the Cauchy stress

$$\boldsymbol{\sigma}_t = \frac{1}{J_t} \frac{\partial \psi_0}{\partial \mathbf{h}_t}(\mathbf{h}_t) = \frac{1}{J_t} (\lambda (\text{tr } \mathbf{h}_t) \mathbb{I} + 2\mu \mathbf{h}_t), \quad (2.35)$$

where  $J_t = \det \mathbf{F}_t$  is the Jacobian determinant.

It should be noted that the variational framework as summarized by Definition 2.1 remains the same. The same energy minimization principle (2.22) can be derived, since the damage problem is naturally defined in the initial reference configuration. On the other hand, by developing the directional derivative of the action integral with respect to  $\mathbf{u}$  similar to (2.19) and supposing that the displacement field is sufficiently regular in time and in space, the elastic-damage dynamic wave equation can be derived in the *deformed* configuration  $\Omega_t = \varphi_t(\Omega)$ , which reads

$$\rho_t \ddot{\mathbf{u}}_t - \text{div } \boldsymbol{\sigma}_t = \bar{\mathbf{f}}_t \quad \text{in } \Omega_t \quad \text{and} \quad \boldsymbol{\sigma}_t \mathbf{n} = \bar{\mathbf{F}}_t \quad \text{on } \varphi_t(\partial \Omega_F), \quad (2.36)$$

where  $\rho_t = \rho/J_t$  is the density in the current configuration and the external power potential is also transformed to the deformed configuration according to (Ciarlet, 1993):

$$\overline{\mathcal{W}}_t(\mathbf{w}_t) = \int_{\Omega_t} \bar{\mathbf{f}}_t \cdot \mathbf{w}_t \, d\mathbf{x} + \int_{\varphi_t(\partial \Omega_F)} \bar{\mathbf{F}}_t \cdot \mathbf{w}_t \, d\mathbf{s}.$$

To obtain (2.36), the work conjugacy condition satisfied by the Hencky's hyperelastic model is used, see (Xiao & Chen, 2002). Specifically, we have

$$\dot{w}_t = \boldsymbol{\tau}_t \cdot \mathbf{D}_t = \boldsymbol{\tau}_t \cdot \dot{\mathbf{h}}_t \implies \boldsymbol{\tau}_t \cdot \nabla^s \mathbf{v}_t = \boldsymbol{\tau}_t \cdot \mathbf{h}'(\mathbf{u}_t) \mathbf{v}_t \quad (2.37)$$

where  $\dot{w}_t$  is the rate of work per unit volume in the reference configuration and  $\mathbf{D}_t$  is the stretching, *i.e.* the symmetrized part of the velocity gradient  $\nabla \mathbf{v}_t = \dot{\mathbf{F}}_t \mathbf{F}_t^{-1}$ .

## 2.2 Tension-Compression Asymmetry

In this section we will discuss several approaches in an attempt to account for the tension-compression asymmetry of damage behavior of materials. The objective is to provide a better understanding of the existing models following a theoretical approach and to point out some improvements that can be done in the future. Both approaches from the gradient damage community and the phase-field community will be analyzed. The thematic subjects covered here are thus summarized in Table 2.3.

Table 2.3 – Thematic subjects covered in this section

	Going dynamical	$\alpha \leftrightarrow \phi$	$\nabla \alpha \rightarrow \Gamma$	Experimental validation
Theoretics		👍		
Numerics				

### 2.2.1 Review of existing models

In general two possibilities can be considered: modification of damage-dependence of the elastic energy density (2.3), and/or modification of the variational principles (of irreversibility, stability and energy balance) outlined in Definition 2.1. The second approach has been discussed in (Lorentz & Kazymyrenko, 2014; Miehe, Schänzel, & Ulmer, 2015) where the damage driving force in the sense of  $\mathcal{H}_t$  in (2.30) deduced from the energy minimization principle (2.22) is replaced by, for example, some stress-based criteria. However it is known from (Sicsic & Marigo, 2013) that the variational formulation plays an essential role in establishing the link between damage and fracture and in the definition of a generalized energy release rate with respect to the crack extension. That's why only the first possibility will be discussed in this section. For notational simplicity, we place ourselves at a particular material point  $\mathbf{x}$  characterized by a strain tensor  $\boldsymbol{\varepsilon} = \boldsymbol{\varepsilon}(\mathbf{u}_t)(\mathbf{x})$  and a current damage state  $\alpha = \alpha_t(\mathbf{x})$ .

Several existing approaches consist of *additively* partitioning the sound elastic energy density  $\psi_0$  in (2.3) into two parts: a *positive* part  $\psi_0^+(\boldsymbol{\varepsilon})$  which is assumed to contribute to damage, and the *negative* part  $\psi_0^-(\boldsymbol{\varepsilon})$  which resists damage. The elastic energy density in (2.3) being acted symmetrically in tension and compression by damage is then replaced by the expression

$$\psi(\boldsymbol{\varepsilon}, \alpha) = \mathbf{a}(\alpha)\psi_0^+(\boldsymbol{\varepsilon}) + \psi_0^-(\boldsymbol{\varepsilon}) \quad (2.38)$$

where the damage degradation function  $\mathbf{a}(\alpha)$  only acts on the *positive* part  $\psi_0^+(\boldsymbol{\varepsilon})$ . By doing so, damage evolution is then driven by the *positive* elastic energy according to (2.22).

Furthermore, if the partition of the sound elastic energy  $\psi_0(\boldsymbol{\varepsilon})$  is based on that of the strain tensor  $\boldsymbol{\varepsilon} = \boldsymbol{\varepsilon}^+ + \boldsymbol{\varepsilon}^-$ , *i.e.* the constitutive behaviors

$$\begin{aligned} \boldsymbol{\varepsilon}^\pm &\mapsto \psi_0^\pm(\boldsymbol{\varepsilon}^\pm) = \frac{1}{2} \mathbf{A}_0 \boldsymbol{\varepsilon}^\pm \cdot \boldsymbol{\varepsilon}^\pm, \\ \boldsymbol{\varepsilon}^\pm &\mapsto \boldsymbol{\sigma}_0^\pm(\boldsymbol{\varepsilon}^\pm) = \mathbf{A}_0 \boldsymbol{\varepsilon}^\pm \end{aligned} \quad (2.39)$$

are characterized by the same elasticity tensor  $\mathbf{A}_0$  both for the *positive* and *negative* strains, then there exists in fact a local variational principle from which several existing tension-compression asymmetry models can be derived. This formulation is adapted from (Freddi & Royer-Carfagni, 2010) where the framework of *structured deformations* is used to decompose the strain tensor into an elastic part and an inelastic one related to microstructures which in our notation is given by  $\alpha \boldsymbol{\varepsilon}^+$ . However here we confine ourselves to macroscopic modeling and interpret the *positive* strain  $\boldsymbol{\varepsilon}^+$  as the part that merely contributes to local material degradation. The mechanical modeling of such *positive* strains will be encapsulated into a *convex* subset  $C$  of all symmetric 2nd-order tensors. The effective computation of  $\boldsymbol{\varepsilon}^+ \in C$  is determined by the following local variational requirement for every material point

$$\|\boldsymbol{\varepsilon}^+ - \boldsymbol{\varepsilon}\|_{\mathbf{A}_0} = \min_{\mathbf{e} \in C} \|\mathbf{e} - \boldsymbol{\varepsilon}\|_{\mathbf{A}_0} = \min_{\mathbf{e} \in C} \mathbf{A}_0(\boldsymbol{\varepsilon} - \mathbf{e}) \cdot (\boldsymbol{\varepsilon} - \mathbf{e}). \quad (2.40)$$

Owing to the convexity of  $C$ , the *positive* strain  $\boldsymbol{\varepsilon}^+$  is unique and is defined as the orthogonal projection of the total strain  $\boldsymbol{\varepsilon}$  onto the space  $C$  with respect to the energy norm defined by the elasticity tensor  $\mathbf{A}_0$ . From convex analysis it is known that  $\boldsymbol{\varepsilon}^+$  that satisfies (2.40) can be equivalently characterized by

$$-\mathbf{A}_0(\boldsymbol{\varepsilon} - \boldsymbol{\varepsilon}^+) \cdot (\mathbf{e} - \boldsymbol{\varepsilon}^+) \geq 0 \text{ for all } \mathbf{e} \in C. \quad (2.41)$$

which implies from the definition (2.39) that the negative sound stress  $\boldsymbol{\sigma}_0^- = \mathbf{A}_0 \boldsymbol{\varepsilon}^-$  is in the polar cone  $C^* = \{ \mathbf{e}^* \mid \mathbf{e}^* \cdot \mathbf{e} \leq 0 \text{ for all } \mathbf{e} \in C \}$ . If the space  $C$  is also a cone, *i.e.* closed with respect to arbitrary



positive rescaling  $\alpha \mathbf{e}$  for  $\alpha > 0$ , then testing (2.41) with  $\mathbf{e} = 2\boldsymbol{\varepsilon}^+$  and  $\mathbf{e} = \frac{1}{2}\boldsymbol{\varepsilon}^+$  furnishes along with the symmetry of  $\mathbf{A}_0$  the following orthogonality conditions

$$\begin{aligned}\boldsymbol{\sigma}_0^- \cdot \boldsymbol{\varepsilon}^+ &= \mathbf{A}_0(\boldsymbol{\varepsilon} - \boldsymbol{\varepsilon}^+) \cdot \boldsymbol{\varepsilon}^+ = 0, \\ \boldsymbol{\sigma}_0^+ \cdot \boldsymbol{\varepsilon}^- &= \mathbf{A}_0(\boldsymbol{\varepsilon} - \boldsymbol{\varepsilon}^-) \cdot \boldsymbol{\varepsilon}^- = 0.\end{aligned}\tag{2.42}$$

This implies that  $\psi_0^+$  and  $\psi_0^-$  defined in (2.39) constitute indeed a partition of the sound elastic energy density

$$2\psi_0(\boldsymbol{\varepsilon}) = \mathbf{A}_0\boldsymbol{\varepsilon} \cdot \boldsymbol{\varepsilon} = \boldsymbol{\sigma}_0^+ \cdot \boldsymbol{\varepsilon}^+ + \boldsymbol{\sigma}_0^- \cdot \boldsymbol{\varepsilon}^-$$

where the crossed terms disappear thanks to (2.42). This provides another interpretation of (2.40) from a mechanical point of view: the *positive* part of the strain minimizes the *negative* part of the elastic energy  $\boldsymbol{\sigma}_0^- \cdot \boldsymbol{\varepsilon}^-$  that resists to damage.

*Remark.* The orthogonality conditions (2.42) are nothing but Moreau's decomposition theorem (Moreau, 1962).

*Remark.* This variational principle (2.40) is similar in essence to that initially proposed in (Ortiz, 1985) for the modeling of microcracks. Here the damage mechanism is based on the partition of a given strain tensor (or the elasticity tensor), however in (Ortiz, 1985) the external stress tensor is regarded as an input and a decomposition of the compliance tensor is performed.

We now turn to the stress tensor derived from (2.38) and (2.39). In general we should have by definition

$$\boldsymbol{\sigma}(\boldsymbol{\varepsilon}, \alpha)\mathbf{e} = a(\alpha)\boldsymbol{\sigma}_0^+ \cdot \frac{\partial \boldsymbol{\varepsilon}^+}{\partial \boldsymbol{\varepsilon}}(\boldsymbol{\varepsilon})\mathbf{e} + \boldsymbol{\sigma}_0^- \cdot \frac{\partial \boldsymbol{\varepsilon}^-}{\partial \boldsymbol{\varepsilon}}(\boldsymbol{\varepsilon})\mathbf{e}\tag{2.43}$$

where derivatives of the decomposed strains  $\boldsymbol{\varepsilon}^\pm$  with respect to the total strain appear. Fortunately, as  $\partial_{\boldsymbol{\varepsilon}}\boldsymbol{\varepsilon}^+ \in C$  and  $\partial_{\boldsymbol{\varepsilon}}\boldsymbol{\sigma}_0^- \in C^*$ , we have due to (2.41)

$$\boldsymbol{\sigma}_0^- \cdot \frac{\partial \boldsymbol{\varepsilon}^+}{\partial \boldsymbol{\varepsilon}}(\boldsymbol{\varepsilon})\mathbf{e} \leq 0 \text{ and } \boldsymbol{\sigma}_0^+ \cdot \frac{\partial \boldsymbol{\varepsilon}^-}{\partial \boldsymbol{\varepsilon}}(\boldsymbol{\varepsilon})\mathbf{e} \leq 0.\tag{2.44}$$

By differentiating the orthogonality condition (2.42) with respect to the total strain  $\boldsymbol{\varepsilon}$ , we find that the sum of the above two non-positive inner products equals to zero, which implies individually that these two expressions in (2.44) vanish. Recalling  $\boldsymbol{\varepsilon} = \boldsymbol{\varepsilon}^+ + \boldsymbol{\varepsilon}^-$ , the stress tensor is readily identified from (2.43)

$$\boldsymbol{\sigma}_t = \boldsymbol{\sigma}(\boldsymbol{\varepsilon}, \alpha) = a(\alpha)\boldsymbol{\sigma}_0^+ + \boldsymbol{\sigma}_0^-.\tag{2.45}$$

This is the stress expression  $\boldsymbol{\sigma}_t$  which will be used in the elastic-damage dynamic wave equation (2.20) or (2.21) when tension-compression asymmetry is considered. It can be noted that this expression is reduced to its negative part  $\boldsymbol{\sigma}(\boldsymbol{\varepsilon}, 1) = \boldsymbol{\sigma}_0^- \in C^*$  for a totally damaged element.

*Remark.* The tension-compression split described above, especially the additive strain decomposition (2.39), applies only to the small displacement case. However it can be extended to the large displacement framework outlined in Section 2.1.5.

Assume that the additive strain decomposition is performed with respect to a same basis, *i.e.* the positive/negative strain  $\boldsymbol{\varepsilon}^\pm$  is coaxial to the total strain  $\boldsymbol{\varepsilon}$ , then the definition of the Hencky logarithmic strain  $\boldsymbol{\varepsilon} = \mathbf{h}_t$  implies (see (2.33))

$$\begin{aligned}\boldsymbol{\varepsilon} &= \boldsymbol{\varepsilon}^+ + \boldsymbol{\varepsilon}^- \\ &= \sum_i (\log \lambda_i) \mathbf{n}_i \otimes \mathbf{n}_i = \sum_i (\log \lambda_i^+ + \log \lambda_i^-) \mathbf{n}_i \otimes \mathbf{n}_i = \sum_i (\log(\lambda_i^+ \lambda_i^-)) \mathbf{n}_i \otimes \mathbf{n}_i.\end{aligned}$$

Thus, an additive decomposition of the logarithmic strain becomes automatically a multiplicative decomposition of the principal stretches

$$\lambda_i = \lambda_i^+ \lambda_i^-.$$

This strategy is adopted for example in (Hesch & Weinberg, 2014). Note that the coaxiality between  $\boldsymbol{\varepsilon}^\pm$  and  $\boldsymbol{\varepsilon}$  is generally verified in the current variational principle (2.40), if elastic isotropy is assumed.

Since the stress measure conjugate to the Hencky logarithmic strain is the Kirchhoff stress, see (2.35). The stress expression (2.45) becomes

$$\boldsymbol{\sigma}_t = \boldsymbol{\sigma}(\boldsymbol{\varepsilon}, \alpha) = \frac{1}{J}(\mathfrak{a}(\alpha)\mathbf{A}_0\boldsymbol{\varepsilon}^+ + \mathbf{A}_0\boldsymbol{\varepsilon}^-),$$

where  $J$  refers to the Jacobian determinant of the total strain, for the particular material point under question.

Using this variational formulation (2.40), the modeling of material tension-compression asymmetry is thus reduced to the setting of such convex cone  $C$  destined to represent the strains that contribute to damage. Several existing phase-field like models of fracture can be derived within this framework (Freddi & Royer-Carfagni, 2010).

- The original symmetric model of (Bourdin et al., 2000) can be trivially obtained by choosing  $C$  to all symmetric 2nd-order tensors. From (2.41) it can be deduced that  $\boldsymbol{\varepsilon}^+ = \boldsymbol{\varepsilon}$ , *i.e.* the total strain contributes to damage irrespective of whether it corresponds to traction or compression.
- The deviatoric model of (Lancioni & Royer-Carfagni, 2009) is retrieved when  $C$  represents all symmetric 2nd-order tensors that have a zero trace (and the condition that  $\mathbf{A}_0$  is isotropic). Only the deviatoric part of the strain participates to damage, *i.e.*  $\boldsymbol{\varepsilon}^+ = \text{dev } \boldsymbol{\varepsilon}$ . The negative stress  $\boldsymbol{\sigma}_0^-$  belongs to the polar cone of  $C$  which is characterized by a zero deviatoric part. Thus for a totally damaged material point the stress is hydrostatic and has the form  $p\mathbb{I}$  for  $p \in \mathbb{R}$ .
- The model of (Amor et al., 2009) is a combination of the previous two models. If the total strain corresponds to an expansion  $\text{tr } \boldsymbol{\varepsilon} \geq 0$ , the damage mechanism is completely active and  $C$  corresponds to all symmetric 2nd-order tensors. However if a compressive strain is present  $\text{tr } \boldsymbol{\varepsilon} < 0$ , only the deviatoric part of the strain participates to damage ( $\boldsymbol{\varepsilon}^+ = \text{dev } \boldsymbol{\varepsilon}$ ) and  $C$  corresponds to all symmetric 2nd-order tensors that have a zero trace. In this case a totally damaged material point experiences a compressive hydrostatic pressure  $p\mathbb{I}$  for  $p \leq 0$ .
- The masonry-like model of (Freddi & Royer-Carfagni, 2010) is obtained when  $C$  is chosen to include all positive semidefinite symmetric tensors. Since  $C$  is a convex cone, the stress tensor can be simplified to (2.45) and hence the stress that can be attained by a totally damaged material point is necessarily negative semidefinite, corresponding in fact to materials that do not support tension (Piero et al., 2007). However the model as suggested by (Freddi & Royer-Carfagni, 2010) with  $C$  containing all symmetric tensors of which all eigenvalues are greater than -1 may present some difficulties, as the orthogonality condition (2.42) and the simplified stress expression (2.45) no longer apply,  $C$  not being closed with respect to arbitrary positive rescaling.

For the masonry-like model (Freddi & Royer-Carfagni, 2010), an explicit formula of the positive strain  $\boldsymbol{\varepsilon}^+$  as a function of the total strain  $\boldsymbol{\varepsilon}$  is obtained for both two-dimensional or three-dimensional problems in the isotropic case. The solution is derived from the minimization structure (2.40) or equivalently the variational inequality (2.41). The coaxiality between  $\boldsymbol{\varepsilon}^+$  and  $\boldsymbol{\varepsilon}$  is also exploited due to isotropy, see (Alfano, Rosati, & Valoroso, 2000; Del Piero, 1989). In the three dimensional case  $\boldsymbol{\varepsilon}^+$  can be calculated according to Algorithm 1. In the plane strain or plane stress case, Algorithm 2 can be used, where the strain space is partitioned into four subdomains, see Figure 2.4. It can be observed that due to the use of the  $\mathbf{A}_0$ -norm during minimization (2.40), the function  $\boldsymbol{\varepsilon} \mapsto \boldsymbol{\varepsilon}^+$  depends on the Poisson's ratio.

The tension-compression asymmetry model of (Miehe, Hofacker, & Welschinger, 2010), that is widely used among the phase field community in for instance (Borden et al., 2012; Hofacker & Miehe, 2012; Klinsmann et al., 2015; May et al., 2015), adopts the elastic energy density split (2.38) but does not fit into the variational formalism (2.40). Denoting  $\boldsymbol{\varepsilon}^+$  (resp.  $\boldsymbol{\varepsilon}^-$ ) as the positive (resp. negative)

---

**Algorithm 1** Explicit formula for  $\boldsymbol{\varepsilon}^+$  as a function of  $\boldsymbol{\varepsilon}$  for the masonry-like model (Freddi & Royer-Carfagni, 2010) in the three-dimensional case according to (Sacco, 1990)

---

- 1: Perform a spectral decomposition of the total strain  $\boldsymbol{\varepsilon} = (\varepsilon_1, \varepsilon_2, \varepsilon_3)$  with  $\varepsilon_1 \geq \varepsilon_2 \geq \varepsilon_3$
  - 2: **if**  $\varepsilon_3 \geq 0$  **then**
  - 3:      $\boldsymbol{\varepsilon}^+ \leftarrow \boldsymbol{\varepsilon}$
  - 4: **else if**  $\varepsilon_2 + \nu \varepsilon_3 \geq 0$  **then**
  - 5:      $\boldsymbol{\varepsilon}^+ \leftarrow (\varepsilon_1 + \nu \varepsilon_3, \varepsilon_2 + \nu \varepsilon_3, 0)$  in the same principal basis as  $\boldsymbol{\varepsilon}$
  - 6: **else if**  $(1 - \nu)\varepsilon_1 + \nu(\varepsilon_2 + \varepsilon_3) \geq 0$  **then**
  - 7:      $\boldsymbol{\varepsilon}^+ \leftarrow (\varepsilon_1 + \frac{\nu}{1-\nu}(\varepsilon_2 + \varepsilon_3), 0, 0)$  in the same principal basis as  $\boldsymbol{\varepsilon}$
  - 8: **else**
  - 9:      $\boldsymbol{\varepsilon}^+ \leftarrow \mathbf{0}$
  - 10: **end if**
  - 11: Transform  $\boldsymbol{\varepsilon}^+$  back to the canonical basis if necessary
- 

---

**Algorithm 2** Explicit formula for  $\boldsymbol{\varepsilon}^+$  as a function of  $\boldsymbol{\varepsilon}$  for the masonry-like model (Freddi & Royer-Carfagni, 2010) in the two-dimensional case according to (Alfano, Rosati, & Valoroso, 2000)

---

- 1: Perform a spectral decomposition of the total strain  $\boldsymbol{\varepsilon} = (\varepsilon_1, \varepsilon_2)$  with  $\varepsilon_1 \geq \varepsilon_2$
  - 2: **if** Plane strain case **then**
  - 3:      $\alpha = \nu/(1 - 2\nu)$
  - 4: **else**
  - 5:      $\alpha = \nu/(1 - \nu)$
  - 6: **end if**
  - 7: **if**  $\varepsilon_2 \geq 0$  **then**
  - 8:      $\boldsymbol{\varepsilon}^+ \leftarrow \boldsymbol{\varepsilon}$
  - 9: **else if**  $(1 + \alpha)\varepsilon_1 + \alpha\varepsilon_2 \geq 0$  **then**
  - 10:      $\boldsymbol{\varepsilon}^+ \leftarrow (\varepsilon_1 + \frac{\alpha}{1+\alpha}\varepsilon_2, 0)$  in the same principal basis as  $\boldsymbol{\varepsilon}$
  - 11: **else**
  - 12:      $\boldsymbol{\varepsilon}^+ \leftarrow \mathbf{0}$
  - 13: **end if**
  - 14: Transform  $\boldsymbol{\varepsilon}^+$  back to the canonical basis if necessary
- 



Figure 2.4 – Calculation of  $\boldsymbol{\varepsilon}^+$  for the masonry-like model (Freddi & Royer-Carfagni, 2010) in the plane strain case

part of the total strain obtained by projecting  $\boldsymbol{\varepsilon}$  onto the space of all symmetric positive (resp. negative) semidefinite tensors *with respect to the natural Frobenius norm*, their model reads

$$\begin{aligned}\psi_0^\pm(\boldsymbol{\varepsilon}) &= \frac{1}{2}\lambda \langle \text{tr } \boldsymbol{\varepsilon} \rangle_\pm^2 + \mu \boldsymbol{\varepsilon}_\pm \cdot \boldsymbol{\varepsilon}_\pm, \\ \boldsymbol{\sigma}_0^\pm(\boldsymbol{\varepsilon}) &= \lambda \langle \text{tr } \boldsymbol{\varepsilon} \rangle_\pm \mathbb{I} + 2\mu \boldsymbol{\varepsilon}_\pm\end{aligned}\tag{2.46}$$

where contrary to the formulation (2.39) there is no more individual constitutive relation separately for the positive or the negative strain. The function  $\boldsymbol{\varepsilon} \mapsto \boldsymbol{\varepsilon}^\pm$  no longer depends on the Poisson's ratio. The orthogonality condition (2.42) is not satisfied, however a partition of the sound elastic energy  $\psi_0 = \psi_0^+ + \psi_0^-$  is achieved. It is due to the fact that the positive bracket operator applies to the trace of the strain tensor. Despite its variational inconsistency, the stress for a totally damaged element is also negative semidefinite as for the model of (Freddi & Royer-Carfagni, 2010). The qualitative differences between these two models will be illustrated in the following section.

### 2.2.2 Uniaxial traction and compression experiment

Here we will investigate the theoretical behavior of the above outlined models under a very simple loading condition to illustrate their individual particularities. It can be understood that the underlying *local* damage model obtained by suppressing the gradient damage  $\nabla \alpha_t$  in the dissipation energy density (2.5) represents the material behavior when no strain or damage localization appears. Hence some general properties of these tension-compression asymmetry models can be extracted under an academic homogeneous 3-dimensional uniaxial traction or compression experiment. Inertia is not essential for this analysis and will be neglected. We suppose that the stress tensor is of form  $\boldsymbol{\sigma}_t = \sigma_{33} \mathbf{e}_3 \otimes \mathbf{e}_3$  corresponding to an imposed axial strain  $\varepsilon_{33} = t$  viewed as a loading parameter. Since  $\mathbf{A}_0$  is isotropic, the goal is to find the evolutions of the transversal strain  $t \mapsto \varepsilon_{11} = \varepsilon_{22}$ , the axial stress  $t \mapsto \sigma_{33}$  and the homogeneous damage  $t \mapsto \alpha_t$ . This amounts to solve the following system when the damage evolves  $\dot{\alpha}_t > 0$

$$\sigma_{11}(t) = (\mathbf{a}(\alpha_t) \boldsymbol{\sigma}_0^+ + \boldsymbol{\sigma}_0^-) \mathbf{e}_1 \cdot \mathbf{e}_1 = 0, \tag{2.47a}$$

$$\frac{\partial \psi}{\partial \alpha_t}(\boldsymbol{\varepsilon}_t, \alpha_t) + w'(\alpha_t) = 0 \tag{2.47b}$$

where  $\boldsymbol{\varepsilon}_t = \varepsilon_{11}(\mathbf{e}_1 \otimes \mathbf{e}_1 + \mathbf{e}_2 \otimes \mathbf{e}_2) + t \mathbf{e}_3 \otimes \mathbf{e}_3$ . The second equation (2.47b) corresponds to the consistency condition (2.25).

We remark that in order to solve (2.47) a particular set of damage constitutive laws also has to be chosen. Strictly speaking the functions  $\alpha \mapsto \mathbf{a}(\alpha)$  and  $\alpha \mapsto w(\alpha)$  should influence the exact behavior of the tension-compression asymmetry models. Nevertheless we discover that the solutions obtained with two particular damage constitutive laws (PAMM) and (AT) share many qualitative properties.

The model of (Amor et al., 2009) has been already studied in this uniaxial traction and compression setting with the damage model (AT). The material undergoes a softening behavior both under tension or compression when a certain *finite* threshold  $\sigma_0^\pm$  is reached. The ratio between these two maximal stresses is given by

$$-\frac{\sigma_0^-}{\sigma_0^+} = \sqrt{\frac{3}{2(1+\nu)}} \leq \sqrt{\frac{3}{2}} \approx 1.22$$

which is not sufficient for applications to brittle materials where this factor can attain 10. This ratio is the same when the damage constitutive law (PAMM) is used.

We then turn to the tension-compression separation proposed in (Miehe, Hofacker, & Welschinger, 2010). Similar as it is to the model of (Freddi & Royer-Carfagni, 2010) since both ones perform spectral decomposition of the total strain (with respect to two different inner products, though), their behavior under compression will be unexpectedly different. For the constitutive model of (PAMM),

the material remains intact until a tensile  $\sigma_0^+$  or a compressive  $\sigma_0^-$  stress threshold is reached

$$\sigma_0^+ = \sqrt{\frac{(1+\nu)}{(1-\nu)(1+2\nu)}} w_1 E,$$

$$\sigma_0^- = -\sqrt{\frac{1+\nu}{2\nu^2}} w_1 E \rightarrow \infty \text{ as } \nu \rightarrow 0.$$

It can be seen that the critical stress  $\sigma_0^+$  increases with the Poisson ratio but stays bounded in tension. The compressive threshold  $\sigma_0^-$  goes to infinity when  $\nu$  is near zero, hence no damage will occur in this case. We use the tensile threshold  $\sigma_0^+$  as well as its corresponding strain  $\varepsilon_0^+$  both evaluated at  $\nu = 0.2$  to normalize the results shown in Figure 2.5.

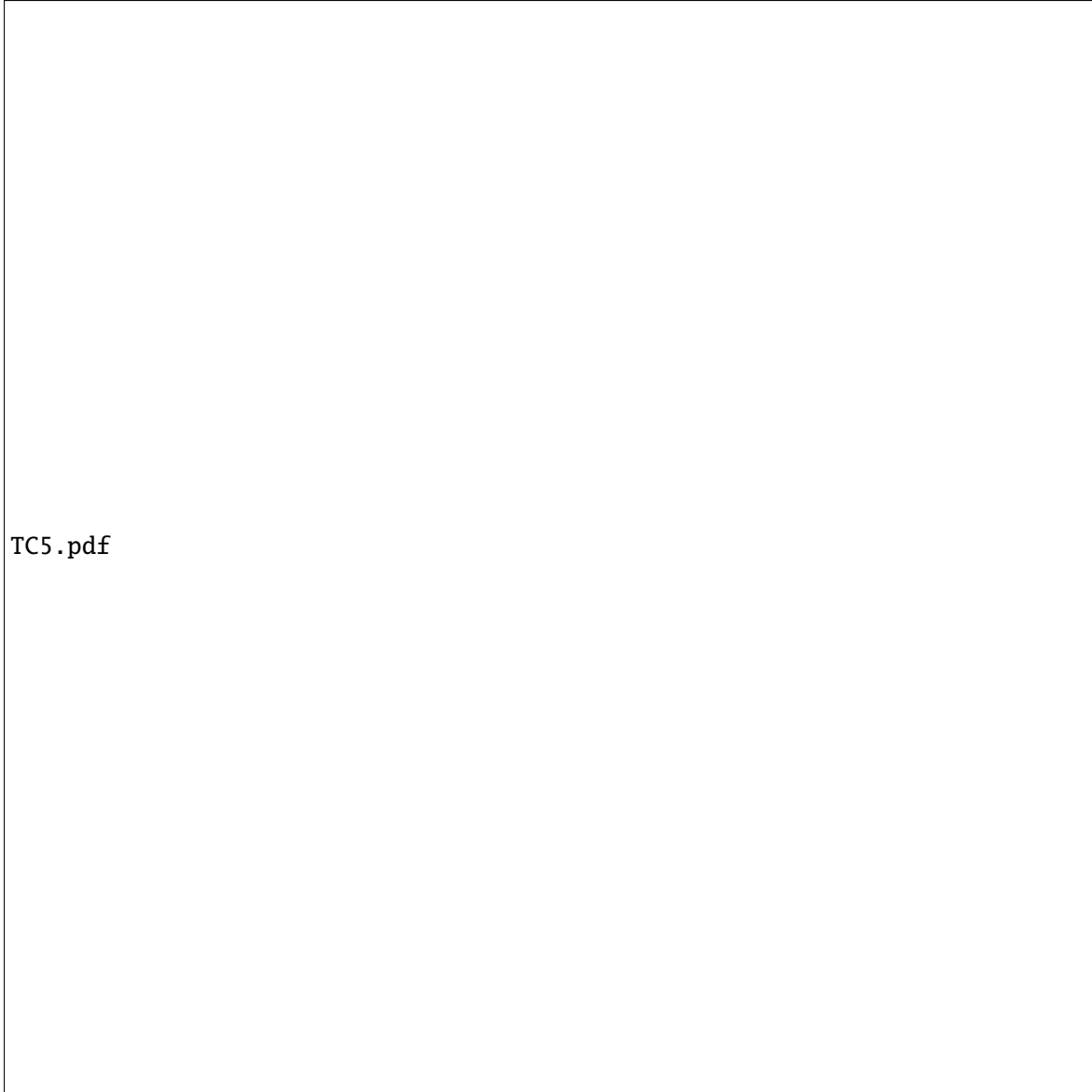


Figure 2.5 – Uniaxial traction  $\varepsilon_{33} \geq 0$  and compression  $\varepsilon_{33} \leq 0$  experiment for the tension-compression asymmetry proposed in (Miehe, Hofacker, & Welschinger, 2010). The damage constitutive law (PAMM) is used

Remark that under a uniaxial tensile loading, the material undergoes a classical softening behavior when the threshold stress is reached. For quasi-incompressible materials  $\nu \approx \frac{1}{2}$  a snap-back is present and hence the evolution of the stress  $\sigma_{33}$  and the strain  $\varepsilon_{11}$  may experience a temporal discontinuity. However this behavior is only limited to the law (PAMM) whereas for (AT) no snap-back is observed.

Unexpectedly, under compression the material may experience a two-phase softening-hardening (with an initial snap-back for  $0 \leq \nu \leq 3/8$  limited to the (PAMM) case), while the damage increases. As  $\alpha_t$  approaches 1, *i.e.* as the material point becomes totally damaged, the uniaxial stress is not bounded and is given by  $\sigma_{33} = 2\mu\epsilon_{33}$ . Moreover, an apparent incompressible behavior is observed  $\text{tr } \epsilon_t = 0$ . These properties can be readily derived using the definitions (2.46). Due to a non-vanishing stress inside a completely damaged element, one may expect large diffusive “damage” for highly compressive zones. This may complicate the physical interpretation of the model of (Miehe, Hofacker, & Welschinger, 2010) in this situation.

In contrast, for any damage constitutive laws the model proposed in (Freddi & Royer-Carfagni, 2010) does not permit any damage under uniaxial compression. The positive strain contributing to damage after projection (2.40) is given by  $\epsilon^+ = (\epsilon_{11} + \nu\epsilon_{33})(\mathbf{e}_1 \otimes \mathbf{e}_1 + \mathbf{e}_2 \otimes \mathbf{e}_2)$ , which vanishes due to the uniaxial stress state  $\sigma_t = \sigma_{33}\mathbf{e}_3 \otimes \mathbf{e}_3$  implying  $\epsilon_{11} = -\nu\epsilon_{33}$ . Under traction and when using the damage law (PAMM), a stress threshold under which no damage appears is given by

$$\sigma_0^+ = \sqrt{\frac{(1-\nu)}{(1-2\nu)(1+\nu)}} w_1 E \rightarrow \infty \text{ as } \nu \rightarrow \frac{1}{2}$$

so cracks cannot appear for incompressible materials. We again use the tensile stress threshold  $\sigma_0^+$  as well as its corresponding strain  $\epsilon_0^+$  both evaluated at  $\nu = 0.2$  to normalize the results shown in Figure 2.6. A classical softening behavior is observed after damage initiation. Analyses show that snapbacks are present for  $\nu > (\sqrt{33} - 1)/16 \approx 0.3$ . However it is only limited to the (PAMM) case.

### 2.2.3 How to choose among different models

Following the previous review and analyses of several existing models on tension-compression asymmetry, a natural question arises as to how to choose the *best* or the *right* one for a particular problem. If the variational formulation (2.40) is used, the problem can be reduced to choose a *good* convex cone  $C$  of the 2nd-order symmetric tensors. As the elastic energy density split (2.38) influences both the displacement and the damage problems through the first order stability condition (2.17), these two aspects will be separately discussed.

- For the  $\mathbf{u}$ -problem, the tension-compression asymmetry model is widely recognized to *approximate* the material non-interpenetration condition (Ambati, Gerasimov, & de Lorenzis, 2015; Amor et al., 2009; Lancioni & Royer-Carfagni, 2009). However we would like to recall that this approximation is merely heuristic. Taking into account the actual non-interpenetration condition at finite strains in the sense of (Ciarlet & Nečas, 1987), *i.e.* local orientation preservation and global injectivity, is a difficult task both from a theoretical or numerical point of view, and hence is often merely checked *a posteriori*. Nevertheless we could expect that the tension-compression decomposition *itself* should depend on the local damage state and the damage gradient  $\nabla\alpha_t$  approximating the local crack normal in the reference frame. A better elastic energy density split of (2.38) could be

$$\psi(\epsilon, \alpha, \nabla\alpha) = a(\alpha)\psi_0^+(\epsilon, \alpha, \nabla\alpha) + \psi_0^-(\epsilon, \alpha, \nabla\alpha). \quad (2.48)$$

When the crack is created, the elastic energy split *itself* should become orientation dependent so that only non-positive normal stress can be applied on crack lips if friction is not considered. This point will be illustrated in several numerical experiments.

- For the  $\alpha$ -problem, the decomposition (2.38) directly controls the type of strain or stress state which initiates and produces further damage: deviatoric part in (Lancioni & Royer-Carfagni, 2009) or in (Pham, Amor, et al., 2011) under compression and positive principal values in (Freddi & Royer-Carfagni, 2010; Miehe, Hofacker, & Welschinger, 2010). We share the remark given in (Ambati et al., 2015) that only experiments conducted with real materials can determine or identify a *good* model. We thus regard the elastic energy split (2.38) or the convex cone  $C$  as

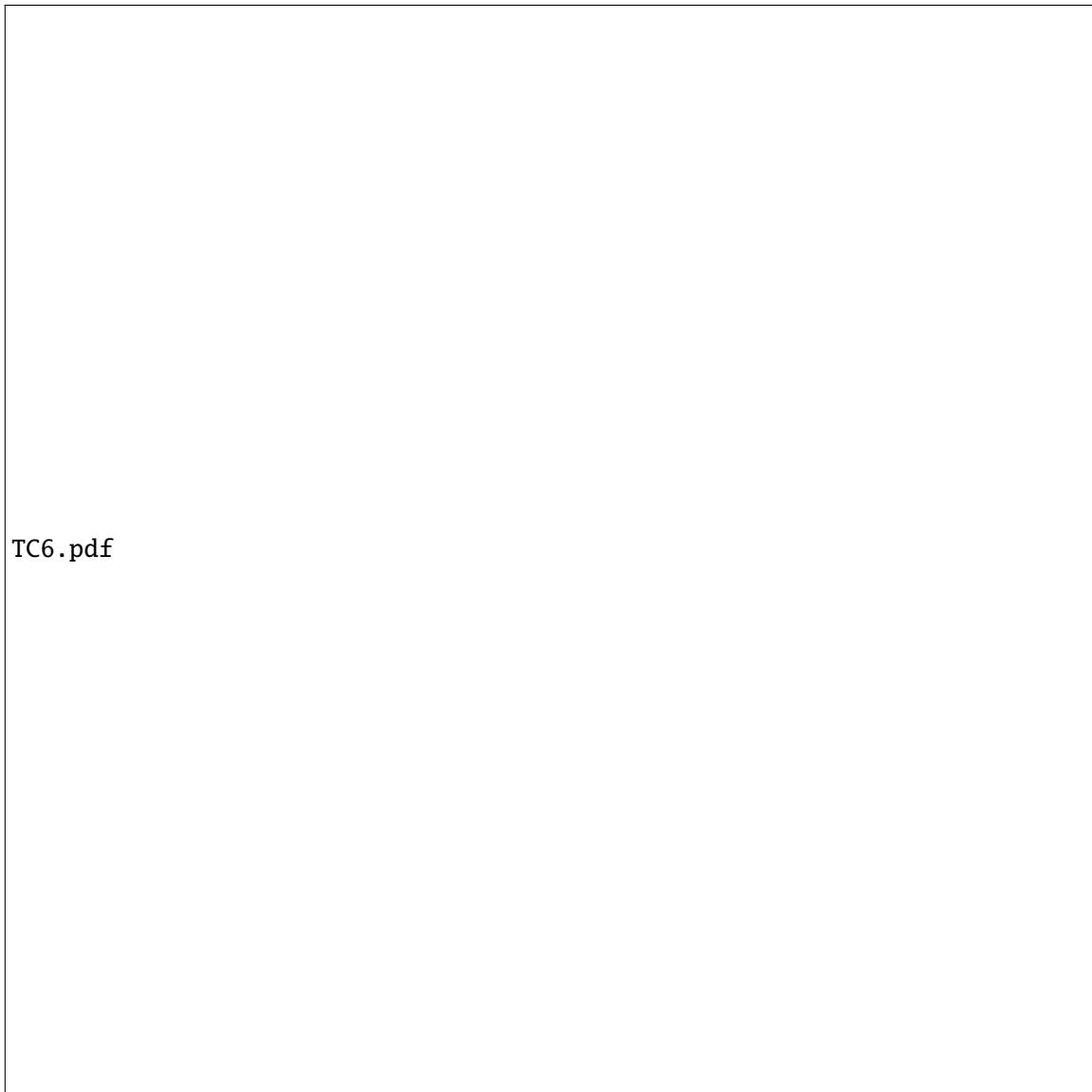


Figure 2.6 – Uniaxial traction  $\varepsilon_{33} \geq 0$  experiment for the tension-compression asymmetry proposed in (Freddi & Royer-Carfagni, 2010). The damage constitutive law (PAMM) is used

another independent material property or parameter characterizing the microstructure. For rocks or stones the deviatoric model may predict realistic crack path, however for more brittle materials such as concrete or glass, models based on a spectral decomposition may be more suitable.

## 2.3 Griffith's Law in Gradient Damage Models

The author proposes in this section to investigate the link between the dynamic gradient damage model and the classical Griffith's theory of dynamic fracture (1.10) during the crack propagation phase. The major difficulty lies in the proper definition of an energy release rate (playing the role of  $G$ ) and an equivalent material fracture resistance (playing the role of  $G_c$ ) in gradient damage models. These concepts involve, generally speaking, the derivative of a certain energy with respect to the crack length, hence the damage zone evolution should be assumed to follow a specific path parametrized by the arc length. Based on an Eulerian approach, authors of (Sicsic & Marigo, 2013) then identify a generalized damage-dependent Rice's  $J$ -integral containing these two concepts, which is automatically induced by the variational formulation of quasi-static gradient damage models.

To accomplish our objective in dynamics, the author proposes a rigorous and systematic methodology of performing the derivative of an energy functional with respect to the crack arc length. It is based on a Lagrangian description in the initial cracked configuration with the help of calculus of variations and shape optimization techniques. The equation of motion of the crack tip predicted by the dynamic gradient damage model is shown to be governed by a generalized Griffith criterion. With the help of a separation of scales, the former derived generalized Griffith criterion admits also an asymptotic interpretation. The thematic subjects covered here are thus summarized in Table 2.4.

Table 2.4 – Thematic subjects covered in this section

	Going dynamical	$\alpha \leftrightarrow \phi$	$\nabla \alpha \rightarrow \Gamma$	Experimental validation
Theoretics	👍		👍	
Numerics				

### 2.3.1 Lagrangian description in the initial cracked configuration

This section will be devoted to a rigorous energetic approach to deriving dynamic energy release rates. The basic assumptions will be a two-dimensional body  $\Omega$  containing a smoothly propagating crack  $\Gamma_t$  with a pre-defined path  $l \mapsto \gamma(l) \in \mathbb{R}^2$  parametrized by its arc length  $t \mapsto l_t \geq 0$ , see Figure 2.7. The symbol  $\mathbf{P}_t = \gamma(l_t)$  will be used to represent the crack tip at time  $t$ . The current cracked configuration will be denoted by  $\Omega \setminus \Gamma_t$  on which the kinematic quantities are defined. For the sake of simplicity, the crack  $\Gamma_t$  is assumed to remain far from the boundary  $\partial\Omega$ . The spatial crack path  $l \mapsto \gamma(l)$  can be curved but in this contribution we will only consider a straight crack with a constant tangent  $\gamma'(l_t) = \tau_t = \tau_0$ . Generalization to a curved crack path will be briefly discussed at the end of Appendix A.

*Remark.* For sharp-interface models (Griffith's theory for example), the crack  $\Gamma_t$  refers to an evolving strong discontinuity in the body. For gradient damage models, the crack  $\Gamma_t$  stands for a totally damage zone where  $\alpha_t = 1$ , see the local damage criterion (2.23) and the consistency condition (2.25). This interpretation will be formalized in Hypothesis 2.3. The essential requirement here is that the energetic quantities of the body can be written in the current cracked configuration  $\Omega \setminus \Gamma_t$ .

The displacement  $\mathbf{u}_t$  is defined in the current crack configuration  $\Omega \setminus \Gamma_t$ , consequently its total variation depends on that of the crack. A Lagrangian description of the fracture problem is thus preferred if one needs to rigorously define an energy release rate with respect to the crack length, see (Destuynder & Djaoua, 1981). The current cracked *material* configuration  $\Omega \setminus \Gamma_t$  is transformed to the initial one  $\Omega \setminus \Gamma_0$  thanks to a well-defined bijection  $\phi_{l_t}$  whose inverse as well as itself is differentiable, see Figure 2.7. Proving existence of such diffeomorphisms may be technical (Khludnev, Sokołowski,





Figure 2.7 – Definition of a diffeomorphism  $\phi_{l_t} : \Omega \setminus \Gamma_0 \rightarrow \Omega \setminus \Gamma_t$  transforming the current cracked material configuration  $\Omega \setminus \Gamma_t$  to the initial one  $\Omega \setminus \Gamma_0$ . It should not be confused with the actual deformation  $\varphi_t$  of the body which takes a particular material point  $\mathbf{x} \in \Omega \setminus \Gamma_t$  to its spatial location  $\varphi_t(\mathbf{x})$  in the deformed configuration  $\varphi_t(\Omega \setminus \Gamma_t)$

& Szulc, 2010) and consequently will be directly admitted. This bijection  $\phi_{l_t}$  should not be confused with the actual deformation  $\varphi_t$  of the body which takes a particular material point  $\mathbf{x} \in \Omega \setminus \Gamma_t$  to its spatial location  $\varphi_t(\mathbf{x})$  in the deformed configuration  $\varphi_t(\Omega \setminus \Gamma_t)$ . Recall that the displacement field  $\mathbf{u}_t$  is defined by  $\varphi_t(\mathbf{x}) = \mathbf{x} + \mathbf{u}_t(\mathbf{x})$  for all  $\mathbf{x}$  in  $\Omega \setminus \Gamma_t$ .

We can explicit this domain transformation by using a virtual perturbation  $\theta^*$  defined on the initial configuration (Destuynder & Djaoua, 1981; Khludnev et al., 2010). An example of such virtual perturbations is given in Figure 2.8. This virtual perturbation should verify the following



Figure 2.8 – A particular virtual perturbation  $\theta^* = \theta\tau_0$  verifying Definition 2.2. It is obtained by solving the Laplace's equation  $\Delta\theta = 0$  inside the crown  $r \leq \|\mathbf{x}^* - \mathbf{P}_0\| \leq R$  with adequate boundary conditions

**Definition 2.2** (Virtual Perturbation).

1. It is sufficiently smooth in space to satisfy the definition of a diffeomorphism.
2. It represents a virtual crack advance along the current crack propagation direction, that is in our case  $\theta^*(\mathbf{P}_0) = \tau_0$ .
3. It does not alter the crack lip *shape*, that is  $\theta^* \cdot \mathbf{n} = 0$  on the crack lip  $\Gamma_0$  with  $\mathbf{n}$  the unit normal vector.
4. The domain boundary remains invariant, *i.e.*  $\theta^* = 0$  on  $\partial\Omega$ .

With an arbitrary virtual perturbation verifying Definition 2.2, we can thus construct the bijection between the initial and current cracked material configurations. In the particular case of a straight crack path, it reads

$$\phi_{l_t} : \mathbf{x}^* \mapsto \mathbf{x} = \mathbf{x}^* + (l_t - l_0)\theta^*(\mathbf{x}^*). \quad (2.49)$$

where  $\mathbf{x} = \phi_{l_t}(\mathbf{x}^*)$  denotes the material point  $\mathbf{x}$  in the current cracked configuration  $\Omega \setminus \Gamma_t$  associated with the material point  $\mathbf{x}^*$  in the initial cracked configuration  $\Omega \setminus \Gamma_0$ . For notational simplicity, we will suppress its subscript by writing  $\phi = \phi_{l_t}$ . The (real) displacement field  $\mathbf{u}_t$  will thus be pulled-back to the initial configuration via the introduced bijection by

$$\mathbf{u}_t \circ \phi = \mathbf{u}_t^* \quad (2.50)$$

from which along with (2.49) we deduce the following useful identities using the classical chain rule

$$\nabla \mathbf{u}_t^*(\mathbf{x}^*) = \nabla \mathbf{u}_t(\mathbf{x}) \nabla \phi(\mathbf{x}^*), \quad (2.51)$$

$$\dot{\mathbf{u}}_t^*(\mathbf{x}^*) = \dot{\mathbf{u}}_t(\mathbf{x}) + \nabla \mathbf{u}_t(\mathbf{x}) \dot{t} \theta^*(\mathbf{x}^*) = \dot{\mathbf{u}}_t(\mathbf{x}) + \nabla \mathbf{u}_t^*(\mathbf{x}^*) \nabla \phi(\mathbf{x}^*)^{-1} \dot{t} \theta^*(\mathbf{x}^*). \quad (2.52)$$

As can be observed, all quantities *referring* to the initial material configuration  $\Omega \setminus \Gamma_0$  are indicated by a superscript  $(\cdot)^*$ . In particular, the Lebesgue integration measure in  $\Omega \setminus \Gamma_0$  will be denoted by  $d\mathbf{x}^*$ . When spatial or temporal differentiation is present, the pullback operation similar to (2.50) is performed first. Hence in (2.51),  $\nabla \mathbf{u}_t^*$  denotes the gradient of  $\mathbf{u}_t^*$  in  $\Omega \setminus \Gamma_0$ , and in (2.52),  $\dot{\mathbf{u}}_t^*$  is understood as the time derivative of the transported displacement.

Note that we can also map the original virtual perturbation  $\theta^*$  defined on the initial configuration to the current one, via a pushforward operation

$$\theta_t = \theta^* \circ \phi^{-1}.$$

All the properties discussed in Definition 2.2 for the initial virtual perturbation should adequately apply for the push-forwarded one by using the current crack tip  $\mathbf{P}_t = \phi(\mathbf{P}_0)$  and  $\text{lip } \Gamma_t$ .

By virtue of (2.51) and (2.52), we can thus formulate the energetic quantities of the body  $\Omega$  using the transported displacement in the initial cracked configuration. In Appendix A, this approach is applied to revisit the Griffith's theory of dynamic fracture reviewed in Section 1.2. The desired evolution laws for the cracked body (elastodynamic equation) and the crack itself (Griffith's law) automatically follow by considering variations of a space-time action integral written in the initial configuration. In particular, a rigorous variational interpretation of the dynamic  $J$ -integral (1.8) is obtained: it can be identified by performing the shape derivative of a space-time action integral involving the Griffith's surface energy (1.1).

### 2.3.2 Generalized Griffith criterion for a propagating damage band

This section is devoted to the application of the shape derivative methods to the dynamic gradient damage model outlined in Definition 2.4. An evolution law similar to Griffith's law (1.10) will be obtained which governs the *crack tip* equation of motion in the gradient damage model. As in (Sicsic & Marigo, 2013), we are interested in the smooth dynamic propagation phase of a damage band concentrated along a certain path. An example of such a damage evolution phase is illustrated in Figure 2.9 where numerical simulations results of an edge-cracked plate under dynamic shearing impact are indicated. We observe initiation of the edge crack and subsequent propagation of the damage

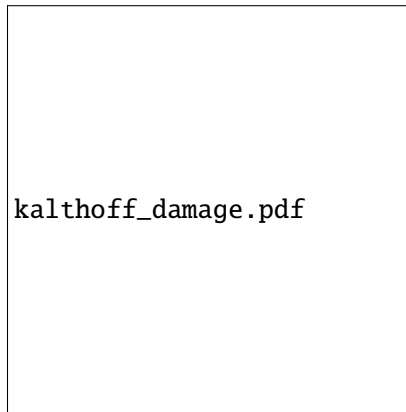


Figure 2.9 – Numerical simulation of an edge-cracked plate under dynamic shearing impact that will be considered in Section 4.5. The damage is concentrated inside a band and varies from 0 (blue zones) to 1 (red zones). It serves as a phase-field indicator of the crack propagating currently in the direction of  $\tau_t$  with its tip located at  $\mathbf{P}_t$

band representing the crack. The objective here is to understand the current crack tip  $\mathbf{P}_t$  evolution

during such *simple* propagation phase. Complex topology changes such as crack kinking, branching or coalescence indicated by the phase-field  $\alpha_t$  remain beyond the scope of the present section. Formally, we admit the following

**Hypothesis 2.3** (Damage Band Structuration).

1. The time-dependent totally damaged zone can be described by a pre-defined curve  $l \mapsto \gamma(l)$  parametrized by its arc-length  $l_t$

$$\Gamma_t = \{ \mathbf{x} \in \Omega \mid \alpha_t(\mathbf{x}) = 1 \} = \{ \gamma(l_s) \in \mathbb{R}^2 \mid 0 \leq s \leq t \} \quad (2.53)$$

with the current propagation direction given by  $\tau_t = \gamma'(l_t)$ . For simplicity, similarly to Appendix A, we only consider a straight crack path with a constant propagation tangent  $\tau_t = \tau_0$ , however generalization to smoothly curved crack path is possible (cf. the end of Appendix A). We focus on the propagation phase when the crack length is much larger than the internal length:  $\ell \ll l_0 \leq l_t$ .



Figure 2.10 – Damage band structuration along a pre-defined path  $l \mapsto \gamma(l)$  indicating a crack propagating in the direction of  $\tau_t$  with its tip located at  $\mathbf{P}_t$

2. During propagation the damage profile along this curve  $l \mapsto \gamma(l)$  develops a cross-section of the same order of  $\ell$ . The current damage evolution rate  $\dot{\alpha}_t$  is partitioned into two components: one that contributes to crack advance in the propagation direction, and the other that describes possible profile evolution in the coordinate system that moves with the crack tip  $\mathbf{P}_t$ . Formally, we make use of the diffeomorphism  $\phi$  introduced in (2.49) that transforms the current cracked configuration to the initial one, in the context of gradient damage models where cracks refer to the totally damaged curve (2.53). The evolution of the damage field  $\alpha_t$  is thus given by

$$\alpha_t \circ \phi = \alpha_t^* \quad (2.54)$$

where the damage profile field  $\alpha_t^*$  corresponds to an initial crack which remains *stationary*

$$\{ \mathbf{x} \in \Omega \mid \alpha_t^*(\mathbf{x}) = 1 \} = \Gamma_0.$$

The establishment of such initial damage field which corresponds to  $\Gamma_0$  is beyond the scope of this document. Using the classical chain rule, the time derivative of the damage reads

$$\dot{\alpha}_t(\mathbf{x}) = \dot{\alpha}_t^*(\mathbf{x}^*) - \dot{l}_t \nabla \alpha_t(\mathbf{x}) \cdot \theta_t(\mathbf{x}), \quad (2.55)$$

which reflects faithfully our partition of the damage rate. Remark that if the crack is arrested  $\dot{l}_t = 0$ , the total damage rate corresponds to that of the profile evolution.

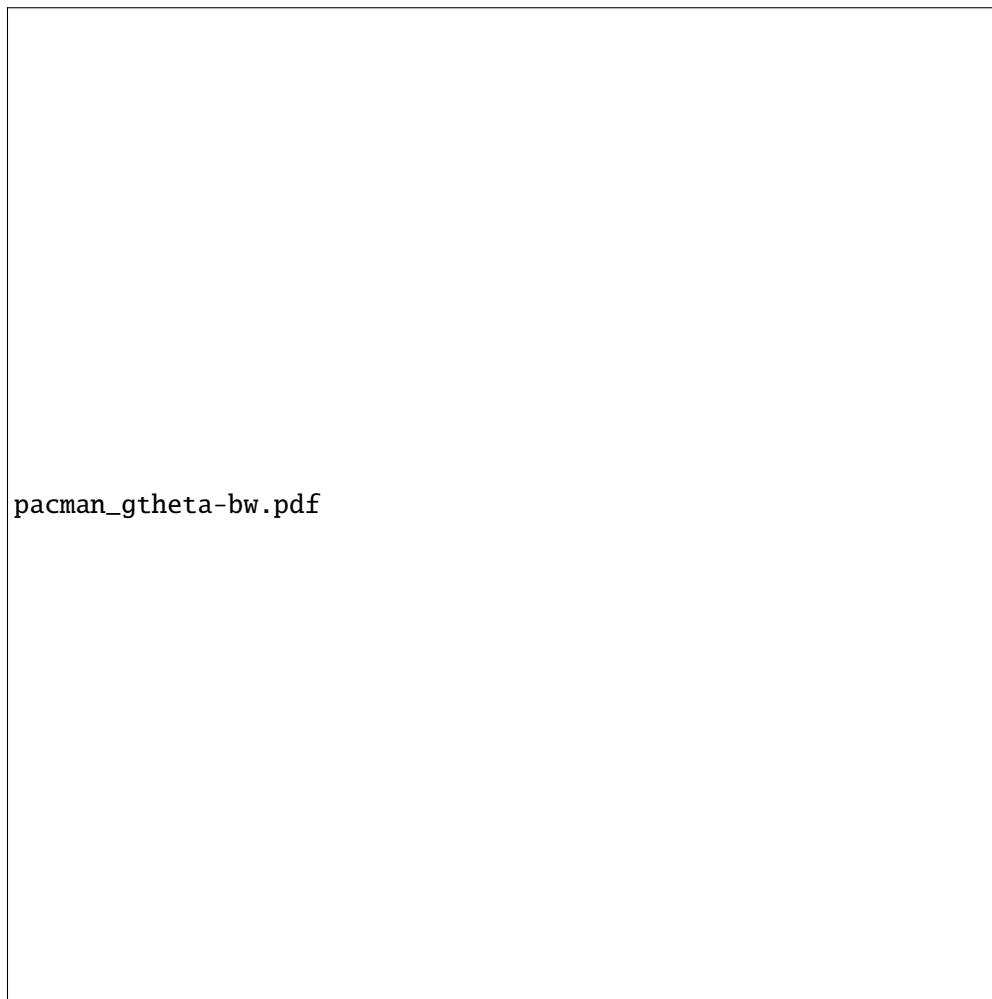


Figure 2.11 – Propagation of an existing damage band via the diffeomorphism  $\phi$

*Remark.* Hypothesis 2.3 highlights the scope of the current contribution: propagation (or arrest) of an *initially existing phase-field crack* (damage band), without complex topology changes such as kinking or branching. For illustration purposes, several situations are presented in Figure 2.12.

- (a) The current section focuses on the further propagation of an *existing damage band* as illustrated in Figure 2.12(a).
- (b) Discrete cracks as a geometric discontinuity in the domain are not to be confused with phase-field like cracks (damage band). The current section does not consider the further “propagation” of the tip  $\mathbf{P}_t$  appearing in Figure 2.12(b), since the damage field is identically zero  $\alpha_t = 0$ . The determination of an initial damage field in such cracked domain refers to the phase-field crack nucleation problem, and is subject to the irreversibility condition, the damage criterion (2.23) and the consistency condition (2.25).
- (c) Complex topology changes in the damage band illustrated in Figure 1.8 and Figure 2.12(c) are not considered in this contribution.

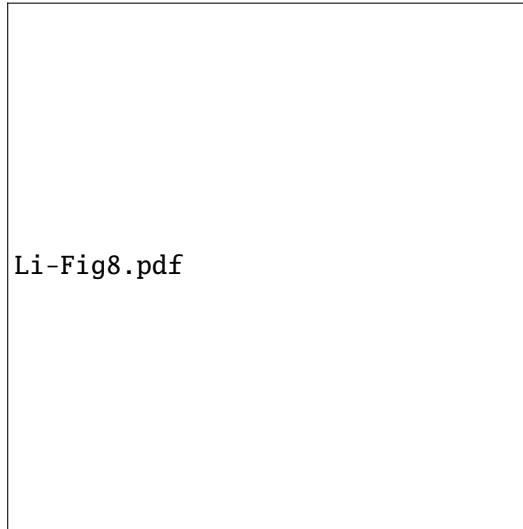


Figure 2.12 – Illustrations of the scope of the present contribution: (a) a *simple* phase-field crack with its tip  $\mathbf{P}_t$ , (b) a *discrete* crack in the domain with an identically zero damage field  $\alpha_t = 0$  and (c) a phase-field crack at *branching*, leading to the existence of two crack tips (similar to Figure 1.8). The damage field varies from 0 (blue zones) to 1 (red zones). The current section focuses on (a), and studies further propagation of the *existing phase-field crack* (damage band)

Furthermore, the crack path, straight or curved, is assumed to be *pre-defined*. Crack path prediction is indeed the *raison d'être* of phase-field models of fracture. A thorough investigation of this point is a very important task to which future work will be devoted. Nevertheless, the current contribution focuses on the behavior of gradient damage models when the crack path is not of concern, which permits a direct comparison with the classical Griffith's theory of dynamic fracture without additional hypotheses, *i.e.* Griffith's law (1.10). We concentrate on “when” cracks propagate (temporal evolution) and not on “how” cracks propagate (spatial evolution).

From (2.54), the current damage field  $\alpha_t$  can be considered as a function depending on the current crack length  $l_t$  and the current damage profile  $\alpha_t^*$ . Using the diffeomorphism we can thus rewrite the space-time action integral (2.16) in the initial cracked configuration  $\Omega \setminus \Gamma_0$ , by transforming the displacement via (2.50). Since we assume that the crack  $\Gamma_t$  (or the totally damaged zone) is of measure zero with respect to  $d\mathbf{x}$  (and hence also to  $d\mathbf{x}^*$ ), contribution on this subset  $\Gamma_t$  can be neglected. By virtue of (2.51) and (2.52), we have

- The damage-dependent elastic energy (2.1) is then given by

$$\mathcal{E}(\mathbf{u}_t, \alpha_t) = \mathcal{E}^*(\mathbf{u}_t^*, \alpha_t^*, l_t) = \int_{\Omega \setminus \Gamma_0} \psi \left( \frac{1}{2} \nabla \mathbf{u}_t^* \nabla \phi^{-1} + \frac{1}{2} \nabla \phi^{-\top} (\nabla \mathbf{u}_t^*)^\top, \alpha_t^* \right) \det \nabla \phi \, d\mathbf{x}^*. \quad (2.56)$$

- The kinetic energy (2.4) admits the following Lagrangian description

$$\mathcal{K}(\dot{\mathbf{u}}_t) = \mathcal{K}^*(\mathbf{u}_t^*, \dot{\mathbf{u}}_t^*, l_t, \dot{l}_t) = \int_{\Omega \setminus \Gamma_0} \kappa(\dot{\mathbf{u}}_t^* - \dot{l}_t \nabla \mathbf{u}_t^* \nabla \phi^{-1} \theta^*) \det \nabla \phi \, d\mathbf{x}^* \quad (2.57)$$

where we note that the transported kinetic energy functional  $\mathcal{K}^*$  depends on the transported displacement  $\mathbf{u}_t^*$ , the crack length  $l_t$  and the crack velocity  $\dot{l}_t$

- The non-local damage dissipation energy (2.5) now reads

$$\mathcal{S}(\alpha_t) = \mathcal{S}^*(\alpha_t^*, l_t) = \int_{\Omega \setminus \Gamma_0} \varsigma(\alpha_t^*, \nabla \phi^{-\top} \nabla \alpha_t^*) \det \nabla \phi \, d\mathbf{x}^*, \quad (2.58)$$

where the identity  $\nabla \alpha_t(\mathbf{x}) = \nabla \phi^{-\top}(\mathbf{x}^*) \nabla \alpha_t^*(\mathbf{x}^*)$  is used following (2.54).

- The external work potential (2.11) written in the initial configuration reads

$$\mathcal{W}_t(\mathbf{u}_t) = \mathcal{W}_t^*(\mathbf{u}_t^*, l_t) = \int_{\Omega \setminus \Gamma_0} (\mathbf{f}_t \circ \phi) \cdot \mathbf{u}_t^* \det \nabla \phi \, d\mathbf{x}^* + \int_{\partial \Omega_F} \mathbf{F}_t \cdot \mathbf{u}_t^* \, ds. \quad (2.59)$$

Remark that the boundary  $\partial \Omega$  is invariant under the transformation  $\phi$ .

- The generalized space-time action integral (2.16) is hence given by

$$\begin{aligned} \mathcal{A}(\mathbf{u}, \alpha) &= \mathcal{A}(\mathbf{u}^*, \alpha^*, l) = \int_I \mathcal{L}_t(\mathbf{u}_t^*, \dot{\mathbf{u}}_t^*, \alpha_t^*, l_t, \dot{l}_t) \, dt \\ &= \int_I (\mathcal{E}^*(\mathbf{u}_t^*, \alpha_t^*, l_t) + \mathcal{S}^*(\alpha_t^*, l_t) - \mathcal{K}^*(\mathbf{u}_t^*, \dot{\mathbf{u}}_t^*, l_t, \dot{l}_t) - \mathcal{W}_t^*(\mathbf{u}_t^*, l_t)) \, dt. \end{aligned} \quad (2.60)$$

The definition of the admissible evolution spaces for the triplet  $(\mathbf{u}^*, \alpha^*, l)$  are discussed as follows. The admissible function space for the displacement (2.14) is slightly modified to reflect the fact that now the displacement is defined in the uncracked bulk:

$$\mathcal{C}(\mathbf{u}^*) = \left\{ \mathbf{v}^* : I \times (\Omega \setminus \Gamma_0) \rightarrow \mathbb{R}^{\dim} \mid \mathbf{v}_t^* \in C_t \text{ for all } t \in I \text{ and } \mathbf{v}_{\partial I}^* = \mathbf{u}_{\partial I}^* \right\}, \quad (2.14')$$

where  $C_t = C_0 + \mathbf{U}_t$  and the associated vector space  $C_0$  is given by

$$C_0 = \left\{ \mathbf{u}_t^* : \Omega \setminus \Gamma_0 \rightarrow \mathbb{R}^{\dim} \mid \mathbf{u}_t^* = \mathbf{0} \text{ on } \partial \Omega_U \right\}.$$

For the admissible crack evolution, we require that the evolution of the crack tip  $t \mapsto l_t$  should be a non-decreasing function of time and virtual advance of the crack tip at every instant should also be non-negative to ensure irreversibility. Concretely, given an arbitrary but non-decreasing crack evolution  $t \mapsto l_t$ , the admissible crack evolution space is given by

$$\mathcal{Z}(l) = \left\{ s : I \rightarrow \mathbb{R}^+ \mid s_t \geq l_t \text{ for all } t \in I \text{ and } s_{\partial I} = l_{\partial I} \right\}, \quad (2.61)$$

where it can be observed that the crack length value is also fixed at both time ends  $l_{\partial I} = (l_0, l_T)$ .

The damage profile  $\alpha^*$  is merely a component contributing to the total damage evolution, hence the temporal irreversibility still applies to the true damage evolution  $t \mapsto \alpha_t$ , which reads  $\dot{\alpha}_t \geq 0$ . Given an arbitrary such evolution verifying Hypothesis 2.3, we want to consider admissible variation of the current damage state  $\alpha_t$  corresponding to a crack length  $l_t$ , based on an admissible crack length variation  $\delta l_t = s_t - l_t \geq 0$  and a crack profile variation  $\beta_t^* - \alpha_t^*$ . At time  $t \in (0, T)$  the induced admissible non-negative variation of the true damage reads

$$\beta_t - \alpha_t = \beta_t^* \circ \phi_{s_t}^{-1} - \alpha_t^* \circ \phi_{l_t}^{-1} \geq 0. \quad (2.62)$$

As can be seen, the damage profile variation  $\beta_t^* - \alpha_t^*$  and the crack length variation  $\delta l_t$  are now involved in a unilateral fashion to ensure irreversibility of the true damage:

- If the crack length variation is zero  $\delta l_t = 0$ , then the damage profile variation  $\beta_t^* - \alpha_t^*$  corresponds exactly to the true damage variation  $\beta_t - \alpha_t$ . Thus it suffices that  $\beta_t^* - \alpha_t^* \geq 0$  to ensure irreversibility.
- However if a finite extension of the crack length is considered  $\delta l_t > 0$ , then the damage profile variation depends non-trivially on the  $\delta l_t$  via (2.62) to obtain  $\beta_t - \alpha_t \geq 0$ .

In practice, it means that if crack length variation is not considered, then the variation of the action integral with respect to the displacement and to the damage (profile) can be separately computed. Otherwise when  $\delta l_t > 0$ , then damage variation must also be taken into account. Given an admissible crack length evolution  $s \in \mathcal{Z}(l)$ , the admissible evolution space for the damage profile will be denoted by  $\mathcal{D}_s(\alpha^*)$ , where the dependence on  $s$  is explicitly indicated by the subscript and  $\alpha^*$  describes the profile of a damage evolution verifying Hypothesis 2.3. As usual, at both ends of the time interval  $I$ , no variations of true damage profile are considered.

Associated with an admissible triplet of displacement, damage profile and crack length evolutions  $(\mathbf{u}^*, \alpha^*, l) \in C(\mathbf{u}^*) \times \mathcal{D}_l(\alpha^*) \times \mathcal{Z}(l)$ , we can now reformulate the dynamic gradient damage model under Hypothesis 2.3 by the following

**Definition 2.4** (Dynamic Gradient Damage Evolution Law for a Propagating Crack).

1. **Irreversibility**: the damage  $t \mapsto \alpha_t$  and the crack length  $t \mapsto l_t$  are non-decreasing functions of time.
2. **First-order stability**: the first-order action variation is non-negative with respect to arbitrary admissible displacement, damage profile and crack evolutions

$$A'(\mathbf{u}^*, \alpha^*, l)(\mathbf{v}^* - \mathbf{u}^*, \beta^* - \alpha^*, s - l) \geq 0$$

for all  $\mathbf{v}^* \in C(\mathbf{u}^*)$ , all  $\beta^* \in \mathcal{D}_s(\alpha^*)$  and all  $s \in \mathcal{Z}(l)$ . (2.63)

3. **Energy balance**: the only energy dissipation is due to crack propagation such that we have the following energy balance

$$\mathcal{H}_t = \mathcal{H}_0 + \int_0^t \left( \int_{\Omega \setminus \Gamma_s} (\boldsymbol{\sigma}_s \cdot \boldsymbol{\varepsilon}(\dot{\mathbf{U}}_s) + \rho \ddot{\mathbf{u}}_s \cdot \dot{\mathbf{U}}_s) \, d\mathbf{x} - \mathcal{W}_s(\dot{\mathbf{U}}_s) - \mathcal{W}_s(\mathbf{u}_s) \right) ds \quad (2.64)$$

where the total energy is defined by

$$\mathcal{H}_t = \mathcal{E}^*(\mathbf{u}_t^*, \alpha_t^*, l_t) + \mathcal{S}^*(\alpha_t^*, l_t) + \mathcal{K}(\mathbf{u}_t^*, \dot{\mathbf{u}}_t^*, l_t, \dot{l}_t) - \mathcal{W}_t^*(\mathbf{u}_t^*, l_t). \quad (2.65)$$

We then exploit the first-order stability condition (2.63) by carefully developing the Gâteaux derivative of the action integral (2.60). With the help of detailed calculations provided in Appendix B and using the same arguments developed before, the first-order action variation testing with  $\beta^* - \alpha^* = 0$  and  $s - l = 0$  leads to the elastic-damage dynamic wave equation on the uncracked domain similar to (2.21)

$$\rho \ddot{\mathbf{u}}_t - \operatorname{div} \boldsymbol{\sigma}_t = \mathbf{f}_t \quad \text{in } \Omega \setminus \Gamma_t, \quad \boldsymbol{\sigma}_t \mathbf{n} = \mathbf{F}_t \quad \text{on } \partial\Omega_F \quad \text{and} \quad \boldsymbol{\sigma}_t \mathbf{n} = \mathbf{0} \quad \text{on } \Gamma_t \quad (2.66)$$

where we recall that here the stress tensor  $\boldsymbol{\sigma}_t$  is damage-dependent and is given by (2.2). The stress-free condition is automatically retrieved. Similarly at fixed displacement and crack length variations, evaluating the directional derivative of the action integral with respect to damage variation  $\beta^* - \alpha^*$  leads to

$$A'(\mathbf{u}^*, \alpha^*, l)(\mathbf{0}, \beta^* - \alpha^*, 0) = \int_I \left( \int_{\Omega \setminus \Gamma_t} -(Y_t + \operatorname{div} \mathbf{q}_t) \cdot (\beta_t - \alpha_t) \, d\mathbf{x} + \int_{\partial\Omega \setminus \Gamma_t} (\mathbf{q}_t \cdot \mathbf{n})(\beta_t - \alpha_t) \, ds \right) dt \geq 0$$



where the integration domain is first transformed to the current cracked one and an integration by parts is then performed. Since the induced true damage variation is non-negative due to (2.62), we obtain thus the same local damage criterion (2.23) as before. Finally, we consider the first-order action variation with respect to crack length evolution variation. Through (2.62), damage profile variation is thus coupled with that of the crack length. We thus merely have

$$\int_{\Omega \setminus \Gamma_t} -(Y_t + \operatorname{div} \mathbf{q}_t) \cdot (\beta_t - \alpha_t) \, d\mathbf{x} + \int_{\partial\Omega \setminus \Gamma_t} (\mathbf{q}_t \cdot \mathbf{n})(\beta_t - \alpha_t) \, ds - \widehat{G}_t \cdot \delta l_t \geq 0 \quad (2.67)$$

with a generalized dynamic energy release rate defined by

$$\widehat{G}_t = G_t^\alpha - \gamma_t. \quad (2.68)$$

This quantity contains the conventional dynamic energy release rate

$$G_t^\alpha = \int_{\Omega \setminus \Gamma_t} \left( (\kappa(\dot{\mathbf{u}}_t) - \psi(\boldsymbol{\varepsilon}(\mathbf{u}_t), \alpha_t)) \operatorname{div} \boldsymbol{\theta}_t + \boldsymbol{\sigma}_t \cdot (\nabla \mathbf{u}_t \nabla \boldsymbol{\theta}_t) + \operatorname{div}(\mathbf{f}_t \otimes \boldsymbol{\theta}_t) \cdot \mathbf{u}_t + \rho \ddot{\mathbf{u}}_t \cdot \nabla \mathbf{u}_t \boldsymbol{\theta}_t + \rho \dot{\mathbf{u}}_t \cdot \nabla \dot{\mathbf{u}}_t \boldsymbol{\theta}_t \right) d\mathbf{x} \quad (2.69)$$

and the damage dissipation rate as the partial derivative of the damage dissipation energy  $\mathcal{S}^*(l_t)$  with respect to the crack length

$$\gamma_t = \frac{\partial}{\partial l_t} \mathcal{S}^*(\alpha_t^*, l_t) = \int_{\Omega \setminus \Gamma_t} (\zeta(\alpha_t, \nabla \alpha_t) \operatorname{div} \boldsymbol{\theta}_t - \mathbf{q}_t \cdot \nabla \boldsymbol{\theta}_t \nabla \alpha_t) \, d\mathbf{x}. \quad (2.70)$$

In (2.67), although the crack length variation is non-negative  $\delta l_t \geq 0$ , the sign of the generalized dynamic energy release rate is undetermined in general, since the first two terms are both positive due to (2.23) and (2.62).

It remains to use the energy balance (2.64) to derive the consistency conditions. With the help of the detailed calculations given in Appendix B, we obtain

$$\int_{\Omega \setminus \Gamma_t} -(Y_t + \operatorname{div} \mathbf{q}_t)(\dot{\alpha}_t + \dot{l}_t \nabla \alpha \cdot \boldsymbol{\theta}) \, d\mathbf{x} + \int_{\partial\Omega \setminus \Gamma_t} (\mathbf{q}_t \cdot \mathbf{n}) \dot{\alpha}_t \, ds - \widehat{G}_t \dot{l}_t = 0 \quad (2.71)$$

where the first term represents energy dissipation due to damage profile evolution following (2.55) and the second term corresponds to damage dissipation on the uncracked boundary where  $\boldsymbol{\theta}_t = \mathbf{0}$ . The third term denotes dissipation due to pure propagation of the phase-field crack. It can be observed that in case of a currently stationary crack  $\dot{l}_t = 0$ , we retrieve directly the classical consistency conditions for damage (2.25). However when the crack propagates  $\dot{l}_t > 0$ , nothing can be deduced from (2.71) since the damage profile evolution  $\alpha^*$  is not necessarily irreversible and the sign of  $\widehat{G}_t$  is not yet known.

From Proposition A.2, the dynamic energy release rate (A.10) in the Griffith's theory of fracture can be written as a path integral. This property can be extended to the dynamic gradient damage model due to the analogies with their respective variational ingredients.

**Proposition 2.5.** *The generalized dynamic energy release rate (2.68) defines a generalized  $\widehat{J}$ -integral*

$$\widehat{J}_t = \lim_{r \rightarrow 0} \int_{C_r} \widehat{\mathbf{J}}_t \mathbf{n} \cdot \boldsymbol{\tau}_t \, ds = \widehat{G}_t + \int_{\Omega \setminus \Gamma_t} (Y_t + \operatorname{div} \mathbf{q}_t) \nabla \alpha_t \cdot \boldsymbol{\theta}_t \, d\mathbf{x} \quad (2.72)$$

where the generalized dynamic  $\widehat{\mathbf{J}}_t$  tensor is defined by

$$\widehat{\mathbf{J}}_t = \left( \psi(\boldsymbol{\varepsilon}(\mathbf{u}_t), \alpha_t) + \kappa(\dot{\mathbf{u}}_t) + \zeta(\alpha_t, \nabla \alpha_t) \right) \mathbb{I} - \nabla \mathbf{u}_t^\top \boldsymbol{\sigma}_t - \mathbf{q}_t \otimes \nabla \alpha_t. \quad (2.73)$$

As in Proposition A.2, here  $\mathbf{n}$  denotes the normal pointing out of the ball  $B_r(\mathbf{P}_t)$  with  $C_r = \partial B_r(\mathbf{P}_t)$  its boundary.

*Proof.* The equation (2.72) can be obtained mainly by following the proof of Proposition A.2. The last term containing the damage gradient results from the identity below which accounts for the damage dependence of the elastic energy and the damage dissipation energy

$$\operatorname{div} \left( (\psi(\boldsymbol{\varepsilon}(\mathbf{u}_t), \alpha_t) + \varsigma(\alpha_t, \nabla \alpha_t)) \boldsymbol{\theta}_t \right) = \boldsymbol{\sigma}_t \cdot \boldsymbol{\varepsilon}(\nabla \mathbf{u}_t) \boldsymbol{\theta}_t - Y_t \nabla \alpha_t \cdot \boldsymbol{\theta}_t + \mathbf{q}_t \cdot \nabla^2 \alpha_t \boldsymbol{\theta}_t + (\psi(\boldsymbol{\varepsilon}(\mathbf{u}_t), \alpha_t) + \varsigma(\alpha_t, \nabla \alpha_t)) \operatorname{div} \boldsymbol{\theta}_t \quad (2.74)$$

together with an additional integration by parts

$$\int_{\Omega_r} \mathbf{q}_t \cdot \nabla \boldsymbol{\theta}_t \nabla \alpha_t \, d\mathbf{x} = - \int_{C_r} (\mathbf{q}_t \otimes \nabla \alpha_t) \mathbf{n} \cdot \boldsymbol{\theta}_t \, ds - \int_{\Omega_r} (\operatorname{div} \mathbf{q}_t \nabla \alpha_t \cdot \boldsymbol{\theta}_t + \mathbf{q}_t \cdot \nabla^2 \alpha_t \boldsymbol{\theta}_t) \, d\mathbf{x}.$$

To pass from the Lagrangian density in (2.68) to the Hamiltonian density in (2.73), it suffices to observe that the most singular part of the time derivatives corresponds to the transport term. Similar calculations at the end of the proof of Proposition A.2 then lead to the desired result.  $\square$

The tensor  $\widehat{\mathbf{J}}_t$  can be seen as the dynamic extension of the quasi-static generalized Eshelby tensor (or energy-momentum tensor) introduced respectively in the quasi-static gradient damage model (Sicsic & Marigo, 2013) and the dissipative phase field model originating from the physics community, see for instance (Ballarini & Royer-Carfagni, 2016; Hakim & Karma, 2009). Inserting (2.72) into (2.71), an equivalent expression of the consistency condition can be obtained

$$\int_{\Omega \setminus \Gamma_t} (Y_t + \operatorname{div} \mathbf{q}_t) \dot{\alpha}_t \, d\mathbf{x} + \int_{\partial \Omega \setminus \Gamma_t} -(\mathbf{q}_t \cdot \mathbf{n}) \dot{\alpha}_t \, ds + \widehat{J}_t \dot{l}_t = 0. \quad (2.75)$$

In (Sicsic & Marigo, 2013), a careful singularity analysis is conducted to determine the sign of the  $\widehat{J}$ -integral with a particular strongly brittle material. Such calculations could be extended to the dynamic setting but are beyond the scope of this work. Based on numerical verifications, we assume the following

**Hypothesis 2.6.** The generalized dynamic  $\widehat{J}$ -integral is non-positive

$$\widehat{J}_t \leq 0 \quad (2.76)$$

for all damage constitutive laws  $\alpha \mapsto \mathbf{a}(\alpha)$  and  $\alpha \mapsto \mathbf{w}(\alpha)$  which characterize the behavior of a strongly brittle material.

Due to the local damage criterion (2.23) and the irreversibility conditions, each term in (2.75) is non-positive while their sum yields zero, which implies that each term vanishes separately

$$(Y_t + \operatorname{div} \mathbf{q}_t) \dot{\alpha}_t = 0 \quad \text{in } \Omega \setminus \Gamma_t, \quad (\mathbf{q}_t \cdot \mathbf{n}) \dot{\alpha}_t = 0 \quad \text{on } \partial \Omega \setminus \Gamma_t \quad \text{and} \quad \widehat{J}_t \dot{l}_t = 0, \quad (2.77)$$

which represent local energy balances. We note that the first two equalities correspond to the consistency condition (2.25) derived without Hypothesis 2.3.

It can be seen from (2.76) and the last equation in (2.77) that the generalized dynamic  $\widehat{J}$ -integral plays the role of  $G_t - G_c$  in the classical Griffith's law (1.10). It involves a path integral on a contour  $C_r$  that shrinks to the crack tip  $r \rightarrow 0$ , which may lead to difficulties in a finite element calculation. From a numerical point of view, the generalized dynamic energy release rate  $\widehat{G}_t$  defined in (2.68) should be preferred since it is written as a cell integral on a finite domain. It turns out that under a particular circumstance, these two objects are equivalent and they both define the following generalized Griffith criterion.

**Proposition 2.7** (Generalized Griffith Criterion). *The crack tip equation of motion predicted by the dynamic gradient damage model is governed by the following generalized Griffith criterion*

$$\dot{l}_t \geq 0, \quad \widehat{J}_t \leq 0 \quad \text{and} \quad \widehat{J}_t \dot{l}_t = 0. \quad (2.78)$$

If we assume that in (2.55) the time derivative of the damage profile is negligible compared to the transport term and furthermore the damage gradient in the direction of crack propagation is non-positive at every time  $t$  and almost everywhere

$$\dot{\alpha}_t \approx -\dot{l}_t \nabla \alpha_t \cdot \boldsymbol{\theta}_t, \quad \nabla \alpha_t \cdot \boldsymbol{\theta}_t \leq 0, \quad (2.79)$$

then the generalized dynamic energy release rate (2.68) can be equivalently used in the above generalized Griffith criterion, which leads to

$$\dot{l}_t \geq 0, \quad \widehat{G}_t \leq 0 \quad \text{and} \quad \widehat{G}_t \dot{l}_t = 0. \quad (2.80)$$

*Proof.* Using the definition of  $\widehat{J}_t$  in (2.72) and the second condition in (2.79), we obtain the equivalent stability condition

$$\widehat{G}_t = \widehat{J}_t - \int_{\Omega \setminus \Gamma_t} (Y_t + \operatorname{div} \mathbf{q}_t) \nabla \alpha_t \cdot \boldsymbol{\theta}_t \, dx \leq 0$$

since  $Y_t + \operatorname{div} \mathbf{q}_t \leq 0$  due to the local damage criterion (2.23). If the first condition in (2.79) holds, then the local consistency condition for damage in (2.71) reads

$$(Y_t + \operatorname{div} \mathbf{q}_t) \dot{l}_t \nabla \alpha_t \cdot \boldsymbol{\theta}_t = 0.$$

Multiplying (2.72) by  $\dot{l}_t$  gives the desired condition  $\widehat{G}_t \dot{l}_t = 0$ .  $\square$

*Remark.* These two conditions (2.79) needed to establish (2.80) can be justified in the crack tip problem when the internal length is small compared to the dimension of the body.

*Remark.* Proposition 2.7 and in particular (2.78) and (2.80) constitute one of the main results of the present contribution. Above all, arbitrary damage evolution in the dynamic gradient damage model is governed by the irreversibility condition, the damage criterion (2.23) and the consistency condition (2.25). However it is shown that the propagation (or arrest) of an existing damage band (phase-field crack) is governed by the above Griffith like *scalar* equations involving several energy release rate concepts.

### 2.3.3 Separation of scales

The generalized dynamic  $\widehat{J}$ -integral as well as the generalized dynamic energy release rate  $\widehat{G}_t$  that enter into the generalized Griffith's law (Proposition 2.7) don't possess directly an intuitive interpretation in fracture mechanics terminology. To establish the link between damage and fracture, we will essentially follow the separation of scales made in the quasi-static case (Sicsic & Marigo, 2013) (and similar in essence to that reviewed in (Hakim & Karma, 2009)) which decomposes the complete gradient damage evolution problem into three subproblems. From now on, all quantities that depend on the internal length will be indicated by a superscript  $\ell$ . We also adopt the assumption made on the internal length dependence of the external loading, namely

$$\mathbf{f}_t^\ell = \sqrt{\ell} \mathbf{f}_t, \quad \mathbf{F}_t^\ell = \sqrt{\ell} \mathbf{F}_t \quad \text{and} \quad \mathbf{U}_t^\ell = \sqrt{\ell} \mathbf{U}_t. \quad (2.81)$$

#### Outer linear elastic dynamic fracture problem

In this elastodynamic problem we assume that the body contains a sharp-interface crack corresponding to the totally damaged region  $\Gamma_t$ . Due to the linear nature of the macroscopic dynamic fracture problem on the cracked domain  $\Omega \setminus \Gamma_t$ , dependence of the real mechanical fields on the internal length can be given by

$$\mathbf{u}_t^\ell = \sqrt{\ell} \mathbf{u}_t + \dots, \quad \dot{\mathbf{u}}_t^\ell = \sqrt{\ell} \dot{\mathbf{u}}_t + \dots, \quad \ddot{\mathbf{u}}_t^\ell = \sqrt{\ell} \ddot{\mathbf{u}}_t + \dots \quad \text{and} \quad \boldsymbol{\sigma}_t^\ell = \sqrt{\ell} \boldsymbol{\sigma}_t + \dots \quad (2.82)$$

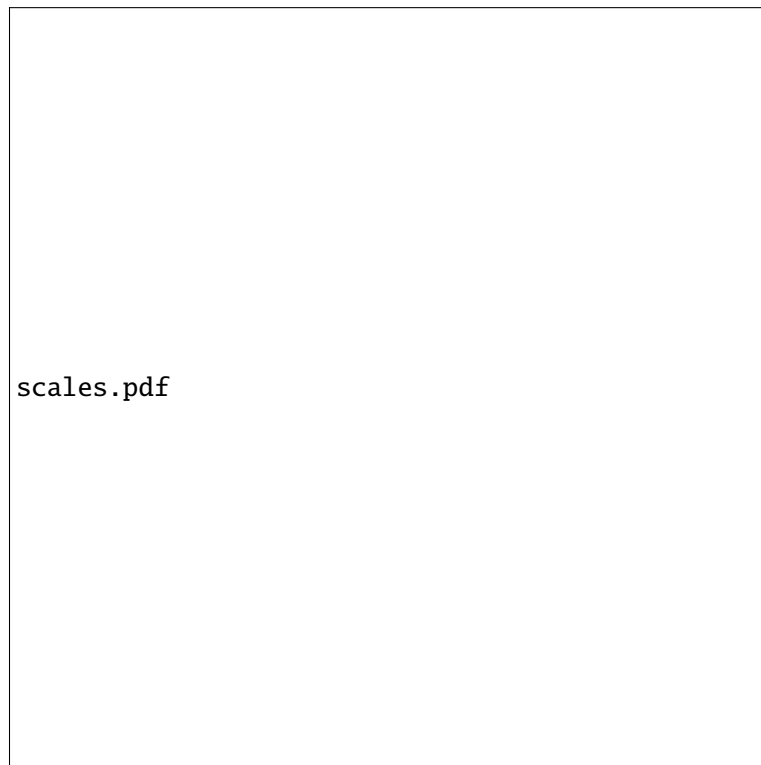


Figure 2.13 – Separation of scales conducted in ([Sicsic & Marigo, 2013](#)) which decomposes the gradient damage evolution problem into three sub-problems: the outer linear elastic fracture mechanics problem where the damage band is replaced by a true crack in the domain, the damage band problem in which the fracture toughness can be identified with the energy dissipated during the damage band creation and the crack tip problem where the matching conditions with the previous two subproblems will be used

The behaviors of the fields are described in Section 1.2. In particular, the rescaled stress  $\sigma_t$  and the rescaled velocity  $\dot{\mathbf{u}}_t$  admit the following asymptotic form

$$\begin{aligned}\sigma_t(r, \theta) &\approx \frac{\bar{K}_I(t)}{\sqrt{2\pi r}} \Sigma_I(\theta, \dot{l}_t) + \frac{\bar{K}_{II}(t)}{\sqrt{2\pi r}} \Sigma_{II}(\theta, \dot{l}_t), \\ \dot{\mathbf{u}}_t(r, \theta) &\approx \frac{\dot{l}_t \bar{K}_I(t)}{\sqrt{2\pi r \mu}} \mathbf{V}_I(\theta, \dot{l}_t) + \frac{\dot{l}_t \bar{K}_{II}(t)}{\sqrt{2\pi r \mu}} \mathbf{V}_{II}(\theta, \dot{l}_t),\end{aligned}\tag{2.83}$$

where  $\bar{K}$ 's is the rescaled stress intensity factors. The true stress intensity factors  $K^\ell$ 's are given by  $K_i^\ell = \sqrt{\ell} \bar{K}_i$  since they are of order  $O(\sqrt{\ell})$  due to (2.82).

An equivalent dynamic energy release rate  $G_t^\ell$  associated with this outer problem is of order  $O(\ell)$ . The rescaled dynamic energy release rate under the plane strain condition is given by

$$\bar{G}_t = \frac{1 - \nu^2}{E} \left( A_I(\dot{l}_t) \bar{K}_I(t)^2 + A_{II}(\dot{l}_t) \bar{K}_{II}(t)^2 \right), \tag{2.84}$$

where the rescaling condition reads

$$G_t^\ell = \ell \bar{G}_t \tag{2.85}$$

### Damage band problem

The damage band problem will be essentially the same as in the quasi-static case (Sicsic & Marigo, 2013), due to the formally identical energy minimization principle (2.22) and its local interpretations (2.23) and (2.25). The first-order term of the damage field  $\alpha_t^\ell$  inside or near the crack band but far from the crack tip admits the following form

$$\alpha_t^\ell(\mathbf{x}) \approx \alpha_*(s, \zeta) = \alpha_*(s, \text{dist}(\mathbf{x}, \Gamma_t)/\ell) \tag{2.86}$$

where  $\alpha_*$  is the normalized (with respect to  $\ell$ ) damage profile along the crack normal at a certain arclength  $s$  of the crack  $\Gamma_t$  and  $\text{dist}(\mathbf{x}, \Gamma_t)$  is the Euclidean distance from the point  $\mathbf{x}$  near the crack band to the crack  $\Gamma_t$ . The damage gradient in the tangential direction is thus negligible compared to that in the normal direction

$$\nabla \alpha_t^\ell \cdot \boldsymbol{\tau}_t \approx 0. \tag{2.87}$$

Using the definition of the dual quantities (2.24), the consistency condition (2.25) during the crack band creation reads

$$\frac{1}{2} \mathbf{A}'(\alpha_*) \boldsymbol{\varepsilon}(\mathbf{u}_t^\ell) \cdot \boldsymbol{\varepsilon}(\mathbf{u}_t^\ell) + w'(\alpha_*) - w_1 \frac{\partial^2 \alpha_*}{\partial \zeta^2} = 0. \tag{2.88}$$

Note that in this damage band problem the term  $\frac{1}{2} \mathbf{A}'(\alpha_*) \boldsymbol{\varepsilon}(\mathbf{u}_t^\ell) \cdot \boldsymbol{\varepsilon}(\mathbf{u}_t^\ell)$  is still of order  $O(\ell)$  due to (2.82) while the other two terms in (2.88) are of order  $O(1)$ , which leads to the following first-order damage profile condition

$$w'(\alpha_*) - w_1 \frac{\partial^2 \alpha_*}{\partial \zeta^2} = 0. \tag{2.89}$$

This problem is thus similar to the construction of the optimal damage profile for a uniaxial traction experiment, see the end of Section 2.1.3. The energy per unit length dissipated during the damage band creation can be calculated by the integral of the damage dissipation density (2.5) over the real cross section, which gives

$$G_c^\ell = \ell \bar{G}_c \quad \text{where} \quad \bar{G}_c = 2\sqrt{2} \int_0^1 \sqrt{w_1 w(\beta)} d\beta. \tag{2.90}$$

This energy as in the quasi-static case (Sicsic & Marigo, 2013) will play the role of the fracture toughness in the asymptotic Griffith's law during the crack propagation phase.

### Crack tip problem

We perform the same translation and rescaling of the system of coordinates  $\mathbf{y} = (\mathbf{x} - \mathbf{P}_t)/\ell$  in the vicinity of the crack tip and assume the following near-tip forms of the displacement, stress and damage fields established in Sect. 3.3 of (Sicsic & Marigo, 2013)

$$\mathbf{u}_t^\ell(\mathbf{x}) = \sqrt{\ell} \mathbf{u}_t(\mathbf{P}_t) + \ell \bar{\mathbf{u}}_t(\mathbf{y}) + \dots, \quad \boldsymbol{\sigma}_t(\mathbf{x}) = \bar{\boldsymbol{\sigma}}_t(\mathbf{y}) + \dots \quad \text{and} \quad \alpha_t(\mathbf{x}) = \bar{\alpha}_t(\mathbf{y}) + \dots$$

with  $\mathbf{u}_t(\mathbf{P}_t)$  the displacement of the crack tip given by the outer problem (2.82) and  $\bar{\boldsymbol{\sigma}}_t = \mathbf{A}(\bar{\alpha}_t) \boldsymbol{\varepsilon}(\bar{\mathbf{u}}_t)$ . In dynamics, the asymptotic expansion of the velocity  $\dot{\mathbf{u}}_t^\ell$  and the acceleration  $\ddot{\mathbf{u}}_t^\ell$  can be obtained by differentiating  $\mathbf{u}_t^\ell$  with respect to time, which gives to their first order with respect to the internal length

$$\begin{aligned} \dot{\mathbf{u}}_t &\approx -\dot{\ell}_t \nabla \bar{\mathbf{u}}_t \boldsymbol{\tau}_t = O(1), \\ \ddot{\mathbf{u}}_t &\approx -\dot{\ell}_t \nabla \dot{\mathbf{u}}_t \boldsymbol{\tau}_t = O(1). \end{aligned} \quad (2.91)$$

These equations illustrate in fact the steady-state condition (1.5) for the crack tip problem. We note that here the stress, the velocity and the acceleration are of order  $O(1)$  while they are of order  $O(\sqrt{\ell})$  in the outer problem. Using the expressions given in (2.83), the behavior of  $\bar{\boldsymbol{\sigma}}_t$  and  $\dot{\mathbf{u}}_t$  far from the crack tip can thus be obtained by virtue of the following matching conditions

$$\begin{aligned} \lim_{r \rightarrow \infty} \left( \bar{\boldsymbol{\sigma}}_t(r, \theta) - \frac{\bar{K}_I(t)}{\sqrt{2\pi r}} \boldsymbol{\Sigma}_I(\theta, \dot{\ell}_t) - \frac{\bar{K}_{II}(t)}{\sqrt{2\pi r}} \boldsymbol{\Sigma}_{II}(\theta, \dot{\ell}_t) \right) &= \mathbf{0}, \\ \lim_{r \rightarrow \infty} \left( \dot{\mathbf{u}}_t(r, \theta) - \frac{\dot{\ell}_t \bar{K}_I(t)}{\sqrt{2\pi r} \mu} \mathbf{V}_I(\theta, \dot{\ell}_t) - \frac{\dot{\ell}_t \bar{K}_{II}(t)}{\sqrt{2\pi r} \mu} \mathbf{V}_{II}(\theta, \dot{\ell}_t) \right) &= \mathbf{0}. \end{aligned} \quad (2.92)$$

Since the body force density  $\mathbf{f}_t^\ell$  is of higher order, the first-order dynamic equilibrium for this crack tip problem reads

$$\rho \ddot{\mathbf{u}}_t - \operatorname{div} \bar{\boldsymbol{\sigma}}_t = \mathbf{0} \quad \text{in} \quad \mathbb{R}^2 \setminus \bar{\Gamma} \quad \text{and} \quad \bar{\boldsymbol{\sigma}}_t \mathbf{n} = \mathbf{0} \quad \text{on} \quad \bar{\Gamma} \quad (2.93)$$

where  $\bar{\Gamma} = (-\infty, 0) \times \{0\}$  corresponds to a rescaled crack along the direction  $\mathbf{e}_1$ , where  $\bar{\alpha}_t = 1$ .

We now turn to damage evolution in the crack tip problem. In the rescaled coordinate system the virtual perturbation admits the form  $\boldsymbol{\theta}_t(\mathbf{y}) = \theta_t(\mathbf{y}) \mathbf{e}_1$  where  $0 \leq \theta_t(\mathbf{y}) \leq 1$ . From the chain rule, the rate of damage (2.55) is of order  $O(1/\ell)$  and reads

$$\dot{\alpha}_t^\ell(\mathbf{x}) = -\frac{\dot{\ell}_t}{\ell} \nabla \bar{\alpha}_t(\mathbf{y}) \cdot \boldsymbol{\theta}_t(\mathbf{y}) + \dots = -\frac{\dot{\ell}_t}{\ell} \theta_t \frac{\partial \bar{\alpha}_t}{\partial y_1}(\mathbf{y}) + \dots \quad (2.94)$$

where the damage profile rate disappears since it is of higher order. This corresponds to the first condition assumed in (2.79). Due to the irreversibility condition of damage, when the crack propagates  $\dot{\ell}_t > 0$  the term  $\nabla \bar{\alpha}_t(\mathbf{y}) \cdot \boldsymbol{\theta}_t(\mathbf{y})$  is necessarily non-positive. We assume that the condition remains true at every time. It is sufficient that the damage remains constant near the crack tip when the crack is arrested.

**Hypothesis 2.8.** We assume that  $\nabla \alpha_t \cdot \boldsymbol{\theta}_t \leq 0$  for every time.

This corresponds to the second condition of (2.79). All the terms in the local damage criterion (2.23) are of order  $O(1)$ , hence at the first order we have

$$\frac{1}{2} \mathbf{A}'(\bar{\alpha}_t) \boldsymbol{\varepsilon}(\bar{\mathbf{u}}_t) \cdot \boldsymbol{\varepsilon}(\bar{\mathbf{u}}_t) + w'(\bar{\alpha}_t) - w_1 \Delta \bar{\alpha}_t \leq 0. \quad (2.95)$$

The damage field  $\bar{\alpha}_t$  should also be matched to its asymptotic expansions for the outer and the damage band problems, which implies

$$\lim_{y_1 \rightarrow +\infty \text{ or } |y_2| \rightarrow \infty} \bar{\alpha}_t(\mathbf{y}) = 0 \quad \text{and} \quad \lim_{y_1 \rightarrow -\infty} \bar{\alpha}_t(\mathbf{y}) = \alpha_*(y_2). \quad (2.96)$$

Since all conditions in (2.79) are satisfied in the crack tip problem, the generalized Griffith criterion admits the form (2.80) involving the above two objects. We will take advantage of the asymptotic behavior of the fields (2.92) and (2.96) to analyze that of the conventional dynamic energy release rate (2.69) and the damage dissipation rate (2.70). Note that they are both of order  $O(\ell)$  as in the case for  $G_t^\ell$  in (2.85) as well as for  $G_c^\ell$  in (2.90), and thus are rescaled accordingly

$$(G_t^\alpha)^\ell = \ell \bar{G}_t^\alpha \quad \text{and} \quad \gamma_t^\ell = \ell \bar{\gamma}_t. \quad (2.97)$$

**Proposition 2.9.** *Using virtual perturbations defined in Figure 2.14, the damage dissipation rate (2.70) converges to the fracture toughness (2.90) defined in the damage band problem in the limit  $r \rightarrow \infty$ .*

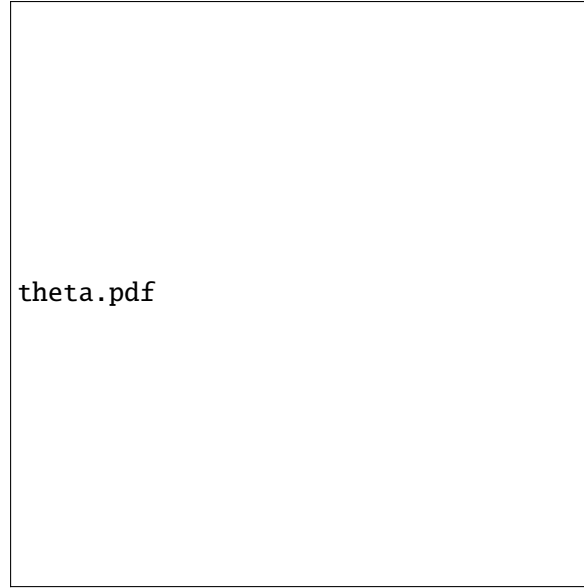


Figure 2.14 – A particular virtual perturbation  $\theta_t$  in the scaled coordinate system  $\mathbf{y} = (\mathbf{x} - \mathbf{P}_t)/\ell$  adapted from Figure 2.8

*Proof.* Within the scaled coordinate system we will construct a particular family of virtual perturbations of form  $\theta_t(\mathbf{y}) = \theta_t(\mathbf{y})\mathbf{e}_1$  as illustrated in Figure 2.14. As can be seen, the definition is adapted from Figure 2.8. The asymptotic behavior of the rescaled damage dissipation rate  $\bar{\gamma}_t$  is analyzed when the inner radius  $r$  goes to infinity with a fixed ratio of  $R/r$ . As  $\nabla\theta_t = \mathbf{0}$  inside  $B_r(\mathbf{P}_t)$ , the scaled damage dissipation rate  $\bar{\gamma}_t$  reads

$$\bar{\gamma}_t = \int_{\odot_r} (\bar{\varsigma}(\bar{\alpha}_t, \nabla\bar{\alpha}_t) \operatorname{div} \theta_t - \bar{\mathbf{q}}_t \cdot \nabla\theta_t \nabla\bar{\alpha}_t) \, d\mathbf{y}$$

where the integral is defined on the uncracked crown by  $\odot_r = (B_R(\mathbf{P}_t) \setminus B_r(\mathbf{P}_t)) \setminus \Gamma_t$  and  $\bar{\varsigma}$  is the rescaled damage dissipation energy given by

$$\bar{\varsigma}(\bar{\alpha}_t, \nabla\bar{\alpha}_t) = w(\bar{\alpha}_t) + \frac{1}{2} w_1 \nabla\bar{\alpha}_t \cdot \nabla\bar{\alpha}_t \implies \bar{\mathbf{q}}_t = w_1 \nabla\bar{\alpha}_t.$$

Integrating by parts the virtual perturbation gradient term and using (2.74), we obtain

$$\bar{\gamma}_t = \int_{\odot_r} \left( \operatorname{div}(\bar{\varsigma}(\bar{\alpha}_t, \nabla\bar{\alpha}_t)\theta_t) - \frac{\partial\bar{\varsigma}}{\partial\alpha}(\bar{\alpha}_t, \nabla\bar{\alpha}_t) \nabla\bar{\alpha}_t \cdot \theta_t + \operatorname{div} \bar{\mathbf{q}}_t (\nabla\bar{\alpha}_t \cdot \theta_t) \right) d\mathbf{y} - \int_{C_r} (\bar{\mathbf{q}}_t \cdot \mathbf{n})(\nabla\bar{\alpha}_t \cdot \theta_t) \, d\mathbf{a}$$

where the boundary integral is due to the fact that  $\theta_t = \mathbf{e}_1 \neq \mathbf{0}$  only on the inner circle  $C_r = \partial B_r(\mathbf{P}_t)$  and  $\theta_t \cdot \mathbf{n} = 0$  on  $\Gamma_t$ . Note that here the vector  $\mathbf{n}$  is defined as the normal pointing into the circle  $C_r$  and  $d\mathbf{a}$  denotes the arc length measure associated with  $d\mathbf{y}$ . From the damage band problem we have

$\nabla \bar{\alpha}_t \cdot \mathbf{e}_1 = 0$  away from the crack tip  $\mathbf{P}_t$ , see (2.87). Hence using the matching condition with the damage band problem (2.96) we have in the limit  $r \rightarrow \infty$

$$\lim_{r \rightarrow \infty} \bar{\gamma}_t = \int_{\odot_\infty} \operatorname{div}(\bar{S}(\bar{\alpha}_t, \nabla \bar{\alpha}_t) \boldsymbol{\theta}_t) \, \mathbf{dy} = \int_{C_\infty} \bar{S}(\bar{\alpha}_t, \nabla \bar{\alpha}_t) \mathbf{e}_1 \cdot \mathbf{n} \, \mathbf{da} = \int_{-\bar{D}}^{\bar{D}} \bar{S}(\alpha_*(y), \nabla \alpha_*(y)) \, \mathbf{dy} = \bar{G}_c$$

where the last equality comes from the definition of  $\bar{G}_c$  in (2.90).  $\square$

**Proposition 2.10.** *Using virtual perturbations defined in Figure 2.14, the conventional dynamic energy release rate (2.69) converges to the equivalent dynamic energy release rate of the outer problem (2.85) in the limit  $r \rightarrow \infty$ ,*

*Proof.* The conventional dynamic energy release rate will still be calculated with the above introduced virtual perturbation of Figure 2.14. The term involving the body force density in (2.69) will be neglected since it is of higher order. By denoting the uncracked inner ball by  $\tilde{B}_r = B_r(\mathbf{P}_t) \setminus \Gamma_t$ , we will partition  $\bar{G}_t^\alpha$  defined on  $B_R(\mathbf{P}_t) \setminus \Gamma_t$  into two parts

$$\begin{aligned} \bar{G}_t^\alpha = \int_{\odot_r} & \left( (\kappa(\dot{\mathbf{u}}_t) - \psi(\boldsymbol{\varepsilon}(\bar{\mathbf{u}}_t), \bar{\alpha}_t)) \operatorname{div} \boldsymbol{\theta}_t + \boldsymbol{\sigma}(\boldsymbol{\varepsilon}(\bar{\mathbf{u}}_t), \bar{\alpha}_t) \cdot (\nabla \bar{\mathbf{u}}_t \nabla \boldsymbol{\theta}_t) + \rho \ddot{\mathbf{u}}_t \cdot \nabla \bar{\mathbf{u}}_t \boldsymbol{\theta}_t + \rho \dot{\mathbf{u}}_t \cdot \nabla \dot{\mathbf{u}}_t \boldsymbol{\theta}_t \right) \mathbf{dy} \\ & + \int_{\tilde{B}_r} (\rho \ddot{\mathbf{u}}_t \cdot \nabla \bar{\mathbf{u}}_t \boldsymbol{\tau}_t + \rho \dot{\mathbf{u}}_t \cdot \nabla \dot{\mathbf{u}}_t \boldsymbol{\tau}_t) \, \mathbf{dy} \end{aligned} \quad (2.98)$$

where we note that the virtual perturbation  $\boldsymbol{\theta}_t$  is constant and is equal to the crack propagation direction  $\mathbf{e}_1$  inside  $B_r(\mathbf{P}_t)$  by definition. Using the identities and integrations by parts similar to (A.11), (A.12) and (2.74), the first line defined in the crown  $\odot_r$  can be written as

$$\begin{aligned} \left( \bar{G}_t^\alpha \right)_1 = \int_{\odot_r} & \left( \operatorname{div} \left( (\kappa(\dot{\mathbf{u}}_t) - \psi(\boldsymbol{\varepsilon}(\bar{\mathbf{u}}_t), \bar{\alpha}_t)) \boldsymbol{\theta}_t \right) + \frac{\partial \psi}{\partial \alpha}(\boldsymbol{\varepsilon}(\bar{\mathbf{u}}_t), \bar{\alpha}_t) \nabla \bar{\alpha}_t \cdot \boldsymbol{\theta}_t \right. \\ & \left. + \rho \ddot{\mathbf{u}}_t \cdot \nabla \bar{\mathbf{u}}_t \boldsymbol{\theta}_t - \operatorname{div} \bar{\boldsymbol{\sigma}}_t \cdot \nabla \bar{\mathbf{u}}_t \boldsymbol{\theta}_t \right) \mathbf{dy} - \int_{C_r} (\nabla \bar{\mathbf{u}}_t^\top \bar{\boldsymbol{\sigma}}_t) \mathbf{n} \cdot \mathbf{e}_1 \, \mathbf{da} \end{aligned}$$

where the integral on the circle  $C_r = \partial B_r(\mathbf{P}_t)$  comes from the integration by parts of the term  $\boldsymbol{\sigma}(\boldsymbol{\varepsilon}(\bar{\mathbf{u}}_t), \bar{\alpha}_t) \cdot (\nabla \bar{\mathbf{u}}_t \nabla \boldsymbol{\theta}_t)$ , the boundary conditions of  $\boldsymbol{\theta}_t$  due to definition, and the fact that  $\mathbf{n}$  is defined as the normal pointing out of the ball  $\partial B_r(\mathbf{P}_t)$ . Thanks to dynamic equilibrium (2.93), we have

$$\begin{aligned} \left( \bar{G}_t^\alpha \right)_1 &= \int_{\odot_r} \left( \operatorname{div} \left( (\kappa(\dot{\mathbf{u}}_t) - \psi(\boldsymbol{\varepsilon}(\bar{\mathbf{u}}_t), \bar{\alpha}_t)) \boldsymbol{\theta}_t \right) + \frac{\partial \psi}{\partial \alpha}(\boldsymbol{\varepsilon}(\bar{\mathbf{u}}_t), \bar{\alpha}_t) \nabla \bar{\alpha}_t \cdot \boldsymbol{\theta}_t \right) \mathbf{dy} - \int_{C_r} (\nabla \bar{\mathbf{u}}_t^\top \bar{\boldsymbol{\sigma}}_t) \mathbf{n} \cdot \mathbf{e}_1 \, \mathbf{da} \\ &= \int_{C_r} \left( (\psi(\boldsymbol{\varepsilon}(\bar{\mathbf{u}}_t), \bar{\alpha}_t) - \kappa(\dot{\mathbf{u}}_t)) (\mathbf{e}_1 \cdot \mathbf{n}) - (\nabla \bar{\mathbf{u}}_t^\top \bar{\boldsymbol{\sigma}}_t) \mathbf{n} \cdot \mathbf{e}_1 \right) \mathbf{da} + \int_{\odot_r} \frac{\partial \psi}{\partial \alpha}(\boldsymbol{\varepsilon}(\bar{\mathbf{u}}_t), \bar{\alpha}_t) \nabla \bar{\alpha}_t \cdot \boldsymbol{\theta}_t \, \mathbf{dy} \end{aligned}$$

where the second equality follows by the integration by parts of the divergence term with the same remarks about the normal and the boundary conditions of  $\boldsymbol{\theta}_t$ .

Using the steady state condition (2.91) for this crack tip problem and the integration by parts similar to (A.14), the second part of (2.98) reads

$$\left( \bar{G}_t^\alpha \right)_2 = \int_{C_r} \rho(\dot{\mathbf{u}}_t \cdot \dot{\mathbf{u}}_t) (\mathbf{e}_1 \cdot \mathbf{n}) \, \mathbf{da} - \int_{\tilde{B}_r} \rho \dot{\mathbf{u}}_t \cdot \dot{\mathbf{u}}_t \operatorname{div} \boldsymbol{\theta}_t \, \mathbf{dy} = \int_{C_r} 2\kappa(\dot{\mathbf{u}}_t) \mathbf{e}_1 \cdot \mathbf{n} \, \mathbf{da}$$

because  $\operatorname{div} \boldsymbol{\theta}_t = 0$  inside the inner ball  $B_r(\mathbf{P}_t)$ . Regrouping  $\left( \bar{G}_t^\alpha \right)_1$  and  $\left( \bar{G}_t^\alpha \right)_2$ , we obtain thus

$$\bar{G}_t^\alpha = \int_{C_r} \left( (\psi(\boldsymbol{\varepsilon}(\bar{\mathbf{u}}_t), \bar{\alpha}_t) + \kappa(\dot{\mathbf{u}}_t)) (\mathbf{e}_1 \cdot \mathbf{n}) - (\nabla \bar{\mathbf{u}}_t^\top \bar{\boldsymbol{\sigma}}_t) \mathbf{n} \cdot \mathbf{e}_1 \right) \mathbf{da} + \int_{\odot_r} \frac{\partial \psi}{\partial \alpha}(\boldsymbol{\varepsilon}(\bar{\mathbf{u}}_t), \bar{\alpha}_t) \nabla \bar{\alpha}_t \cdot \boldsymbol{\theta}_t \, \mathbf{dy}.$$

When the inner radius  $r$  tends to infinity, we observe that the angular sector corresponding to  $\bar{\alpha}_t > 0$  goes to zero. Using the matching conditions of the mechanical fields (2.92) and of the damage field (2.96) which implies that  $\nabla \bar{\alpha}_t \cdot \mathbf{e}_1 \rightarrow 0$ , see (2.87), we obtain in this limit

$$\lim_{r \rightarrow \infty} \bar{G}_t^\alpha = \int_{C_\infty} \left( (\psi(\boldsymbol{\varepsilon}(\bar{\mathbf{u}}_t), 0) + \kappa(\dot{\mathbf{u}}_t)) (\mathbf{e}_1 \cdot \mathbf{n}) - (\nabla \bar{\mathbf{u}}_t^\top \bar{\boldsymbol{\sigma}}_t) \mathbf{n} \cdot \mathbf{e}_1 \right) \mathbf{da} = \int_{C_\infty} (\bar{\mathbf{J}}_t \mathbf{n} \cdot \mathbf{e}_1) \mathbf{da} = \bar{G}_t$$



where  $\bar{\mathbf{J}}_t$  is the rescaled dynamic  $\mathbf{J}$  tensor (1.8) corresponding to the outer problem and the last equality comes from Proposition A.2 and (2.85).  $\square$

**Proposition 2.11** (Asymptotic Griffith's Law). *The crack tip evolution in the dynamic gradient damage model is governed by the following asymptotic Griffith's law as long as the material internal length is sufficiently small compared to the dimension of the body*

$$\dot{l}_t \geq 0, \quad G_t^\ell \leq G_c^\ell \quad \text{and} \quad (G_t^\ell - G_c^\ell)\dot{l}_t = 0.$$

*Proof.* Irreversibility follows directly by the generalized Griffith criterion (2.80). Using its definition (2.68) and the rescaling condition (2.97), the generalized dynamic energy release rate reads

$$\widehat{G}_t^\ell = \ell(\bar{G}_t^\alpha - \bar{\gamma}_t)$$

Thanks to the two asymptotic results from Propositions 2.9 and 2.10 and the rescaling conditions (2.85) and (2.90), the desired crack stability and energy balance conditions can be obtained by passing the limit  $r \rightarrow \infty$  using virtual perturbations defined in Figure 2.14.  $\square$

*Remark.* Proposition 2.11 constitutes another main result of the present contribution. It can be regarded as an asymptotic interpretation of Proposition 2.7. When the internal length is small, it is shown that the propagation of a phase-field like crack is driven by the dynamic energy release rate of the outer mechanical response. Numerical verification of this asymptotic Griffith's law is performed in Section 4.2 for a mode-III crack propagation situation.

*Remark.* Based on a generalized energy-momentum tensor in the quasi-static phase-field model of fracture, authors of (Ballarini & Royer-Carfagni, 2016; Hakim & Karma, 2009) also established a link between the phase-field crack evolution and classical Griffith's theory, by providing an equivalent energy release rate. The separation of scales considered in Section 2.3.3 summarizes and justifies the asymptotic behaviors of the displacement and damage fields assumed in their analyses.

## Summary of this Chapter

In this chapter a general variational framework of the dynamic gradient damage model is outlined in Definition 2.1. The evolution laws for the displacement and the damage are governed by three physical principles of irreversibility, first-order stability (2.17) and energy balance (2.18), similarly to the quasi-static gradient damage model. The first-order stability (2.17) is based on an extension of Hamilton's principle which involves a generalized space-time action integral (2.16). Due to the link between damage and fracture, the gradient damage model can be regarded as a genuine model of fracture. Several damage constitutive laws can be used as long as they verify certain physics-based properties. The phase-field models in the sense of (Miehe, Hofacker, & Welschinger, 2010; Miehe, Welschinger, & Hofacker, 2010) can be obtained by using the (AT) model. To take into account possible large rotation effects, a large displacement extension of the model is discussed in an explicit dynamics context. It is based on the Eulerian Hencky logarithmic strain, see (2.33).

Brittle materials present significantly different fracture or damage behaviors under tension and compression, hence the use of these models is essential especially in dynamics due to wave refraction at the boundary. Several tension-compression asymmetry models that fit into the variational framework of Definition 2.1 are then reviewed. A variational interpretation is given to several existing approaches, see (2.40). It is based on the definition of a convex subset  $\mathcal{C}$  which mathematically achieves a distinction between *tension* and *compression*. A uniaxial traction/compression experiment is performed to highlight the properties of several models. In particular, the model of (Miehe, Hofacker, & Welschinger, 2010) widely used in the phase-field community leads to a non-vanishing stress for a completely damaged material point under compression. It should be used with caution in the presence of highly compressive loads.

A better understanding of dynamic gradient damage models is then obtained via a comparison with the dynamic Griffith's law (1.10). In the formulation of dynamic gradient damage models, inertia

effects are taken into account solely via an inclusion of the kinetic energy (2.4) into the space-time action integral (2.16). Static equilibrium is thus replaced by an elastic-damage wave equation (2.21), however the same energy minimization principle (2.22) still governs the damage evolution similarly in the quasi-static model. Nevertheless it turns out that the crack tip equation of motion becomes automatically rate-dependent and follows a dynamic evolution law summarized in Proposition 2.7, thanks to the definition of the generalized dynamic  $\widehat{J}$ -integral and the generalized dynamic energy release rate  $\widehat{G}_t$ . Assuming that the internal length  $\ell$  is small compared to the dimension of the body, we retrieve the classical Griffith's law of cracks outlined in Proposition 2.11 involving the dynamic energy release rate of the outer problem and the material toughness defined as the amount of energy dissipated across the damage process zone. This theoretic analysis justifies the interpretation of these models as a genuine fracture model.



# 3

## Numerical Implementation

### Contents

<b>3.1 Spatial Discretization</b>	<b>67</b>
<b>3.2 Temporal Discretization</b>	<b>70</b>
<b>3.3 Implementation</b>	<b>74</b>
3.3.1 Numerical solving of the damage problem	74
3.3.2 Details of implementation in EPX	75

This chapter is devoted to the numerical implementation of the dynamic gradient damage model outlined in Definition 2.1. Semi-spatial discretization is performed in Section 3.1 based on the classical  $C^0$  finite element method. The coupled two-field evolution problem is then discretized in the time domain based on the general  $\beta$ -Newmark scheme, see Section 3.2. Some implementation issues are indicated in Section 3.3.

In this contribution the spatial and temporal discretization is as usual decoupled and will be discussed below separately. Space-time finite element methods, see (Hughes & Hulbert, 1988), exploits fully the variational nature of the formulation (2.17) and can be considered as a possible improvement in the future. The elastic energy density split (2.38) is adopted to take into account tension-compression asymmetry. The two damage constitutive laws (AT) and (PAMM) will be used. In this work the irreversibility condition and the variational inequality (2.17) will be effectively implemented, which amounts to solve numerically the weak wave equation (2.20) and the minimality principle for damage (2.22) at every time step.

### 3.1 Spatial Discretization

The spatial discretization described here constitutes a dynamic extension of the work of (Bourdin et al., 2008; Pham, Amor, et al., 2011) for the regularized fracture model (1.18) and the quasi-static gradient damage model outlined in Definition 1.1. A discussion on the large-displacement situations is indicated at the end. The thematic subjects covered here are thus summarized in Table 3.1.

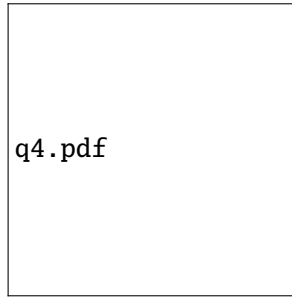
A semi spatial discretization is performed from a mesh  $\Omega_h$  of the original domain  $\Omega$ . It should be ideally unstructured and uniform in mesh sizes otherwise some directions may be preferred when cracks propagate, see (Negri, 1999; Pham, Amor, et al., 2011) and references therein for a discussion on the ideal mesh properties in order to achieve a better modeling of fracture via gradient-damage approaches. In particular, the typical element size  $h$  of the mesh should be preferably smaller with respect to the internal length  $\ell$  in order to calculate correctly the damage band profile, the dissipation

Table 3.1 – Thematic subjects covered in this section

	Going dynamical	$\alpha \leftrightarrow \phi$	$\nabla \alpha \rightarrow \Gamma$	Experimental validation
Theoretics				
Numerics	👍			

energy (2.5) and the material response inside the crack process zone of order  $O(\ell)$ . It leads often to a computationally demanding calculation which requires massive parallelization.

The displacement  $\mathbf{u}_t$  and the damage field  $\alpha_t$  will be both discretized with classical  $C^0$  isoparametric finite elements based on  $\Omega_h$ . For two-dimensional plane problems, an arbitrary element possesses at every node 3 nodal degrees of freedom corresponding to 2 components of the displacement and 1 scalar value of the damage, see for example Figure 3.1. The symbols  $\underline{\mathbf{u}}$  and  $\underline{\alpha}$  are used to denote the

Figure 3.1 – Local interpolation of  $(\mathbf{u}, \alpha)$  based on nodal values inside the element

current global displacement and damage nodal vectors. Inside a given physical element  $\Omega_e \in \Omega_h$ , their local nodal vectors  $\underline{\mathbf{u}}^e$  and  $\underline{\alpha}^e$  achieve an interpolation of the displacement and damage fields as well as their derivatives

$$\begin{aligned} \mathbf{u}_t(\mathbf{x}) &= \mathbf{N}(\mathbf{x})\underline{\mathbf{u}}^e \quad \text{and} \quad \boldsymbol{\varepsilon}(\mathbf{u}_t)(\mathbf{x}) = \mathbf{B}(\mathbf{x})\underline{\mathbf{u}}^e, \\ \alpha_t(\mathbf{x}) &= \mathbf{N}_\alpha(\mathbf{x})\underline{\alpha}^e \quad \text{and} \quad \nabla \alpha_t(\mathbf{x}) = \mathbf{B}_\alpha(\mathbf{x})\underline{\alpha}^e \end{aligned} \quad (3.1)$$

where  $\mathbf{N}$ 's and  $\mathbf{B}$ 's are respectively the interpolation and differentiation matrices. The Voigt notation is assumed for the strain tensor  $\boldsymbol{\varepsilon}(\mathbf{u}_t)$  and the damage gradient  $\nabla \alpha_t$ , which are written as column vectors. *Linear* interpolation is used due to its low computational cost in a dynamic calculation. According to (Bourdin et al., 2008), linear elements for the displacement and damage fields perform equally well compared to higher-order elements in terms of  $\Gamma$ -convergence of the damage dissipation energy. Finally this P1-P1 finite element discretization is not forbidden according to (Simone, Askes, Peerlings, & Sluys, 2003).

**Displacement problem** Plugging (3.1) into the weak elastic-damage dynamic wave equation (2.20) and adopting the same interpolation for the testing function  $\mathbf{w}_t$ , we obtain the following spatially discretized dynamic evolution equation

$$\mathbf{M}\ddot{\underline{\mathbf{u}}} = \mathbf{F}_{\text{ext}} - \mathbf{F}_{\text{int}}(\underline{\mathbf{u}}, \underline{\alpha}) \quad (3.2)$$

with  $\mathbf{M}$  the consistent mass matrix,  $\mathbf{F}_{\text{ext}}$  the external force vector corresponding to the potential (2.11) and  $\mathbf{F}_{\text{int}}$  the internal force vector. The mass matrix is assembled from the elementary mass matrices which reads inside  $\Omega_e$

$$\mathbf{M} = \int_{\Omega_e} \rho \mathbf{N}^T \mathbf{N} \, d\mathbf{x}.$$

For explicit dynamic situations, this matrix is lumped  $\mathbf{M} \mapsto \overline{\mathbf{M}}$  using the classical row-summing techniques to improve computational efficiency and spectral properties, see (Hughes, 1987). The global

internal force vector is constructed from its elementary counterparts which are given by

$$\begin{aligned}\mathbf{F}_{\text{int}}^e &= \int_{\Omega_e} \mathbf{B}^\top \boldsymbol{\sigma}(\mathbf{B}\underline{\mathbf{u}}^e, \mathbf{N}_\alpha \underline{\boldsymbol{\alpha}}^e) d\mathbf{x} \\ &= \int_{\Omega_e} \mathbf{B}^\top (a(\mathbf{N}_\alpha \underline{\boldsymbol{\alpha}}^e) \boldsymbol{\sigma}_0^+(\mathbf{B}\underline{\mathbf{u}}^e) + \boldsymbol{\sigma}_0^-(\mathbf{B}\underline{\mathbf{u}}^e)) d\mathbf{x},\end{aligned}\quad (3.3)$$

where the stress expression (2.45) that takes into account tension-compression asymmetry is used. In explicit dynamics a residual stiffness  $k_{\text{res}}$  is not needed in the stiffness degradation function since no matrix inversion is needed, contrary to the implicit cases (Pham, Amor, et al., 2011; Schlüter et al., 2014).

For simplex finite elements (triangular and tetrahedral elements) the Jacobian of the transformation (between the reference and the physical elements) as well as the differentiation matrix  $\mathbf{B}$  are constant, thus (3.3) can be integrated exactly using an effective stress

$$\mathbf{F}_{\text{int}}^e = |\Omega_e| \mathbf{B}^\top \boldsymbol{\sigma}_{\text{eff}} = |\Omega_e| \mathbf{B}^\top (a_{\text{eff}} \boldsymbol{\sigma}_0^+ + \boldsymbol{\sigma}_0^-), \quad (3.4)$$

where  $|\Omega_e|$  denotes the measure (area of volume) of  $\Omega_e$  and  $a_{\text{eff}}$  stands for the effective stiffness degradation

$$a_{\text{eff}} = \frac{1}{|\Omega_e|} \int_{\Omega_e} a(\mathbf{N}_\alpha \underline{\boldsymbol{\alpha}}) d\mathbf{x}. \quad (3.5)$$

Explicit expression of  $a_{\text{eff}}$  can be readily computed and are given as follows.

- Triangular elements

$$a_{\text{eff}} = \frac{1}{3} \left( \left(1 - \frac{\alpha_1}{2} - \frac{\alpha_2}{2}\right)^2 + \left(1 - \frac{\alpha_2}{2} - \frac{\alpha_3}{2}\right)^2 + \left(1 - \frac{\alpha_1}{2} - \frac{\alpha_3}{2}\right)^2 \right)$$

- Tetrahedral elements

$$a_{\text{eff}} = 1 + \frac{1}{10} \sum_{i=1}^4 \sum_{j=1}^4 \alpha_i \alpha_j - \frac{1}{2} \sum_{i=1}^4 \alpha_i$$

The use of the effective stress  $\boldsymbol{\sigma}_{\text{eff}}$  improves computational efficiency and may also be served as an output of the current element.

For tensor product finite elements, a loop on the Gauss points is necessary and our experience suggests that 4 Gauss points for quadrilateral elements and 8 for hexagonal elements are sufficient. An effective stress can no longer be defined and the stress evaluated at these Gauss points will be used as the output variable.

*Remark* (Extension to large-displacements). Numerical implications of the large-displacement extension proposed in Section 2.1.5 are discussed here. It is based on the explicit dynamics situations, where at the beginning of every time step the current configuration  $\boldsymbol{\varphi}_t(\Omega)$  is known and is updated from the last iteration. The Eulerian elastic-damage dynamic wave equation (2.36) will be naturally solved in the current deformed mesh obtained by constantly updating the mesh coordinates  $\mathbf{x}_t = \mathbf{x} + \mathbf{u}_t(\mathbf{x}) \in \Omega_t$ .

This implies that the interpolation of the displacement and the damage (3.1), as well as the calculation of the global internal force vector (3.3) should be performed in the deformed element  $\boldsymbol{\varphi}_t(\Omega_e)$ . If the interpolation  $\mathbf{N}$ 's can always be transformed to a reference element, the differentiation matrices  $\mathbf{B}$ 's should be evaluated with respect to the current deformed element geometry and hence require being constantly updated at the beginning of every time step.

The Hencky logarithmic strain  $\mathbf{h}_t$  defined in (2.33) replaces the use of the linearized strain in the calculation of the stress tensor in (3.3). Although the polar decomposition is indeed unnecessary by remarking that  $\log \mathbf{V}_t = \frac{1}{2} \log \mathbf{B}_t$ , spectral decomposition of the left Cauchy-Green tensor  $\mathbf{B}_t = \mathbf{F}_t \mathbf{F}_t^\top$  is unavoidable.

**Damage problem** Plugging the interpolation expression (3.1) into the energy minimization principle (2.22) and using the elastic energy density split (2.38) leads to the following spatially discretized variational inequality

$$q_{\underline{\mathbf{u}}}(\underline{\alpha}) \leq q_{\underline{\mathbf{u}}}(\underline{\beta}) \text{ for all } \underline{\beta} \text{ that } 0 \leq \underline{\alpha} \leq \underline{\beta} \leq 1 \quad (3.6)$$

which involves the following discrete functional which reads inside each element

$$q_{\underline{\mathbf{u}}}^e(\underline{\alpha}) = \int_{\Omega_e} (a(\mathbf{N}_\alpha \underline{\alpha}^e) \psi_0^+(\mathbf{B}\underline{\mathbf{u}}^e) + w(\mathbf{N}_\alpha \underline{\alpha}^e) + w_1 \eta^2 \underline{\alpha}^{e\top} \mathbf{B}_\alpha^\top \mathbf{B}_\alpha \underline{\alpha}^e) \, d\mathbf{x}. \quad (3.7)$$

For sophisticated damage constitutive laws such as that used in (Lorentz & Godard, 2011), it is a nonlinear convex functional where the Hessian matrix depends on the damage state during numerical solving. Fortunately, using the damage constitutive laws (AT) and (PAMM), this functional  $q_{\underline{\mathbf{u}}}(\underline{\alpha})$  is quadratic with respect to the damage vector  $\underline{\alpha}$  and is given by

$$q_{\underline{\mathbf{u}}}(\underline{\alpha}) = \frac{1}{2} \underline{\alpha}^\top \mathbf{H}(\underline{\mathbf{u}}) \underline{\alpha} - \mathbf{b}(\underline{\mathbf{u}})^\top \underline{\alpha}. \quad (3.8)$$

The Hessian matrix  $\mathbf{H}$  and the second member vector  $\mathbf{b}$  depend solely on the current deformation state  $\underline{\mathbf{u}}$  and hence are constant during the solving process of the damage problem. Their exact forms depend on the damage constitutive law used:

- For the (PAMM) law for instance, they can be assembled from the elementary matrix and vector given by

$$\begin{aligned} \mathbf{H}^e &= \int_{\Omega_e} \left( 2\psi_0^+(\mathbf{B}\underline{\mathbf{u}}^e) \mathbf{N}_\alpha^\top \mathbf{N}_\alpha + 2w_1 \eta^2 \mathbf{B}_\alpha^\top \mathbf{B}_\alpha \right) \, d\mathbf{x}, \\ \mathbf{b}^e &= \int_{\Omega_e} (2\psi_0^+(\mathbf{B}\underline{\mathbf{u}}^e) - w_1) \mathbf{N}_\alpha \, d\mathbf{x}. \end{aligned}$$

- For the (AT) model, they are given by

$$\begin{aligned} \mathbf{H}^e &= \int_{\Omega_e} \left( 2 (\psi_0^+(\mathbf{B}\underline{\mathbf{u}}) + w_1) \mathbf{N}_\alpha^\top \mathbf{N}_\alpha + 2w_1 \eta^2 \mathbf{B}_\alpha^\top \mathbf{B}_\alpha \right), \\ \mathbf{b}^e &= \int_{\Omega_e} 2\psi_0^+(\mathbf{B}\underline{\mathbf{u}}) \mathbf{N}_\alpha \, d\mathbf{x}. \end{aligned}$$

These quantities can be evaluated exactly for simplex finite elements. For quadrilateral and hexahedral elements, an approximated using a numerical integration with respectively 4 and 8 Gauss points will be used.


*Remark* (Extension to large-displacements). According to (2.22), the damage minimality condition is naturally formulated in the initial reference configuration. From a physical point of view, this corresponds to the fact that the damage dissipation energy is destined to measure the length or the area of cracks defined in the reference configuration. Technically the concerned energetic functional can be written in the deformed mesh (at the expense of additional unpleasant  $\mathbf{F}_t$  and  $J_t$  terms), however it is not necessary (Piero et al., 2007).

From a implementation point of view, it implies that the interpolation and differentiation matrices  $\mathbf{N}$ 's and  $\mathbf{B}$ 's that corresponds to the initial configuration should be stored and will be used throughout the calculation.

## 3.2 Temporal Discretization

This section described a temporal discretization of the dynamic gradient damage model. The thematic subjects covered here are thus summarized in Table 3.2.

Table 3.2 – Thematic subjects covered in this section

	Going dynamical	$\alpha \leftrightarrow \phi$	$\nabla \alpha \rightarrow \Gamma$	Experimental validation
Theoretics				
Numerics				

Consider an arbitrary discretization ( $t^n$ ) of the time interval  $I = [0, T]$  where the superscript  $n$  denotes a quantity evaluated at the  $n$ -th time step. We will mainly focus on the time stepping procedures bringing the current known states ( $\underline{\mathbf{u}}^n, \underline{\dot{\mathbf{u}}}^n, \underline{\ddot{\mathbf{u}}}^n, \underline{\alpha}^n$ ) to the next time step ( $\underline{\mathbf{u}}^{n+1}, \underline{\dot{\mathbf{u}}}^{n+1}, \underline{\ddot{\mathbf{u}}}^{n+1}, \underline{\alpha}^{n+1}$ ). In the time-continuous model the weak elastic-damage dynamic wave equation (2.20) and the damage minimality condition (2.22) are coupled in the first-order stability principle (2.17). After temporal discretization  $\underline{\mathbf{u}}$  and  $\underline{\alpha}$  evaluated at the last time step  $t = t^n$  and the current time step  $t = t^{n+1}$  are in general involved in an implicit fashion. However, we observe that the energy minimization principle (2.22) for damage is not a genuine time evolution problem since time dependence is only introduced via the irreversibility condition. After a temporal discretization (3.6) at time  $t = t^{n+1}$  reads

$$q_{\underline{\mathbf{u}}^{n+1}}(\underline{\alpha}^{n+1}) \leq q_{\underline{\mathbf{u}}^{n+1}}(\underline{\beta}) \text{ for all } \underline{\beta} \text{ that } 0 \leq \underline{\alpha}^n \leq \underline{\beta} \leq 1 \quad (3.9)$$

where the Hessian matrix and the second member vector in (3.8) are evaluated at  $\underline{\mathbf{u}}^{n+1}$ . The equation (3.9) can be interpreted as a numerical minimization problem of the quadratic functional  $q$  under the irreversible constraint that the current sought damage state  $\underline{\alpha}^{n+1}$  is pointwise within the bound  $[\underline{\alpha}^n, 1]$

$$\underline{\alpha}^{n+1} = \operatorname{argmin} q_{\underline{\mathbf{u}}^{n+1}}(\cdot) \text{ subject to the constraints } 0 \leq \underline{\alpha}^n \leq \underline{\alpha}^{n+1} \leq 1. \quad (3.10)$$

The next damage state  $\underline{\alpha}^{n+1}$  can thus be accurately calculated as long as the next deformation state  $\underline{\mathbf{u}}^{n+1}$  is known.

It remains then to specify the temporal discretization method used for the  $\underline{\mathbf{u}}$ -problem. In this work we adopt the classical second-order accurate Newmark- $\beta$  integrator, which assumes the following time-stepping procedure

$$\underline{\dot{\mathbf{u}}}^{n+1} = \underline{\dot{\mathbf{u}}}^n + \frac{\Delta t}{2} (\underline{\ddot{\mathbf{u}}}^n + \underline{\ddot{\mathbf{u}}}^{n+1}), \quad (3.11)$$

$$\underline{\mathbf{u}}^{n+1} = \underline{\mathbf{u}}^n + \Delta t \underline{\dot{\mathbf{u}}}^n + \frac{1-2\beta}{2} \Delta t^2 \underline{\ddot{\mathbf{u}}}^n + \beta \Delta t^2 \underline{\ddot{\mathbf{u}}}^{n+1}. \quad (3.12)$$

The implicit method  $0 < \beta \leq \frac{1}{2}$  may be suitable for intermediate situations between a quasi-static and an explicit dynamic calculation. In the present work it will be used to numerically investigate the quasi-static limit of the dynamic model, see Section 4.2. The explicit method  $\beta = 0$  with a lumped mass matrix  $\bar{\mathbf{M}}$  should be preferred mainly in terms of computational efficiency for applications where the loading speed or the crack propagation speed is comparable to the material sound speed, since in general the time scale involved is typically of order  $O(1 \text{ ms}) \ll O(1 \text{ s})$ . The explicit method is conditionally stable. The constraint prescribed on the current time increment  $\Delta t$  is often determined by the CFL condition  $\Delta t < \Delta t_{\text{CFL}} = \min(h/c)$  where  $h$  is the mesh size,  $c$  is the material sound speed and the smallest value is chosen among all elements. This is not a very inconvenient feature since in the presence of high geometrical and material nonlinearities even unconditionally stable implicit schemes need a small time increment comparable to  $\Delta t_{\text{CFL}}$ . In the calculation of the material sound speed, the current damage state  $\alpha_t$  as well as the tension-compression split formulation (2.38) is taken into account. Thus a totally damaged element under tension does not penalize the total computational time.

The spatially discretized elastic-damage equation reads

$$\mathbf{M} \underline{\ddot{\mathbf{u}}}^{n+1} = \mathbf{F}_{\text{ext}}^{n+1} - \mathbf{F}_{\text{int}}(\underline{\mathbf{u}}^{n+1}, \underline{\alpha}^{n+1}). \quad (3.13)$$

It can be seen that the determination of the the new acceleration  $\underline{\ddot{\mathbf{u}}}^{n+1}$  requires the knowledge of the new deformation state  $\underline{\mathbf{u}}^{n+1}$  which itself determines the new damage field at time  $t = t^{n+1}$  via (3.10).



For the implicit Newmark method  $\beta \neq 0$ , (3.12) can thus be regarded as a nonlinear equation in  $\underline{\mathbf{u}}^{n+1}$ , where nonlinearity results from the irreversibility condition when minimizing the total energy (3.10). To decouple the  $(\underline{\mathbf{u}}^{n+1}, \underline{\boldsymbol{\alpha}}^{n+1})$  problem, we use a staggered time-stepping procedure as used in (Borden et al., 2012; Bourdin et al., 2011; Hofacker & Miehe, 2012) among others. The idea is to update the acceleration  $\underline{\ddot{\mathbf{u}}}^{n+1}$  while fixing the damage state at its *previous* known value  $\underline{\boldsymbol{\alpha}}^n$ . Hence (3.13) becomes

$$\mathbf{M}\underline{\ddot{\mathbf{u}}}^{n+1} \approx \mathbf{F}_{\text{ext}}^{n+1} - \mathbf{F}_{\text{int}}(\underline{\mathbf{u}}^{n+1}, \underline{\boldsymbol{\alpha}}^n). \quad (3.14)$$

When a relatively small time-step is used, it is expected that the damage increment  $\underline{\boldsymbol{\alpha}}^{n+1} - \underline{\boldsymbol{\alpha}}^n$  is bounded and the staggered time-discrete model will converge to the continuous one, cf. (Larsen, Ortner, & Süli, 2010). Introducing the displacement prediction at time  $t = t^{n+1}$

$$\tilde{\underline{\mathbf{u}}}^{n+1} = \underline{\mathbf{u}}^n + \Delta t \underline{\dot{\mathbf{u}}}^n + \frac{1-2\beta}{2} \Delta t^2 \underline{\ddot{\mathbf{u}}}^n,$$

from (3.12) we obtain the equation for  $\underline{\mathbf{u}}^{n+1}$

$$\mathbf{M} \frac{\underline{\mathbf{u}}^{n+1} - \tilde{\underline{\mathbf{u}}}^{n+1}}{\Delta t^2} = \beta (\mathbf{F}_{\text{ext}}^{n+1} - \mathbf{F}_{\text{int}}(\underline{\mathbf{u}}^{n+1}, \underline{\boldsymbol{\alpha}}^n)). \quad (3.15)$$

In general due to the use of tension-compression asymmetry models (2.38), it is a nonlinear equation which requires several Newton iterations and the evaluation of the current tangent stiffness. The time-stepping procedure for the dynamic gradient damage model based on the implicit Newmark- $\beta$  method in a prediction-correction form is summarized in Algorithm 3.

---

**Algorithm 3** Staggered time-stepping procedure for the dynamic gradient damage model based on the implicit Newmark- $\beta$  method

---

- 1: **for** every successive time step  $n \geq 0$  **do**
  - 2:   Prediction  $\tilde{\underline{\mathbf{u}}}^{n+1} = \underline{\mathbf{u}}^n + \Delta t \underline{\dot{\mathbf{u}}}^n + \frac{1-2\beta}{2} \Delta t^2 \underline{\ddot{\mathbf{u}}}^n$ .
  - 3:   Prediction  $\tilde{\underline{\mathbf{v}}}^{n+1} = \underline{\dot{\mathbf{u}}}^n + \frac{\Delta t}{2} \underline{\ddot{\mathbf{u}}}^n$ .
  - 4:   Solve  $\underline{\mathbf{u}}^{n+1}$  via (3.15).
  - 5:   Update  $\underline{\ddot{\mathbf{u}}}^{n+1} = (\underline{\mathbf{u}}^{n+1} - \tilde{\underline{\mathbf{u}}}^{n+1})/(\beta \Delta t^2)$ .
  - 6:   Update  $\underline{\dot{\mathbf{u}}}^{n+1} = \tilde{\underline{\mathbf{v}}}^{n+1} + \frac{\Delta t}{2} \underline{\ddot{\mathbf{u}}}^{n+1}$ .
  - 7:   Solve  $\underline{\boldsymbol{\alpha}}^{n+1}$  via (3.10).
  - 8: **end for**
- 

*Remark.* After temporal discretization, the elastic-damage dynamic wave equation (2.20) and the damage minimality condition (2.22) can also be solved in a monolithic fashion inside a nonlinear Newton solver described for example in (Borden et al., 2012; Schlüter et al., 2014). The irreversible condition contained in (3.10) should be included in the monolithic solver to ensure that the damage variable is subject to a bound constraint during solving. Future work could be devoted to a detailed analysis of these schemes in terms of computational efficiency.

*Remark.* In the staggered time-stepping procedure, the approximation  $\underline{\ddot{\mathbf{u}}}^{n+1} \approx \underline{\ddot{\mathbf{u}}}^n$  simplifies the coupled solving of the displacement and the damage. However, we admit that the  $(\underline{\mathbf{u}}^{n+1}, \underline{\boldsymbol{\alpha}}^{n+1})$  couple obtained at the end of the current time step do not necessarily satisfy the weak elastic-damage dynamic wave equation (2.20) and the damage minimality condition (2.22). Following the alternate minimization procedure common for quasi-static models, see (Pham, Amor, et al., 2011), several alternate iterations could also be performed here until convergence. However in dynamics, since the time-step is in general close to the critical time-step (*i.e.* very small), convergence could be reached within the first iteration. In any case when  $\Delta t \rightarrow 0$ , the discrete staggered model converges to the continuous one, see the remark given at the end of this section.

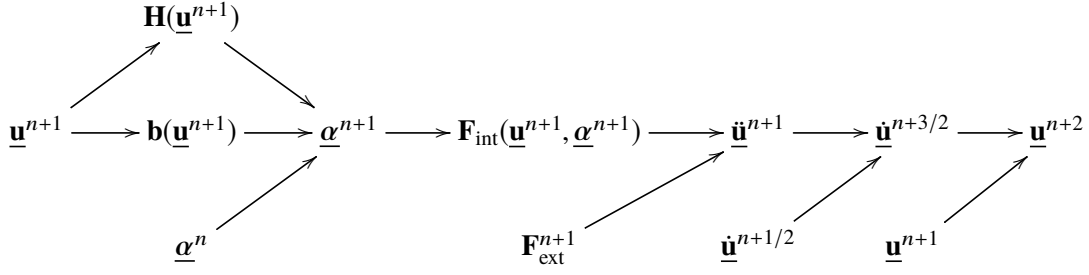


Figure 3.2 – Updating flow of the explicit time-stepping procedure for the discretized dynamic gradient damage model at the time step  $t^{n+1}$

In the explicit case when  $\beta = 0$ , it turns out that the time evolution system in  $(\underline{\mathbf{u}}, \underline{\alpha})$  is automatically decoupled and the two subproblems separately in  $\underline{\mathbf{u}}^{n+1}$  and in  $\underline{\alpha}^{n+1}$  can be solved in a sequence at every time step, see Figure 3.2. Indeed according to (3.12), the current displacement state  $\underline{\mathbf{u}}^{n+1}$  can be directly determined from the previous kinematic states, which itself determines then the damage state via (3.10). Introducing the middle-step velocity

$$\underline{\dot{\mathbf{u}}}^{n+1/2} = \underline{\dot{\mathbf{u}}}^n + \frac{\Delta t}{2} \underline{\ddot{\mathbf{u}}}^n,$$

the Newmark time-stepping (3.11) and (3.12) reads

$$\begin{aligned} \underline{\mathbf{u}}^{n+1} &= \underline{\mathbf{u}}^n + \Delta t \underline{\dot{\mathbf{u}}}^{n+1/2}, \\ \underline{\dot{\mathbf{u}}}^{n+1} &= \underline{\dot{\mathbf{u}}}^{n+1/2} + \frac{\Delta t}{2} \underline{\ddot{\mathbf{u}}}^{n+1}, \\ \underline{\dot{\mathbf{u}}}^{n+1/2} &= \underline{\dot{\mathbf{u}}}^{n-1/2} + \Delta t \underline{\ddot{\mathbf{u}}}^n. \end{aligned}$$

The explicit time-stepping procedure for the discretized dynamic gradient damage model is then summarized in Algorithm 4. It is implemented by the author in the explicit dynamics software EPX, see (CEA & EC, 2015).

---

**Algorithm 4** Explicit time-stepping procedure for the dynamic gradient damage model

---

- 1: **for** every successive time step  $n \geq 0$  **do**
  - 2:   Update  $\underline{\dot{\mathbf{u}}}^{n+1/2} = \underline{\dot{\mathbf{u}}}^n + \frac{\Delta t}{2} \underline{\ddot{\mathbf{u}}}^n$ .
  - 3:   Update  $\underline{\mathbf{u}}^{n+1} = \underline{\mathbf{u}}^n + \Delta t \underline{\dot{\mathbf{u}}}^{n+1/2}$ .
  - 4:   Solve  $\underline{\alpha}^{n+1}$  via (3.10).
  - 5:   Solve  $\underline{\ddot{\mathbf{u}}}^{n+1}$  via (3.13) with the lumped mass matrix  $\overline{\mathbf{M}}$ .
  - 6:   Update  $\underline{\dot{\mathbf{u}}}^{n+1} = \underline{\dot{\mathbf{u}}}^{n+1/2} + \frac{\Delta t}{2} \underline{\ddot{\mathbf{u}}}^{n+1}$ .
  - 7: **end for**
- 

The initialization phase for the above implicit and explicit time-stepping procedure is described in Algorithm 5. We observe that the initial damage is recomputed  $\underline{\alpha}^{-1} \mapsto \underline{\alpha}^0$  in the step 2. The role of  $\underline{\alpha}^{-1}$  is to bring some *a priori* knowledge of the damage field resulting from a previous calculation or more frequently to represent an initial crack  $\underline{\alpha}^{-1} = 1$  on  $\Gamma_0$ . This step thus renders it compatible with the initial displacement condition and the energy minimization structure. Remark that in phase field approaches for example in (Borden et al., 2012), the initial crack is introduced via an initial history field  $\mathcal{H}_0$  which is localized along the desired initial defect. It is due to the fact that the irreversible constraint is dropped during energy minimization (2.22) in their models.

*Remark* (Temporal convergence). Remark that only the irreversibility condition  $\dot{\alpha}_t \geq 0$  and the variational inequality (2.17) is effectively implemented. The former condition is reinforced during

---

**Algorithm 5** Initialization for the implicit and explicit time-stepping procedure described in Algorithms 3 and 4

---

- 1: Given initial conditions  $\underline{\mathbf{u}}^0, \underline{\dot{\mathbf{u}}}^0$  and  $\underline{\alpha}^{-1}$ .
  - 2: Reinitialize the damage  $\underline{\alpha}^0 = \arg\min q_{\underline{\mathbf{u}}^0}(\cdot)$  subjected to constraints  $0 \leq \underline{\alpha}^{-1} \leq \underline{\alpha}^0 \leq 1$ .
  - 3: Initialize the acceleration  $\mathbf{M}\underline{\ddot{\mathbf{u}}}^0 = \mathbf{F}_{\text{ext}}^0 - \mathbf{F}_{\text{int}}(\underline{\mathbf{u}}^0, \underline{\alpha}^0)$ .
- 

energy minimization (3.10). It is shown in (Larsen et al., 2010) that the time-discrete numerical model summarized by Algorithms 3 and 4 will converge to the continuous model, *i.e.* Definition 2.1. In particular, it will thus also balance energy as required in (2.18), when the time increment becomes small. Their constructive proof makes use of the implicit Euler scheme used in (Bourdin et al., 2011), however our experience suggests the same for the implicit and explicit Newmark schemes.

*Remark* (Approximation of the Hencky logarithmic strain). An approximation of the Hencky strain based on the following remarkable property established in (Xiao et al., 1997) can be used: within a proper corotational frame the rate of the Hencky strain equals the stretching tensor. An increment of the Hencky strain can thus be given by  $\Delta \mathbf{h}^n \approx \nabla^s(\Delta \mathbf{u}^n)$  where  $\nabla^s$  denotes the symmetrized gradient operator and the displacement increment  $\Delta \mathbf{u}^n = \mathbf{u}^n - \mathbf{u}^{n-1}$  is written in the current deformed configuration. To have better accuracy, a second-order approximation based on the incremental Almansi strain is used


$$\Delta \mathbf{h}^n \approx \frac{1}{2} (\nabla \Delta \mathbf{u}^n + \nabla^T \Delta \mathbf{u}^n - (\nabla^T \Delta \mathbf{u}^n)(\nabla \Delta \mathbf{u}^n)).$$

Finally the current Hencky strain is incremented  $\mathbf{h}^n = \mathbf{h}^{n-1} + \Delta \mathbf{h}^n$ .

### 3.3 Implementation

This section provides some details on the implementation of the discretized numerical model summarized by Algorithms 3 and 4. The thematic subjects covered here are thus summarized in Table 3.3.

Table 3.3 – Thematic subjects covered in this section

	Going dynamical	$\alpha \leftrightarrow \phi$	$\nabla \alpha \rightarrow \Gamma$	Experimental validation
Theoretics				
Numerics				

#### 3.3.1 Numerical solving of the damage problem

In this work, the damage energy minimization problem (3.10) will be directly solved at the structural scale. It could be converted into an equivalent local problem defined for each element. This possibility requires introduction of Lagrange multipliers at every Gauss points and an identification between the nodal damage field and the damage defined at Gauss points, see (Beaurain, 2011, p. 49). The principal motivation of this kind of Lagrangian modeling is the ability in the software Code-Aster to impose more naturally the irreversibility condition, however the computational cost is higher due to additional unknown variables.

Consequently, (3.10) can be regarded as a large scale bound-constrained minimization problem defined at the structural level. Due to the damage constitutive requirement, the problem is convex and gradient-based numerical algorithms can be applied. These methods call for the evaluation of the objective functional (3.8) as well as its first and second derivatives (Hessian matrix  $\mathbf{H}$ ). An efficient storage and manipulation of these objects is essential especially in an explicit dynamics context.

Here the library PETSc is adopted due to its optimized efficiency, see (Balay et al., 2015). As a high-level C++/Fortran numerical linear algebra backend, PETSc provides in particular the Vec and

the `Mat` classes for defining vectors and matrices. The actual storage format is not fixed in advance and it suffices to call the function `Vec/MatSetType` to affect a particular format. The computational arrays (the CSR format for example) can be extracted for output but in general all operations of these objects `Vec/Mat` are independent of the storage format used and thus transparent to the user. As an example, a unique interface is available to conduct a matrix-vector product

**CALL** MATMULT(H,X,GRAD,PETSCERR)

where the vector `GRAD` stocks the result of  $\mathbf{H}\underline{\alpha}$ . PETSc is built on the Message Passing Interface (MPI) standard and only one generic version exists which can be run either in sequential or parallel. The calling functions are almost the same in both cases, thus the code could be parallelized with minor interface changes.

Specifically the Gradient Projection Conjugate Gradient (GPCG) algorithm proposed in (Moré & Toraldo, 1991) is used to numerically solve (3.10) in an iterative fashion. It is already implemented in the TAO package of PETSc and is designed for quadratic bound-constrained minimization problems. Due to the bound constraint, approximate solutions  $\underline{\beta}$  to (3.10) can be defined using the projected gradient  $[\mathbf{g}]$  of which the  $i$ -th component is given by

$$0 \stackrel{?}{\approx} [\mathbf{g}]_i = \begin{cases} \partial_i q & \text{if } \underline{\beta}_i \in (\underline{\alpha}_i^n, 1), \\ \min(\partial_i q, 0) & \text{if } \underline{\beta}_i = \underline{\alpha}_i^n, \\ \max(\partial_i q, 0) & \text{if } \underline{\beta}_i = 1. \end{cases}$$

At each solving iteration, the method consists of several gradient projections

$$\underline{\beta} \leftarrow \mathbb{P}(\underline{\beta} - c \nabla q(\underline{\beta}))$$

to *approximately* identify the *active* nodes, *i.e.* those either  $\underline{\alpha}_i^{n+1} = \underline{\alpha}_i^n$  or  $\underline{\alpha}_i^{n+1} = 1$ . Note that here we perform a gradient descent followed by a projection  $\mathbb{P}$  onto the bound to ensure that  $\underline{\alpha}^n \leq \underline{\beta} \leq 1$ . Then it applies the preconditioned conjugate gradient method to minimize an unconstrained reduced problem of the *free* variables, *i.e.* those satisfying  $\underline{\alpha}_i^n < \underline{\alpha}_i^{n+1} < 1$ . The method proceeds to the next iteration until convergence. Interested readers are referred to (Moré & Toraldo, 1991) for a more detailed explanation of the algorithm. The incomplete Cholesky factorization preconditioner is applied block-wise into each decomposed subdomain. Computational load is also well balanced in parallel computations based on domain decomposition, see (Benson, McInnes, & Moré, 2001).

Using the PETSc library, both the implicit and explicit time-stepping Algorithms 3 and 4 are implemented by the author as a Python package named “FEniCS Dynamic Gradient Damage”, see (Li, 2015). It is based on the FEniCS Project (Logg, Mardal, & Wells, 2012) for automated solution of partial differential equations. A specific C++ interface PETScTAOSolver is developed by the author which brings various mathematical optimization algorithms defined in PETSc/TAO into FEniCS. In this implementation the tension-compression asymmetry is not taken into account. A linearized strain theory is also assumed.

The explicit time-stepping procedure for the dynamic gradient damage model summarized in Algorithm 4 is also implemented in EPX by the author, an explicit dynamics program dedicated to transient phenomena involving fluid-structure interaction (CEA & EC, 2015). Here all the tension-compression asymmetry models discussed in Section 2.2 are implemented. The large-displacement extension, see Section 2.1.5, is also by default activated in the software.

### 3.3.2 Details of implementation in EPX

**Initialization** The initialization `INIT_ENDOGRAD` of the gradient damage model is performed at the end of the routine `initia.ff`. It has several objectives

- Allocate various Fortran arrays needed in the model: the damage field `ALPHA`, the damage dissipation energy for all elements `EFISS`...

- Initialize the PETSc solver and several objects: the minimization solver TAOSOLV, the global Hessian matrix for damage HALPHA, the PETSc viewer VIEWER to have access to convergence information. . .

To guarantee a good efficiency when assembling sparse matrices, it is essential that we preallocate enough memory by indicating to PETSc the number of non-zero elements at every row of the matrix. In parallel, the non-zeros elements should be treated separately depending whether they appear in the diagonal or off the diagonal of the current processor. If this preallocation phase is omitted, PETSc will allocate the needed memory by calling `PetscMalloc` every time it encounters a new unexpected non-zero term, which causes the execution time to increase significantly, see (Balay et al., 2015). An overestimation of the sparse structure of the mesh connectivity is performed: for every node in the mesh, we consider all the elements containing that node and count the total node numbers possessed by these elements. Only one loop on all the elements is needed during the initialization. This overestimation does virtually no harm to the overall computational efficiency, as during the final assembly of matrices in PETSc, the routines `MatAssemblyBegin/End` will be called to release all unnecessary preallocated memories.

During a MPI parallel computation, a permutation of nodes is needed according to the PETSc convention described by the documentation of the routine `MatMPIAIJSetPreallocation`. It is achieved during initialization by a loop on all the processors based on the mesh partition performed by EPX. At the end two integer Fortran arrays are provided: `CONV_EP(I)` which gives the position of the  $i$ -th EPX node in the PETSc convention, while `CONV_PE` converts the PETSc node ordering to the EPX one.

**Time-stepping** The change to the EPX time iteration routines `calcul.ff` and `d_calcul.ff` is minimal. We simply add the following pseudo code concerning the assembly and the solving of the damage problem before the elastodynamics part.

```
...
IF (L_ENDOGRAD) THEN
  CALL SEQ/MPI_ASSEM_ALPHA(...)
  CALL RESO_ALPHA(...)
END IF
...
CALL CELEM(...)
...
```

We note that the routine `SEQ/MPI_ASSEM_ALPHA` constructs the Hessian matrix  $\mathbf{H}$  and the second member  $\mathbf{b}$  associated to the quadratic damage minimization problem by performing a first loop on all the elements. The copy and the correspondence between the global damage vector and the local damage vector specific to each element are conducted without modifying the arguments of all existing routines: `celem.ff`, `loopelm.ff`, `wpgen.ff` and all element routines `triang.ff` for example. The elementary variables associated with the current element  $\alpha^e$ ,  $\mathbf{H}^e$  and  $\mathbf{b}^e$  are all stored globally inside the module `m_endograd_data.ff`. They are preallocated during the initialization phase depending on the maximum local nodes. This current implementation is not thread-safe, thus OpenMP parallelization is not available.

**Element routines** At every time step, the following two loops on elements are needed:

1. Knowing the current configuration  $\mathbf{x}^n$  and  $\mathbf{u}^n$ , the routine `SEQ/MPI_ASSEM_ALPHA` opens a first loop on elements to calculate the elementary matrices  $\mathbf{H}^e$  and vectors  $\mathbf{b}^e$  for the damage problem (3.10). During this first loop, the current damage field is not yet known.
2. After energy minimization (3.10), the current damage is solved in `RESO_ALPHA`. We then open a loop for the second time in `CELEM` on all the elements to calculate the internal force vector  $\mathbf{F}_{\text{int}}^e$  which depends on the current damage state.

Since it is needed to perform two loops on elements at every time step, the element routines should be carefully restructured to minimize the computational cost. Some logical indicators are specially used and introduced to partition the code:

- `MATPRI(NTH) == 115` indicates if the current element is affected by a gradient damage material. If so, the following two logical indicators are then relevant.
- `L_FIRSTLOOP` encloses the lines that should be run during the calling of `SEQ/MPI_ASSEM_ALPHA`, *i.e.* in order to calculate the elementary matrices  $\mathbf{H}^e$  and vectors  $\mathbf{b}^e$  for the damage problem. In particular, the strain tensor will be calculated at this stage via `DSDX2D` or `DSDX3D`. The tension-compression asymmetry is also performed here to calculate  $\sigma_0^+$  and  $\sigma_0^-$ . The positive stress is stored temporarily in the `SIG` array while the negative stress in the `ECR` vector.
- `L_SECONDLLOOP` encloses the lines that should be run during the calling of `CELEM` where the stress tensor and the internal force vector  $\mathbf{F}_{\text{int}}^e$  will be calculated. In particular the stress tensor will be updated via (2.45)

**Improved method of calculating eigenvalues** For the tension-compression asymmetry model described in (Freddi & Royer-Carfagni, 2010; Miehe, Hofacker, & Welschinger, 2010), we need to perform the spectral decomposition of the strain tensor, see for example Algorithms 1 and 2. The `DSYEV` routine of LAPACK is purely numerical (iterative method) and consequently robust but slow. Here we use and implement an analytical method described in (Scherzinger & Dohrmann, 2008) that is both robust (in the presence of two or three identical or near eigenvalues) and computationally efficient. Consider the problem

$$\mathbf{A} \approx \mathbb{I} = \begin{bmatrix} 1 & & \\ & 1 + \frac{\epsilon}{4} & \frac{3\sqrt{\epsilon}}{4} \\ & \frac{3\sqrt{\epsilon}}{4} & 1 + \frac{3\epsilon}{4} \end{bmatrix}$$

with  $\epsilon = 1 \times 10^{-7}$ . Theoretical solution  $(d_i, \mathbf{v}_i)$  is given by

$$\begin{aligned} d_1 &= 1 + \epsilon, & d_2 &= d_3 = 1, \\ \mathbf{v}_1 &= (0, 1/2, \sqrt{3}/2), & \mathbf{v}_2 &= (-1, 0, 0) \quad \text{and} \quad \mathbf{v}_3 = (0, \sqrt{3}/2, -1/2). \end{aligned} \tag{3.16}$$

The analytical solution (3.16) is compared with the numerical ones given by `DSYEV` and the method described in (Scherzinger & Dohrmann, 2008):

- `DSYEV`: 15 significant figures for eigenvalues and eigenvectors, within 63.7 s for  $1 \times 10^8$  calculations.
- New method: 15 significant figures for eigenvalues and 10 for eigenvectors, within 23.5 s for  $1 \times 10^8$  calculations.

As can be seen, a factor of 2.7 in time is gained.

## Summary of this Chapter

In this chapter we describe a direct numerical implementation of the dynamic gradient damage model. It applies to both 1-d, 2-d and 3-d physical problems. Its efficiency will be demonstrated via simulation results in Chapter 4. The spatial discretization is based on classical  $C^0$  finite element method and is presented in Section 3.1. It is decoupled from the time-stepping scheme described in Section 3.2 for the  $\mathbf{u}$ -problem governed by the discrete elastic-damage dynamic wave equation (3.13). The explicit Newmark method will be used whenever inertial effects are dominant. Implicit methods parametrized by the  $\beta$ -parameter are applied for intermediate cases between explicit dynamic and quasi-static situations. Due to the same mathematical structure for the damage problem (bound-constrained convex

optimization problem), (3.10) is solved at the structural scale similarly to the quasi-static settings. The discrete numerical model is summarized in Algorithms 3 and 4.

The computational architecture is summarized in Section 3.3. The numerical solving of the damage problem is based on the numerical linear algebra library PETSc. It is introduced to the explicit dynamics software EPX for storage and manipulation of sparse matrices and vectors. The Gradient Projection Conjugate Gradient method is used to numerically solve (3.10).

# 4

## Simulation Results

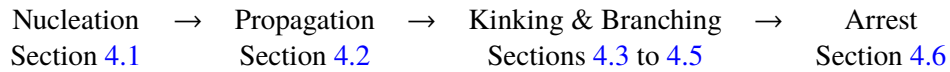
### Contents

<b>4.1 Crack Nucleation in a Bar Under Impact</b>	<b>80</b>
4.1.1 Analytical solutions for local strain-softening materials	81
4.1.2 Gradient-damage modeling	83
4.1.3 Numerical convergence properties	85
4.1.4 Energy dissipation at fracture	85
4.1.5 Size effect	89
4.1.6 Link with local strain-softening models	91
<b>4.2 Antiplane Tearing</b>	<b>93</b>
4.2.1 Link between damage and fracture in dynamics	95
4.2.2 Quasi-static limit of the dynamic model	100
<b>4.3 Plane Crack Kinking</b>	<b>107</b>
<b>4.4 Dynamic Crack Branching</b>	<b>111</b>
4.4.1 Computational efficiency in a parallel computing context	112
4.4.2 Comparison between two damage constitutive laws	113
4.4.3 Physical insights into the branching mechanism	116
<b>4.5 Edge-Cracked Plate Under Shearing Impact</b>	<b>122</b>
4.5.1 Gradient-damage modeling of dynamic fracture	125
4.5.2 Velocity effect and use of different tension-compression models	127
<b>4.6 Crack Arrest Due to the Presence of a Hole</b>	<b>130</b>
<b>4.7 Brazilian Splitting Test on Concrete Cylinders</b>	<b>132</b>
4.7.1 Fracture pattern predicted by different tension-compression models	135
4.7.2 Temporal evolution of global quantities and fields	136
4.7.3 Size effect	137
<b>4.8 Dynamic Fracture of L-Shaped Concrete Specimen</b>	<b>138</b>
4.8.1 Path prediction	139
4.8.2 Dynamical effects	142
<b>4.9 CEA Impact Test on Beams</b>	<b>144</b>

In this chapter the numerical discrete dynamic gradient damage model summarized in Algorithms 3 and 4 is applied to investigate numerous academic or real-world fracture problems. Since this part constitutes an essential part of the present work, the organization of these simulation results is described as follows:



- **Ordering:** the fracture problems considered in this chapter are ordered in terms of *computational complexity*. The FEniCS implementation is used first to analyze some academic problems under the small displacement hypothesis: the crack nucleation problem in a one-dimensional bar (Section 4.1), the 2-d scalar antiplane tearing problem (Section 4.2) and the 2-d plane crack kinking problem (Section 4.3). Afterwards, real-world dynamic fracture problems are considered in the EPX software environment: the 2-d plane crack branching problem (Section 4.4), the Kalthoff experiment (Section 4.5) and the crack arrest problem (Section 4.6). Application to concrete structures are considered at the end: the Brazilian test on concrete cylinders (Section 4.7), the dynamic fracture problem of a L-shaped concrete specimen (Section 4.8) and the CEA impact test on beams (Section 4.9). If one focuses on different phases of crack evolution, the following diagram can be obtained. Sections 4.7 to 4.9 constitute an application of the dynamic gradient damage model to real concrete structures and are not listed in the diagram.



- **Objectives:** using the classification given in Section 1.5, the scope of these simulations is to carry out an investigation of several damage constitutive laws and tension-compression asymmetry formulations (link with phase-field approaches represented by  $\alpha \leftrightarrow \phi$ ), to provide a better understanding of gradient-damage modeling of fracture  $\nabla\alpha \rightarrow \Gamma$ ) and to compare the simulation results with the experimental data (simulation validation). The precise objectives and the thematic subjects covered will be as usual recalled at the beginning of each section.

Contrary to previous chapters, a conclusion is provided at the end of each numerical simulation. According to the definition of the thematic subjects given in Section 1.5, these numerical simulations can be classified in Table 4.1.


Table 4.1 – Thematic subjects covered in the numerical simulations of this chapter

	$\alpha \leftrightarrow \phi$	$\nabla\alpha \rightarrow \Gamma$	Experimental validation
Numerics	Sections 4.4, 4.5 and 4.7	Sections 4.1 to 4.5, 4.7 and 4.8	Sections 4.4 to 4.9

## 4.1 Crack Nucleation in a Bar Under Impact

This section is devoted to a numerical analysis of a one-dimensional bar under impact loading conditions. The focus is on crack nucleation in dynamics using the gradient damage model. In the absence of an initial crack in the problem setting, the classical Griffith's theory of fracture is incapable of predicting material and structural failure. Hence here the simulation results will be compared to local strain-softening models (conventional damage models for instance). The objective is to illustrate the crack nucleation criterion in gradient damage models and the role played by the internal length in such process. The thematic subjects covered here are thus summarized in Table 4.2.

Table 4.2 – Thematic subjects covered in this section

	Going dynamical	$\alpha \leftrightarrow \phi$	$\nabla\alpha \rightarrow \Gamma$	Experimental validation
Theoretics				
Numerics				

### 4.1.1 Analytical solutions for local strain-softening materials

This problem is initially considered by (Bazant & Belytschko, 1985) for an elastic strain-softening material. The one-dimensional initially stationary bar occupying the interval  $[-L, L]$  is subject at both ends to a tensile shock  $\mathbf{U}_t = \pm v t \mathbf{e}_1$  where  $v$  measures the intensity, see Figure 4.1. Due to the jump condition, the strain waves propagate with an initial value of  $\varepsilon = v/c$  at the wave speed  $c = \sqrt{E/\rho}$ . At  $t = \frac{L}{c}$  when the two waves meet at the center, the strain at  $x = 0$  is doubled  $\varepsilon = 2v/c$  and continues to propagate to the rest part of the bar. We will only focus on the dynamic evolution in the time interval  $[0, \frac{2L}{c}]$  before the waves travel the whole length. In (Bazant & Belytschko, 1985), the material strain-softening condition is satisfied at a given critical strain level  $\varepsilon_c$ . If this criterion is never met, the analytical solution corresponds to a purely elastodynamic problem, which is given by

$$u = -v \left\langle t - \frac{x+L}{c} \right\rangle + v \left\langle t + \frac{x-L}{c} \right\rangle,$$

$$\varepsilon = \frac{v}{c} H \left( t - \frac{x+L}{c} \right) + \frac{v}{c} H \left( t + \frac{x-L}{c} \right),$$

where  $\langle x \rangle = (|x| + x)/2$  and  $H$  denotes the Heaviside step function. The strain field evolution is illustrated in Figure 4.1(a). Otherwise, two cases could be separately discussed concerning the intensity of the impact velocity  $v$  and the strain-softening criterion  $\varepsilon_c$ :

1. If  $v$  is sufficiently high such that at  $t = 0$  the strain-softening criterion is met, *i.e.*  $\frac{v}{c} > \varepsilon_c$ , then fracture takes place immediately at  $t = 0$  when the impact is applied. The impacted ends  $x = \pm L$  are broken and the rest part of the bar remains stationary.
2. If the strain-softening criterion  $\varepsilon_c$  is satisfied when the two tensile waves arrive at the center at  $t = \frac{L}{c}$ , *i.e.*  $\frac{2v}{c} > \varepsilon_c$  but  $\frac{v}{c} < \varepsilon_c$ , then according to (Bazant & Belytschko, 1985), the analytical solution becomes

$$u = -v \left\langle t - \frac{x+L}{c} \right\rangle - v \left\langle t - \frac{L-x}{c} \right\rangle,$$

$$\varepsilon = \frac{v}{c} H \left( t - \frac{x+L}{c} \right) - \frac{v}{c} H \left( t - \frac{L-x}{c} \right) + 4v \left\langle t - \frac{L}{c} \right\rangle \delta_0, \quad (4.1)$$

which is applicable for  $x \leq 0$ . For  $x > 0$  a symmetric solution applies. The strain field before and after the wave-crossing is illustrated in Figure 4.1(b). At  $t = \frac{L}{c}$  the bar breaks instantaneously at the center. For  $t \geq \frac{L}{c}$ , the displacement develops at the center a discontinuity of magnitude  $4v \left\langle t - \frac{L}{c} \right\rangle$ . Hence a Dirac distribution is present in the strain field expression.

Several remarks can be given concerning the physical deficiencies of local strain-softening models in this particular dynamic problem:

- The ultimate fracture takes place instantaneously when the strain-softening criterion is satisfied. The structural failure mechanism is size-independent.
- Fracture takes place instantaneously with a vanishing energy dissipation, consequently spurious mesh dependency is observed for finite element solutions, see our discussions on this point in Section 1.4.2. It can be observed that (4.1) corresponds to the elastodynamic solution of the bar initially broken at  $x = 0$ , which implies total mechanical energy conservation and no additional energy dissipation when fracture happens at  $t = \frac{L}{c}$ .

As we shall see in the sequel, the gradient-damage approach of fracture permits a better modeling of crack nucleation, via the introduction of a length scale.



Figure 4.1 – Strain field before and after the wave crossing at  $t = \frac{L}{c}$  for (a) the elastodynamic model (or if the strain-softening criterion  $\varepsilon_c$  is never met) and (b) the local strain-softening model if  $\varepsilon_c$  is met at  $t = \frac{L}{c}$

### 4.1.2 Gradient-damage modeling

The dynamic gradient damage model outlined in Definition 2.1 is applied for this particular one-dimensional problem. Symmetry is taken into account and only the interval  $\Omega = [0, L]$  is modeled. The displacement at  $x = 0$  is blocked due to symmetry. The explicit time-stepping described by Algorithm 4 is used in the FEniCS implementation, see (Li, 2015).

The Lagrangian involved in the generalized space-time action integral (2.16) reads

$$\mathcal{L}(u_t, \dot{u}_t, \alpha_t) = \int_{\Omega} \left( \frac{1}{2} a(\alpha_t) E u_t'^2 + w(\alpha_t) + w_1 \eta^2 \alpha_t'^2 - \frac{1}{2} \rho \dot{u}_t^2 \right) dx.$$

A rescaling of the displacement by  $u_c$  and a normalization of the space/time scales is performed to obtain a non-dimensional problem. Specifically, displacement is scaled by a factor of  $u_c = \sigma_c L / E$  where  $\sigma_c$  corresponds to the critical stress of the gradient damage material, see (2.6), and  $u_c$  is thus the critical displacement at the end  $x = L$  of a bar fixed at  $x = 0$  in the quasi-static condition. The half-bar length  $L$  and the corresponding time  $L/c$  for the elastic wave to travel such distance is used to normalize the spatial and temporal scales. We have thus

$$\begin{aligned} u(x, t) &= u_c \hat{u} \left( \frac{x}{L}, \frac{ct}{L} \right) = u_c \hat{u}(y, \tau), \\ \alpha(x) &= \hat{\alpha} \left( \frac{x}{L} \right) = \hat{\alpha}(y), \end{aligned} \quad (4.2)$$

where  $y$  and  $\tau$  designate respectively the normalized space and time coordinates.

In this work the damage constitutive law (PAMM) is used. According to Section 2.1.1, the critical stress is then given by  $\sigma_c = \sqrt{w_1 E}$ , which leads to the following non-dimensional Lagrangian

$$\hat{\mathcal{L}}(\hat{u}_\tau, \dot{\hat{u}}_\tau, \hat{\alpha}_\tau) = w_1 L \int_0^1 \left( \frac{1}{2} (1 - \hat{\alpha}_\tau)^2 \hat{u}_\tau'^2 + \hat{\alpha}_\tau + \hat{\eta}^2 \hat{\alpha}_\tau'^2 - \frac{1}{2} \dot{\hat{u}}_\tau^2 \right) dy. \quad (4.3)$$

For a given finite  $\eta$ , the length scale  $\hat{\eta} = \eta / L$  is the only non-dimensional parameter influencing the qualitative behaviors of the problem. Numerically, this amounts to solve the evolution problem in the normalized interval  $[0, 1]$  with the parameters indicated in Table 4.3. The relationship (2.9) between  $w_1$  and  $G_c$  is also used.

Table 4.3 – Geometric and material parameters for the crack nucleation problem

$L$	$\rho$	$E$	$G_c$	$\sigma_c$
1	1	1	$\frac{8}{3}\eta$	1

Using the normalized space and time scales, we assume that at  $y = 1$  the bar is subject to the impact condition  $\hat{\mathbf{U}}_\tau = \hat{v}_\tau \mathbf{e}_1$ . The time interval of interest is  $\tau \in [0, 2]$ . Using the definition of the critical stress (2.6), after normalization, the damage initiation criterion (2.26) for an initially sound body (with  $\hat{\alpha}_\tau = 0$  almost everywhere) reads hence

$$\hat{u}_\tau'^2 = 1. \quad (4.4)$$

This implies that damage could takes place wherever (4.4) is satisfied. Tension-compression asymmetry (2.38) is not considered here. Using the jump condition, we have thus

- If  $\hat{v} > 1$ , then the damage criterion is instantaneously met at  $y = 1$  and subsequent crack nucleation could take place soon.
- If  $0.5 < \hat{v} < 1$ , then the damage criterion is satisfied at  $\tau = 1$  when the two waves arrive at the center. A typical strain and damage evolution obtained with the dynamic gradient damage model is indicated in Figure 4.2. Strain localization takes place and damage evolves at the center, which resembles the result obtained with the local strain-softening model in Figure 4.1.



Figure 4.2 – Strain (a) and damage (b) before and after the wave crossing at  $t = \frac{L}{c}$  in the dynamic gradient damage model with  $\widehat{\eta} = 0.01$

### 4.1.3 Numerical convergence properties

We first analyze the numerical convergence properties of dynamic gradient damage models given a fixed length ratio  $\eta/L$ . With a uniform linear finite element interpolation with typical mesh size  $h$  and the explicit Newmark scheme (along with mass lumping) with a time increment corresponding to the CFL time step  $\Delta\tau = \Delta\tau_{\text{CFL}} = h$  (since the wave speed is normalized to 1), it is known that the displacement  $u_h$  at time  $\tau \in [0, 2]$  for an elastodynamic problem (without damage or strain-softening) converges with order  $O(h^2)$  in the  $L^2$  norm for the error defined by

$$e_h = \frac{\|u_h - u_{\text{ref}}\|_{L_2}}{\|u_{\text{ref}}\|_{L_2}} = \frac{\sqrt{\int_{\Omega} (u_h - u_{\text{ref}})^2 dx}}{\sqrt{\int_{\Omega} u_{\text{ref}}^2 dx}}. \quad (4.5)$$

Furthermore, superconvergence can be observed for this particular one-dimensional problem with the above numerical parameters, see (Hughes, 1987). In this case the obtained results are exact (with respect to the original time-space continuous problem) at discretization nodes independently of how few elements are used. The convergence rate as well as this property can be illustrated numerically by considering an elastic bar subject to  $\widehat{\mathbf{U}}_{\tau} = \frac{1}{2}(1 - \cos(\pi\tau)) \mathbf{e}_1$  at  $y = 1$ . A snapshot of the dynamic system state at  $\tau = 1$  is taken. In (4.5),  $u_{\text{ref}}$  is taken to be a reference solution obtained with  $h = 1 \times 10^{-3}$ . From Figure 4.3, the quadratic convergence as well as the superconvergence property is verified. If a velocity shock is applied here, since the analytical solution is piecewise linear, the finite element solution would coincide exactly with the theoretic one.

In the dynamic gradient damage model, numerical convergence is studied for the displacement and the damage at  $\tau = 2$ , with an impact speed  $\widehat{v} = 0.6$  and two length scales  $\widehat{\eta} = 0.1$  or  $0.2$ . The results are indicated in Figures 4.4 and 4.5. The reference solution is obtained with  $h = \widehat{\eta}/100$ . Several remarks are given as follows.

- The superconvergence property is lost, since it can be observed that solutions with different discretization sizes no longer agree with each other exactly at the nodes.
- The quadratic convergence rate for the displacement and the damage may degenerate according to the value of the length scale  $\widehat{\eta}$ . As  $\widehat{\eta} \rightarrow 0$  (see Figure 4.4), strain is more localized near  $y = 0$ , which may lead to a lower convergence rate. In any case, convergence is ensured. We assume that  $h = \widehat{\eta}/10$  gives sufficiently accurate results and hence will be used in all subsequent calculations.

### 4.1.4 Energy dissipation at fracture

Consider the case when the damage criterion (4.4) will be first satisfied at  $\tau = 1$  when the two tensile waves encounter at the center. Fracture in gradient damage models is defined as the event when/where  $\widehat{a}_t(y) \approx 1$  somewhere in the bar. Numerically the value of 0.99 is used as the threshold. For the shock velocity  $\widehat{v} = 0.6$  and the length scale  $\widehat{\eta} = 0.1$ , the final damage field at fracture is illustrated in Figure 4.6. The analytical quasi-static optimal damage field (2.7) is also indicated. Recall that the optimal damage field (2.27) corresponds to the equivalent fracture toughness (2.9). Since here the damage band obtained is wider than the optimal one, more energy is dissipated than the  $G_c$  defined via (2.9).

This overdissipation is analyzed for different length scales and shock velocities, see Figure 4.7. The energy dissipated at fracture is normalized by the quasi-static fracture toughness defined via (2.9). We observe that the overdissipation of approximately 30% seems to be independent of the length ratio  $\eta/L$  and shows little dependence on the shock velocity. In any case, with a gradient damage modeling of fracture, fracture takes place always with a non-vanishing energy dissipation. Future work will be devoted to a better understanding of this over-dissipation.

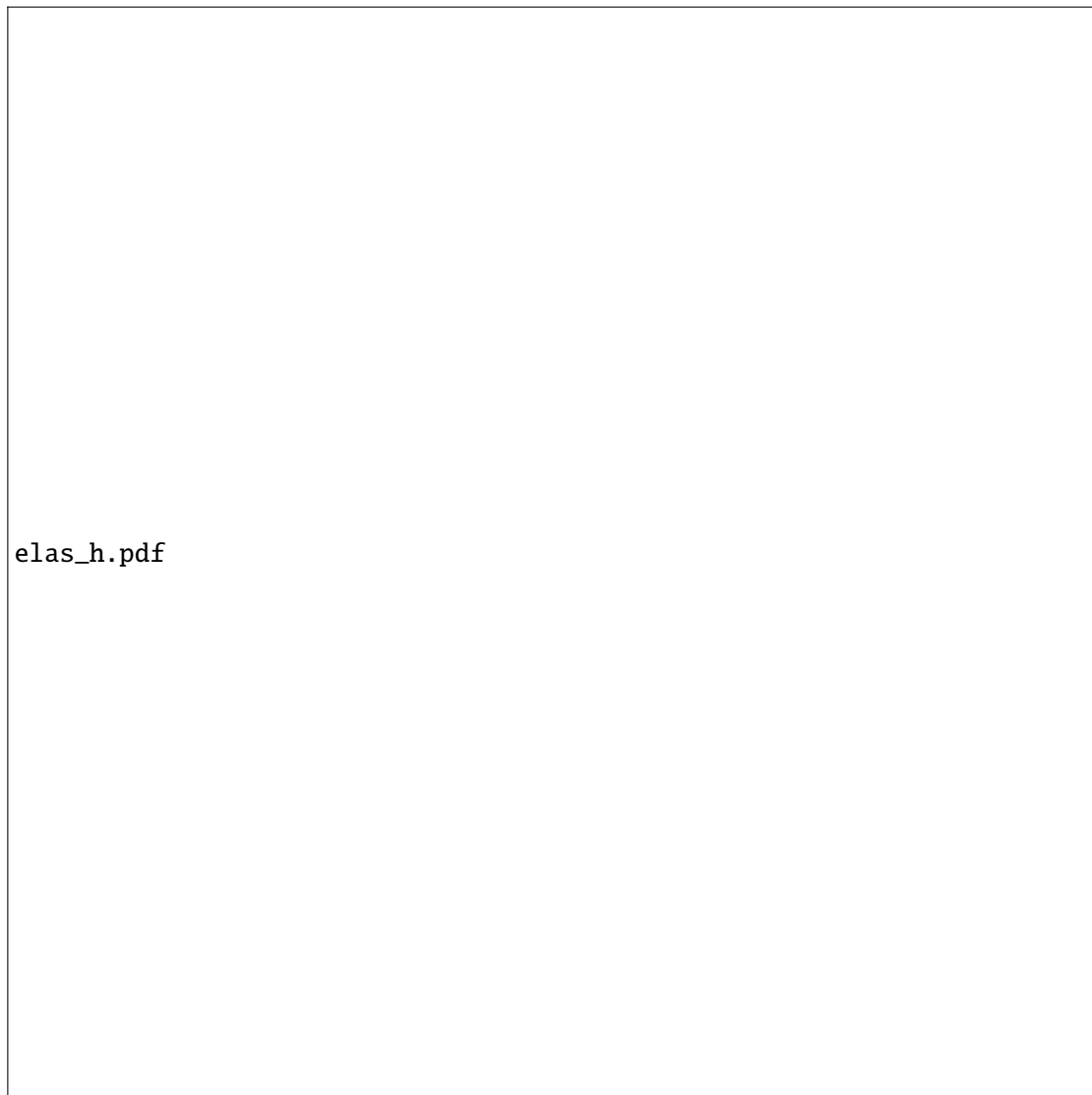


Figure 4.3 – Numerical convergence for the elastodynamic problem



Figure 4.4 – Numerical convergence study for  $\hat{\eta} = 0.1$ : (a) displacement at  $\tau = 2$  and (b) convergence rates



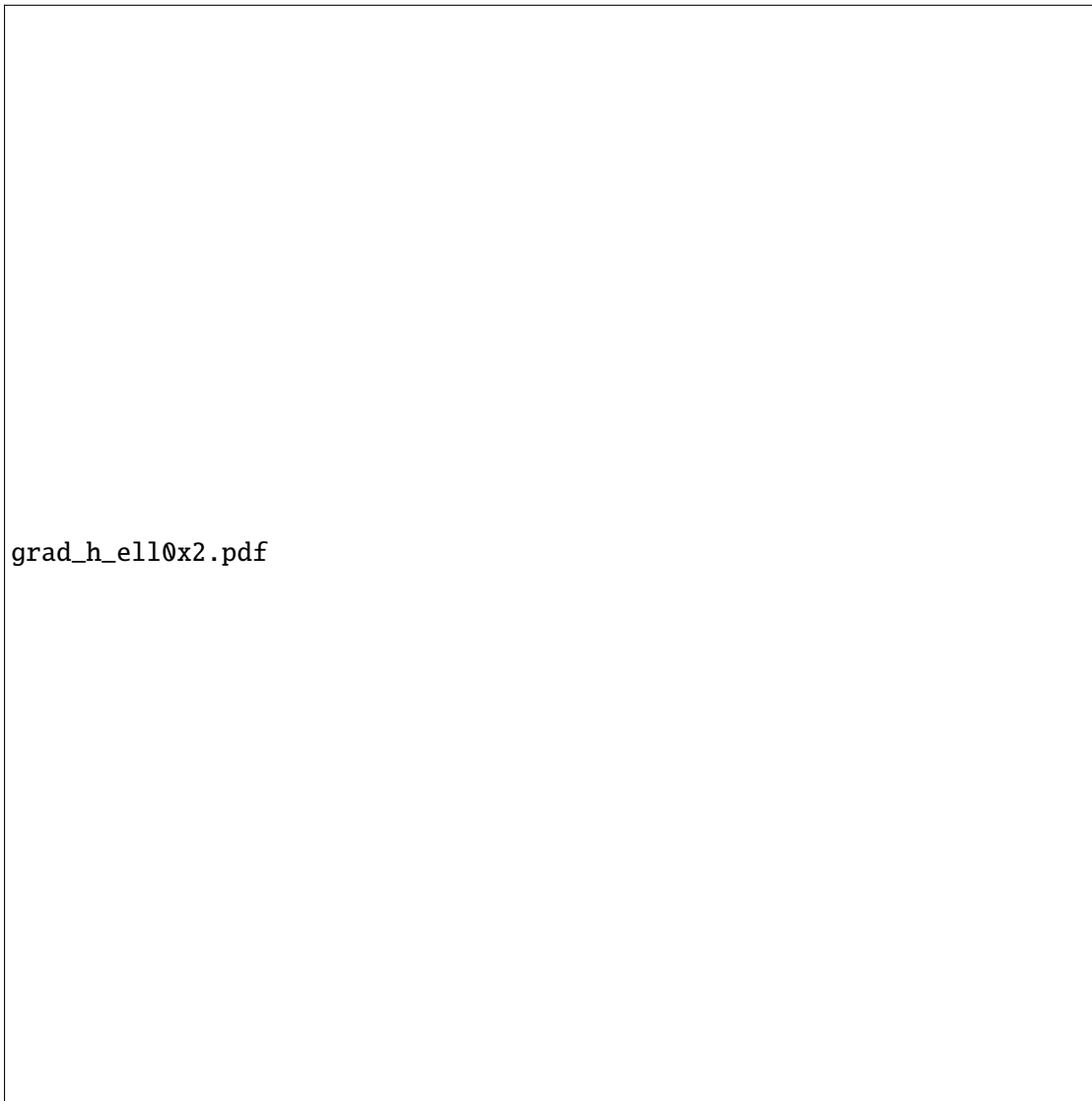


Figure 4.5 – Numerical convergence study for  $\hat{\eta} = 0.2$ : (a) displacement at  $\tau = 2$  and (b) convergence rates

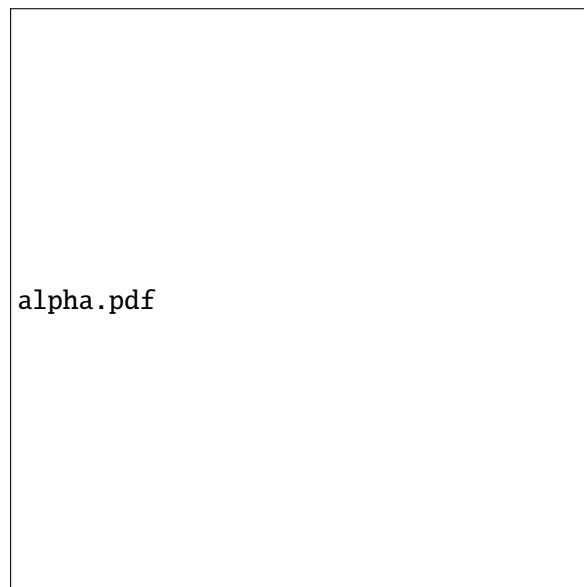


Figure 4.6 – Damage field at fracture with  $\hat{v} = 0.6$  and  $\hat{\eta} = 0.1$

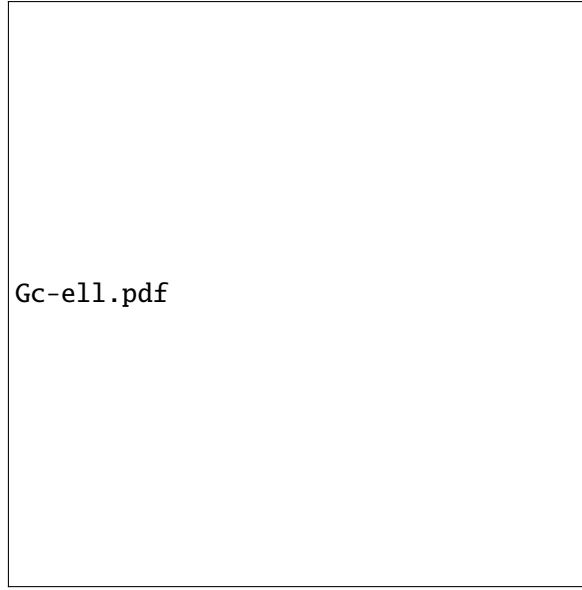
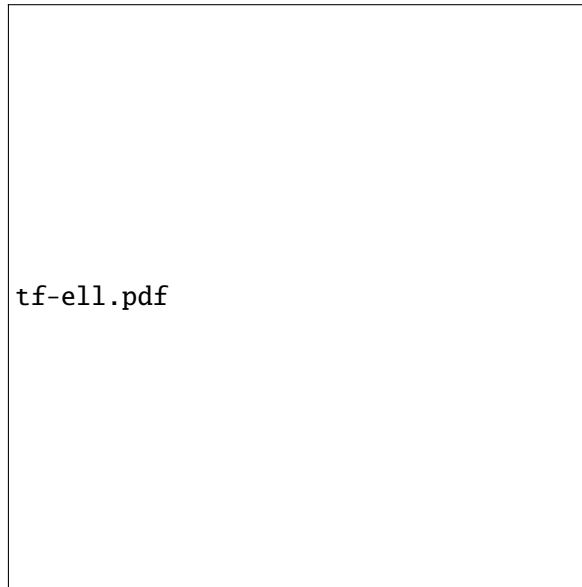


Figure 4.7 – Dissipated energy when the bar breaks

#### 4.1.5 Size effect

Recall that in local strain-softening models the instant of fracture coincides with the instant when the strain-softening mechanism is satisfied. This implies that the structural failure is size-independent. Consider first the case when fracture takes place at  $\tau = 1$  in local models, *i.e.* for  $\widehat{v} \in (0.5, 1)$ . The instant of fracture  $\tau_f$  for different length scales  $\eta/L$  is illustrated in Figure 4.8, where the result  $\tau_f = 1$  for local models is also indicated. Several remarks are given as follows.

Figure 4.8 – Size effect illustrated by the instant of fracture for different length scales for  $\widehat{v} \in (0.5, 1)$ 

- With dynamic gradient damage models, the instant of fracture normalized by the factor  $\frac{L}{c}$  depends on the length scale  $\eta/L$ , which illustrates a size effect. In local strain-softening models fracture takes place always at  $t = \frac{L}{c}$ , or  $\tau = 1$ .
- At fixed internal length  $\eta$  (material property), shorter bars delay ultimate fracture (*smaller is stronger*), while for longer bars the fracture behavior is similar to that predicted by the local

model. Comparison between these two models can be analyzed in the limit  $\eta/L \rightarrow 0$ . It will be performed in the next section.

- Contrary to quasi-static situations, this size effect depends also on the shock velocity. For higher velocities  $\hat{v} \approx 1^-$ , the fracture instant approaches that of the local strain-softening model. The reverse is observed for lower shock speeds for  $\hat{v} \approx 0.5^+$ .

For higher shock speeds  $\hat{v} > 1$ , fracture will take place immediately at  $\tau = 0$  for local models independently of the size of the bar. For gradient damage models, another size effect diagram is observed, see Figure 4.9(a). It can be seen that longer bars behave exactly like the local strain-softening models, *i.e.*  $\tau_f \rightarrow 0$ . Again, fracture can be delayed for shorter bars. For small length ratios  $\eta/L$ , the instant of fracture  $\tau_f$  scales linearly with  $\eta/L$ . With  $\eta/L = 0.01$ , the dependence of the instant of fracture on the shock velocity is analyzed in Figure 4.9(b). According to these two diagrams in Figure 4.9, we have the following estimation for small length scales  $\eta/L \ll 1$  and large shock velocities  $\hat{v} \gg 1$

$$\tau_f \propto \hat{\eta} \cdot \hat{v}^{-1.75}.$$

tf-ell2v.pdf

Figure 4.9 – (a) Size effect illustrated by the instant of fracture for different length scales  $\hat{v} > 1$ . (b) Dependence of the instant of fracture on the shock velocity with  $\eta/L = 0.01$

Using the definition of the rescaled time  $\tau$ , the linear scaling of the rescaled instant of fracture with respect to the length scale  $\tau_f \propto \widehat{\eta}$  leads to

$$t_f \propto \frac{\eta}{c}. \quad (4.6)$$

It can be seen that here the value of the internal length determines the actual structural failure instant and should be considered as a material parameter. Future work will be devoted to a theoretic understanding of (4.6).

#### 4.1.6 Link with local strain-softening models

As indicated by Figures 4.8 and 4.9, the fracture behaviors of longer bars are similar to that predicted by the local strain-softening model. At  $\tau = 0.6$ , the asymptotic behavior of the rescaled displacement when  $\eta/L \rightarrow 0$  is indicated in Figure 4.10 for two shock velocities. The solution due to the local strain-softening model is also indicated.

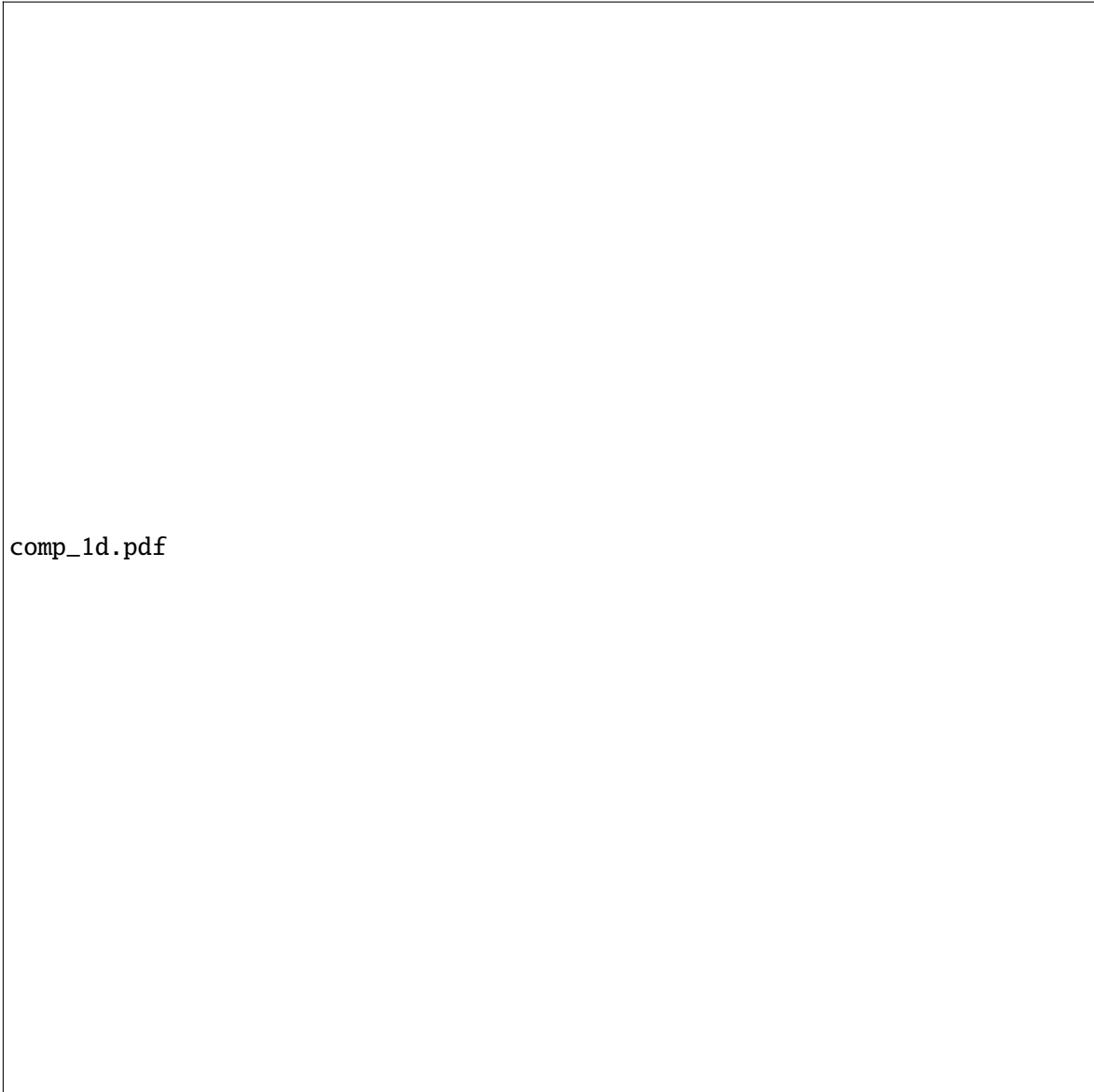


Figure 4.10 – Asymptotic behavior of the rescaled displacement when  $\eta/L \rightarrow 0$  compared with the local strain-softening model: (a)  $\widehat{v} = 0.6$  and (b)  $\widehat{v} = 0.9$

A slow convergence can be observed in the  $L^2$ -norm of the normalized displacement, see Figure 4.11. The convergence rate shows dependence on the shock velocity. In the limit  $\ell/L \rightarrow 0$ , the normalized displacement  $\widehat{u}$  thus converges to that predicted by the local strain-softening model.

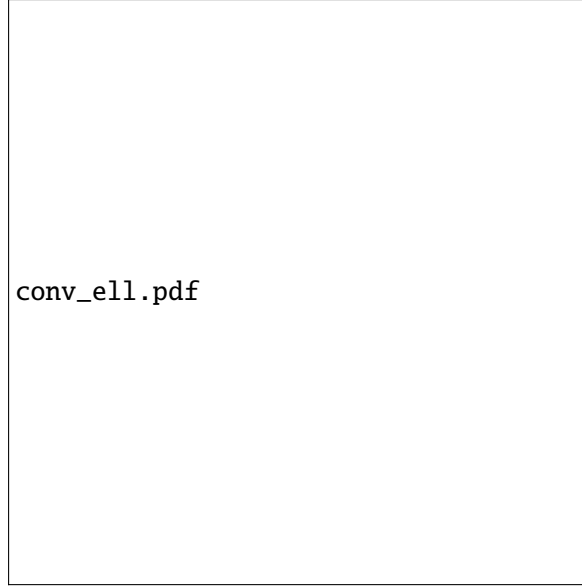


Figure 4.11 – Convergence rate for the rescaled displacement when  $\eta/L \rightarrow 0$

However note that this convergence toward the local strain-softening model can never be attained and should only be considered as a limiting behavior of dynamic gradient damage models, see also the discussion between the variational approach to fracture and gradient damage approaches in Section 1.4.2. Several remarks are given as follows.

- The above convergence is established for the normalized displacement. Using the definition (4.2), for  $\widehat{v} \in (0.5, 1)$  the real displacement tends to develop a sharp discontinuity at  $x = 0$  with a jump of magnitude

$$\llbracket u_t(0) \rrbracket = 4v u_c \left\langle t - \frac{L}{c} \right\rangle = 4v \sqrt{\frac{3G_c}{8E\eta}} L \left\langle t - \frac{L}{c} \right\rangle.$$

- For very long bars  $L \rightarrow \infty$ , the two tensile waves can never arrive at the center and for  $\widehat{v} \in (0.5, 1)$  fracture will never take place, since  $\llbracket u_t(0) \rrbracket \rightarrow 0$  when  $L \rightarrow \infty$ .
- Very small internal lengths  $\ell \rightarrow 0$  imply an infinite critical stress  $\sigma_c \rightarrow \infty$  through (2.6), hence again fracture can never take place. Instead  $\ell$  should be considered as a material parameter, see Section 1.4.2.

## Conclusion

As is demonstrated by numerical simulations, a gradient-damage approach of dynamic fracture leads to a better modeling of crack nucleation in the following aspects:

- In the Griffith's theory crack nucleation is not possible for an initially sound body. In the gradient damage model (with a fixed internal length  $\ell$ ), crack can nucleate and the damage initiation criterion is given by (4.4).
- The internal length  $\ell$  influences numerical convergence properties and needs further investigation concerning in particular the convergence rates.
- In gradient damage models, fracture takes place with a finite non-vanishing energy dissipation while in local strain-softening models it is not the case. In dynamics a systematic over-dissipation is observed for all internal lengths and needs further investigation.

- In local strain-softening models the fracture mechanism is size-independent. In gradient damage models the length ratio  $\ell/L$  achieves a size effect in terms of the fracture instant. The general belief *smaller is stronger* is verified.
- A certain link between gradient damage models and local strain-softening models is found by investigating the limit  $\ell/L \rightarrow 0$ . In such process, the fracture behavior of gradient damage models is qualitatively similar to that of local models, if the normalized displacement (4.2) is considered.

## 4.2 Antiplane Tearing

In Section 4.1 the crack *nucleation* is considered and a stress-based criterion (2.26') governs the damage initiation. This section discusses a particular numerical experiment tailored to highlight the properties of the dynamic gradient damage model while focusing on the *initiation* and *propagation* phases of defect evolution. Specifically, we will investigate the fracture mechanics criterion for an existing phase-field crack to *initiate*, and then to *propagate* along a certain path. This experiment constitutes a numerical verification of the generalized Griffith criterion given in Proposition 2.7 and its asymptotic interpretation outlined in Proposition 2.11. Recall that these properties can also be considered as a dynamic extension of the theoretic results established in (Sicsic & Marigo, 2013) for quasi-static gradient damage models. Another objective is to investigate the quasi-static limit of the dynamic model summarized in Definition 2.1. The thematic subjects covered here are thus summarized in Table 4.4.

Table 4.4 – Thematic subjects covered in this section

	Going dynamical	$\alpha \leftrightarrow \phi$	$\nabla \alpha \rightarrow \Gamma$	Experimental validation
Theoretics				
Numerics	👍		👍	

**Problem setting** We consider a mode-III antiplane tearing of a two dimensional plate  $\Omega = [0, L] \times [-H, H]$  subject to a hard device  $\mathbf{U}_t = \text{sgn}(y)kt \mathbf{e}_3$  on its left border  $x = 0$ , see Figure 4.12. An

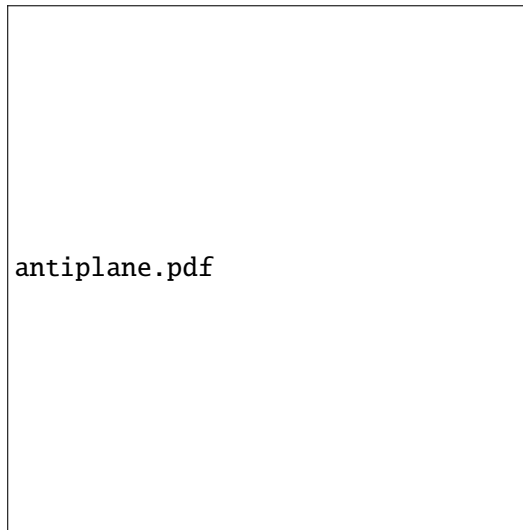


Figure 4.12 – Mode III antiplane tearing of a two dimensional plate  $\Omega = [0, L] \times [-H, H]$  with a loading speed parametrized by  $k$ . An initial crack  $[0, l_0] \times \{0\}$  is present in the domain. The crack is enforced to propagate along the constant direction  $\mathbf{e}_1$

initial damage field corresponding to a preexisting crack  $\Gamma_0 = \{ \mathbf{x} \in \mathbb{R}^2 \mid \alpha_0(\mathbf{x}) = 1 \} = [0, l_0] \times \{ 0 \}$  is present in the domain. For that we prescribe naturally  $\underline{\alpha}^{-1} = 1$  on  $\Gamma_0$  using Algorithm 5. The loading velocity  $k$  will be varied and its effect on the crack propagation speed will be studied. With a modification of the damage dependence of the elastic energy  $\mathcal{E}(\mathbf{u}_t, \alpha_t)$  proposed in (Bourdin et al., 2011), the crack tip  $t \mapsto \mathbf{P}_t$  is enforced to propagate along the constant direction  $\mathbf{e}_1$ , which prohibits consequently crack kinking or branching. Denoting  $u$  as the out-of-plane displacement, the elastic energy density (2.1) in this particular situation reads

$$\psi(\nabla u_t, \alpha_t) = \frac{1}{2} \mu \left( a(\alpha_t) \left( \frac{\partial u_t}{\partial x_2} \right)^2 + \left( \frac{\partial u_t}{\partial x_1} \right)^2 \right), \quad (4.7)$$

where damage acts only on the  $\partial_2 u$  component of the displacement gradient. We assume that this modification (4.7) can be regarded as a particular case of the original model (2.1) when the crack actually propagates along a specific path without kinking or branching. It allows us to focus on the crack propagation stage.

*Remark.* If the original model is used, *i.e.* when the degradation function also acts on  $\frac{\partial u_t}{\partial x_1}$ , numerically it is observed that for low propagation speeds crack curving (including kinking and branching) does not take place and the modification (4.7) produces the same response as the original model. However for higher propagation speeds (for example due to a larger loading velocity  $k$ ), crack curving is observed (see for example (Bourdin et al., 2011)) and these two models no longer predict the same crack evolution. Crack path prediction is exactly the *raison d'être* of phase-field models of fracture. An investigation of crack kinking/branching phenomena is a very important task and will be separately considered in Section 4.3 and Section 4.4. Nevertheless, the current contribution focuses on the behavior of gradient damage models when these dynamic instabilities (kinking, branching) are somehow suppressed (see for example (Livne, Ben-David, & Fineberg, 2007) for an experimental investigation on this point), which permits a direct comparison with the classical Griffith's theory of dynamic fracture.

This problem is initially raised in (Bourdin et al., 2011). In their model the crack surface energy is approximated by the Ambrosio and Tortorelli elliptic regularization (the (AT) model), whereas here the damage constitutive law (PAMM) is used. The objective is to compare the crack evolution obtained in the dynamic gradient damage model with that predicted by Griffith's law which determines initiation and propagation of cracks. Two experiments will be considered:

1. In the first case, the fracture toughness  $G_c$  is assumed to be homogeneous throughout the domain. The loading speed is of the same order of the material sound speed  $c = \sqrt{\mu/\rho}$  and we will use the explicit Newmark time-stepping method, *i.e.* Algorithm 4.
2. In the second case,  $G_c$  may admit a spatial discontinuity in the propagation direction. We also prescribe a relatively small loading speed in order to investigate the quasi-static limit of the dynamic model. Depending on whether the crack propagation speed itself is smaller with respect to the sound speed or not (the term *unstable* propagation often refers to this case), the implicit (Algorithm 3) or the explicit Newmark method will be used.

A rescaling of the displacement and a normalization of the space/time scales are performed to obtain a non-dimensional problem. Specifically, a reference elastic constant  $\bar{\mu}$ , material density  $\bar{\rho}$  and fracture toughness  $\bar{G}_c$  have been chosen and the displacement is scaled by a factor of

$$\bar{u} = \sqrt{\bar{G}_c H / \bar{\mu}}.$$

The height of the plate  $H$  and the corresponding time  $H/\bar{c}$  for the reference elastic wave (with speed  $\bar{c} = \sqrt{\bar{\mu}/\bar{\rho}}$ ) to travel such distance is used to normalize the spatial and temporal scales. We have thus

$$\begin{aligned} \mathbf{u}(\mathbf{x}, t) &= \bar{u} \hat{u} \left( \frac{\mathbf{x}}{H}, \frac{\bar{c}t}{H} \right) \mathbf{e}_3, \\ \alpha(\mathbf{x}, t) &= \hat{\alpha} \left( \frac{\mathbf{x}}{H}, \frac{\bar{c}t}{H} \right). \end{aligned}$$

Rewriting Lagrangian defined in (A.3) using  $\widehat{u}$  and  $\widehat{\alpha}$  amounts to adopt the following non-dimensional quantities

$$\widehat{\rho} = \frac{\rho}{\rho}, \quad \widehat{\mu} = \frac{\mu}{\mu}, \quad \widehat{G_c} = \frac{G_c}{G_c} \quad \text{and} \quad \widehat{\ell} = \frac{\ell}{H}.$$

For notational simplicity, we drop the bar and use directly non-dimensional quantities in the sequel.

A structured crossed triangular mesh with a uniform discretization spacing  $\Delta x = \Delta y = h$  is generated. For the explicit time-stepping method, the Courant–Friedrichs–Lewy (CFL) time-step is used

$$\Delta t_{\text{CFL}} = \frac{h}{c} = \frac{h}{\sqrt{\mu/\rho}}. \quad (4.8)$$

The parameters adopted for all subsequent calculations are summarized in Table 4.5. A typical damage

Table 4.5 – Geometric, material and numerical parameters for the antiplane tearing experiment

$L$	$H$	$l_0$	$\mu$	$\rho$	$G_c$	$\eta$	$h$	$\Delta t$
5	1	1	0.2	1	0.01	0.05	0.01	$\Delta t_{\text{CFL}}$

field obtained in this simulation is illustrated in Figure 4.13, where the damage varies from 0 (blue zones) to 1 (red zones). Thanks to the  $\Gamma$ -convergence result summarized in Sections 1.3 and 1.4, the current crack length  $l_t$  could be approximately derived from the damage dissipation energy using the estimation (1.20). For the (PAMM) model, the coefficient  $c$  in (1.21) reads  $c = 3/8$  (see (Hossain et al., 2014)), hence the following effective fracture toughness is used

$$(G_c)_{\text{eff}} = \left(1 + \frac{3h}{8\eta}\right) G_c.$$

However (1.20) does not immediately apply to the case where  $G_c$  admits a spatial discontinuity. For consistency, the current crack tip  $\mathbf{P}_t = (l_t, 0)$  is located on the contour  $\alpha = 0.5$ . The crack speed can thus be obtained by a linear regression analysis during the steady propagation phase.

#### 4.2.1 Link between damage and fracture in dynamics

**Comparison with the Griffith's theory of dynamic fracture** In the first case a homogeneous plate will be considered. This antiplane tearing example is physically similar to the 1-d film peeling problem which can be studied using the classical Griffith's theory of dynamic fracture. According to (Dumouchel, Marigo, & Charlotte, 2008) and (Bourdin et al., 2008), the crack speed, with respect to the loading displacement  $U = kt$  or to the physical time  $t$ , as a function of the loading velocity  $k$ , is given by

$$\frac{dl}{dU}(k) = \sqrt{\frac{\mu H}{G_c + \rho H k^2}} \quad \text{or} \quad \frac{dl}{dt}(k) = \sqrt{\frac{\mu H k^2}{G_c + \rho H k^2}} \quad (4.9)$$

from which we retrieve the quasi-static limit  $dl/dU(0) = \sqrt{\mu H/G_c}$  predicted in (Bourdin et al., 2008) and the dynamic limit as the shear wave speed  $dl/dt(\infty) = \sqrt{\mu/\rho}$ , which is a classical result of the Griffith's theory of dynamic fracture, see Section 1.2. We also observe that for low loading speeds  $k \approx 0$ , the dynamic crack speed  $dl/dt \approx k \sqrt{\mu H/G_c}$  scales linearly in  $k$ , which agrees with the remark given in (Bourdin et al., 2011). Comparisons between the numerical results using the dynamic gradient model and this theoretic result (4.9) with  $G_c$  replaced by  $(G_c)_{\text{eff}}$  are illustrated in Figure 4.14. Despite the transverse wave reflection present in the two-dimensional numerical model, a very good quantitative agreement is found between them. In particular, as it is also observed in (Bourdin et al., 2011), the numerically obtained crack speed indeed approaches the limiting shear wave speed when the loading speed increases. The explicit time-stepping described in Algorithm 4 as well as its FEniCS implementation work fine even at supersonic loading speeds.



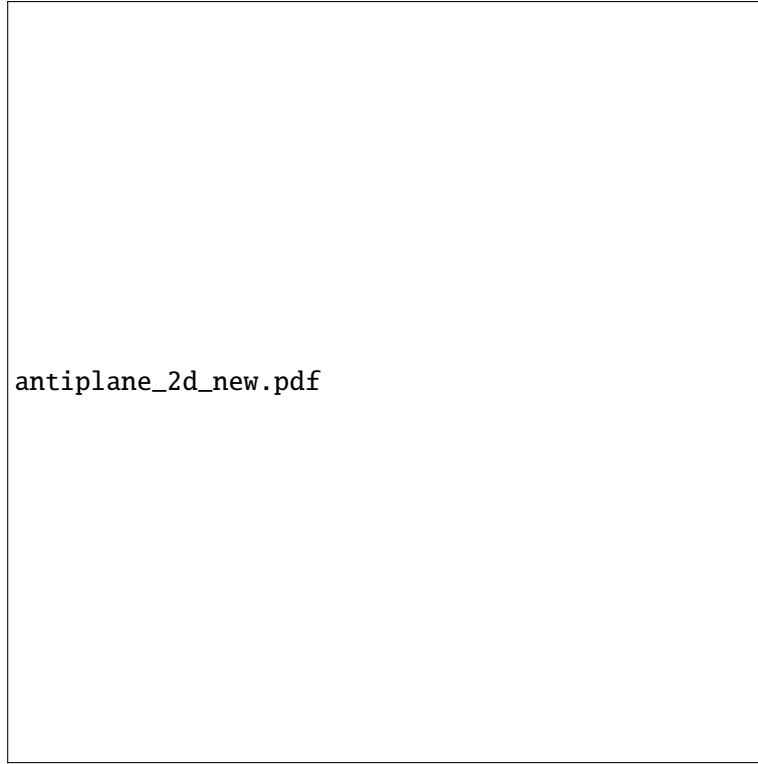


Figure 4.13 – Typical damage field obtained in the antiplane tearing example. The damage varies from 0 (blue zones) to 1 (red zones)

**Verification of Griffith's law** Next we investigate how exactly the crack propagates in the dynamic gradient damage model, *i.e.* provide a fracture mechanics interpretation of the three physical principles given in Definition 2.1. We propose hence to verify the generalized Griffith criterion (Proposition 2.7) and the asymptotic interpretation (Proposition 2.11), by comparing the conventional dynamic energy release rate  $G_t^\alpha$  and the damage dissipation rate  $\gamma_t$ . Written in the form of (2.69),  $G_t^\alpha$  involves an integral in the cells and hence is more convenient and accurate compared to a path integral ( $J$ -integral for instance) in a finite element calculation. The use of traditional  $J$ -integrals in a gradient damage or phase-field modeling of fracture can be found in (Hossain et al., 2014; Klinsmann et al., 2015) for instance.

A widely used definition of the virtual perturbation (Destuynder, Djaoua, & Lescure, 1983) is recalled as follows. Suppose that the crack  $\Gamma_t$  lies on the  $x$ -axis and its current crack tip  $\mathbf{P}_t = (l_t, 0)$  is propagating along the  $\mathbf{e}_1$  direction. The virtual perturbation  $\theta_t$  which introduces a fictive crack advance admits the form  $\theta_t = \theta_t \mathbf{e}_1$ . The construction of the continuous scalar field  $0 \leq \theta_t \leq 1$  parametrized by two radii  $r < R$  is given in Figure 4.15.

The conventional dynamic energy release rate (2.69) is numerically computed and the validity of the asymptotic Griffith's law (Proposition 2.11) is analyzed by varying the inner radius  $r$  of virtual perturbations defined in Figure 4.15. During the propagation phase  $\dot{l}_t > 0$ , three arbitrary time instants are taken when the crack length attains respectively  $l_t \approx 1.6$ ,  $l_t \approx 2$  and  $l_t \approx 2.4$ . An evident  $r$ -dependence of  $G_t^\alpha$  is illustrated in Figure 4.16, where the ratio  $R/r = \frac{5}{2}$  is fixed. In the Griffith's theory of linear elastic dynamic fracture, according to Proposition A.2, the energy release rate  $G_t$  is independent of the virtual perturbation field  $\theta_t$  since it is related directly to the dynamic stress intensity factors at the crack tip. In gradient damage models however, there is no more stress singularities. When  $r$  is small, we go directly into the process zone (crack tip problem) dominated by damage-induced strain softening and  $G_t^\alpha \rightarrow 0$  is expected as  $r \rightarrow 0$ . However, as  $r$  increases,  $G_t^\alpha$  captures well the outer mechanical fields of the outer Griffith's fracture problem. An equivalent energy release rate can thus be defined, and according to Proposition 2.11, we have the desired result  $G_t^\alpha = \gamma_t \rightarrow (G_c)_{\text{eff}}$ .

We will then turn to the evolution of the conventional dynamic energy release rate when the existing

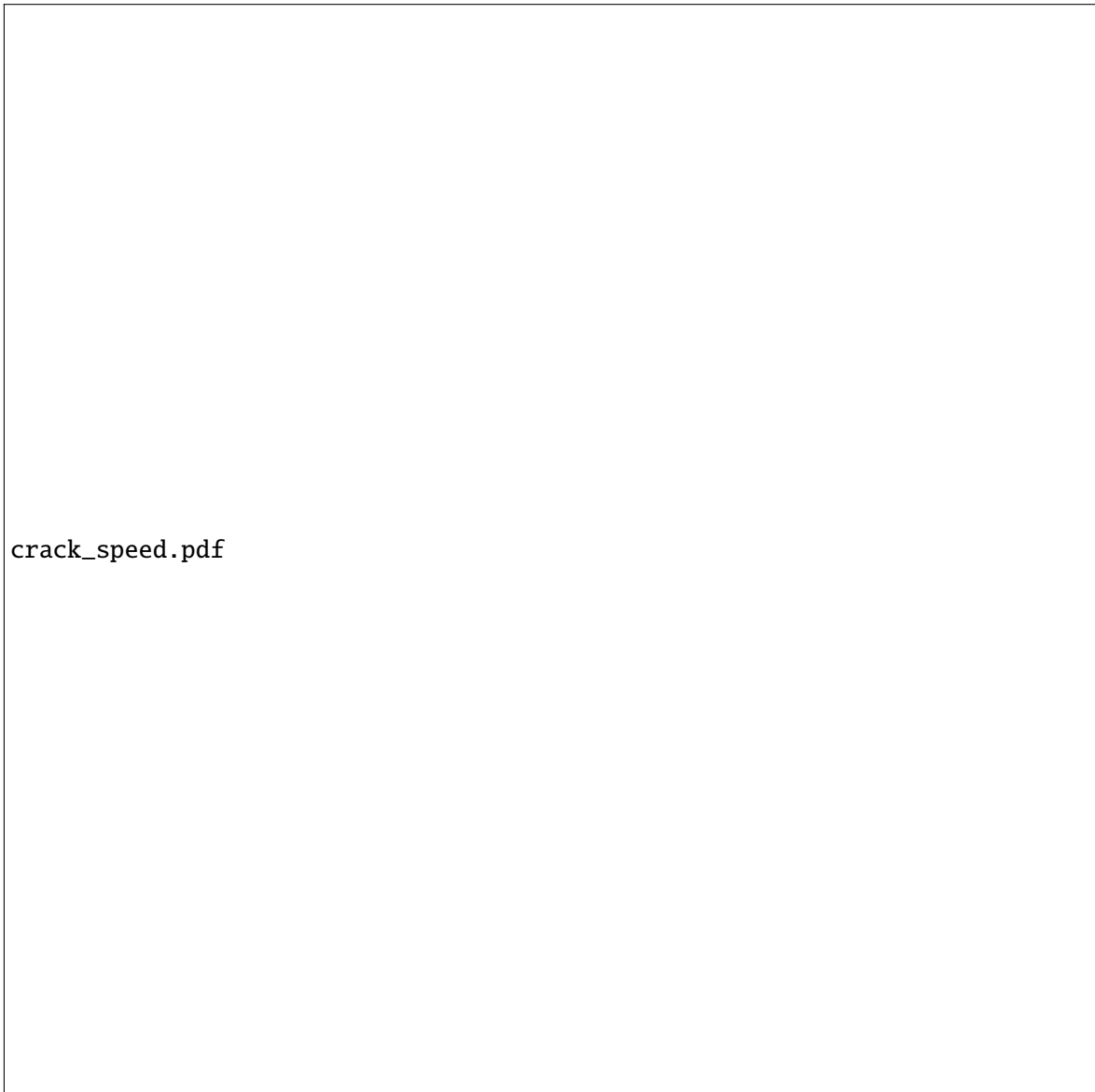


Figure 4.14 – Crack speeds as a function of the loading velocity. The crack speed respect to  $t$  is indicated in (a), while in (b) the crack speed with respect to  $U$  is used. Comparison with the 1-d analytical solution (4.9) based on the Griffith's criterion

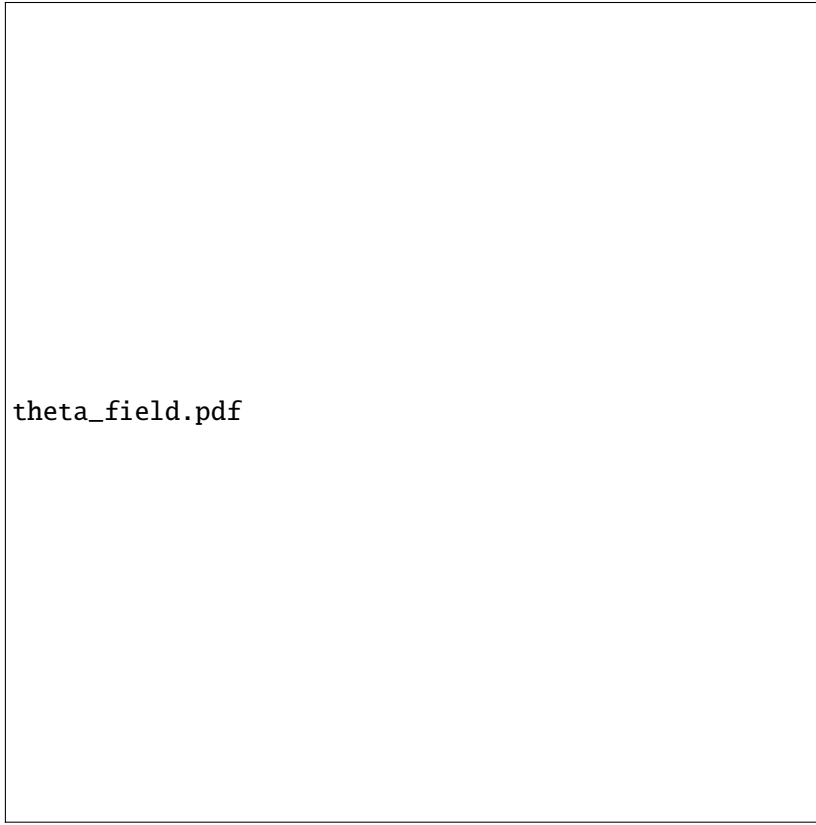


Figure 4.15 – A particular virtual perturbation  $\theta_t = \theta_t \mathbf{e}_1$  parametrized by two radii  $r < R$ . We have  $\theta_t = 1$  inside the ball  $B_r(\mathbf{P}_t)$ ,  $\theta_t = 0$  outside the ball  $B_R(\mathbf{P}_t)$ , and a linear interpolation in between

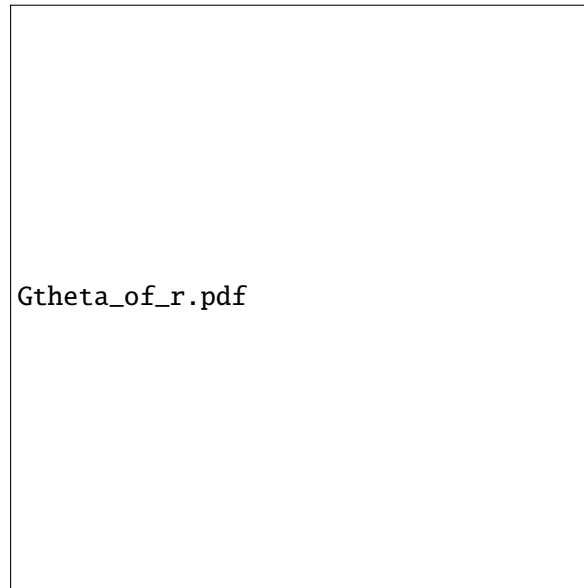


Figure 4.16 – Conventional dynamic energy release rate  $G^\alpha$  as a function of the inner radius  $r$  of the virtual perturbation  $\theta_t$  with a fixed ratio  $R/r = \frac{5}{2}$ . Three arbitrary instants when the crack propagates  $\dot{l}_t > 0$  are chosen

crack initiates and further propagates. From the above  $r$ -dependence analysis, a fixed inner radius  $r = 2\eta$  is used which should already correctly capture the far mechanical fields. The crack length  $l_t$  given by (1.20) as well as the calculated  $G_t^\alpha$  are given as a function of the loading displacement in Figure 4.17, where three separate calculations corresponding to three loading speeds  $k$  are reported. Recall that an initial crack of length 1 is present in the body and we observe  $G_t^\alpha = 0$  before the waves

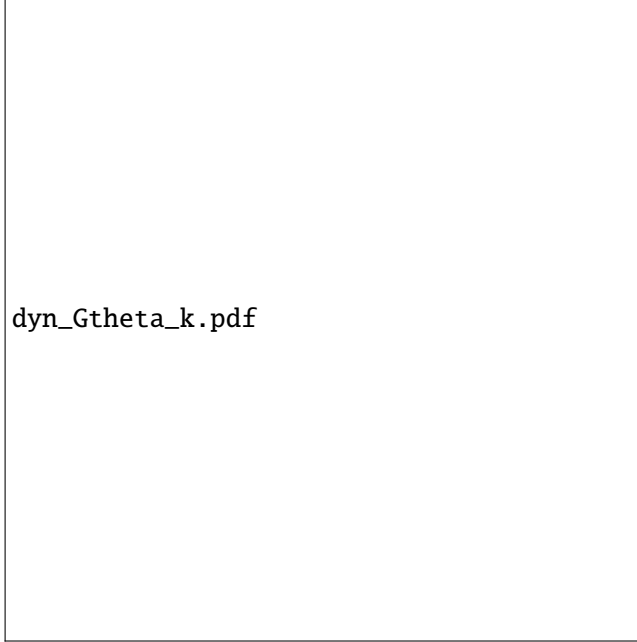


Figure 4.17 – Conventional dynamic energy release rate  $G^\alpha$  as a function of the loading displacement. Three loading speeds  $k$  are used:  $k = 0.1 \approx 0.2c$ ,  $k = 0.2 \approx 0.4c$  and  $k = 0.3 \approx 0.7c$

arrive at the initial crack tip. When the energy release rate  $G_t^\alpha$  at the initial crack tip attains the fracture toughness  $(G_c)_{\text{eff}}$ , the existing crack  $\Gamma_0 = [0, 1] \times \{0\}$  initiates and then propagates with the equality  $G_t^\alpha = (G_c)_{\text{eff}}$  if the spatial and temporal numerical discretization errors are ignored. Indeed this equality is not enforced algorithmically during the solving of the  $(\mathbf{u}, \alpha)$  evolution which is instead determined by Algorithm 4. We may conclude that the crack-tip evolution (initiation and propagation) is well governed by the asymptotic Griffith's law (Proposition 2.11) in the dynamic gradient damage model, when outer fields are considered.

The internal length  $\ell$  (hence the maximal material stress (2.6)) plays a rather subtle role during the propagation phase. The crack tip is governed by the asymptotic Griffith's law (Proposition 2.11) if and only if a separation of scales between the inner damage problem and the outer LEFM is possible, *i.e.* only when the internal length is sufficiently small compared to any other structural length. Although  $\ell$  is indeed hidden in Proposition 2.11, the validity of the latter depends directly on it. Below we present the simulation results with a fixed loading speed  $k = 0.2$  and three small enough internal lengths. As can be seen from Figure 4.18, the crack evolution is globally conforming with Griffith's law, as long as the involved quantities are calculated with a virtual perturbation  $\theta_t$  capturing correctly the far fields. Here according to Figure 4.16, we use an inner radius adapted with the internal length  $r = 2\eta$ , which should produce an error less than 3%.

The stress distribution along a vertical slice  $\{(x, y) \in \mathbb{R}^2 \mid x = l_t\}$  passing by the current crack tip  $\mathbf{P}_t$  will illustrate and highlight the separation of scales when  $\ell$  is small. For the sake of simplicity, we consider a stationary crack  $[0, 2] \times \{0\}$  and solve the static problem with the gradient damage model and the LEFM model (linear elastic body with a sharp crack embedded in the domain). On the one hand, we can verify from Figure 4.19 that the LEFM develops a well-known inverse square root singularity for the two stress components  $\sigma_{13}$  and  $\sigma_{23}$  and their near-tip fields are well approximated by the theoretic asymptotic solutions. On the other hand, the gradient damage model provides a better modeling of the stress field near the crack tip as their values are bounded. A good matching can be

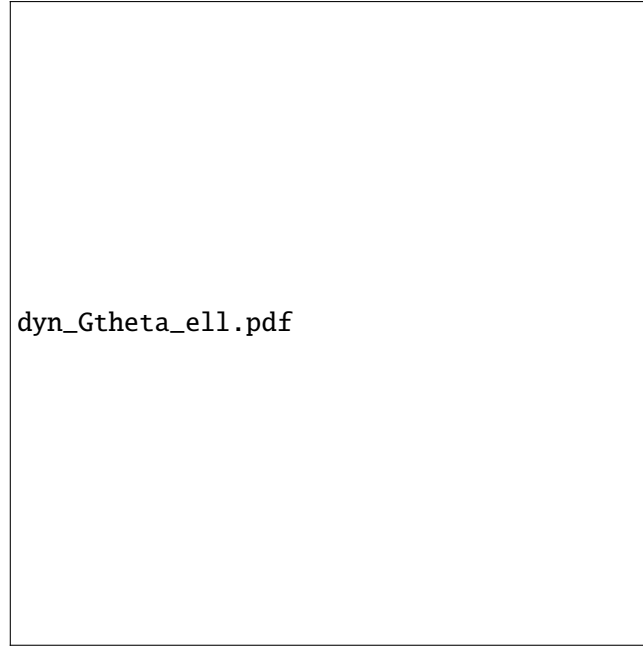


Figure 4.18 – Crack evolution as a function of the loading displacement. Three small enough internal lengths are used

observed far from the crack tip whereas the discrepancy with the outer LEFM model is concentrated within a process zone proportionally dependent on the internal length. When  $\ell$  is very large, the process zone could cover the whole structural domain and a separation of scales is no longer possible. In this case the asymptotic Griffith's law (Proposition 2.11) is not applicable since we are no longer dealing with a fracture mechanics problem.

#### 4.2.2 Quasi-static limit of the dynamic model

As another illustration of the Griffith-conforming crack evolution obtained with the dynamic gradient damage model, we consider the quasi-static limits of the model in the presence of a possible fracture toughness discontinuity in the previous plate

$$G_c = \begin{cases} K_1 & x \leq x_0 \\ K_2 & x > x_0 \end{cases}$$

A preexisting crack is always present and is introduced via an initial damage field.

A theoretic convergence investigation of the dynamic gradient damage model with a vanishing loading speed  $k \rightarrow 0$  is performed in (Versieux, 2016). The analysis is based on the hypothesis that the crack evolution  $t \mapsto l_t$  is at least continuous in time (as in the classical Griffith's theory). This implies that in the presence of brutal or unstable crack propagation, the convergence may not be observed. Nevertheless in the absence of these situations, the dynamic gradient damage model (Definition 2.1) should converge to the following

**Definition 4.1** (First-Order Quasi-Static Gradient Damage Evolution Law).

1. **Irreversibility:** the damage  $t \mapsto \alpha_t$  is a non-decreasing function of time.
2. **First-order stability:** the first-order variation of the potential energy is non-negative with respect to arbitrary admissible displacement and damage fields

$$\mathcal{P}'(\mathbf{u}_t, \alpha_t)(\mathbf{v}_t - \mathbf{u}_t, \beta_t - \alpha_t) \geq 0 \text{ for all } \mathbf{v}_t \in C_t \text{ and all } \beta_t \in \mathcal{D}(\alpha_t). \quad (4.10)$$

3. **Energy balance:** the only energy dissipation is due to damage such that the energy balance condition (1.24) is satisfied.

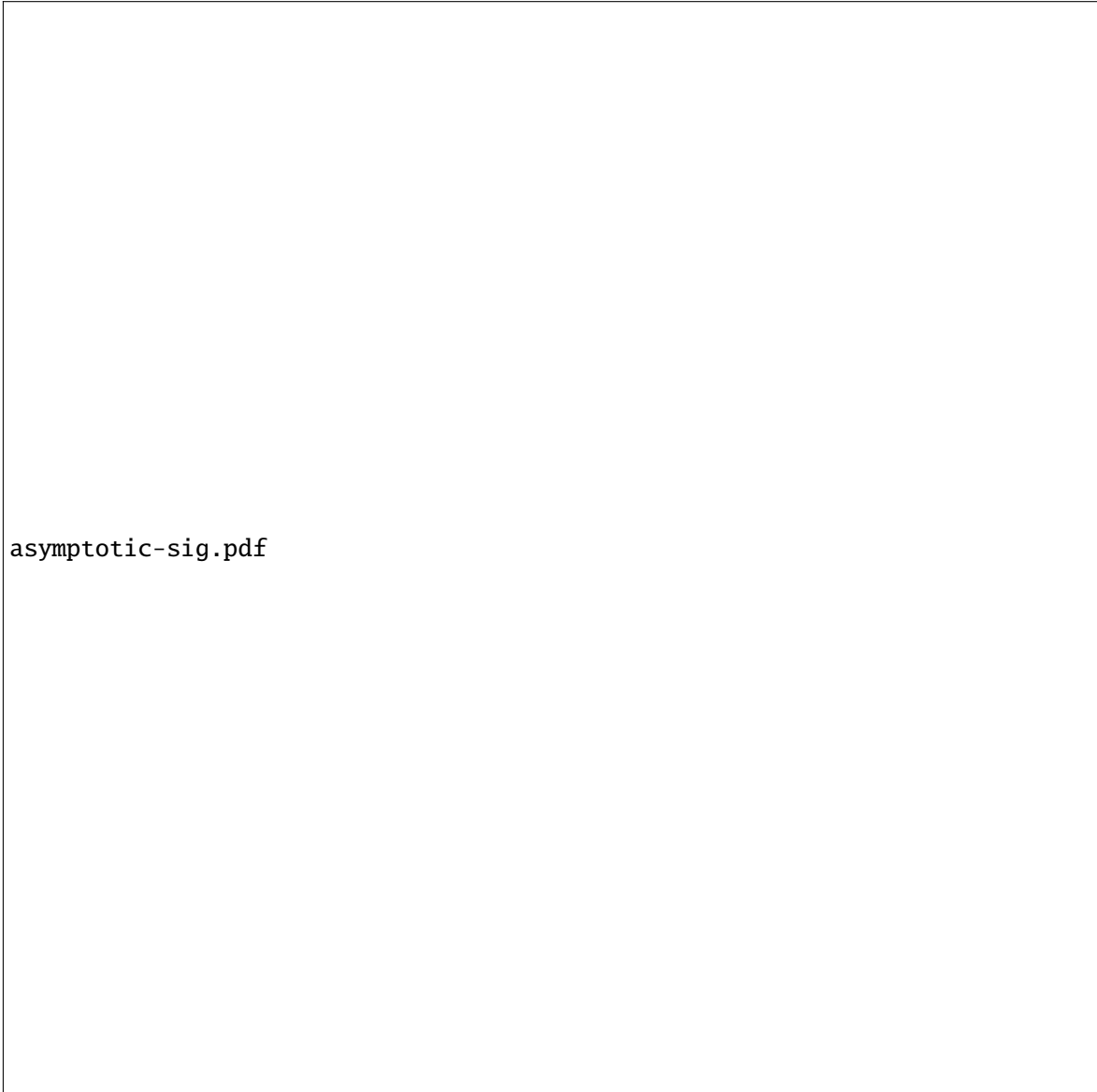


Figure 4.19 – Stress distribution along a vertical slice  $\{ (x, y) \in \mathbb{R}^2 \mid x = l_t \}$  passing by the current crack tip  $\mathbf{P}_t$ . The  $\sigma_{13}$  (a) and the  $\sigma_{23}$  (b) components are indicated. The gradient damage model and the LEFM model are compared

Compared to the original quasi-static model (Definition 1.1), the more general meta-stability principle (1.23) is replaced by its first-order condition (4.10). However as it is noted in Section 1.3.2, numerically it is the first-order stability condition (4.10) that is effectively implemented by the alternate minimization procedure, while the energy balance condition (1.24) can only be at best checked *a posteriori*. From this viewpoint, Definition 4.1 can thus be considered as the effective quasi-static gradient-damage model.

**Homogeneous case  $K_1 = K_2$**  The homogeneous antiplane tearing problem is firstly solved by the dynamic gradient damage model and the above first-order quasi-static gradient damage model. In the dynamic calculation a small loading speed  $k = 0.001 \approx 0.2\%$  is assumed and we use the unconditionally stable implicit Newmark scheme as described in Algorithm 3, with  $\beta = \frac{1}{4}$ . The time step is set to  $\Delta t = 10\Delta t_{\text{CFL}}$ . In Figure 4.20 we plot the crack length evolution as well as the conventional energy release rate  $G_t^\alpha$  both for the dynamic model and the first-order quasi-static model. It is recalled that the static  $G_t^\alpha$  can be simply obtained by setting  $\dot{\mathbf{u}}_t$  and  $\ddot{\mathbf{u}}_t$  to zero in (2.69). We

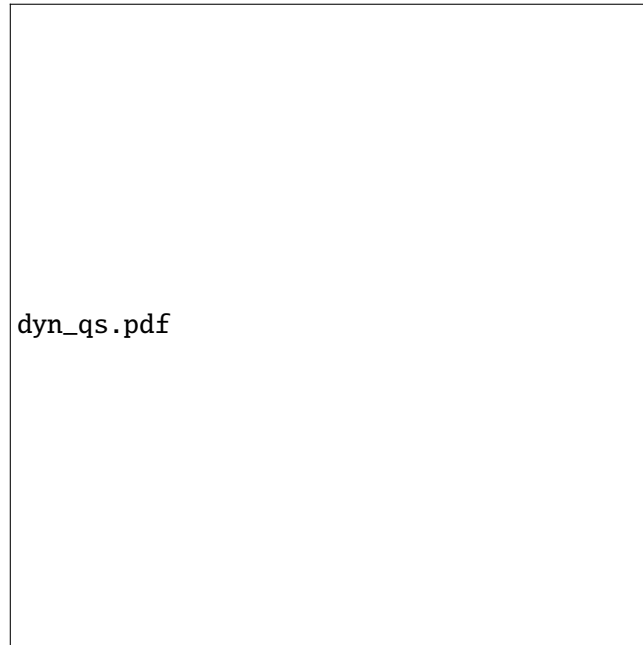


Figure 4.20 – Crack length and conventional energy release rate  $G^\alpha$  for the homogeneous fracture toughness plate at a very slow loading speed. Comparison between the dynamic model and the first-order quasi-static model

observe that these two solutions coincide, and both present a time-continuous crack evolution (initiation and propagation) conforming to the asymptotic Griffith's law (Proposition 2.11). The numerically computed quasi-static crack speed (with respect to  $U = kt$ ) is compared in Table 4.6 to the analytical value  $\sqrt{\mu H/G_c}$  announced in (Bourdin et al., 2008). A very good agreement can be found if the numerically amplified fracture toughness  $(G_c)_{\text{eff}}$  is used in the formula.

Table 4.6 – Comparison of the numerically computed quasi-static crack speed in the homogeneous case with the theoretic one  $\sqrt{\mu H/G_c}$  given in (Bourdin, Francfort, & Marigo, 2008)

	Numerical	Theoretic	Error
Quasi-static crack speed	4.326	4.391	1.5%

**When  $K_1 < K_2$**  We then turn to the case where the fracture toughness jumps suddenly from a lower value  $K_1 = 0.01$  to a higher one  $K_2 = 2K_1 = 0.02$  at  $x = 2$ . The unconditionally stable implicit

Newmark scheme with  $\beta = \frac{1}{4}$  is used again with a time increment  $\Delta t = 10\Delta t_{\text{CFL}}$ . As can be observed from Figure 4.21 the convergence of the dynamic model toward the quasi-static one is verified and the crack initiates and propagates following Griffith's law. A temporary arrest phase is present shortly after the crack reaches the interface at  $x = 2$ . Due to continuous loading the energy release rate increases and the crack then restarts and begins to propagate in the second material when the energy release rate  $G_t^\alpha$  attains the higher fracture toughness  $K_2$ .

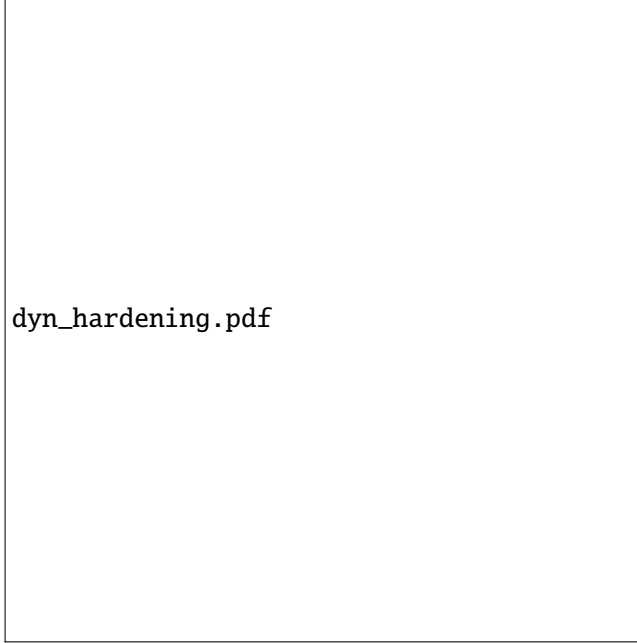


Figure 4.21 – Crack length and conventional energy release rate  $G^\alpha$  for the hardening fracture toughness plate at a very slow loading speed. Comparison between the dynamic model and the first-order quasi-static model. The numerically amplified fracture toughness  $(G_c)_{\text{eff}}$  is calculated based on  $K_1 = 0.01$

**When  $K_1 > K_2$**  However, for the case where the fracture toughness  $K_1 = 2K_2 = 0.02$  suddenly drops to a smaller value  $K_2 = 0.01$  at  $x = 1$  (exceptionally here the initial crack length is  $\frac{1}{4}$ ), a relatively good matching can only be found before and after the jump phase produced at the discontinuity, both in terms of the crack length evolution and the energy release rate. It is exactly at the jump phase that these two models strongly disagree, cf. Figure 4.22. Here due to the unstable crack propagation during the jump, the explicit Newmark scheme is used for the dynamic calculation with  $\Delta t = \Delta t_{\text{CFL}}$ . When the crack arrives at the discontinuity, the *first-order* quasi-static *numerical* model underestimates the crack jump and predicts no further crack arrest, by relating directly the static energy release rate  $G_t^\alpha$  to the fracture toughness  $K_2$  just after the jump. For the dynamic model, the jump length is bigger and a subsequent temporary crack arrest is observed, as the dynamic energy release rate oscillates with a high frequency but remains smaller than the fracture toughness  $K_2$  after the jump. We observe that in both cases the jump takes place at  $x \approx 0.9$  somewhat prior to the fracture toughness discontinuity  $x = 1$ . We suspect that this is due to the damage regularization of cracks with a half-band  $D = 2\eta = 0.1$  using the constitutive laws of (PAMM). The crack length after the jump with this effect ignored is recorded in Table 4.7 for each case. From the static energy release rate evolution, we see that the crack length  $l_m$  after the jump predicted in the *first-order* quasi-static *numerical* model is governed by  $G(l_m) = G_c(l_m)$  from which authors of (Dumouchel et al., 2008) find  $l_m = \sqrt{K_1/K_2} = \sqrt{2}$ . However their dynamic analysis shows that the crack length after the jump  $l_c$  should instead be given by the total (quasi-static) energy conservation principle  $\mathcal{P}(1) = \mathcal{P}(l_c)$ , which results in  $l_c = K_1/K_2 = 2$ . We see from Table 4.7 that our dynamic gradient damage model indeed reproduces this correct value.

To better analyze the jump phase, energy evolutions are investigated against the crack length in



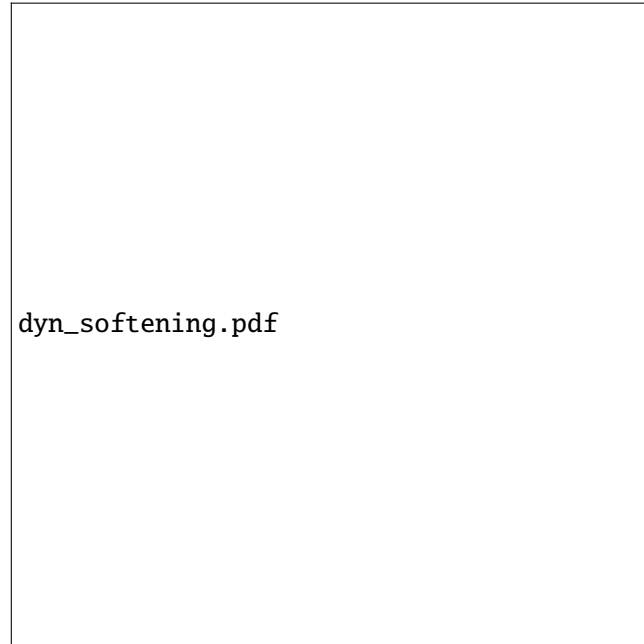


Figure 4.22 – Crack length and the conventional energy release rate  $G^a$  for the softening fracture toughness plate at a very slow loading speed. Comparison between the dynamic model and the first-order quasi-static model. The numerically amplified fracture toughness  $(G_c)_{\text{eff}}$  is calculated based on  $K_2 = 0.01$

Table 4.7 – Comparison of the numerical crack lengths after the jump with the theoretic predictions

	Quasi-static	Dynamic
Numerical	1.465	1.995
Theoretic	$\sqrt{2}$	2
Error	3.6%	0.25%

Figure 4.23. In the quasi-static case we pick the total energy  $\mathcal{P} = \mathcal{E} + \mathcal{S}$  while in the dynamic case



Figure 4.23 – Energy variation as a function of the crack length for the softening fracture toughness plate at a very slow loading speed. Comparison between the dynamic model and the first-order quasi-static model

we plot separately the static energy  $\mathcal{P} = \mathcal{E} + \mathcal{S}$  and the kinetic one  $\mathcal{K}$ . Before and sufficiently after the jump a good agreement between these two potential energies can be found. We observe that the (incorrect) quasi-static jump (*i.e.*, an *unstable* or *brutal* crack propagation) is accompanied by a slight loss of the total energy  $\Delta\mathcal{P}_{\text{stat.}}$ , contradicting the balance condition (1.24). This phenomenon has already been observed by several authors such as (Amor et al., 2009; Bourdin et al., 2008; Bourdin et al., 2011; Pham, Amor, et al., 2011). On the one hand, it can be regarded as a numerical issue as the effective implementation of the quasi-static model is solely based on the first-order stability condition (4.10). For this particular problem based on quasi-static energy conservation we could predict a correct quasi-static crack evolution toward which the dynamic solution converges when the loading speed becomes small, see (Dumouchel et al., 2008). On the other hand, from a theoretic point of view, it is already known in (Pham, 2010) that there may not exist an energy-conserving evolution which also respects the stability criterion at every time. Moreover even equipped with the energy balance condition, the quasi-static model may still differ from the dynamic analysis (Lazzaroni, Bargellini, Dumouchel, & Marigo, 2012). A natural and physical remedy for all general unstable crack propagation cases is to introduce inertial effects. In Figure 4.23 the dynamic jump process is *continuous* (the crack propagates at a finite speed bounded by the shear wave speed) compared to the quasi-static one where the jump occurs necessarily in a discontinuous fashion between two iterations. We verify the conclusions drawn in (Dumouchel et al., 2008) that the kinetic energy  $\mathcal{K}$  plays only a transient role in this problem, as it attains a finite value during the jump and becomes again negligible after. The dynamic potential energy  $\mathcal{P} = \mathcal{E} + \mathcal{S}$  after the jump is slightly bigger than its value before the jump, due to the fact that the loading speed  $k = 0.001$  is small but not zero.

During the jump, the crack propagates at a speed comparable to the material speed of sound which, according to (Dumouchel et al., 2008), is given by

$$v_{\text{jump}} = \frac{\left(\sqrt{\widehat{K}_1 + \epsilon^2 + \epsilon}\right)^2 - \widehat{K}_2}{\left(\sqrt{\widehat{K}_1 + \epsilon^2 + \epsilon}\right)^2 + \widehat{K}_2} \cdot c \quad (4.11)$$

with the non-dimensional fracture toughness  $\widehat{K}_i = K_i/(2\mu H)$  and the normalized loading speed  $\epsilon = k/c$ . The crack length evolution during the jump is illustrated in Figure 4.24. Due to transverse wave

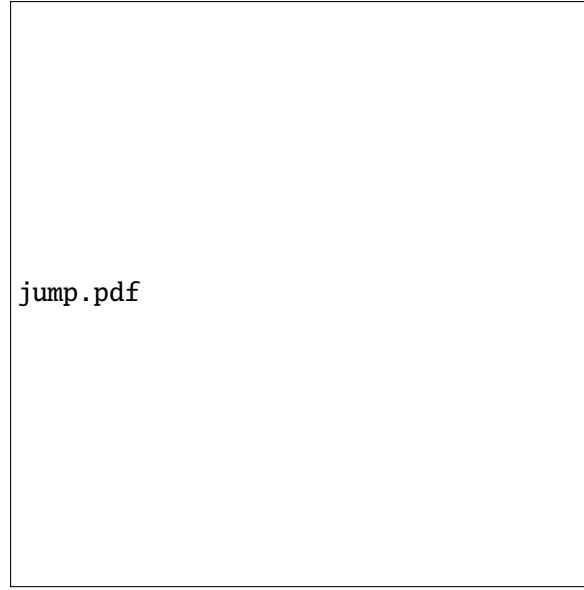


Figure 4.24 – Zoom in time at the crack length jump due to sudden toughness softening for the dynamic model

reflection in this 2-d problem, the crack propagates during this interval with a small fluctuation of period  $T$  approximately corresponding to the first standing wave between the boundary and the crack  $T \approx 2H/c \approx 4.5$ . That is why we calculate from Figure 4.24 only the initial crack speed at jump for comparison in Table 4.8. A good agreement can be found between the numerical and the theoretic ones.

Table 4.8 – Comparison of the numerically computed crack jump speed with the theoretic one (4.11) given in (Dumouchel, Marigo, & Charlotte, 2008)

	Numerical	Theoretic	Error
Relative jump speed $v_{\text{jump}}/c$	0.3325	0.3396	2%

## Conclusion

Further physical insights into the dynamic gradient damage model are provided via a simple antiplane tearing experiment. As a phase-field approach to brittle fracture, it can indeed be regarded as a generalization or a superset of the LEFM theory, since the crack evolution is shown to be Griffith-conforming in several situations:

- In the dynamic tearing example of a homogeneous plate, it is verified that the crack evolution is governed by the asymptotic Griffith's law (Proposition 2.11), as long as the material internal length is sufficiently small to establish a separation of scales between the inner damage problem and the outer LEFM problem. The conventional dynamic energy release rate is numerically computed and verified as a tool to translate gradient damage mechanics results in fracture mechanics terminology. We conducted a comparison with the 1-d peeling problem (Dumouchel et al., 2008) analytically studied with the classical Griffith's theory of dynamic fracture. A good agreement between them can be found in terms of the crack speeds prediction as a function of the loading speed.
- We then investigated the quasi-static limits of the dynamic gradient damage model. In the absence of *brutal* or *unstable* crack propagation when the classical static Griffith's theory fails, the dynamic model converges to the first-order quasi-static gradient damage model, when the

loading speed decreases. However when the crack may propagate at a speed comparable to the material speed of sound, the dynamic model should be preferred in order to correctly account for inertial effects. The crack evolution in the dynamic gradient damage model is in quantitative accordance with the LEFM predictions on the 1-d peeling problem.

These numerical experiments provide hence a justification of the dynamic gradient damage model along with its current implementation, when it is used as a genuine physical model for complex real-world dynamic fracture problems.

### 4.3 Plane Crack Kinking

The three physical principles of Definition 2.1 determine *when* and *how* the crack propagates. In Section 4.2 the initiation and propagation phases of defect evolution are considered. According to Section 1.1, it focuses on *when* cracks propagate. In this section, we will focus on the path along which the crack propagates, *i.e.* *how* cracks evolve. Specifically, this section is devoted to a numerical analysis of plane crack kinking predicted by the gradient damage model. The thematic subjects covered here are thus summarized in Table 4.9.

Table 4.9 – Thematic subjects covered in this section

	Going dynamical	$\alpha \leftrightarrow \phi$	$\nabla \alpha \rightarrow \Gamma$	Experimental validation
Theoretics				
Numerics			👍	

**Problem setting** The problem setting is adapted from (Hakim & Karma, 2005, 2009). We consider a unit disk centered at the origin  $\Omega = B_1(\mathbf{0})$  subject to a mixed-mode hard device  $\mathbf{U}(\bar{G}, K_2/K_1)$  prescribed on its boundary  $\partial\Omega$ , see Figure 4.25. An existing *stationary* plane crack  $\Gamma_0 = [-1, 0] \times \{0\}$  is modeled

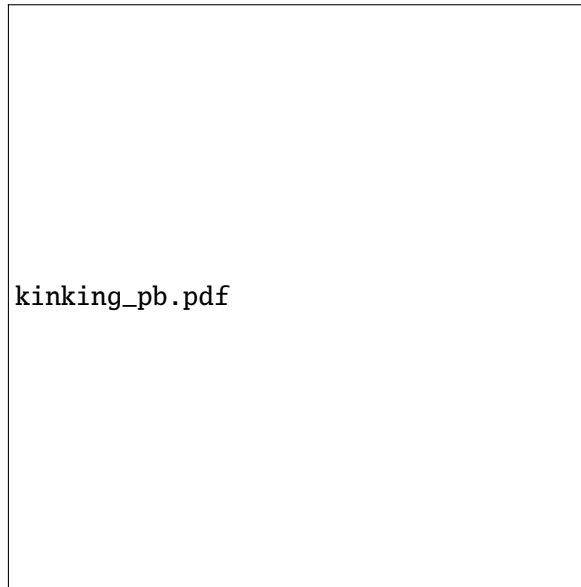


Figure 4.25 – Plane crack kinking problem in a pre-cracked unit ball centered at the origin  $\Omega = B_1(\mathbf{0})$ . A hard device  $\mathbf{U}(\bar{G}, K_2/K_1)$  is prescribed on the boundary  $\partial\Omega$

by an initial damage field via  $\underline{\alpha}^{-1} = 1$  on  $\Gamma_0$ , see Algorithm 5. In the presence of this *stationary* damage field  $\alpha_0$ , the elasto-static displacement corresponding to the mixed-mode Dirichlet condition  $\mathbf{U}(\bar{G}, K_2/K_1)$  is pre-computed and will be used as the initial condition for the subsequent dynamic

calculation. For this problem the initialization procedure is summarized in Algorithm 6. The dynamic analysis is performed in an interval  $[0, T]$ , while the external displacement  $\mathbf{U}(\bar{G}, K_2/K_1)$  is maintained constant.

---

**Algorithm 6** Initialization for the plane crack kinking problem adapted from Algorithm 5

---

- 1: Given initial conditions  $\underline{\mathbf{u}}^0 = \mathbf{0}$ ,  $\underline{\dot{\mathbf{u}}}^0 = \mathbf{0}$  and  $\underline{\alpha}^{-1} = 1$  on  $\Gamma_0$ .
- 2: Reinitialize the damage by solving

$$\underline{\alpha}^0 = \operatorname{argmin} q_0(\cdot) \text{ subjected to constraints } 0 \leq \underline{\alpha}^{-1} \leq \underline{\alpha}^0 \leq 1.$$

- 3: Initialize the displacement by solving the following elasto-static problem with the previously computed  $\underline{\alpha}^0$

$$\underline{\mathbf{u}}^0 = \operatorname{argmin} \mathbf{F}_{\text{int}}(\cdot, \underline{\alpha}^0) - \mathbf{F}_{\text{ext}}^0(\cdot).$$

- 4: Initialize the acceleration  $\mathbf{M}\underline{\ddot{\mathbf{u}}}^0 = \mathbf{F}_{\text{ext}}^0 - \mathbf{F}_{\text{int}}(\underline{\mathbf{u}}^0, \underline{\alpha}^0)$ .
- 

The precise objective here is to compare the apparent kinking angle  $\theta$  with several theoretic criteria commonly used in the Griffith's theory of fracture, cf. Section 1.2.2. The prescribed displacement  $\mathbf{U}(\bar{G}, K_2/K_1)$  corresponds to the asymptotic expansion of the displacement field near the *stationary* crack tip  $\mathbf{P}_0 = (0, 0)$  with the opening and sliding intensity factors  $K_1 > 0$  and  $K_2 \geq 0$ , see (1.4). The plane stress condition is assumed. By virtue of Irwin's formula (1.9) the imposed energy release rate is given by

$$\bar{G} = \frac{K_1^2 + K_2^2}{E}.$$

Thanks to Griffith's law (Propositions 2.7 and 2.11) in the gradient damage model as well as its numerical verification in Section 4.2, to ensure that the gradient-damage crack will indeed propagate to another point  $\mathbf{P}^*$  under  $\mathbf{U}$ , the value of  $\bar{G}$  should be larger than the effective material toughness  $G_0 > (G_c)_{\text{eff}}$ . To represent different types of mixed-mode loading, the ratio  $K_2/K_1$  will be varied and its influence on the kinking behavior will be analyzed.

A non-structured triangular mesh is used to discretize the domain  $\Omega$ . The damage constitutive law (PAMM) is used. We use the explicit time stepping procedure outlined in Algorithm 4 for the solving of the dynamic  $(\mathbf{u}, \alpha)$  problem. The material, loading and numerical parameters used in this problem are summarized in Table 4.10.

Table 4.10 – Material, loading and numerical parameters for the plane crack kinking experiment

$\rho$	$E$	$\nu$	$G_c$	$\eta$	$\bar{G}$	$h$
1	1	0.2	1	5% or 1%	1.1 or 1.5	$\eta/5$

**Simulation results and discussion** The dynamic evolution of the damage field  $\alpha_t$  is indicated in Figure 4.26. An apparent crack kinking is observed due to the initial mixed-mode loading condition. Several simulations corresponding to different  $K_2/K_1$  ratio are performed. Typical numerical results are illustrated by the damage field after kinking in Figure 4.27. The apparent kinking angle predicted by the gradient damage model is compared in Figure 4.28 with several commonly used kinking criteria in fracture mechanics, see Section 1.2.2. The influence of the mixed-mode ratio  $K_2/K_1$ , the internal length  $\ell$  and the intensity of the prescribed displacement  $\bar{G}$  is analyzed as follows.

- Numerically obtained kinking angles are conforming to the theoretic predictions of several kinking criteria in fracture mechanics. In the isotropic case, the PLS, the  $\sigma_{\theta\theta}$ -max and the  $G$ -max criteria give similar kinking angles, see for instance (Chambolle et al., 2009). Anisotropy may be needed to distinguish between them, cf. (Hakim & Karma, 2005).



Figure 4.26 – Damage field evolution obtained with  $\eta = 1\%$  and  $\bar{G} = 1.5$  for  $K_2/K_1 = 0.6$ : (a)  $t = 0$ , (b)  $t = 0.25$  and (c)  $t = 0.5$



Figure 4.27 – Damage field obtained with  $\eta = 1\text{‰}$  and  $\bar{G} = 1.5$  for three  $K_2/K_1$  ratios: (a)  $K_2/K_1 = 0.6$ , (b)  $K_2/K_1 = 0.8$  and (c)  $K_2/K_1 = 1$



Figure 4.28 – Apparent kinking angle predicted by the gradient damage model compared with some commonly used kinking criteria in fracture mechanics

- The internal length  $\ell$ , or equivalently the maximal stress (2.6), again plays a subtle role here similarly to the antiplane problem in Section 4.2. From Figure 4.28, the kinking angle shows little dependence with respect to the internal length used. This confirms that as long as the internal length is sufficiently small compared to that of the body, the gradient-damage crack behaves just like a real sharp-interface crack.
- The intensity  $\bar{G}$  determines how brutal the kinking process is, which can be measured by the post-kink add-crack length  $\delta l$ . According to the simulation results, a smaller  $\bar{G}$  produces also a smaller  $\delta l$ . However the kink angle seems independent of  $\bar{G}$  in Figure 4.28.
- By comparing the three figures in (4.27), it can be observed that the mixed-mode ratio  $K_2/K_1$  also determines how unstable the crack propagation is during the kink. In particular, a larger  $K_2/K_1$  leads to a larger  $\delta l$ . This point needs further theoretical investigation in the future.

In this section the kinking of an initially stationary crack is analyzed by the gradient damage model. Dynamics are not expected to play an essential role during such process. For a crack propagating at a given velocity, the spatial path undertaken by the crack could be different (kinking and/or branching). Future work could be devoted to a thorough dynamic analysis of this problem.

## 4.4 Dynamic Crack Branching

In this section we will study the dynamic crack branching problem for a 2-d plane stress glass plate under constant pressure applied on its upper and lower boundaries. This particular problem has already been investigated within the phase-field community (Borden et al., 2012; Schlüter et al., 2014) where the numerical convergence aspect as well as some physical insights into the branching mechanism are analyzed. Here in this work we will first focus on the computational efficiency of Algorithm 4 implemented in the EPX software as well as the possible use of several damage constitutive laws to approximate fracture. This last strengthens the bridge between the phase-field and the gradient-damage communities. Finally we provide some fracture mechanics interpretations of the branching mechanism predicted in the gradient damage model. The thematic subjects covered here are thus summarized in Table 4.11.

Table 4.11 – Thematic subjects covered in this section

	Going dynamical	$\alpha \leftrightarrow \phi$	$\nabla \alpha \rightarrow \Gamma$	Experimental validation
Theoretics				
Numerics		👍	👍	👍

**Problem setting** The geometry as well as the loading conditions are depicted in Figure 4.29. Due to symmetry only the upper half part is modeled. The initial crack  $\Gamma_0$  is introduced via an initial damage field  $\alpha^{-1}$ . Material parameters are borrowed from (Borden et al., 2012) where the internal length  $\eta$  is set to 0.25 mm. We use a structured quadrilateral elements of equal discretization spacing  $h \approx 0.045$  mm in both directions achieving approximately 1 million elements. The current time increment is calculated based on the CFL condition with a security factor of 0.8. An unstructured mesh should be in general preferred. However the original analysis on mesh-induced anisotropy is conducted on structured triangular elements (Negri, 1999). Furthermore the numerical study of (Lorentz & Godard, 2011) shows that the crack direction is insensitive to the orientation of a structured quadrilateral grids. We firstly use the damage constitutive law (PAMM). The symmetric tension-compression formulation is also adopted. This choice is justified by an *a posteriori* verification of non-interpenetration of matter. The simulation result is illustrated in Figure 4.29 by the damage field  $\alpha_t$  at  $t = 8 \times 10^{-5}$  s ranging from 0 (gray) to 1 (white). Similar contours have been obtained in (Borden et al., 2012; Schlüter et al., 2014).



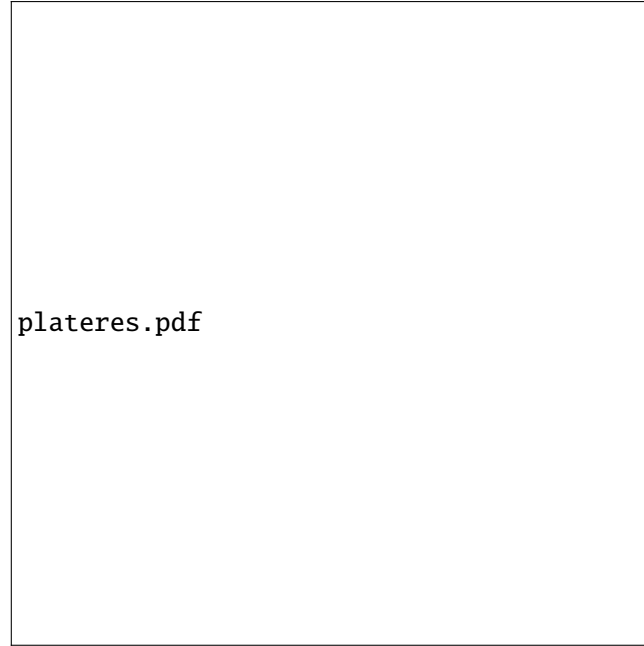


Figure 4.29 – Geometry and loading conditions for the dynamic crack branching problem. Damage field  $\alpha_t$  at  $t = 8 \times 10^{-5}$  s ranging from 0 (gray) to 1 (white) obtained by the (PAMM) model

#### 4.4.1 Computational efficiency in a parallel computing context

The parallel computing framework for the dynamic gradient damage model has been developed by the author in the EPX software (CEA & EC, 2015). A strong scaling analysis is here conducted for several processor cores NP in the cluster ASTER5 provided by the Electricité de France. We have verified that all simulations give nearly the same results in terms of global energy evolution and field contours. The difference of the elastic energy at  $t = 8 \times 10^{-5}$  s is within 0.2% between the sequential and the parallel NP = 16 cases, which may be due to floating point arithmetic and different setting of preconditioners. The scaling results are given in Figure 4.30. The calculation time is partitioned into 4 items:

1. The “elastodynamics” part related to the solving of (3.2),
2. The “damage assembly” part where the global Hessian matrix  $\mathbf{H}$  and the second member  $\mathbf{b}$  is constructed,
3. The “damage solving” part where (3.9) is solved,
4. The “communication” part corresponding to the data exchange among processors.

The computational load is well balanced and the maximum value among all processors are used. Quasi-ideal scaling is observed for the total computational time. The proportion of the “elastodynamics” and the “damage assembly” parts are decreasing, due to the increase of the “communication” overhead reaching 15% with 16 cores and becoming comparable to that of the “damage solving”.

We remark that the quadratic bound-constrained minimization problem (3.9) solved by the GPCG scheme implemented in PETSc is not very costly and represents in sequential and parallel calculations only 13% of the total computational time. In the phase-field literature the damage problem is often solved by an unconstrained minimization of (3.9) corresponding to a linear system (2.28). The irreversibility condition is then approximated by several physical or numerical methods, see Section 2.1.4. However, it should be kept in mind that the above computationally-appealing strategy only applies to the damage constitutive law (AT), where the solution of (2.28) lies necessarily between 0 and 1 and the objective functional (3.7) is indeed quadratic with respect to  $\underline{\alpha}$ . Otherwise a specific numerical scheme for bound-constrained problems is needed. Nevertheless we would like to point out that the GPCG solver is extremely efficient even compared to the above strategy consisting of only one linear system. The

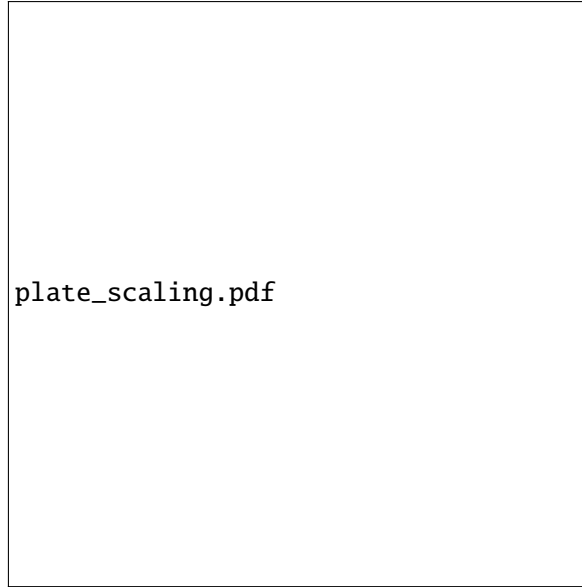


Figure 4.30 – Strong scaling results for the dynamic crack branching problem with 1 million elements

same crack branching analysis is conducted using the damage constitutive model (AT) and a same internal length  $\eta = 0.25$  mm, and the results obtained with the GPCG solver and the *a posteriori* projection method described in Section 2.1.4 are compared. In the latter case the same preconditioned conjugate gradient method is employed to solve (2.28). The results are slightly different as expected, since the projection method does not solve exactly the full minimization problem (3.9). To compare their relative computational costs, the time consumed in damage solving is separately normalized by that corresponding to the elastodynamic problem in Table 4.12.

Table 4.12 – Relative damage-solving cost normalized by the time devoted to the elastodynamic part during a parallel calculation  $NP = 16$ . The damage constitutive law (AT) is used. Comparison between the GPCG solver and the *a posteriori* projection method

	CG + projection	GPCG
Damage-solving cost	50%	77%

Opposed to what is suggested by (Amor et al., 2009), the use of a bound-constrained minimization solver implies a relative computational cost only 27% higher than a traditional linear solver. This can be seen in the normalized histogram of CG iterations per time step illustrated in Figure 4.31. We recall that each CG iteration implies a matrix-vector multiplication, the most costly part of the algorithm. When only one linear system is to be solved in the *a posteriori* projection method, approximately 20 CG iterations are needed in 35% of all time steps. When the GPCG solver is used, we observe that the histogram is more spread out and more than 50 CG iterations may be needed for some time steps. Nevertheless the distribution is more concentrated around 10 to 30 iterations.

#### 4.4.2 Comparison between two damage constitutive laws

We then turn to the choice of different damage constitutive laws from a computational and physical point of view. We take the simulation results using (PAMM) as a reference and compare them with results obtained by the widely used damage constitutive law (AT) in the phase-field modeling of fracture. The quantitative effects of the internal length actually depend on the damage constitutive model used. Here we propose two natural choices of  $\ell$  in the (AT) case: one corresponding to the same value  $\eta = 0.25$  mm as used in the (PAMM) case, the other corresponding to a same maximal tensile stress as used in the (PAMM) case, which gives  $\eta \approx 0.07$  mm according to (2.6) and (2.9). The same

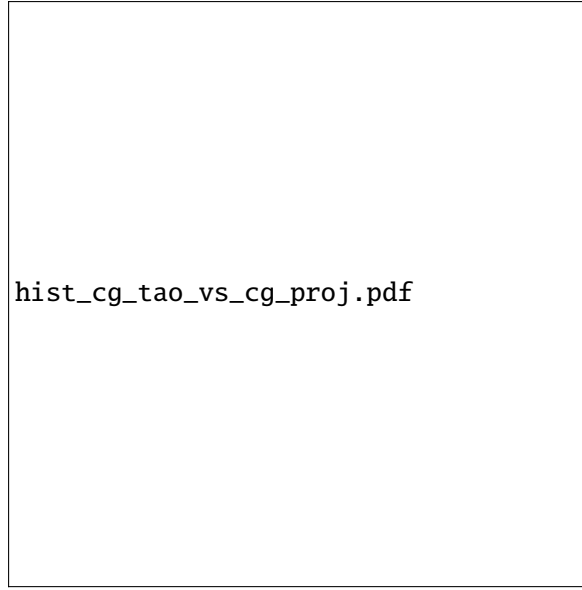


Figure 4.31 – Normalized histogram of CG iterations per time step. The damage constitutive law (AT) is used. Comparison between the GPCG solver and the *a posteriori* projection method

GPCG solver is used and the relative damage-solving costs separately normalized by the time devoted to the elastodynamic part are reported in Table 4.13.

Table 4.13 – Relative damage-solving cost normalized by the time devoted to the elastodynamic part during a parallel calculation  $NP = 16$ . The GPCG solver is used. Comparison between different constitutive laws

	Damage-solving cost
(PAMM)	32%
(AT) with a same $\ell$	77%
(AT) with a same $\sigma_m$	36%

We remark that the use of the constitutive law (PAMM) or a smaller internal length  $\ell$  reduces significantly the *relative* damage-solving cost. A viable explanation is given as follows. The theoretical 1-d damage profile of (AT) corresponds to an exponential function without a finite support, see (2.8). The numerically obtained damage band, *i.e.* in which  $\alpha_t > 0$ , is much wider than in the (PAMM) case (2.7). Consequently, less *active* nodes are present and the GPCG solver identifies much more *free* nodes for the (AT) case, which induces a bigger linear system to be solved. Similarly, a reduction of the material internal length will imply finer mesh along the crack path (hence more computational cost in absolute values), however the damage is more concentrated and the *relative* solving cost of (3.9) is decreased.

The damage field  $\alpha_t$  at  $t = 8 \times 10^{-5}$  s obtained with the constitutive law (AT) is illustrated in Figure 4.32. Recall that the same mesh with  $h = 0.05$  mm is used and should be sufficient for both calculations. Compared to Figure 4.29 obtained with (PAMM), the *transition area* where  $0 < \alpha_t < 1$  is more pronounced especially in Figure 4.32 with  $\eta = 0.25$  mm, conforming to the above discussions on the damage band. Another reason behind a relatively large zone with intermediate damage values is due to the different stress-strain behavior of these two constitutive laws during a homogeneous traction experiment discussed in Section 2.1.1. In the (PAMM) case the material possesses a purely elastic domain and damage doesn't evolve as long as the maximal stress is not reached. Then the material follows a classical softening behavior as damage grows from 0 to 1. However for the constitutive law (AT) widely used in phase-field modeling, damage evolves the instant when the material is subjected to external loadings. An elastic domain is absent and stress-hardening is observed within the interval

$[0, \frac{1}{4}]$ . In this case the phase-field  $\alpha_t$  loses its physical interpretation as *damage*, and hence correctly handling and interpreting crack healing is not trivial, see Section 2.1.4.



Figure 4.32 – Damage field  $\alpha_t$  at  $t = 8 \times 10^{-5}$  s ranging from 0 (blue) to 1 (red) for the dynamic branching problem. Comparison between (a)  $\eta = 0.25$  mm and (b)  $\eta \approx 0.07$  mm with the same constitutive model (AT)

Furthermore, this peculiar behavior of the constitutive law (AT) also contributes to an overestimation of the dissipated energy, as is noted in (Borden et al., 2012; Vignollet, May, de Borst, & Verhoosel, 2014). The energy evolution in this dynamic crack branching problem is given in Figure 4.33. It is observed that the (AT) law produces a dissipated energy much bigger than the (PAMM) case, although according to Figure 4.32 the damage fields are similar.

As can be seen from Figures 4.32 and 4.33, apparently the results obtained with the same internal length  $\ell$  resembles better the (PAMM) calculation in Figure 4.29, even though it corresponds to a smaller maximal stress than the latter case. It should be reminded that  $\ell$  does not play merely the role of determination of the maximal stress as in (2.6). From Sections 2.3, 4.2 and 4.3, this parameter also contributes qualitatively to the separation of the outer linear elastic fracture mechanics problem and the inner crack tip problem in an asymptotic context. A smaller internal length implies a wider region outside the crack where the fracture mechanics theory may apply. We admit that the choice of this parameter is not a simple one and may constitute one of the difficulties in phase-field modeling of fracture problems.

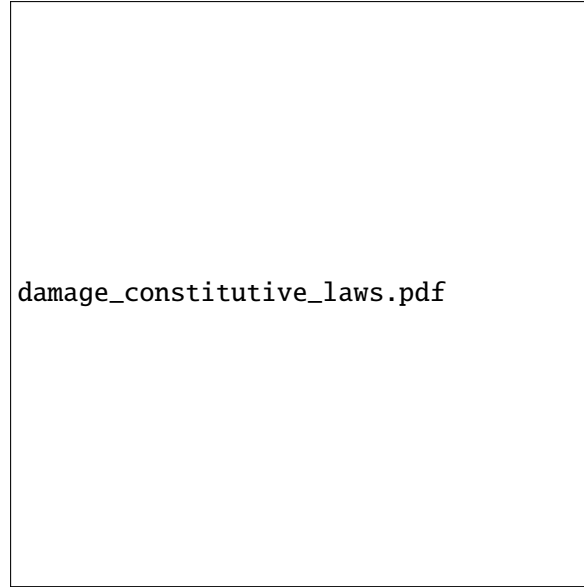


Figure 4.33 – Energy evolution for the dynamic crack branching problem obtained with several constitutive laws

#### 4.4.3 Physical insights into the branching mechanism

Here a physical understanding of crack branching predicted by the dynamic gradient damage model is proposed. According to a brief discussion in Section 1.1.1, two different branching mechanisms can be distinguished *a priori*.

1. The first one concerns micro-branching, where micro-cracks nucleate and propagate along the main crack.
2. The second refers to macro-branching, where the main crack splits into two or more branches.

However it is observed experimentally that macro-branching is always preceded by the micro-branching phenomenon. Using the terminology used in (Sharon & Fineberg, 1996), micro-branches corresponds to “frustrated” branching events while macro-branches are “successful” ones. It is experimental evidence that the microstructure of the crack surface, or equivalently the fracture process zone where nonlinearities dominate, plays an essential role during such branching events, see the pioneer work of (Ravi-Chandar & Knauss, 1984b, 1984c) and a review of these aspects in (Fineberg & Marder, 1999). In the presence of such events, from a macroscopic modeling viewpoint the main crack propagates with an ensemble of many interacting microcracks. More energy is thus dissipated due to the evolution of these micro-branches, see (Sharon et al., 1996).

In gradient damage models, the cross-section of a crack is modeled by a damage profile of a finite band proportional to the internal length, see Section 2.1.1. The fracture toughness  $G_c$  can be identified by the energy consumed during the creation of an optimal damage profile (2.27) in a quasi-static setting, see Section 2.1.1. In dynamics, our numerical simulations indicate that in some circumstances the damage would develop a wider band across the gradient-damage crack, which results in an over-dissipation of energy. We suspect that this phenomenon could be considered as a macroscopic representation of micro-branching with the gradient-damage approach. In Figure 4.34, the final damage field obtained with the (PAMM) model is indicated. Before a critical time  $t_c$ , the initial crack  $\mathbf{P}_0$  propagates with an optimal damage profile  $\alpha_*$ . This kind of *simple* propagation is theoretically and numerically investigated in Sections 2.3 and 4.2. From a critical time  $t_c$ , we observe that the damage band across the crack is wider than the previous case. The continuous widening (micro-branching) eventually leads to the macro-branching of the main gradient-damage crack.

The damage profile at the initial crack tip  $\mathbf{P}_0$  and at a crack tip after this critical time  $t_c$  is compared with the optimal damage profile in Figure 4.35. In the absence of micro-branching, the damage develops

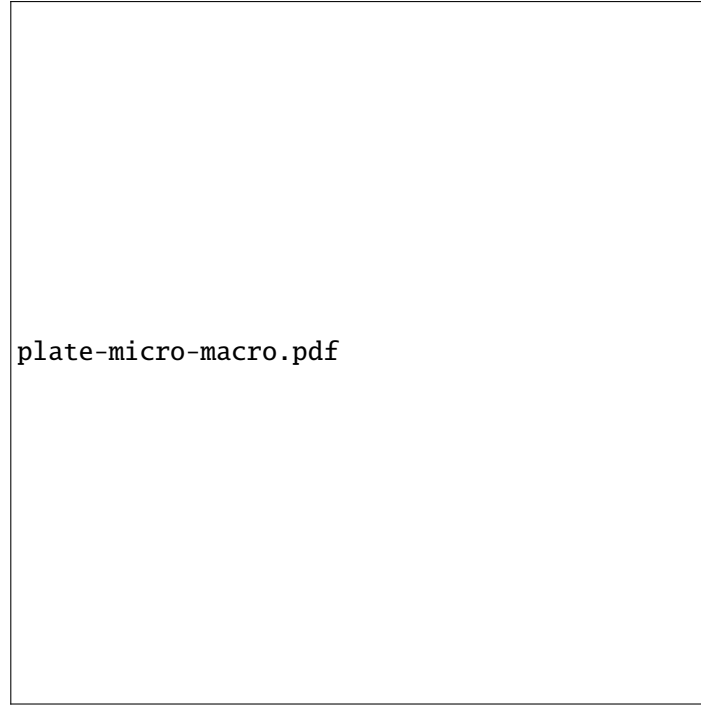


Figure 4.34 – Distinction between micro and macro branching in gradient damage models

an optimal damage profile across the crack if the spatial discretization error (where  $\alpha = 1$  in an interval of width approximately  $h$ , see (1.21)) is ignored, see Section 1.3.2. However during micro-branching, the damage band is even more widened. This implies an increased damage dissipation and may be considered to represent macroscopically the interaction of micro-branches.

Now we propose to perform a zoom in time and in space at  $t_c$  to better understand the physics behind the micro-branching event. Note that during microbranching the classical  $\Gamma$ -convergence estimation (1.20) is no longer valid, since the damage profile varies along the main crack and not necessarily corresponds to the optimal damage profile (2.27). It may only be used to estimate the current energy dissipation rate normalized by the quasi-static fracture toughness

$$\overset{\circ}{l}_t = \frac{\dot{S}_t}{(G_c)_{\text{eff}}} \quad (4.12)$$

where spatial discretization effect is taken into account, see (1.21). The current location of the main crack given by its length  $l_t$  is tracked on the contour  $\alpha_t(l_t, 0) = 0.95$ , where  $y = 0$  refers to the propagation path. The current crack velocity  $\overset{\circ}{l}_t$  is then deduced by applying a second-order difference scheme. The comparison between  $\overset{\circ}{l}_t$  and  $\dot{l}_t$  is illustrated in Figure 4.36. Several remarks are given below.

- Before micro-branching (for example at the point  $A$ ), these two estimations give the same crack velocity. It implies that in the absence of micro-branching a dynamic gradient-damage crack also dissipates the same amount of energy when propagating. This energy dissipation corresponds again to the creation of an optimal damage profile (2.27).
- From the point  $B$  or for  $t > t_c$ , these two estimations of the crack velocity diverge quickly. This point  $B$  or the time  $t_c$  marks the onset of micro-branching. From this point, the value of  $\overset{\circ}{l}_t$  no longer measures the crack speed but only a normalized total energy dissipation due to crack propagation. According to (4.12), much more energy is dissipated during the propagation of the main crack  $l_t$ , while its velocity  $\dot{l}_t$  is well below a fraction (60%) of the Rayleigh wave speed  $c_R$ . In this work, we share the viewpoint announced in (Sharon & Fineberg, 1996) that a lower limiting fracture velocity compared to the Griffith's theory (see Section 1.2.2) can be attributed

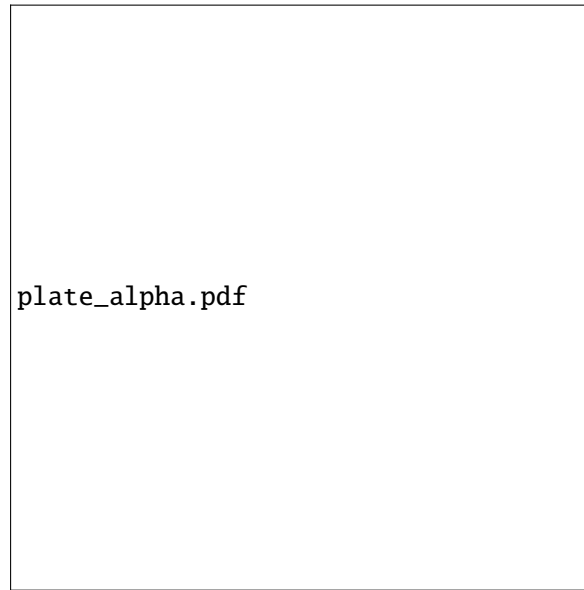


Figure 4.35 – Damage profile in absence (for instance at the initial crack tip  $\mathbf{P}_0$ ) and in presence (for instance at a crack tip just after the critical time  $t_c$ ) of micro-branching, compared with the optimal damage profile

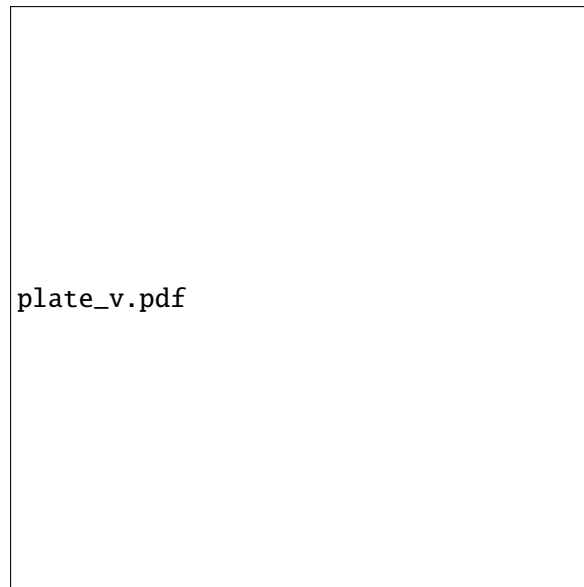


Figure 4.36 – Crack velocity evolution derived from the dissipated energy  $\mathcal{S}$  using (4.12) or from the contour where  $\alpha_t(l_t, 0) = 0.95$ .  $A$  denotes an instant before micro-branching,  $B$  denotes the onset of micro-branching and  $C$  refers to the macro-branching event

to an energy over-dissipation due to micro-branching. This leads to the definition of a velocity dependent apparent fracture toughness  $\Gamma(\dot{l}_t)$  for the main crack, see (Sharon & Fineberg, 1996, 1999). Note that  $\Gamma(\dot{l}_t)$  is only apparent for a single macroscopic crack containing an ensemble of interacting micro-cracks. It measures the total surface creation due to not only the main crack but also micro-cracks nucleated along the previous one. However the real energy dissipated per unit crack surface creation is still constant and is given by the quasi-static  $G_c$ , see (Sharon & Fineberg, 1996).

- The critical velocity  $v_c$  above which the main crack develops micro-branches is approximately  $v_c = 0.4c_R$ . This value agrees with the experimental evidence reported for brittle materials such as PMMA in (Fineberg, Gross, Marder, & Swinney, 1992). A comprehensive review on the microbranching mechanism can be found in (Fineberg & Marder, 1999). The gradient damage model provides thus a better modeling of the critical velocity than several theoretical approaches based on a sharp-interface crack without microbranch interaction (approximately  $0.6c_R$  according to Yoffe, see Figure 1.6 and  $0.46c_R$  obtained in (Katzav et al., 2007)). This confirms the viewpoint shared in (Ravi-Chandar, 1998) that the determination of the critical speed itself  $v_c$  calls for a theory of process zone describing nonlinear material behaviors near the crack tip. The gradient damage approach seems to be a good candidate.

The next objective is to investigate stress distribution before and at the onset of micro-branching. In particular, the hoop (circumferential) stress  $\sigma_{\theta\theta}$  is analyzed near the current crack tip. Its evolution as a function of the distance to the crack  $r$  and as a function of the angle  $\theta$  with respect to the propagation direction ( $x$ -axis) are separately considered. For the latter case, at several distances  $r$  from the crack tip, the hoop stresses are separately normalized by their values at  $\theta = 0$  which gives

$$\Sigma_H(r, \theta) = \frac{\sigma_{\theta\theta}(r, \theta)}{\sigma_{\theta\theta}(r, 0)}.$$

The angular variation of these normalized hoop stresses  $\Sigma_H$  will be compared to the asymptotic expansion of the stress tensor in the Griffith's theory (LEFM) given in (1.4), where the current crack speed  $\dot{l}_t$  derived from the gradient damage crack tip is used in the angular functions  $\Theta_i(\theta, \dot{l}_t)$ . A least-square analysis is performed to identify the possible  $\hat{K}_{II} = K_{II}/K_I$  perturbation in the simulation. The hoop stress variation situated at  $r = D$  is used for such analysis, since according to the analysis in Section 2.3.3 the stress outside the damage process zone contributes to the fracture behavior of the material.

Before the micro-branching event we consider an arbitrary instant  $A$  in Figure 4.36 where the current crack speed  $\dot{l}_t = 0.26c_R$ . The hoop stress distribution is indicated in Figure 4.37. To normalize the spatial distance, the damage band  $D = 2\eta$  is used. Several remarks are given below.

- Contrary to the Griffith's theory, the stress tensor is no more singular at the "crack tip", see also Figure 4.19. The hoop stress is maximized just outside the damage band at  $r \approx D = 2\eta$ .
- Mode-II perturbation is not detected and the angular variation matches perfectly with the linear elastic Griffith's theory in particular for  $r > D$ , *i.e.* outside the damage process zone. The gradient-damage crack just behaves like a Griffith crack similar to the antiplane experiment in Section 4.2 and a separation between the outer linear elastic problem and the inner damage crack tip problem can be achieved. The curve at  $r = 0.5D$  is situated a little above the theoretic prediction, hence the  $r$ -dependence and the  $\theta$ -dependence of the stress tensor is no longer decoupled compared to the linear elastic prediction (1.4). It can be verified that the stress is indeed maximal in front of the crack tip at  $\theta = 0$ .

At the onset of microbranching  $t \approx t_c$ , two arbitrary but close instants near point  $B$  in Figure 4.36 are chosen and the normalized hoop stress distribution is indicated in Figure 4.38. Compared to situation at point  $A$ , several qualitative behaviors of the stress distribution near the crack tip are noteworthy. Using the angular variation at  $r = D$ , a slight mode-II perturbation  $\hat{K}_{II} \approx 0.09$  is detected at the





Figure 4.37 – Hoop stress distribution before micro-branching: (a) dependence on the distance to the crack  $r$  and (b) dependence on the angle  $\theta$  with respect to the propagation direction. To normalize the spatial distance, the damage band  $D = 2\eta$  is used

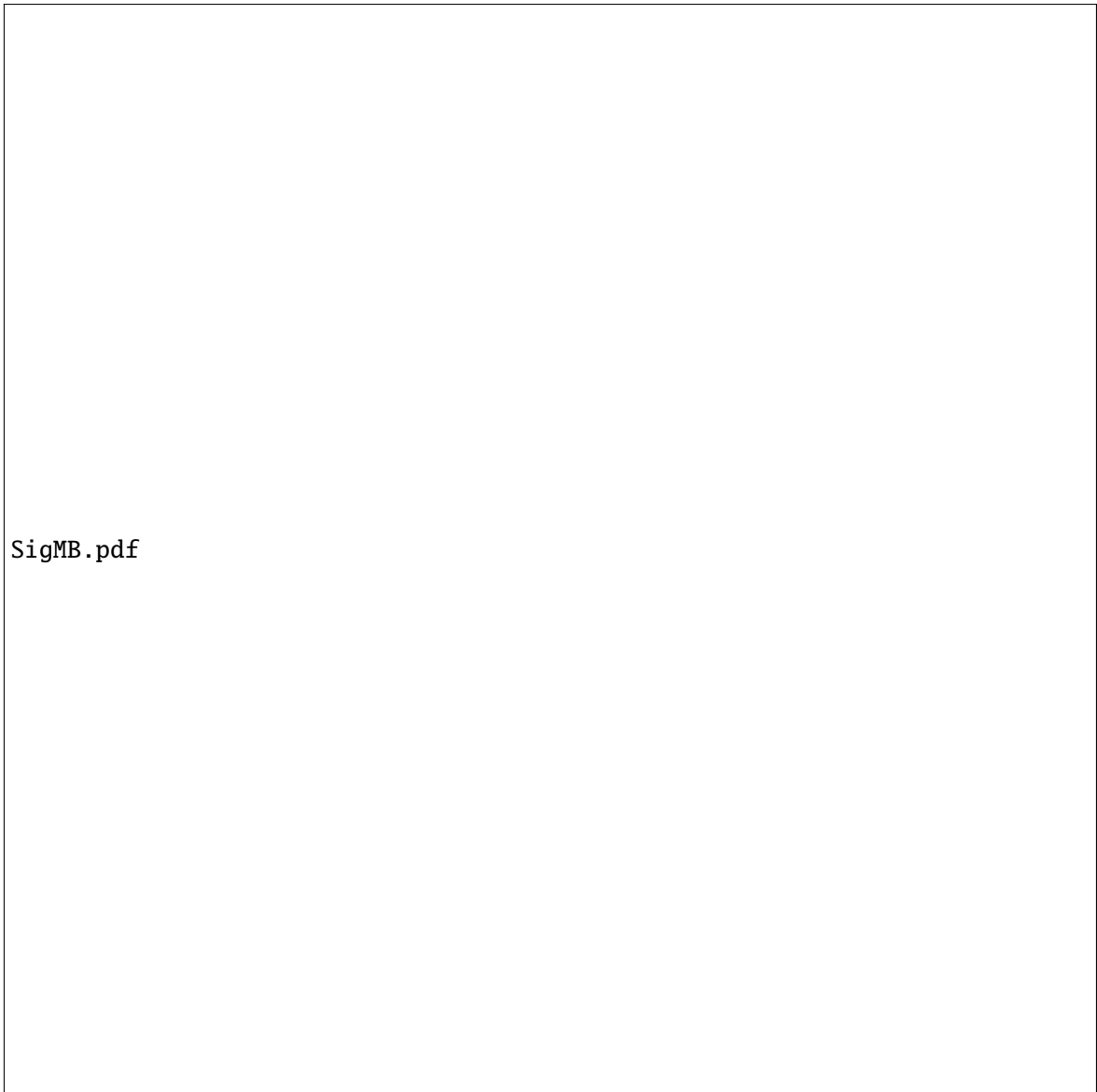


Figure 4.38 – Normalized hoop stress distribution at the onset of micro-branching: (a)  $\dot{l}_t \approx 0.36c_R$  and (b)  $\dot{l}_t \approx 0.43c_R$

onset of microbranching, *i.e.* a loss of symmetry. The existence of such perturbations may be due to structural effects and has already been observed in dynamic fracture experiments, see (Boué, Cohen, & Fineberg, 2015). A mode-II component in the stress tensor contributes to the crack branching instability, but it is not taken into account in many theoretic approaches to crack branching. From Figure 4.38, we observe that the maximum of the normalized hoop stress begins to deviate from the propagation direction  $\theta = 0$ , especially for the curve  $r = 0.5D$ . This indicates that the microbranching phenomenon satisfies a generalized Yoffe's criterion, since in gradient damage models the angular variation depends also on the distance  $r$  to the crack. Such criterion should be only considered as a necessary condition of crack branching. However it could be used to indicate a possible crack branching event. Only mode-I asymptotic expansions are considered in the original Yoffe's criterion, which leads to a higher branching speed  $v_c \approx 0.6c_R$ . According to Figure 4.38, this critical velocity can be reduced by including a mode-II perturbation.

## Conclusion

The dynamic gradient damage model could be computationally more demanding compared to traditional approaches based on a sharp description of cracks. Griffith's law combined with specialized numerical methods could perform reasonably well with much less computational cost for fracture problems in the absence of crack nucleation and complex topology changes. The major advantage of phase-field modeling reside in its generality in treating 2d and 3d crack evolution problems by providing a unified framework from onset to structural failure. Thanks to an efficient parallelization of the solving algorithm (Algorithm 4), the computing time can also be significantly reduced as demonstrated in Figure 4.30.

Two particular damage constitutive laws (AT) and (PAMM) are compared both from a computational and physical point of view. On one hand, the widely used crack surface density function (AT) is less suitable to model brittle fracture since an elastic domain is absent. On the other hand the actual solving of the damage minimization problem (3.9) is more costly than the damage constitutive law (PAMM) which possesses an optimal damage profile of finite band. It is also illustrated that the cost of a general quadratic bound-constrained minimization solver (GPCG) is acceptable.

Finally a better understanding of crack branching predicted by the dynamic gradient damage model is provided. The nucleation of micro-cracks and their subsequent interaction with the main crack is macroscopically identified by a widening of the damage profile perpendicular to the gradient-damage crack. Through numerical simulations, a critical velocity  $v_c \approx 0.4c_R$  is detected above which microbranching events take place, which implies an over-dissipation of energy as the main crack propagates. This critical velocity agrees with the experimental findings and gives a better prediction compared to other theoretical approaches based on a sharp-interface description of cracks which neglects the nonlinear fracture process zone near the crack tip.

Before microbranching, the stress distribution agrees well with the Griffith's theory especially outside the damage process zone with a pure mode-I contribution. However at the onset of microbranching, a mode-II component perturbs the stress distribution. It provides a necessary condition toward an explanation of the branching instability reproduced by the dynamic gradient damage model. Future work will be devoted to a thorough theoretic investigation of this point. In particular, the exact role played by the internal length should be analyzed.

## 4.5 Edge-Cracked Plate Under Shearing Impact

We consider in this section a pre-notched two-dimensional plane strain plate impacted by a projectile. In the dynamic fracture community this is often referred as the Kalthoff-Winkler experiment reported by *e.g.* (Kalthoff, 2000) where a failure mode transition from brittle to ductile fracture is observed for a high strength maraging steel when the impact velocity is increased. The objective here is to investigate the use of several tension-compression asymmetry formulations analyzed in Section 2.2 in a dynamic brittle fracture problem. In particular, the widely used elastic energy density split proposed in (Miehe, Hofacker, & Welschinger, 2010) among the phase-field community will be compared with

other models. Furthermore, some dynamic fracture phenomena reproduced by the gradient damage model are also presented. The thematic subjects covered here are thus summarized in Table 4.14.

Table 4.14 – Thematic subjects covered in this section

	Going dynamical	$\alpha \leftrightarrow \phi$	$\nabla \alpha \rightarrow \Gamma$	Experimental validation
Theoretics				
Numerics		👍	👍	👍

**Problem setting** Due to symmetry, only the upper half part of the plate will be considered. The geometry and the boundary conditions for the reduced problem are described in Figure 4.39. As in

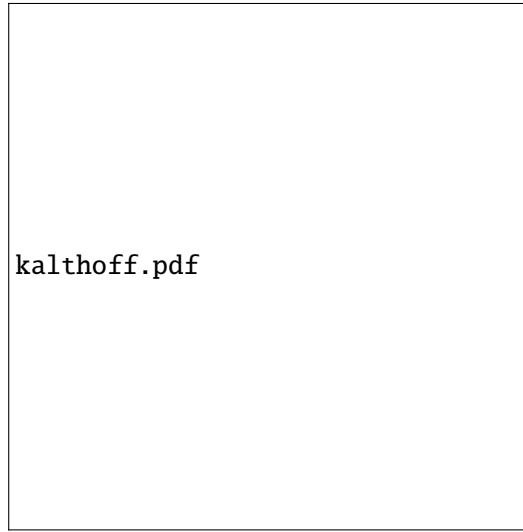


Figure 4.39 – Geometry and boundary conditions for the edge-cracked plate under shearing impact problem. Damage field  $\alpha_t$  at  $t = 8 \times 10^{-5}$  s ranging from 0 (gray) to 1 (white)

(Borden et al., 2012; Hofacker & Miehe, 2012), the projectile impact is modeled by a prescribed velocity with an initial rise time of  $1 \times 10^{-6}$  s to avoid velocity shocks. The material parameters are borrowed from (Borden et al., 2012) except that the internal length  $\eta$  is set to 0.2 mm. An unstructured and uniform triangular mesh with  $h \approx 0.1$  mm is used, arriving at approximately 3 million elements. The explicit time-stepping (Algorithm 4) implemented in the EPX software is adopted. The current time increment is again calculated based on the CFL condition with a security factor of 0.8. Due to a lower computational cost and a more brittle material behavior, the damage constitutive law (PAMM) is used for this simulation.

As a reference, we use the elastic energy split proposed in (Freddi & Royer-Carfagni, 2010) where the positive semidefinite part of the total strain will contribute to damage. The initial crack is introduced via a real notch in the geometry. A similar strong scaling curve as Figure 4.30 is obtained with up to 16 cores, see Figure 4.40. Due to the additional spectral decomposition, the “damage assembly” phase represents now approximately 50% of the total computational time while the “damage solving” still accounts for only 10%. The actual computation of the eigenvalues and eigenvectors of a  $3 \times 3$  symmetric matrix is described in Section 3.3. The energy evolution obtained by varying the number of processors is indicated in Figure 4.41. Similar to Section 4.4, small differences can be observed between these parallel computations in terms of global energy evolution, which may be again due to floating point arithmetic and different setting of preconditioners. With an imposed impact speed  $v = 16.5$  m/s, the damage field  $\alpha_t$  at  $t = 8 \times 10^{-5}$  s produced by the EPX software is depicted in Figure 4.39. The initial ( $73^\circ$ ) and average ( $64^\circ$ ) propagation angles are in good agreement with the experimental results and other phase-field simulations (Borden et al., 2012; Hofacker & Miehe,



Figure 4.40 – Strong scaling results for the Kalthoff problem with 3 million elements

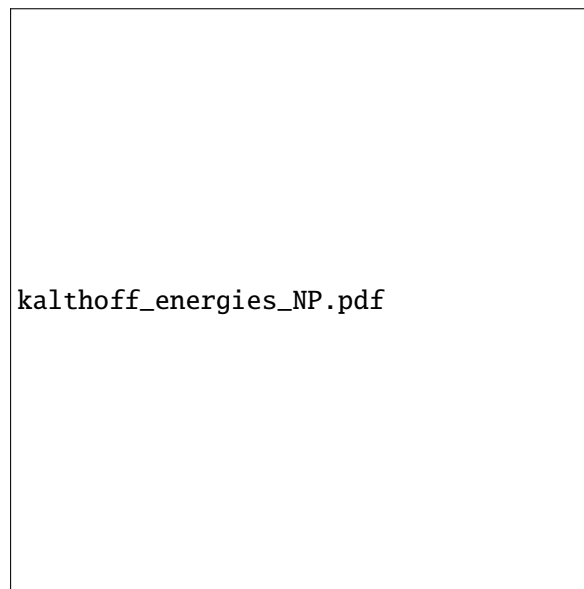


Figure 4.41 – Energy evolution obtained by varying the number of processors

2012) based on the damage constitutive law (AT) and the tension-compression asymmetry formulation proposed by (Miehe, Hofacker, & Welschinger, 2010).

#### 4.5.1 Gradient-damage modeling of dynamic fracture

If the initial crack  $\Gamma_0$  is modeled via an initial damage field  $\alpha^{-1}$ , as for the previous dynamic crack branching example, no crack propagation is observed and the structures behaves as if the crack does not exist, *i.e.* the crack closure phenomenon. The horizontal displacement  $u_x$  obtained in both cases at  $t \approx 2.4 \times 10^{-5}$  s when the real notch case starts to propagate is presented in Figure 4.42. In the real

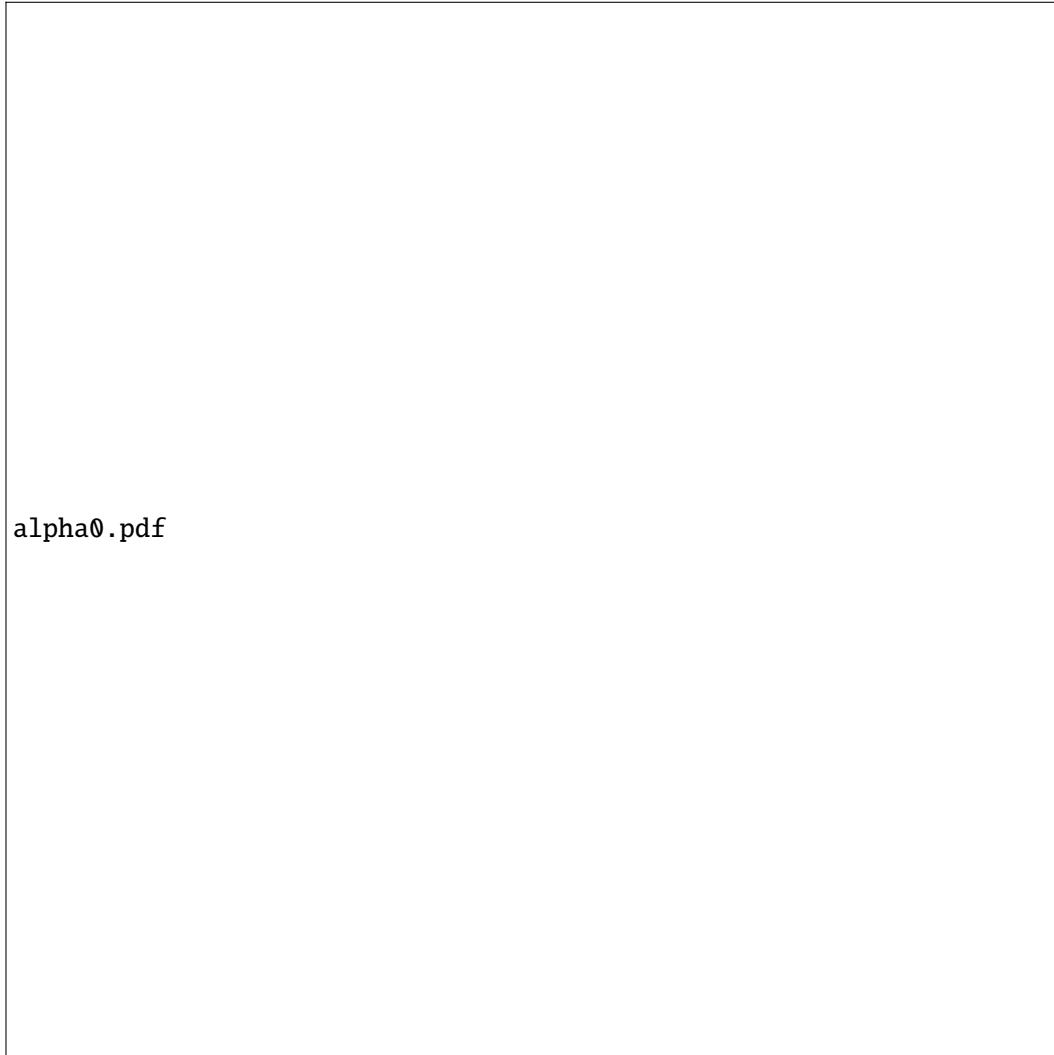


Figure 4.42 – Displacement  $u_x$  ranging from 0 mm (blue) to 0.4 mm (red) for (a) the real notch induced initial crack and (b) the damage induced initial crack, at  $t \approx 2.4 \times 10^{-5}$  s when the crack starts to propagate in the real notch case (a)

notch induced initial crack case, *contact condition is not prescribed* on the initial crack lips distanced by a finite height  $\approx h$  in the geometry. As can be checked from Figure 4.42, no material interpenetration happens in the real notch case and waves propagate in the plate through the lower impacted edge. However in the damage induced initial crack case, possible normal compressive stresses can indeed be transferred to the upper part of the plate, via the tension-compression asymmetry model (Freddi & Royer-Carfagni, 2010) which simulates a crack closure. Nevertheless, our simulation illustrates that this model also prohibits tangential relative movement along the crack lips, and a *perfect adhesion* (no-slip condition) is observed, *i.e.* exactly the opposite situation compared to the real notch case. This result is expected from our discussions on future improvement of these tension-compression

formulations in Section 2.2.3. The failure of these elastic energy decompositions to account for the actual damage value or its gradient approximating the crack normal has been reported by (May et al., 2015; Strobl & Seelig, 2015). In the subsequent discussions we will only consider the case where the initial crack is introduced via a real notch in the geometry.

The numerically obtained damage profile on a cross-section in the reference configuration parallel to the crack normal is compared to the theoretical one (2.7). From Figure 4.43, it can be observed that the numerical damage profile is wider than the analytical prediction by approximately  $h = 0.1$  mm. This phenomena leads to the definition of a numerically amplified effective fracture toughness  $(G_c)_{\text{eff}}$ , see (1.21), which in this example is given by  $(G_c)_{\text{eff}} = (1 + 3h/(8\eta))G_c$  corresponding to the constitutive law (PAMM) adapted from (Hossain et al., 2014).



Figure 4.43 – Damage profile perpendicular to the crack

Assuming that micro-branching does not take place, from the  $\Gamma$ -convergence result the crack length  $l_t$  can be estimated by (1.20). A 2nd-order difference scheme is then used to calculate the crack velocity. The temporal evolution of the crack length and the velocity is indicated in Figure 4.44. As can be seen from Figure 4.44, the crack speed is well bounded by the Rayleigh wave speed (here  $0.7c_R$ ), the theoretical limiting speed for an in-plane crack. It should be noted that this upper bound is rooted in the stability condition (2.17) and the energy balance (2.18), contrary to the thick level set approach (Moreau et al., 2015) where this limiting speed is considered as an additional modeling parameter. The crack length is approximately 90 mm at  $t = 8 \times 10^{-5}$  s when the crack is about to reach the boundary, cf. Figure 4.39. This estimation agrees fairly well with a direct calculation based on a straight crack propagating at  $64^\circ$ , which gives about 83 mm. We believe that the discrepancy on crack length as well as a smaller limiting speed for brittle materials reported in experiments can be attributed to the dynamic instability mechanism reviewed in (Fineberg & Marder, 1999) and discussed in this work in Section 4.4.3. As the crack speed approaches a critical speed approximately  $0.4c_R$ , micro-branches appear along the main crack and hence more energy is dissipated during propagation. In that case (1.20) is no longer valid and the apparent fracture toughness should be adapted to be velocity-dependent. With the (AT) constitutive law, authors of (Borden et al., 2012; Vignollet et al., 2014) report a systematic overestimation of the damage dissipation energy with (1.20). Following our discussion in Section 4.4, it could be mainly due to the absence of a purely elastic domain and the fact that damage evolves even in the stress-hardening phase. However in the definition of the fracture toughness, this phenomena is not taken into account, see (Bourdin et al., 2008).



Figure 4.44 – Crack length and velocity obtained for the edge-cracked plate with an imposed impact speed  $v = 16.5$  m/s

#### 4.5.2 Velocity effect and use of different tension-compression models

When the prescribed impact velocity is increased from  $v = 16.5$  m/s to  $v = 100$  m/s, successive crack branching and nucleation of cracks at the lower-right corner due to high tensile stresses are observed as can be seen from Figure 4.45. The hydrostatic stress  $p_t = \frac{1}{2} \text{tr } \sigma_t$  is presented in the deformed configuration and we verify that no damage is produced in the compression zones. To visualize the crack, elements with  $\alpha_t > 0.9$  are hidden in the graphical output. Similar phenomena have been reported in (Hofacker & Miehe, 2012) with  $v = 50$  m/s. Recall that in the Kalthoff-Winkler experiment a failure-mode transition from mode-I to mode-II is observed when the impact velocity increases. The discrepancy between our simulation and the experiment is due to the material constitutive behavior. As a material parameter, the tension-compression formulation of (Freddi & Royer-Carfagni, 2010) coupled with a purely elastic model favors propagation of mode-I cracks in the direction perpendicular to the maximal principle stress. On the contrary, the high strength steel used in the experiment develops a considerable plastic zone along the mode-II crack and an elastic-plastic-damage model should be more suitable, see for example the work of (Miehe, Hofacker, Schänzel, & Aldakheel, 2015). Nevertheless, experimentally more bifurcations are indeed observed for brittle materials such as glass when the impact velocity is increased, which is known as a *velocity effect* in (Schardin, 1959).

On the other hand, the widely used elastic energy density split proposed in (Miehe, Hofacker, & Welschinger, 2010) produces diffusive damage in compression zones. From Figure 4.46, we observe appearance of damage at the lower-left corner and at the lower surface of the initial crack edge, even though they are both under compression. This phenomena is conforming to our previous theoretical analysis of this model on a homogeneous uniaxial compression experiment in Section 2.2.2, where it is found that damage grows even though the compressive stress is still increasing in its absolute value.

The tension-compression split based on the trace of the total strain (Amor et al., 2009) is also tested. In (Lancioni & Royer-Carfagni, 2009), the pure compression version of this model is used to simulate shear cracking behavior in the stone ashlar. In this dynamic impact problem, we also observe at  $t \approx 7 \times 10^{-6}$  s appearance of mode-II cracks originating from the impacted-edge, see Figure 4.47. We conclude that the tension-compression split (2.38) could indeed be considered as a material parameter as it represents the fracture mechanism determined by the microstructure and leads to different macroscopic fracture patterns. Note however that the calculation suddenly stops after that time due to an extremely small CFL time step  $\Delta t_{\text{CFL}} = h/c$ , which is caused by a highly distorted





Figure 4.45 – Simulation results at  $t = 4 \times 10^{-5}$  s with an impact speed  $v = 100$  m/s: (a) the damage field  $\alpha_t$  ranging from 0 (blue) to 1 (red), and (b) the hydrostatic stress  $\frac{1}{2} \text{tr } \sigma_t$  ranging from less than  $-1 \times 10^4$  MPa (blue) to more than  $1.5 \times 10^3$  MPa (red). The tension-compression asymmetry model (Freddi & Royer-Carfagni, 2010) is used



Figure 4.46 – Simulation results at  $t = 4 \times 10^{-5}$  s with an impact speed  $v = 100$  m/s: (a) the damage field  $\alpha_t$  ranging from 0 (blue) to 1 (red), and (b) the hydrostatic stress  $\frac{1}{2} \text{tr } \sigma_t$  ranging from less than  $-1 \times 10^4$  MPa (blue) to more than  $1.5 \times 10^3$  MPa (red). The tension-compression asymmetry model (Miehe, Hofacker, & Welschinger, 2010) is used

element  $h \rightarrow 0$  in the explicit dynamics context. The same numerical issue has been reported by (Piero et al., 2007) in which an Ogen hyperelastic model is used. Remark that the use of a tension-compression split based on the positive eigenvalues of the strain, *i.e.* that of (Freddi & Royer-Carfagni, 2010; Miehe, Hofacker, & Welschinger, 2010), actually circumvents this problem by revising the material constitutive behavior.

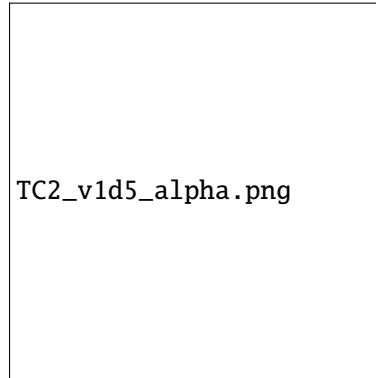


Figure 4.47 – Damage field at  $t \approx 7 \times 10^{-6}$  s obtained for the edge-cracked plate with an imposed impact speed  $v = 100$  m/s. The elastic energy split (Amor, Marigo, & Maurini, 2009) is used

## Conclusion

Different tension-compression asymmetry formulations in Section 2.2 are analyzed numerically here. Some physical properties derived through a uniaxial traction experiment are verified in actual dynamic fracture problems. The elastic energy split proposed by (Freddi & Royer-Carfagni, 2010) is recommended for brittle materials because homogeneous (diffusive) damage does not occur under compression. However these models should be modified to correctly account for the unilateral contact condition. A better strategy may be to use a transition algorithm between the smeared and the sharp-interface description of cracks. To successfully model the transition from mode-I to mode-II, one may need to couple a plasticity model with the current dynamic gradient damage model.

## 4.6 Crack Arrest Due to the Presence of a Hole

This section is devoted to a two-dimensional experimental validation of the dynamic gradient damage model for brittle materials. The thematic subjects covered here are thus summarized in Table 4.15.

Table 4.15 – Thematic subjects covered in this section

	Going dynamical	$\alpha \leftrightarrow \phi$	$\nabla \alpha \rightarrow \Gamma$	Experimental validation
Theoretics				
Numerics				👍

**Problem setting** The problem considered is the “one crack two holes” test studied in (Haboussa et al., 2011), where it is found that in dynamics cracks may be pushed away from the holes present in the domain due to wave reflections. The geometry and the boundary conditions are recalled in Figure 4.48. Plane stress condition is assumed. Initial crack is introduced via a real notch in the geometry. The damage constitutive law (PAMM) is used again due to its interesting properties discussed in the dynamic crack branching problem. Since PMMA is a brittle material (Grégoire et al., 2007) and the model of (Miehe, Hofacker, & Welschinger, 2010) possesses a peculiar behavior under high compression, the tension-compression asymmetry formulation proposed by (Freddi & Royer-Carfagni, 2010) is adopted.

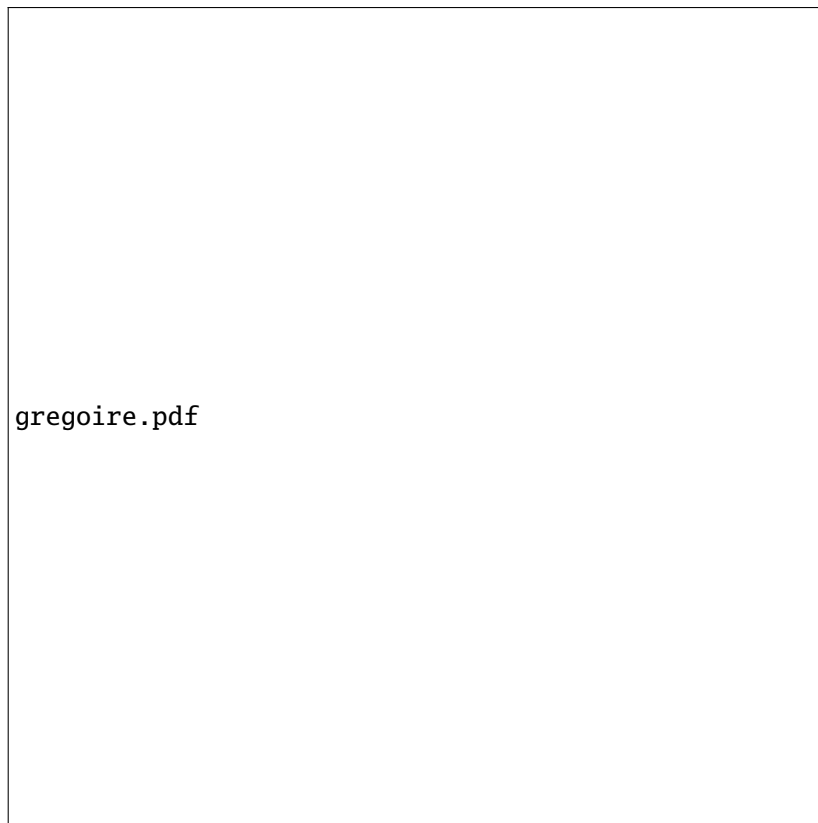


Figure 4.48 – Geometry and boundary conditions for the “one crack two holes” experiment studied in (Haboussa, Grégoire, Elguedj, Maigre, & Combescure, 2011). Damage field  $\alpha_t$  at  $t = 2 \times 10^{-4}$  s ranging from 0 (gray) to 1 (white)

Materials properties of PMMA, including the density, the dynamic Young's modulus and the Poisson ratio, are borrowed from (Haboussa et al., 2011). In their calculations, crack propagation is based on a variant of the Griffith's law where one critical stress intensity factor  $K_{IC} = 1.03 \text{ MPa}\sqrt{\text{m}}$  predicts initiation and another  $K_{IA} = 0.8 \text{ MPa}\sqrt{\text{m}}$  determines crack propagation and arrest. The latter one is used in our calculation as it deals with the most important phase of crack evolution. It is then converted to the fracture toughness

$$G_c = \frac{K_{IA}^2}{E} \approx 0.2667 \text{ N/mm} \quad (4.13)$$

thanks to the Irwin's formula under plane stress condition. The material internal length, or equivalently the maximal tensile stress of PMMA through (2.6), is unknown. Two reasonable values are tested corresponding respectively to a critical stress 70 MPa or 80 MPa, which gives along with (4.13) either  $\eta \approx 0.05 \text{ mm}$  or  $\eta \approx 0.0375 \text{ mm}$ . An unconstrained mixed triangular-quadrilateral mesh refined with  $h \approx 2 \times 10^{-2} \text{ mm}$  near the initial crack and all possible nucleation sites is used, arriving at approximately 400 000 elements. The explicit time-stepping (Algorithm 4) implemented in the EPX software is adopted. The current time increment is updated based on the CFL condition with a security factor of 0.8.

**Simulation results and discussion** The simulations results are illustrated in Figure 4.49. In both cases crack arrest is reproduced due to the high compression area under the right circular hole. In the case when the maximal tensile stress is set to  $\sigma_m = 70 \text{ MPa}$ , secondary crack nucleation is observed at the right circular hole boundary under high tension. This phenomena is not observed in experiments and hence the critical stress value of  $\sigma_m = 70 \text{ MPa}$  is thus underestimated. In the  $\sigma_m = 80 \text{ MPa}$  case, no secondary crack nucleation is found. This result again highlights the role played by the internal length  $\ell$  as a material parameter.

As the crack front is not explicitly tracked in phase-field modeling of fracture, here the current crack tip is located on the contour  $\alpha = 0.9$  at the farthest point in the  $x$ -direction. We then compare the numerical crack tip abscissa evolution with the experimental one (Haboussa et al., 2011), in Figure 4.50. Very good agreement can be found in the crack initiation and propagation phase. The crack arrest predicted is slightly conservative compared to the experimental one. This could be due to the small deviation of the initial crack from the symmetry axis in the experiment (Haboussa et al., 2011). Meanwhile the maximal tensile stress  $\sigma_m \geq 80 \text{ MPa}$  could be considered as an adjusting parameter of the model. More simulations could be performed to determine its best value, at a price of using a more refined mesh since  $\ell \propto 1/\sigma_m^2$  according to (2.6).

**Conclusion** The dynamic gradient damage model outlined in Definition 2.1 along with the (PAMM) damage constitutive law and the tension-compression model of (Freddi & Royer-Carfagnini, 2010) is experimentally validated for PMMA specimens. Further studies will focus on applications to concrete structures.

## 4.7 Brazilian Splitting Test on Concrete Cylinders

This section is devoted to three-dimensional numerical simulations of the Brazilian tests on concrete cylinders. Due to an increasing compressive load applied along the diameter direction, eventually fracture takes place along the loading direction and the cylinder splits vertically into two parts. One objective here is to verify the EPX implementation of the explicit time-stepping procedure summarized in Algorithm 4 during a three-dimensional calculation. Furthermore, different tension-compression asymmetry formulations analyzed in Section 2.2 are compared with respect to their aptitude to reproduce such fracture pattern. The size effect reported by various authors such as (Rocco, Guinea, Planas, & Elices, 1999; Ruiz, Ortiz, & Pandolfi, 2000) is also investigated using the dynamic gradient damage model. The thematic subjects covered here are thus summarized in Table 4.16.

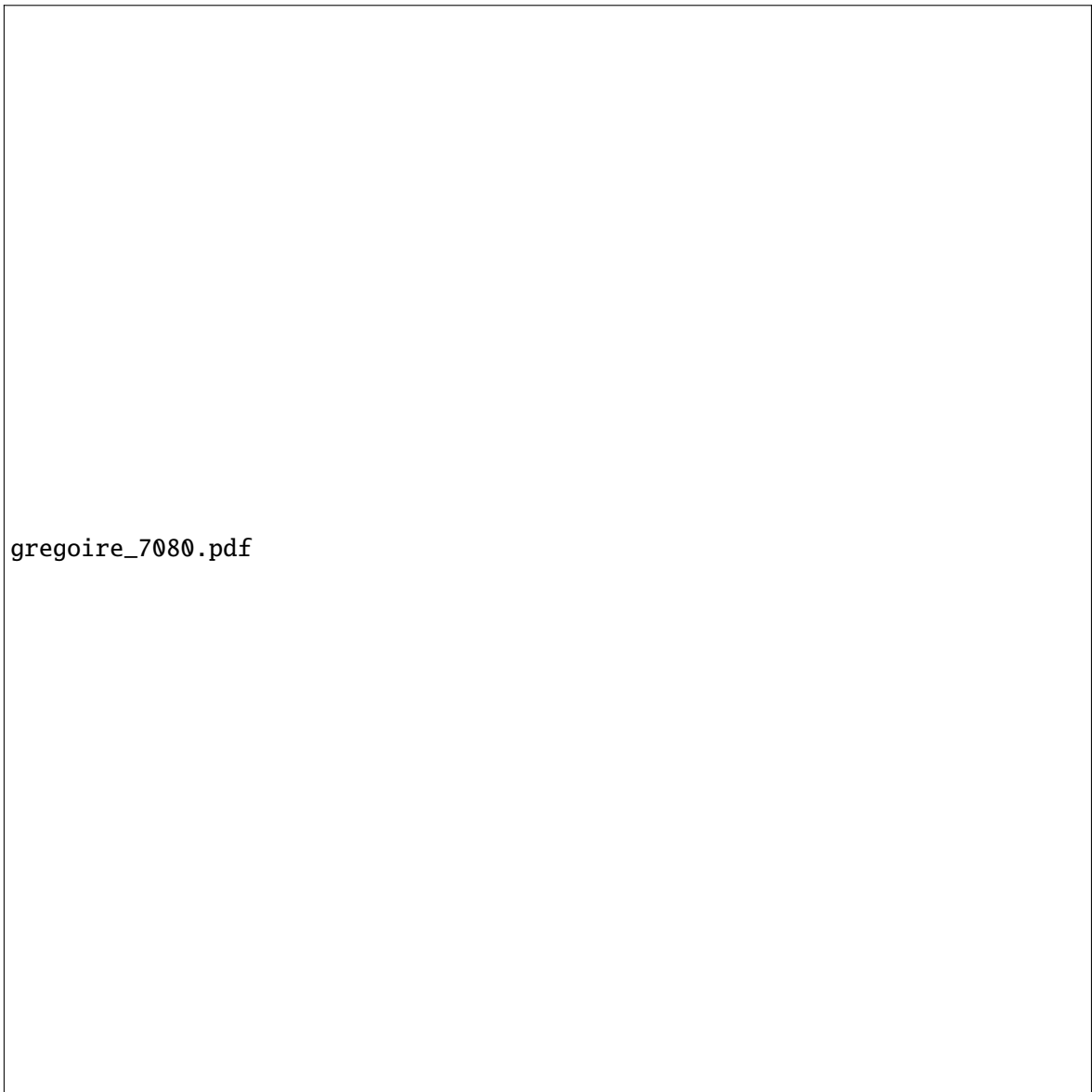





Figure 4.49 – Hydrostatic stress  $p_t = \frac{1}{2} \operatorname{tr} \sigma_t$  ranging from less than  $-30$  MPa (blue) to more than  $30$  MPa (red) for (a)  $\sigma_m = 70$  MPa at  $t \approx 1.6 \times 10^{-4}$  s, and (b)  $\sigma_m = 80$  MPa at  $t \approx 1.8 \times 10^{-4}$  s, in the crack arrest problem

Table 4.16 – Thematic subjects covered in this section

	Going dynamical	$\alpha \leftrightarrow \phi$	$\nabla \alpha \rightarrow \Gamma$	Experimental validation
Theoretics				
Numerics				

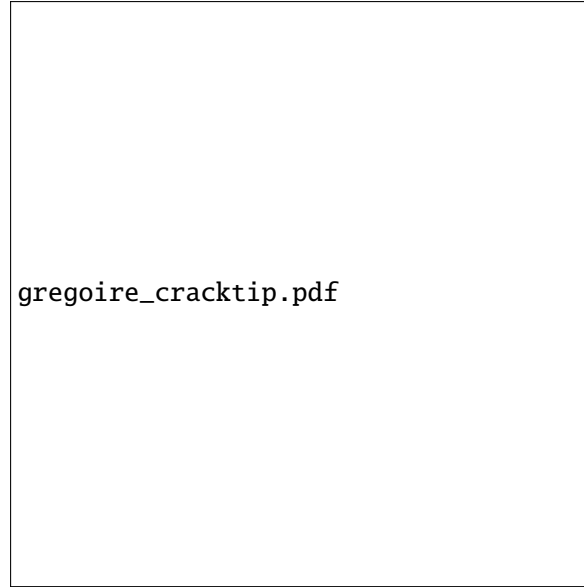


Figure 4.50 – Crack tip abscissa evolution in the crack arrest problem. Comparison between the  $\sigma_m = 80$  MPa case and the experimental results

**Problem setting** The geometry and loading conditions are summarized in Figure 4.51. Two diameters will be considered here to investigate possible size effects:  $D = 500$  mm and  $D = 200$  mm. The bearing strips are introduced to prevent ill-posed concentration. In this work they are assumed to be a part of the cylinder for the sake of simplicity, however more realistic modeling involving unilateral contact conditions is possible. The compressive loads are prescribed by a given velocity evolution  $\mathbf{V}_t$  on the outer surface of the strips. In this work the dynamic effect is not the main objective and hence a relatively low loading velocity is used  $\|\mathbf{V}_t\| = \pm 0.1$  m/s. An initial rise time of  $1 \times 10^{-6}$  s is introduced to avoid velocity shocks. The material parameters for a typical concrete are borrowed from (Ruiz et al.,

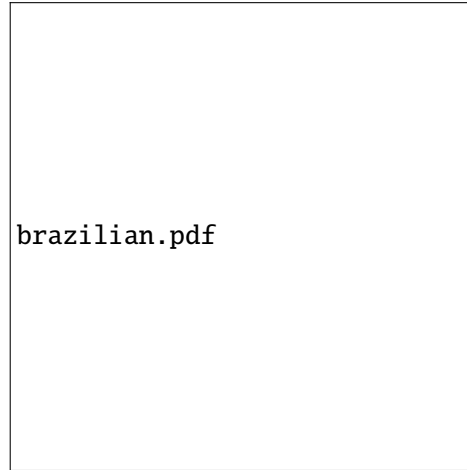


Figure 4.51 – Three-dimensional Brazilian test on a concrete cylinder characterized by its diameter  $D$  and its height  $W$ . The compressive loads modeled as prescribed velocities are transmitted to the cylinder along the vertical diameter direction via two bearing strips of width  $D/16$

2000). Numerically an unstructured tetrahedral mesh is used to discretize the cylinder volume. A uniform mesh size of  $h \approx 10$  mm leads to approximately  $1 \times 10^5$  finite elements for  $D = 500$  mm and 25 000 elements for the small cylinder with  $D = 200$  mm. The material and numerical parameters are summarized in Table 4.17. The damage constitutive law (PAMM) is used. Using the identification of the equivalent fracture toughness (2.9), the internal length  $\eta$  can be derived from  $G_c$  and  $\sigma_c$ , which gives  $\eta \approx 46$  mm.

Table 4.17 – Material and numerical parameters for the Brazilian test

$\rho$	$E$	$\nu$	$G_c$	$\sigma_c$	$h$
2450 kg/m <sup>3</sup>	37.9 GPa	0.15	66.2 N/m	4.53 MPa	10 mm

#### 4.7.1 Fracture pattern predicted by different tension-compression models

Pursuing the work of Section 4.5, the use of different tension-compression asymmetry formulations as discussed in Section 2.2 are investigated here with respect to their aptitude to reproduce the desired vertical splitting fracture pattern of the cylinder. As a genuine material parameter, the choice of these formulations in a numerical simulation should be justified by experimental facts on the specific material. In this work two particular models are compared: the approach proposed by (Amor et al., 2009) by separating the deviatoric and spheric part of the sound elastic energy and the model proposed by (Freddi & Royer-Carfagni, 2010) which is recommended following our analyses in Section 4.5. The big cylinder with  $D = 500$  mm is first used. The final fracture pattern obtained by these two formulations is indicated in Figure 4.52. Several remarks are given as follows.



Figure 4.52 – Fracture pattern represented by the damage field ranging from 0 (blue) to 1 (red) for the Brazilian splitting test obtained by two tension-compression asymmetry models: (a) the model of (Amor, Marigo, & Maurini, 2009) and (b) the model of (Freddi & Royer-Carfagni, 2010)

- With the model proposed by (Amor et al., 2009), damage is concentrated where the loads are



applied. This experiment illustrates its deficiency to describe the microscopic/macrosopic fracture mechanism of concrete.

- Vertical splitting is reproduced by the formulation of (Freddi & Royer-Carfagni, 2010). It illustrates that the damage mechanism in concrete is indeed induced by local tensile stresses. It can be seen that fracture is homogeneous in the height  $W$  direction. A two-dimensional modeling could suffice. In this work the obtained three-dimensional simulation results verify the generality of the variational formulation outlined in Definition 2.1 and the robustness of the EPX implementation described in Section 3.3.2.

#### 4.7.2 Temporal evolution of global quantities and fields

The evolution of global quantities and fields is now investigated. A useful reference time scale  $t_{\text{ref}} = D/c$ , which corresponds to the time for the elastic wave to travel across the cylinder diameter, is used to normalize the time variable. First, we are interested in the temporal evolution of the applied vertical load  $F_t$  transmitted through the bearing strip. From basic static elastic analyses, the load  $F_t$  induces a maximum splitting tensile stress  $\sigma$  at the center of the diameter which is given by

$$\sigma = \frac{2F}{\pi WD} \quad (4.14)$$

According to the damage criterion (2.23) for an initially sound body (as analyzed in Section 4.1), damage or fracture is expected to take place at the center where the criterion is firstly satisfied. A critical load  $F_{\text{ref}}$  which corresponds to the critical stress  $\sigma_c$  in (4.14) can thus be defined. It is used for normalization. The evolution for  $t \mapsto F_t$  is illustrated in Figure 4.53. Some snapshots of the damage field at some particular instants are taken to complement the curve.

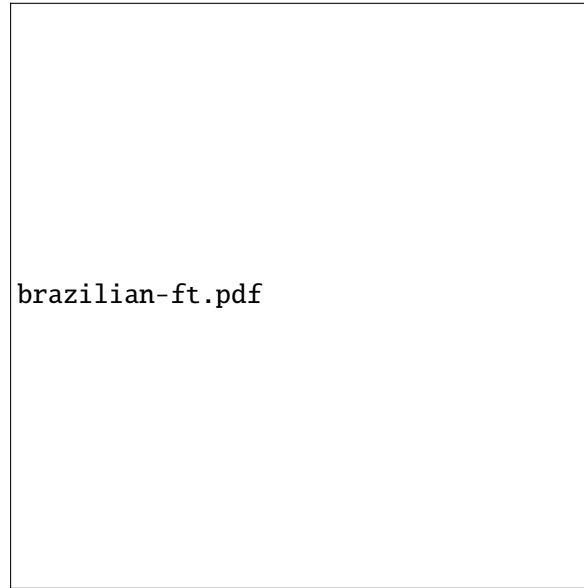


Figure 4.53 – Temporal evolution of the applied load transmitted through the bearing strip with or without activation of the erosion mechanism available in the EPX software, illustrated by snapshots of the damage field ranging from 0 (blue) to 1 (red)

The curve labeled “Without erosion” is first analyzed. It can be verified that damage begins to evolve at the center when the splitting stress induced by the transmitted load  $F_t$  attains the material critical stress. As  $F_t$  increases, damage develops and propagates into a crack band along the vertical diameter direction until a complete split of the cylinder. However the temporal evolution of  $F_t$  requires further investigation:

- The applied load attains a peak of approximately  $1.2F_{\text{ref}}$ , which may be due to structural hardening effects between the damage initiation when  $F_t \approx F_{\text{ref}}$  and the onset of fracture.

- After the peak, unexpectedly the load is not instantaneously decreasing to zero. However, its temporal evolution indicates that there exists still some residual stiffness along the vertical crack. Remark that the loading condition is very similar to the edge-cracked plate experiment studied in Section 4.5, *i.e.* sliding loads parallel to an existing or established gradient-damage crack. Continuing our analyses there, it is suspected that this peculiar temporal evolution is again due to the deficiency of the existing tension-compression models to represent a genuine unilateral condition, see Section 2.2.3. In particular, the crack normal direction is not considered in these models, hence some residual stresses may be present parallel to the crack. The definition of such normal vectors, nevertheless, is not trivial due to the smeared description. We reiterate the conclusion of Section 4.5 that a better strategy may be to use a transition algorithm between the smeared and the sharp-interface description of cracks.
- A possible remedy within the EPX environment may be to activate the “erosion” mechanism. When a crack is detected (for example when the effective degradation (3.5) approaches zero within a tolerance) for a certain finite element, its contribution to the internal force vector (3.3) will be ignored. By doing so, an approximative stress-free condition is thus by default prescribed along the crack lip. With the activation of the erosion mechanism, the fracture pattern is not altered however as can be seen from Figure 4.53, the transmitted load quickly decreases to zero after the peak value, which corresponds to ultimate structural failure. Future work will be devoted to a thorough investigation of the erosion mechanism to take into account for instance unilateral effects.

Temporal evolution of global energetic quantities is illustrated in Figure 4.54. It can be seen that initially inertia is not important which in turn ensures the validity of (4.14). During crack nucleation and propagation along the diameter, the kinetic energy suddenly develops and becomes comparable to the elastic energy, which illustrates the unstable or brutal nature of the crack propagation phase. A full dynamic analysis is indeed more appropriate for this Brazilian test.

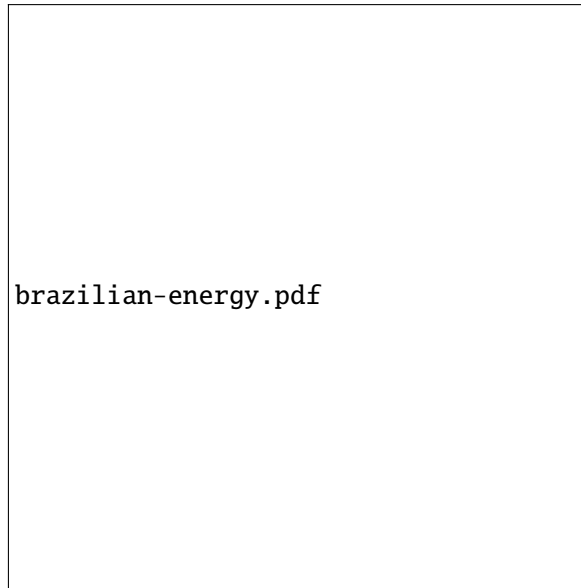


Figure 4.54 – Temporal evolution of global energetic quantities with the erosion mechanism

### 4.7.3 Size effect

A size effect is present for the present Brazilian test following the analyses in (Rocco et al., 1999; Ruiz et al., 2000). In particular, smaller cylinders should produce higher peak loads (normalized by  $F_{\text{ref}}$  determined by the material critical stress and the diameter) at the onset of fracture, confirming the commonly acknowledged idea *smaller is stronger*. On the other hand, bigger cylinders should break as

soon as the critical material stress is reached. The temporal evolution of the applied load  $F_t$  for two concrete cylinders with different diameters are indicated in Figure 4.55. It can be seen that the fracture pattern remains similar. The above size effect is numerically verified and reproduced by the dynamic gradient damage model. The existence of such size effects is due to the introduction of the material internal length  $\ell$ , see also the work on crack nucleation of a bar in Section 4.1.



Figure 4.55 – Temporal evolution of the applied load transmitted through the bearing strip for two concrete cylinders with different diameters

## Conclusion

In terms of fracture pattern prediction for concrete structures, the tension-compression model proposed by (Freddi & Royer-Carfagni, 2010) seems to be a good candidate compared to other choices. However the crack normal vector is not taken into account and residual stiffness may be present along and parallel to the crack lip. The “erosion” mechanism available in the EPX software could produce a real crack however its use need further investigation. Size effect for Brazilian tests on concrete cylinders is reproduced by the gradient damage model. The existence of such experimentally validated size effects is due to the introduction of the material internal length  $\ell$ .

## 4.8 Dynamic Fracture of L-Shaped Concrete Specimen

This section is devoted to a gradient-damage modeling of the dynamic tensile test on a two-dimensional plane-strain L-shaped concrete specimen. Compared to Section 4.7, the objective here is to investigate dynamic or velocity effects in dynamic fracture problems on concrete structures, *i.e.* their influence on the temporal evolution of global quantities and spatial crack path. An experimental validation of the model is also considered against the results obtained in (Ožbolt, Bede, Sharma, & Mayer, 2015). The thematic subjects covered here are thus summarized in Table 4.18.

Table 4.18 – Thematic subjects covered in this section

	Going dynamical	$\alpha \leftrightarrow \phi$	$\nabla \alpha \rightarrow \Gamma$	Experimental validation
Theoretics				
Numerics			👍	👍

**Problem setting** The geometry and loading conditions are adapted from (Ožbolt et al., 2015) and are summarized in Figure 4.56. A hard device (displacement control) is applied on the lower left arm



Figure 4.56 – Geometry and loading conditions for the L-specimen problem. Damage field  $\alpha_t$  at  $t = 6 \times 10^{-4}$  s ranging from 0 (gray) to 1 (white) obtained by  $\eta = 1$  mm, for  $v = 0.74$  m/s

30 mm from the edge through a disc of  $D = 45$  mm to avoid local concentration. The load is applied through unilateral contact (EPX keyword **IMPACT**) with an imposed velocity  $\mathbf{V}(t) = \bar{V}f(t)\mathbf{e}_2$ . The intensity is scaled via the factor  $\bar{V}$ . The function  $f(t)$  defined below ensures that at crack initiation the loading velocity is approximately  $V$ :

FONC 1 TABL 5 0D0 0D0 1.5D-4 1D0 2D-4 1D0 4D-4 2D0 1D0 2D0.

The concrete material properties are borrowed from (Ožbolt et al., 2015) and are summarized in Table 4.19. The damage constitutive law (PAMM) is used. Using (2.9), the internal length  $\eta$  can be derived from  $G_c$  and  $\sigma_c$ , which gives  $\eta \approx 72$  mm. The analysis is performed in the temporal interval  $[0, 6 \times 10^{-4}$  s] and the explicit time-stepping method (Algorithm 4) is used. According to the comparative analyses in Sections 4.5 and 4.7, the tension-compression model proposed by (Freddi & Royer-Carfagni, 2010) should be preferred for brittle materials. The domain is discretized by a non-structured quadrilateral mesh with a typical size  $h \approx 10$  mm, arriving at approximately 2000 elements.

Table 4.19 – Material and numerical parameters for the L-specimen test

$\rho$	$E$	$\nu$	$G_c$	$\sigma_c$	$h$
2210 kg/m <sup>3</sup>	32.2 GPa	0.18	58.56 N/m	3.12 MPa	10 mm

#### 4.8.1 Path prediction

The internal length here  $\eta \approx 72$  mm is not small by comparison with the dimension of the body (with a side length 250 mm). We had the same situation for the Brazilian test in Section 4.7 with  $D = 200$  mm. However in Section 4.7 due to symmetry crack nucleates and propagates along the central diameter direction away from the boundary. Furthermore dynamic effects are not important and diffuse damage is not observed. In this problem however, crack path prediction is one of the objectives of the simulation and a large internal length, which implies a large damage band and a more smeared description of cracks, may complicate the identification of the crack path.

In Figure 4.57 the final damage field obtained with  $\eta \approx 72$  mm for two different loading speeds is indicated. The simulation results are to be compared with the experimental fracture patterns indicated



Figure 4.57 – Damage field  $\alpha_t$  ranging from 0 (blue) to 1 (red) for two different loading speeds obtained with  $\ell \approx 72$  mm: (a)  $v = 0.74$  m/s and (b)  $v = 1.2$  m/s

in Figure 4.58. For a lower loading speed  $v = 0.74$  m/s, the initial nucleation angle is close to the experimental one. However the damage field simulated seems to indicate a crack branching event which is not observed in the experiment. For a higher loading speed  $v = 1.2$  m/s, a relatively large diffusive damage zone is produced near the nucleation corner. The crack branching is reproduced, however the branching location and subsequent crack propagation path do not agree with the experimental results.



Figure 4.58 – Fracture patterns observed in experiments conducted by (Ožbolt, Bede, Sharma, & Mayer, 2015)

The failure to reproduce the experimentally observed fracture pattern in this example can be partially attributed to the followings difficulties:

- With a relatively large internal length, the elliptic damage problem interferes with the border  $\partial\Omega$  through the boundary condition prescribed in the damage criterion (2.23) and the consistency condition (2.25). The value of  $\ell$  should be “reduced” for smaller structures, see (Lorentz & Godard, 2011). Furthermore, the separation of scales between the outer fracture mechanics problem and the inner damage strain-softening problem considered in Sections 2.3, 4.2 and 4.3 is no longer possible with a large internal length. In that case the gradient damage model can not be considered as an approximation of the *fracture* problem.
- With the damage constitutive law (PAMM) (but also with (AT)), since no additional parameters are introduced, the internal length is directly computed from (2.9) from the fracture toughness and the maximal material stress. For brittle materials such as PMMA considered in Section 4.6, it leads to an extremely small internal length ( $\eta \approx 0.0375$  mm is used there) compared to industrial

specimen or structures. It calls for a computationally costly numerical simulation with parallel computing techniques, however a confined damage process zone leads to a separation of scales described above and a link between damage and fracture can be achieved. For concrete on the other hand, one obtains with (2.9) an internal length of several centimeters. The modeling of fracture phenomena in small concrete specimens with these kind of constitutive laws is questionable.

Due to this reason, another series of simulation is performed with  $\eta = 1$  mm. Using the definition of the maximal stress (2.6) and the fracture toughness (2.9), it leads to an overestimation of the maximal tensile strength  $\sigma_m \approx 27$  MPa of the concrete. At a lower loading speed  $v = 0.74$  m/s, the final fracture pattern indicated by the damage field with  $\eta = 1$  mm is illustrated in Figure 4.56. A better agreement between the simulation and the experimental observed crack path is found.

The temporal evolution of the applied force is then analyzed for two different internal lengths. In Figure 4.59, it can be observed that they predict different global structural behaviors only during the post-crack initiation phase. In particular, the peak load is not sensible to the internal length. It could be explained by the presence of the geometric singularity where the damage initiates, which implies that the material critical stress is quickly reached when the waves arrive at the corner.



Figure 4.59 – Temporal evolution of the applied force with  $v = 0.74$  m/s

#### 4.8.2 Dynamical effects

We then turn to the global dynamic structural response obtained with different loading rates. As it is expected, the peak load increases with the prescribed velocity, cf. Figure 4.60(a). A good agreement with the experimental measurement is also found at  $v = 1.5$  m/s as illustrated in Figure 4.60(b). Knowing that no strain rates effects is currently taken into account in the material constitutive modeling, this increase of peak load for higher loading rates can be attributed to inertia. According to (Ožbolt et al., 2015), this progressive increase of resistance is a pure consequence of inertial effects and not from velocity-dependent material strength or fracture energy.

The final crack pattern for  $v = 1.5$  m/s is also indicated in Figure 4.60(b). As it is observed in experiments, crack branching is reproduced. However the crack path corresponds not exactly to what is seen in real concrete specimens. We suspect that it is mainly due to the loading condition which is not described in detail in (Ožbolt et al., 2015). Another possible reason could be the use of a smaller internal length chosen due to the small size of the specimen. Using the true internal length derived from the maximal tensile strength of the concrete, a different branching direction appears to take place in Figure 4.57.



Figure 4.60 – Temporal evolution of the applied force: (a) dynamical effects illustrated by two loading speeds and (b) comparison with experimental measurement at  $v = 1.5$  m/s



## Conclusion


The dynamic gradient damage model is here applied to a relatively small concrete structure with the (PAMM) damage constitutive model. Since the internal length deduced from the fracture toughness and the tensile strength is not small compared to the dimension of the body, relatively diffuse damage takes place and the gradient damage model can no longer be considered as a good approximation of brittle fracture. The damage process zone where strain softening dominates is large and the link between damage and fracture outlined in Section 2.3 and numerically verified in Section 4.2 is not possible. The dynamic gradient damage model does not give a satisfactory prediction of the experimentally observed crack path.

The difficulty resides in the simplicity of the (PAMM) damage constitutive model. No additional parameters are introduced and the internal length  $\ell$ , which determines the damage band, is fixed as long as  $G_c$  and  $\sigma_m$  are. Future work will be devoted to the use of more sophisticated constitutive models proposed by (Alessi et al., 2015; Lorentz et al., 2011) which introduce additional modeling parameters. Note however that this implies that the minimization problem for the damage variable (2.22) is no more quadratic, which leads to a higher computational cost.

## 4.9 CEA Impact Test on Beams

Finally we propose a preliminary gradient-damage modeling of a three-dimensional reinforced concrete beam under impact. The original experimental campaign is performed in the *laboratoire d'étude de dynamique* (DYN) of CEA Saclay, see for example (Guilbaud, 2015) for an overview of the test setting. The objective is to investigate the application of the dynamic gradient damage model to industrial concrete structures with steel reinforcements. The thematic subjects covered here are thus summarized in Table 4.20.

Table 4.20 – Thematic subjects covered in this section

	Going dynamical	$\alpha \leftrightarrow \phi$	$\nabla \alpha \rightarrow \Gamma$	Experimental validation
Theoretics				
Numerics				

**Problem setting** The geometric and loading conditions are recalled in Figure 4.61. Due to symmetry, only a quarter  $\Omega$  of the reinforced beam is modeled (corresponding to the gray domain in Figure 4.61). The beam is 1.3 m long and is subject to a steel projectile with a vertical impact velocity of  $v = 8.3$  m/s. It is unilaterally supported with a span of 1 m both at the upper and lower surface via bearing strips of width 30 mm. In this example, the concrete beam is reinforced by two 8 mm steel rebars at the top and two 12 mm rebars at the bottom. Perfect bonding between these rebars and the concrete beam is assumed. The impact is modeled by a unilateral contact condition between the steel projectile with an initial speed  $v$  and the upper surface of the beam. The exact dimensions and other details can be found in (Guilbaud, 2015) and references therein. The problem setting described here is also similar to that investigated in (Adhikary, Li, & Fujikake, 2012; Ožbolt & Sharma, 2011).

We now turn to a gradient-damage modeling of the problem. The concrete is governed by a gradient damage material the parameters of which are summarized in Table 4.21. Using (2.9), the internal length  $\eta$  can be derived from  $G_c$  and  $\sigma_c$ , which gives  $\eta \approx 60$  mm. The rebars obey a typical elasto-plastic law with isotropic hardening for steels. They are considered to be non-damageable in the analysis. Hence the energy minimization principle (2.22), *i.e.* the damage criterion, is now written only for the concrete domain. Due to its appropriate physical properties and a lower computational cost, the damage constitutive law (PAMM) is used for this simulation. Similar to previous examples, the tension-compression model proposed by (Freddi & Royer-Carfagni, 2010) is preferred to characterize tensile fracture behaviors of brittle materials.

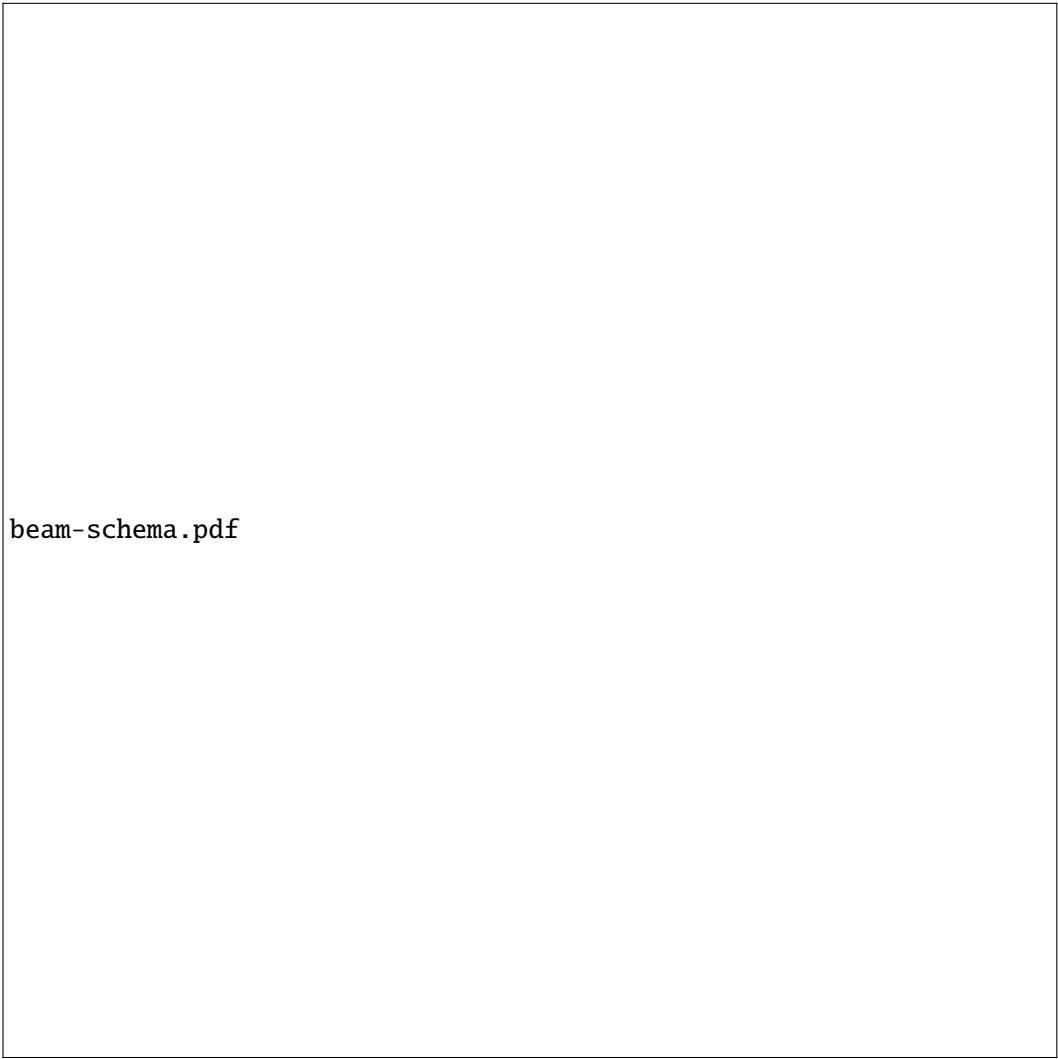


Figure 4.61 – Geometric and loading conditions for the CEA impact test on beams

Table 4.21 – Material and numerical parameters for the beam test

$\rho$	$E$	$\nu$	$G_c$	$\sigma_c$	$h$
2300 kg/m <sup>3</sup>	25 GPa	0.2	57 N/m	3 MPa	5 mm

Numerically a uniform 8-node hexahedral solid elements are used to discretize the concrete domain with a typical mesh size  $h \approx 5$  mm, arriving at approximately 80 000 elements, see Figure 4.62. The steel rebars are also discretized with the same solid elements. The explicit time-stepping (Algorithm 4) implemented in the EPX software is adopted. The current time increment is calculated based on the CFL condition with a security factor of 0.8.

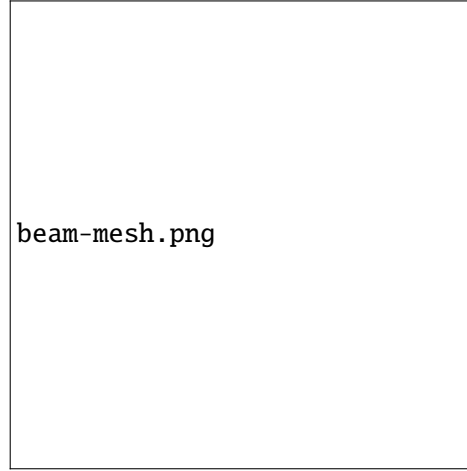


Figure 4.62 – 8-node hexahedral solid elements used to discretize the concrete domain after symmetry considerations

**With original concrete parameters** Using the material parameters given in Table 4.21, it can be observed that while the material internal length  $\eta$  is small by comparison to the beam length (about 0.05%), it still accounts for 30% of the height. According to the previous analysis in Section 4.8, it may lead to some modeling difficulties when the crack direction possesses a component parallel to the length direction. The damage field obtained during numerical simulation is illustrated in Figure 4.63.

This numerical result (Figure 4.63) is to be compared with the experimentally observed fracture pattern reported in (Guilbaud, 2015), see Figure 4.64. In the experiment, the structural failure is characterized by the nucleation of two main inclined cracks forming a cone at the center of the beam. Several minor vertical cracks are also observed in the shear plug. However here a large diffuse damage region is produced at the center of the beam, which implies that the concrete material is totally disintegrated. Diffuse damage also takes place at the upper surface and near the lower supporting location. Although the central damage region is well delimited by a similar inclined cone, the presence of the diffuse damage compromises the use of gradient damage approaches for an appropriate modeling of brittle fracture. Furthermore, we observe a gradual propagation of the diffuse damage in the beam such that at  $t = 7 \times 10^{-4}$  s a large region of the beam is totally damaged.

**Use of a smaller internal length** Similarly to Section 4.8, we expect that the use of a more sophisticated damage constitutive law that introduces additional parameters could provide a better characterization of brittle behaviors of concrete for relatively small structures. Future work will be devoted to this point. Here we present in the sequel some preliminary results obtained with a smaller internal length.

We artificially decrease the internal length to  $\eta = 10$  mm, which amounts to increase the critical stress to  $\sigma_m = 7$  MPa. The damage field obtained at  $t = 4 \times 10^{-4}$  s is illustrated in Figure 4.65. The formation of two main inclined cracks becomes more apparent. Some minor vertical cracks are also reproduced on the upper surface of the beam, as it is observed in the experiment described in (Ožbolt & Sharma, 2011). However diffuse damage still takes place at the center of the beam.

The temporal evolution of certain quantities is analyzed. In particular, we illustrate in Figure 4.66 the vertical displacement evolution of the projectile. On the one hand, using the standard critical stress  $\sigma_m = 3$  MPa of concrete, we observe progressive descending of the projectile. The resistance of the

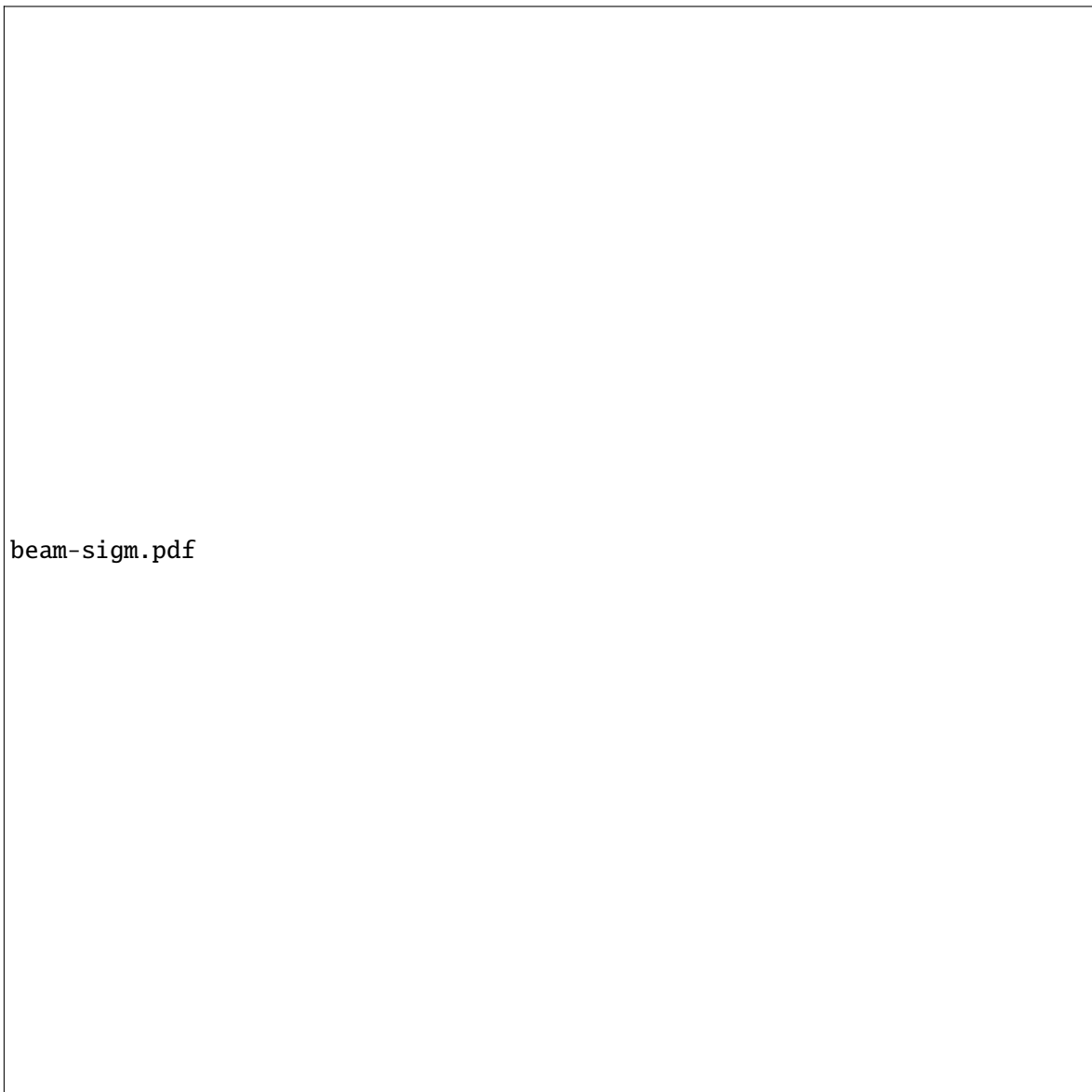


Figure 4.63 – Fracture pattern with the parameters indicated in Table 4.21 at (a)  $t = 4 \times 10^{-4}$  s and (b)  $t = 7 \times 10^{-4}$  s

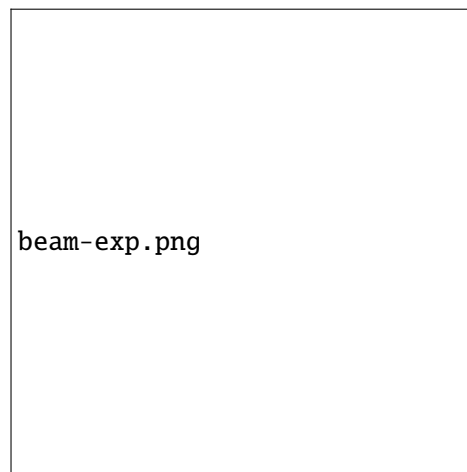


Figure 4.64 – Experimentally observed fracture pattern corresponding to the formation of a shear plug at the center under the projectile

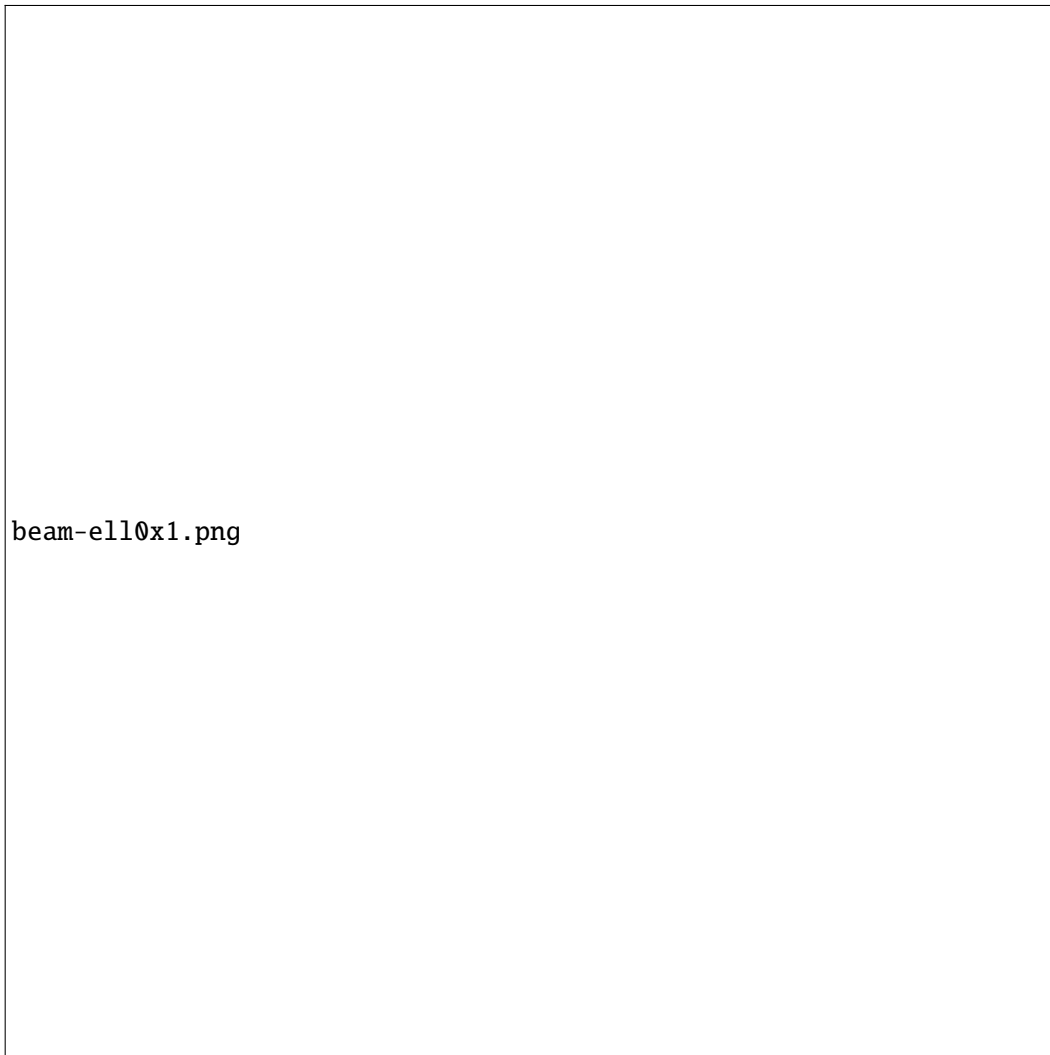


Figure 4.65 – Fracture pattern obtained with  $\eta = 10$  mm at  $t = 4 \times 10^{-4}$  s

beam is not strong enough to stop the impactor. On the other hand, when using a larger critical stress obtained with  $\eta = 10$  mm, the rebound of the projectile is observed after a transient descending phase when structural fracture of the beam takes place. In the experiment reported in (Guilbaud, 2015), the final vertical displacement is stabilized at  $u_y \approx -24$  mm. The current gradient-damage modeling fails to give an accurate global evolution prediction.

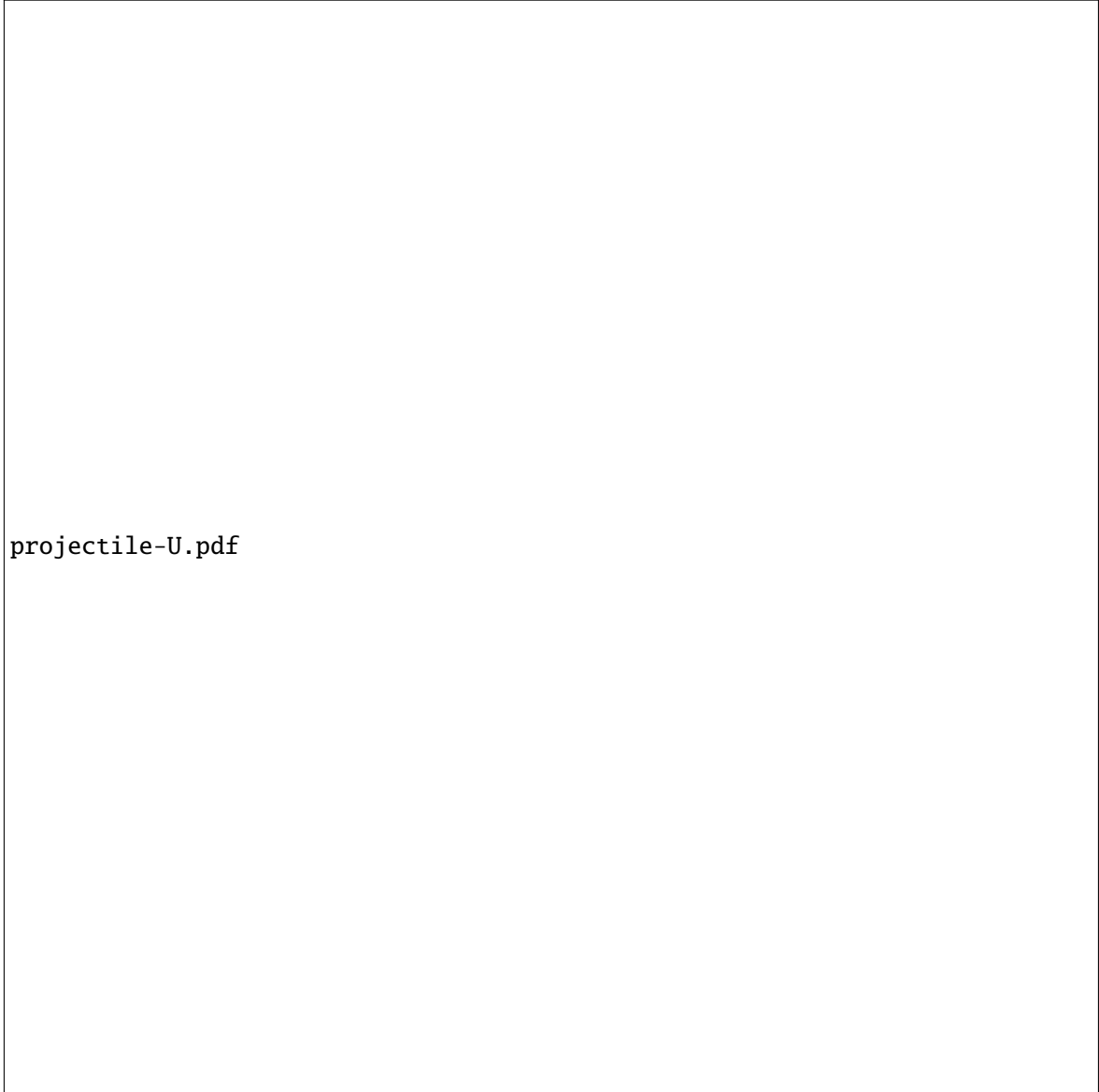


Figure 4.66 – Vertical displacement of the impactor for two internal lengths: (a) comparison between  $\sigma_m = 3$  MPa and  $\eta = 10$  mm ( $\sigma_m \approx 7$  MPa) and (b) temporal zoom for  $\eta = 10$  mm

If the internal length is further decreased to  $\eta = 5$  mm ( $\sigma_m \approx 10$  MPa), several shear cracks forming an angle of approximately  $45^\circ$  with respect to the  $x$ -axis are observed under the impactor, see Figure 4.67(a). For this calculation a more refined mesh with  $h = 2.5$  mm is used, arriving at approximately 640 000 8-nodes hexahedral elements. This fracture pattern is commonly observed in impact experiments on concrete beams, see (Ožbolt & Sharma, 2011). The angle also matches well with the experimental results reported in (Guilbaud, 2015). A diffuse damage region due to high tensile stresses is produced on the lower surface under the projectile.

As can be seen from Figure 4.67, secondary cracks appear and then propagate from the upper surface of the beam. This phenomenon is also produced in the numerical study of (Adhikary et al., 2012). The biggest eigenvalue of the stress tensor at  $t = 1.6 \times 10^{-4}$  s is illustrated in Figure 4.68 just before crack nucleation in the beam. The compressive area is localized on the upper surface just under



Figure 4.67 – Fracture pattern obtained with  $\eta = 5$  mm at (a)  $t = 2 \times 10^{-4}$  s and (b)  $t = 3 \times 10^{-4}$  s

the impactor and is not visible in the figure. We observe tensile stress areas generated by the impactor which correspond to the crack nucleation sites observed in Figure 4.67. This fracture pattern is thus the result of the tension-compression asymmetry formulation (Freddi & Royer-Carfagni, 2010) which favors mode-I cracks induced by positive principal stresses.

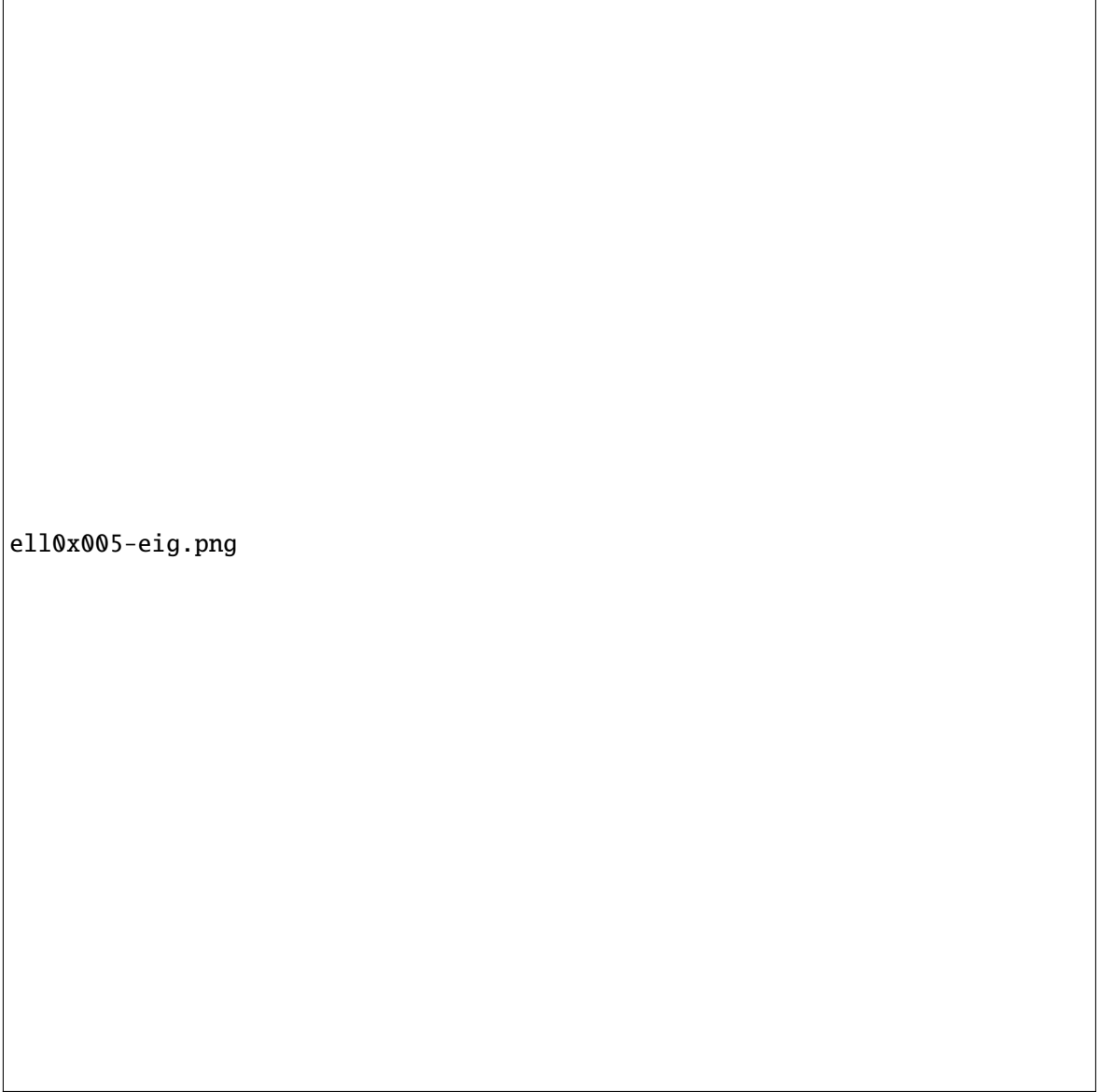


Figure 4.68 – The biggest eigenvalue of the stress tensor at  $t = 1.6 \times 10^{-4}$  s ranging from less than  $-7$  MPa (blue) to more than  $3$  MPa (red). The compressive area is localized on the upper surface just under the impactor

Finally we turn to the computational aspect of a parallel 3d calculation with the dynamic gradient damage model. Domain decomposition using 64 processors is performed. The final calculation time is fixed to  $t = 4 \times 10^{-4}$  s after the structural failure of the beam, see Figure 4.67. The partition of the total computational time using the convention given in Section 4.4 is given in Table 4.22. The mean value among all processors is used. Since the damage is a scalar field, the actual solving of the damage problem (3.10) through the GPCG algorithm described in Section 3.3 still accounts for approximately 10% of the total computational time as in the 2d cases, see Figures 4.30 and 4.40. If the communication overhead is ignored, the cost of a gradient-damage constitutive modeling of brittle materials (damage assembly and solving) represents less than 2 times the cost for the  $\mathbf{u}$ -problem. The same observation is found for two-dimensional problems. Note however if a more sophisticated damage constitutive law is used, the cost for the damage problem may increase due to variable Hessian matrix.



Table 4.22 – Partition of the total computational time for the CEA impact test on beams with 64 processors

Total time	Elastodynamics	Damage assembly	Damage solving	Communication
39 mn	32%	43%	13%	12%

**Conclusion** In this experiment the dynamic gradient damage model is used to investigate the structural failure of a reinforced beam under severe impact. Similarly to Section 4.8, it is illustrated that a more sophisticated damage constitutive law could be devised for the concrete material that introduces additional modeling parameters. Indeed, the internal length  $\eta$  derived from the other material parameters in the (PAMM) law may not be small by comparison with other structural length, which leads to a degenerated modeling of brittle fracture phenomena. By introducing additional modeling parameters such as in (Alessi et al., 2015; Lorentz et al., 2011), a relatively small internal length could be used. Theoretical and numerical investigation of these laws in dynamics could be performed in the future.

On the other hand, the discrepancy between the numerical result presented in particular in Figure 4.63 and the experimental one reported in (Guilbaud, 2015) could also be attributed to the complex constitutive behaviors of concrete under compression. Under such loading conditions, strain softening is often accompanied by extensive plastic deformation, which is typical of a ductile material. In highly confined compression, stiffness degradation and inelastic expansion could also be significantly reduced. Future work could be devoted to a coupling between a plastic model that takes into account possible inelastic strains and the current gradient damage approach that accounts for brittle fracture in tension.

Another possible reason concerns strain-rate effects in the material constitutive modeling. From a macroscopic modeling point of view, a rate-dependent damage criterion could be used to account for a higher resistance of concrete for large strain rates, see (Hentz, 2003). In the current variational formulation of the dynamic gradient damage model outlined in Definition 2.1, it is not taken into account. By introducing for example viscosity into the plasticity model, we would obtain a threshold for damage initiation that increases with the strain-rate. This rate-dependency need further investigation in the future for a better modeling of concrete behaviors.

# 5

## Conclusion and Future Work

### Contents

<b>5.1</b>	<b>Going Dynamical</b>	<b>153</b>
5.1.1	Position with respect to other approaches	154
5.1.2	Variational nature of the formulation	154
5.1.3	Numerical implementation	155
<b>5.2</b>	<b>Link with Phase-Field Approaches</b>	<b>156</b>
5.2.1	Damage constitutive laws	156
5.2.2	Tension-compression asymmetry formulations	156
<b>5.3</b>	<b>Better Understanding of Gradient Damage Modeling</b>	<b>157</b>
5.3.1	Nucleation	157
5.3.2	Initiation, propagation and arrest	157
5.3.3	Kinking	158
5.3.4	Branching	159
<b>5.4</b>	<b>Experimental Validation</b>	<b>159</b>

In this chapter some concluding remarks of the present work are given. It provides an updated state-of-the-art in the gradient-damage modeling of dynamic fracture following the objectives fixed in Section 1.5. In Section 5.1, the dynamic extension of the variational formulation as well as the numerical implementation is reviewed. Then in Section 5.2, we give some remarks concerning the use of several modeling parameters in the gradient-damage model and how it is linked with other phase-field approaches. A better understanding of the gradient damage model constitutes another major contribution of the present work. It is reviewed in Section 5.3. Finally we discuss the application of the dynamic gradient damage model to real-world structures, in Section 5.4.

To facilitate the reading, the future work arising from the current studies will be underlined.

### 5.1 Going Dynamical

This section provides some concluding remarks concerning the dynamic extension of the original quasi-static gradient damage model. The thematic subjects covered are summarized in Table 5.1.

Table 5.1 – Thematic subjects covered in this section

	Going dynamical	$\alpha \leftrightarrow \phi$	$\nabla \alpha \rightarrow \Gamma$	Experimental validation
Theoretics	👍			
Numerics	👍			

### 5.1.1 Position with respect to other approaches

Chapter 1 provides an overview of several existing modeling approaches to brittle fracture. In particular, the Griffith's theory of dynamic fracture and the variational approach to fracture are respectively recalled in Section 1.2 and Section 1.3. The choice of these two models is not arbitrary. Indeed, the gradient damage model can be regarded as a genuine physical model of fracture *per se* that lies between these two approaches. On the one hand, the gradient damage model agrees with the Griffith's law (1.10) when applied to preexisting cracks that propagate along a predefined path in the body without complex topology changes, see Sections 2.3 and 4.2. It can thus be regarded as a superset of the Griffith's theory which is represented below by  $\mathcal{A}(\mathbf{u}, l)$ , see Appendix A for its variational reformulation.

On the other hand, the gradient damage approach can be regarded as an effective numerical implementation of the variational approach to fracture using the  $\Gamma$ -convergence theory, at least in the quasi-static setting, see Section 1.4. The potential energy  $\mathcal{P}(\mathbf{u}, \alpha)$  of the quasi-static gradient damage model outlined in Definition 1.1 can be formally obtained by omitting the kinetic energy  $\mathcal{K}$  in the generalized action integral  $\mathcal{A}(\mathbf{u}, \alpha)$  in the dynamic model. As  $\ell \rightarrow 0$ , the  $\ell$ -regularized functional  $\mathcal{P}(\mathbf{u}, \alpha)$  converges in a certain sense to the sharp-interface Francfort-Marigo variational fracture model  $\mathcal{P}(\Gamma)$ . In the gradient damage model, the  $\ell$ -parameter is regarded as a physical parameter and its role should be investigated with respect to the material and structural behavior of a gradient-damage body. Nevertheless, the limit  $\ell \rightarrow 0$  defines a limiting behavior of the gradient damage model for small internal lengths and provides a better understanding of the model. In dynamics, the exact behavior for the dynamic gradient damage model when  $\ell \rightarrow 0$  is still unknown. Furthermore, a precise modeling of a sharp-interface dynamic fracture model is still lacking and recalls for collaborations from both the mathematics and mechanics community. The relationship between these models is summarized in Figure 5.1.

$$\begin{array}{ccccc}
 \mathcal{A}(\mathbf{u}, l) & \xleftarrow{\text{Griffith's hypothesis}} & \mathcal{A}(\mathbf{u}, \alpha) & \xrightarrow{\ell \rightarrow 0} & ? \\
 & & \downarrow -\mathcal{K} & & \uparrow +\mathcal{K} \\
 & & \mathcal{P}(\mathbf{u}, \alpha) & \xrightarrow{\ell \rightarrow 0} & \mathcal{P}(\Gamma)
 \end{array}$$

Figure 5.1 – On the one hand, the dynamic gradient damage model  $\mathcal{A}(\mathbf{u}, \alpha)$  agrees with the Griffith's theory  $\mathcal{A}(\mathbf{u}, l)$  when applied to pre-existing cracks that propagate in the body without complex topology changes. On the other hand, the gradient damage approach is connected to the variational approach to fracture  $\mathcal{P}(\Gamma)$  through the  $\Gamma$ -convergence theory in the quasi-static setting. The exact behavior when  $\ell \rightarrow 0$  in dynamics is currently unknown and a precise modeling of a sharp-interface dynamic fracture model is still lacking, which is here symbolized by adding  $\mathcal{K}$  in  $\mathcal{P}(\Gamma)$

### 5.1.2 Variational nature of the formulation

The variational formulation of the dynamic gradient damage model outlined in Definition 2.1 settles down a general framework of an elastic body that undergoes a brittle fracture behavior. The first-order stability condition Equation (2.17) states that the true dynamic coupled evolution of the displacement field and the damage field corresponds to a stationary generalized space-time action integral (2.16). By virtue of the energy minimization principle (2.22), the spatial (kinking, branching, ...) and temporal

evolution (initiation, arrest, . . .) of the gradient-damage crack can be predicted without any additional physical or numerical criteria.

The formulation of the dynamic gradient damage model itself can be regarded as a generalization of the Griffith's theory, which is also variational in nature. In Appendix A, a rigorous reformulation of the dynamic Griffith's law (1.10) is also achieved by exploiting the stationarity of a similar sharp-interface space-time action integral (A.3). The difference between (2.16) and (A.3) resides in the definition of the dissipated energy  $\mathcal{S}$  due to fracture. In the gradient damage model a smeared description is adopted and the dissipated energy (2.5) is written as a volume integral in the body involving only the damage variable. On the contrary, the Griffith's theory adopts a sharp-interface description and the dissipated energy corresponds to the original Griffith's hypothesis of energy dissipation (1.19). The link between these two descriptions is achieved via the  $\Gamma$ -convergence result (A.2) as well as the definition (2.9) of the fracture toughness in gradient damage models.

The major constraint prescribed in the Griffith's theory refers to a predefined crack path and an existing crack. By applying the stability principle (A.4) in the variational formulation of the Griffith's theory of dynamic fracture, one obtains the well known Griffith's law (1.10) which is then effectively used to derive an equation of motion of the crack tip. The exact procedure is then performed for the dynamic gradient damage model in Section 2.3, in order to obtain a similar scalar equation governing the crack tip of the gradient-damage crack. The attentive reader can not fail to realize the essential role played by the variational nature of the formulation in the derivation of several energy release rate concepts (the conventional dynamic energy release rate (2.69) and the damage dissipation rate (2.70)) in the gradient damage model, which is applicable for a large class of damage constitutive laws. Using the three physical principles of irreversibility, stability and energy balance, analogies between these two models can be rigorously formalized. Properties derived in the one model can be translated to the other, see Table 5.2. In particular, the equation of motion governing the crack tip can be obtained by calculating the first-order action variation with respect to arbitrary crack evolution and by using the energy balance condition. This procedure could be repeated for other variational formulations of crack evolutions. An interesting extension would be the gradient damage model coupled with plasticity proposed in (Alessi et al., 2015).

Table 5.2 – Analogies between the variational formulation of the Griffith's theory of dynamic fracture (Definition A.1) and the dynamic gradient damage evolution law for a propagating crack (Definition 2.4)

	Griffith's theory	Dynamic gradient damage model
Irreversibility	$\dot{l}_t \geq 0$	$\dot{\alpha}_t \geq 0$ and $\dot{l}_t \geq 0$
Elastic energy	$\mathcal{E}^*(\mathbf{u}_t^*, l_t)$	$\mathcal{E}^*(\mathbf{u}_t^*, \alpha_t^*, l_t)$
Kinetic energy	$\mathcal{K}^*(\mathbf{u}_t^*, \dot{\mathbf{u}}_t^*, l_t, \dot{l}_t)$	$\mathcal{K}^*(\mathbf{u}_t^*, \dot{\mathbf{u}}_t^*, l_t, \dot{l}_t)$
Dissipated energy	$\mathcal{S}(l_t) = G_c \cdot l_t$	$\mathcal{S}^*(\alpha_t^*, l_t)$
Stability condition	$\mathcal{A}'(\mathbf{u}^*, l)(\mathbf{v}^* - \mathbf{u}^*, \delta l) \geq 0$	$A'(\mathbf{u}^*, \alpha^*, l)(\mathbf{v}^* - \mathbf{u}^*, \beta^* - \alpha^*, \delta l) \geq 0$
Eq. for $\mathbf{u}$	$\rho \ddot{\mathbf{u}}_t = \text{div } \mathbf{A} \boldsymbol{\varepsilon}(\mathbf{u}_t) + \mathbf{f}_t$	$\rho \ddot{\mathbf{u}}_t = \text{div } \mathbf{A}(\alpha_t) \boldsymbol{\varepsilon}(\mathbf{u}_t) + \mathbf{f}_t$
Eq. for $l$	Griffith's law (1.10)	Generalized Griffith criterion (2.78)
Energy release rate	Classical $J$ -integral (1.8)	Generalized $\widehat{J}$ -integral (2.72)

### 5.1.3 Numerical implementation

In Chapter 3 a space-time discretization of the continuous dynamic gradient damage model is performed. In the quasi-static setting the numerical implementation exploits fully the variational nature since the static equilibrium can be effectively solved by a mathematical optimization algorithm. In the present work, the spatial discretization is decoupled from the temporal one and a temporal finite difference scheme is used for the time-stepping of the spatially discretized finite element system. Future work can be devoted to the investigation of space-time finite element methods, see (Hughes & Hulbert, 1988).

The dynamic gradient damage model has been successfully implemented by the author in the EPX software (CEA & EC, 2015). The two damage constitutive laws (PAMM) and (AT), as well as several

tension-compression asymmetry models mentioned in Section 2.2 are available. In the meanwhile, an open-source implementation (Li, 2015) based on the FEniCS project (Logg et al., 2012) is also performed by the author.



In an explicit dynamics context, the damage problem (3.10) appears as a bound-constrained convex optimization problem which is solved at the structural scale at every time step. Fortunately, by using the (PAMM) damage constitutive law, the numerical solving of the current damage field together with the construction of the matrices represent approximately 50% of the total computational time, which is quite reasonable for other classical local nonlinear material constitutive laws. Furthermore, thanks to an efficient parallel implementation using the PETSc framework, a quasi-perfect strong scaling diagram is obtained, see Figure 4.30. The computational wall time can thus be significantly reduced by using several processors.

The implementation is also applied to three-dimensional dynamic problems in Sections 4.7 and 4.9. One of the advantage of the gradient-damage approach (and other models based on a smeared description of cracks) consists of a unified treatment of 2-d and 3-d fracture problems without any other additional numerical crack surface tracking techniques.

## 5.2 Link with Phase-Field Approaches

This section discusses several modeling parameters in the gradient damage model and strengthens the link with other phase-field approaches. The thematic subjects covered are summarized in Table 5.3.

Table 5.3 – Thematic subjects covered in this section

	Going dynamical	$\alpha \leftrightarrow \phi$	$\nabla \alpha \rightarrow \Gamma$	Experimental validation
Theoretics				
Numerics				

### 5.2.1 Damage constitutive laws

In this work two particular damage constitutive laws (PAMM) and (AT) are compared with respect to their aptitude to model brittle fracture inside the variational framework of the dynamic gradient damage model. In particular, the latter model leads to the widely-used regularized crack functional in the phase-field community. The present work can thus be considered as a bridge between these two communities. According to the crack branching experiment Section 4.4, it is confirmed that the (PAMM) model performs better than the (AT) one in terms of physical properties and computational efficiency due to a small damage band. Future work could be devoted to the application of more sophisticated damage constitutive laws in dynamic fracture problems.

In terms of computational efficiency, a bound-constrained minimization algorithm is needed for the (PAMM) model. On the other hand, a simple linear system is required for the (AT) one. However it is illustrated in Section 4.4 that such nonlinear solvers is not very costly. For more complex damage constitutive laws, the Hessian matrix for the damage problem is no more constant and the numerical efficiency should be reevaluated.

### 5.2.2 Tension-compression asymmetry formulations

In Section 2.2 we give a variational interpretation of several existing tension-compression asymmetry formulations. Their respective properties are then highlighted through a uniaxial traction experiment. The variational structure (2.40) provides a novel interpretation of these models. Future work can be devoted to the proposal of several new elastic energy splits (2.38) within the framework.

The tension-compression asymmetry model of (Miehe, Hofacker, & Welschinger, 2010), that is widely used among the phase field community does not fit into this variational setting. Furthermore,



it develops diffuse damage with a strange strain-hardening behavior under the uniaxial compression state thanks to a theoretic study in Section 2.2.2. This property is numerically verified for the Kalthoff experiment in Section 4.5. Due to this reason, we recommend the elastic energy split developed for masonry-like materials, *i.e.* that of (Freddi & Royer-Carfagni, 2010). With this tension-compression asymmetry formulation, correct propagation path for brittle materials such as PMMA and concrete is reproduced by comparison with the experimental observations, cf. Sections 4.5 and 4.7 to 4.9.

However the existing tension-compression asymmetry models, including that proposed by (Freddi & Royer-Carfagni, 2010), do not correctly account for true non-interpenetration condition, as is illustrated during several numerical simulations, see Sections 4.5 and 4.7. It is due to the fact that these energy splits do not depend on the current damage state as well as the damage gradient which approximates the crack normal direction. In particular, it appears that stress can be transmitted parallel to the gradient-damage crack with the (Freddi & Royer-Carfagni, 2010) model. Future work could be devoted to a thorough investigation of the erosion mechanism available in the EPX software to realize a transition from a continuous to a discrete description of cracks. Another possibility is to consider an equivalent cohesive crack that replaces the gradient-damage crack, see for instance (Cazes et al., 2009; Cuvilliez et al., 2012). Other numerical techniques frequently used in the sharp-interface fracture models can also be borrowed: for instance the X-FEM method, see (Comi, Mariani, & Perego, 2007).

### 5.3 Better Understanding of Gradient Damage Modeling

In this section we provide a summary of the properties of dynamic gradient damage models when applied to investigate dynamic brittle fracture. Different temporal or spatial events or phases as outlined in Section 1.1.1 are studied both theoretically and numerically in this work. The thematic subjects covered are summarized in Table 5.4.

Table 5.4 – Thematic subjects covered in this section

	Going dynamical	$\alpha \leftrightarrow \phi$	$\nabla \alpha \rightarrow \Gamma$	Experimental validation
Theoretics				
Numerics				

#### 5.3.1 Nucleation

Compared to the Griffith's approach, crack nucleation from a perfectly sound body is able to be predicted in the gradient damage model. If damage initiation is governed by a local condition (2.26), crack nucleation (when the damage variables attains 1 somewhere in the body) could be subject to structural effects depending on the relative size between the material internal length  $\ell$  and the dimension of the body. This size effect is numerically investigated in Section 4.1 for a one-dimensional bar under impact and in Section 4.7 for a three-dimensional Brazilian test for concrete cylinders. Simulation results, cf. Figures 4.8, 4.9 and 4.55 confirm the well-acknowledged belief: “smaller is stronger”.

A comparison between the gradient damage model and local strain-softening models is also performed in Section 4.1. In the limit  $\ell \rightarrow 0$ , the fracture behaviors with the gradient-damage approach converge to that predicted by ill-posed local models. This result enhances the stand that the parameter  $\ell$  should be considered as a material parameter and not as a purely numerical parameter, see Section 1.4.2. Future work could be devoted to a theoretic investigation of this one-dimensional problem and in particular the size effect.

#### 5.3.2 Initiation, propagation and arrest

**Theoretic investigation** The apparent crack evolution in gradient damage models under the Griffith's fundamental hypothesis (predefined crack path and an existing crack) is first analyzed from a theoretic



approach in Section 2.3. It is shown that the crack tip equation of motion is governed by the generalized Griffith criterion (Proposition 2.7) and the asymptotic Griffith's law (Proposition 2.11). Generally speaking, when the internal length is small compared to the dimension of the body, the gradient-damage crack behaves exactly like a Griffith's one, in the absence of complex topology changes. Note that the crack nucleation phase is not governed by these two principles since an initial crack is absent and a separation of scales is not possible.

The novelty concerns the application of shape derivative methods (Destuynder & Djaoua, 1981) to the gradient damage model. Thanks to a well-defined diffeomorphism (2.49), in the sharp-interface Griffith's fracture model the current cracked material configuration on which mechanical quantities are defined is transformed to the initial cracked one. Similarly in the phase-field approach the current damage field representing a propagating crack is mapped from a damage profile field which corresponds to a stationary initial crack. This Lagrangian formalism gives a rigorous sense to the shape derivative of the action integral with respect to the current crack length, which leads in return to the definition of an energy release rate even in the absence of stress singularities.

The most essential assumption behind the generalized Griffith criterion resides in the non-positivity of the generalized  $J$ -integral. A theoretic proof of Hypothesis 2.6 calls for a careful singularity analysis similar to that conducted in (Sicsic & Marigo, 2013). Let's recall that during the analysis the crack topology is restricted to a single straight line. Following the discussion at the end of Appendix A, predefined curved crack paths can as well be considered. When several cracks are present in the body, as long as a diffeomorphism similar to (2.49) can be constructed between the initial cracked configuration and a perturbed multi-cracked configuration (generally speaking when those cracks do not interact with each other), the formalism described here can still be applied. By relaxing furthermore the hypothesis of a pre-defined crack propagation path, we may hope to identify a macroscopic kinking/branching criterion hidden behind the stability condition (2.17). An interesting challenge would be to use more adequate shape derivative methods (Hintermüller & Kovtunen, 2011) in order to differentiate the action integral (2.16) with respect to the propagation angle. Furthermore we assume that the totally damaged zone corresponds to a subset of measure zero with respect to  $dx$ . When it is not the case, more energy would be dissipated during crack propagation which could represent an increase of the apparent fracture toughness observed during dynamic crack microbranching processes investigated in Section 4.4. Future work could be devoted to this point to theoretically investigate the micro-branching phenomenon.

**Numerical investigation** In Section 4.2 a numerical verification of the generalized Griffith criterion (Proposition 2.7) and the asymptotic Griffith's law (Proposition 2.11) is performed for an antiplane tearing experiment. The conventional dynamic energy release rate (2.69) is numerically computed and verified as a tool to translate gradient damage mechanics results in fracture mechanics terminology. The crack length evolution predicted by the dynamic gradient damage model agrees well with the Griffith's theory applied to the 1-d peeling problem.

The quasi-static limit of the dynamic gradient damage model is also investigated. Convergence of the dynamic model toward the quasi-static one should be observed in the absence of unstable crack propagation. Otherwise a full dynamic analysis should be preferred.

### 5.3.3 Kinking

Numerical investigation of crack kinking is investigated in Section 4.3. It is verified that the kinking angle for an initially stationary crack predicted by the dynamic gradient damage model corresponds to several commonly used kinking criteria in quasi-static fracture mechanics, see Figure 4.28. Toughness anisotropy may be needed to discriminate between them. Future work could be devoted to a full dynamic path analysis for a crack that propagates initially at a velocity, since it is not sure that the crack will kink or branch.

According to (Chambolle et al., 2009), kinking is always accompanied by a temporal brutal or unstable crack propagation. Following the work in Section 4.2, we could expect that the crack length at arrest is different for the first-order quasi-static model (Definition 4.1) and the dynamic model

(Definition 2.1) after the kink. This unstable propagation in the presence of a kink needs further investigation and a parametric study on the ratio  $K_2/K_1$  could be performed.

5.3.4 Branching


In Section 4.4, some physical insights into the branching mechanism predicted by the dynamic gradient damage model are provided. It is observed that in dynamics the damage field perpendicular to the gradient-damage crack may not correspond always to the optimal damage profile (2.27) which defines an equivalent fracture toughness (2.9) in gradient damage models. On the contrary, widening of the damage band takes place whenever a critical speed is reached. From a macroscopic modeling point of view, this may corresponds to the nucleation and subsequent interaction of several micro-branches along the main crack. Additional energy dissipation is thus reproduced. According to our numerical simulations, this critical speed is estimated to be  $v_c \approx 0.4c_R$ , which agrees well with experimental results for brittle materials.

A space-time zoom at the micro-branching event is performed. The stress distribution satisfies a generalized Yoffe-type criterion. Indeed, it is observed that the hoop stress variation is no longer maximal in front of the crack for some distance  $r$ , when the velocity of the main crack reaches  $v_c$ . A smaller value of  $v_c$  compared to the original Yoffe criterion (see Figure 1.6) can also be attributed to the presence of a mode-II perturbation. This also agrees with some experimental findings, see (Boué et al., 2015).

5.4 Experimental Validation

The dynamic gradient damage model as well as its current numerical implementation in the EPX software are applied to several real-world dynamic fracture problems for experimental validation. The thematic subjects covered are summarized in Table 5.5.

Table 5.5 – Thematic subjects covered in this section

Going dynamical	$\alpha \leftrightarrow \phi$	$\nabla \alpha \rightarrow \Gamma$	Experimental validation
Theoretics			
Numerics			

**Application to materials possessing a small damage band** In Section 4.6, the dynamic gradient damage model is used to investigate crack evolution inside a pre-cracked PMMA plate. Using standard values of the critical stress, the use of the (PAMM) model leads to an internal length much smaller than 1 millimeter. This leads to a relatively fine mesh and hence a computationally demanding simulation for a normal mechanical or industrial specimen or structure. However since the internal length is small compared to the dimension of the body, a separation between the damage process zone and the outer linear elastic fracture problem can be achieved. Diffuse damage does not takes place and the gradient-damage approach is expected to give an appropriate modeling of brittle fracture. For this crack arrest problem, a quantitative comparison between the gradient-damage prediction and the experimental observation is performed in terms of the crack tip evolution. A good agreement is found between them.

**Application to concrete** For concrete, the damage band corresponds to several centimeters. In the Brazilian splitting test in Section 4.7, this does not constitute a problem since the crack path is *a priori* determined due to a particular stress distribution. The crack nucleates at the center of the cylinder, which then propagates along the vertical diameter direction. The global temporal evolution of the applied load agrees with the elasticity prediction. Similarly to experimental observations, vertical splitting of the concrete cylinder is reproduced.



For the L-shaped concrete specimen in Section 4.8, a relatively large internal length begins to raise difficulties when crack path prediction is the main objective of the numerical simulation. Due to a large damage zone, not only the crack is extremely diffused in the structure leading to a difficult identification of the crack path, the gradient-damage modeling of fracture itself could also be questionable. The strain-softening region spreads to a large subset of the body, the material behavior can no longer be considered to be brittle. Hence, the crack path prediction is less satisfactory.

A major reason behind it lies in the simplicity of the (PAMM) model, since no additional parameters are introduced. By using more sophisticated damage constitutive laws such as that proposed by (Lorentz & Godard, 2011), the damage band itself can be considered as a modeling parameter. Future work could be devoted to the investigation of a better damage constitutive law for the concrete material.

Nevertheless, if a small internal length is assumed in Section 4.8, more or less satisfactory simulation results are obtained. Dynamical effects are then investigated by varying the loading speed. On the one hand, crack branching is reproduced which corresponds to the velocity effects observed in brittle materials, cf. (Schardin, 1959). On the other hand, the peak load also increases with the external loading speed. Since no material strain-rate effects are introduced (yet), this corresponds to pure inertia effects as concluded by experimental observations of (Ožbolt et al., 2015).

Finally, the gradient damage model is applied to the CEA impact test on concrete beams. Apart from a relatively large internal length with respect to the height direction, it appears that plastic effects and rate-dependency should be introduced in the material constitutive modeling to account for the complex behaviors of concrete under compression. Future work could be devoted to the formulation and analysis of a better constitutive modeling of concrete coupled with gradient damage approaches.



## Griffith Revisited

In this chapter we revisit the Griffith's theory of dynamic fracture and provide a variational formulation of Griffith's law (1.10). The basic problem setting is similar to that assumed in Section 2.3. Here the symbol  $\Gamma_t$  refers to a sharp-interface crack inside a two-dimensional linear elastic body.

### Reformulation Based on a Space-Time Action Integral

The sharp-interface dynamic fracture problem will be formulated in line with the dynamic gradient damage model outlined in Definition 2.1. We will construct a space-time action integral similar to that introduced in (Adda-Bedia et al., 1999) and then calculate directly the action variation corresponding to arbitrary virtual displacement variation and crack advance. The basic energetic ingredients of the dynamic fracture problem are defined as follows. By virtue of (2.51) and (2.52), they can be directly formulated in the initial configuration.

- The elastic energy is given by

$$\mathcal{E}(\mathbf{u}_t, l_t) = \mathcal{E}^*(\mathbf{u}_t^*, l_t) = \int_{\Omega \setminus \Gamma_0} \psi \left( \frac{1}{2} \nabla \mathbf{u}_t^* \nabla \phi^{-1} + \frac{1}{2} \nabla \phi^{-\top} (\nabla \mathbf{u}_t^*)^\top \right) \det \nabla \phi \, d\mathbf{x}^*. \quad (\text{A.1})$$

where  $\psi$  refers to the classical (damage-independent) linear elastic energy density. The stress tensor conjugate to the strain variable is thus given by  $\sigma_t = A_0 \varepsilon(\mathbf{u}_t)$ .

- The kinetic energy is formally given by (2.57) as long as we interpret  $\Gamma_t$  as a sharp-interface strong discontinuity in the body.
- The Griffith surface energy (1.1) reads in our case

$$\mathcal{S}(l_t) = G_c \cdot (l_t - l_0). \quad (\text{A.2})$$

It is the sharp-interface counterpart of the damage dissipation energy (2.58).

- The external work potential  $\mathcal{W}_t$  is formally given by (2.59) as long as we interpret  $\Gamma_t$  as a sharp-interface strong discontinuity in the body.

The admissible function spaces for the displacement  $\mathbf{u}^*$  and for the crack evolution  $l$  are still formally given by respectively (2.14') and (2.61). We can now form the space-time action integral given by

$$\mathcal{A}(\mathbf{u}^*, l) = \int_I \mathcal{L}_t(\mathbf{u}_t^*, \dot{\mathbf{u}}_t^*, l_t, \dot{l}_t) \, dt = \int_I (\mathcal{E}^*(\mathbf{u}_t^*, l_t) + \mathcal{S}(l_t) - \mathcal{K}^*(\mathbf{u}_t^*, \dot{\mathbf{u}}_t^*, l_t, \dot{l}_t) - \mathcal{W}_t^*(\mathbf{u}_t^*, l_t)) \, dt \quad (\text{A.3})$$

which involves a generalized Lagrangian  $\mathcal{L}_t(\mathbf{u}_t^*, \dot{\mathbf{u}}_t^*, l_t, \dot{l}_t)$ . The coupled evolution described by the couple  $(\mathbf{u}^*, l) \in C(\mathbf{u}^*) \times \mathcal{Z}(l)$  will then be governed by

**Definition A.1** (Variational Formulation of the Griffith's Theory of Dynamic Fracture).

1. **Irreversibility**: the crack length is a non-decreasing function of time  $\dot{l}_t \geq 0$ .
2. **First-order stability**: the first-order action variation is non-negative with respect to arbitrary admissible displacement and crack evolutions

$$\mathcal{A}'(\mathbf{u}^*, l)(\mathbf{v}^* - \mathbf{u}^*, s - l) \geq 0 \text{ for all } \mathbf{v}^* \in C(\mathbf{u}^*) \text{ and all } s \in \mathcal{Z}(l). \quad (\text{A.4})$$

3. **Energy balance**: the only energy dissipation is due to crack propagation such that we have the following energy balance

$$\mathcal{H}_t = \mathcal{H}_0 + \int_0^t \left( \int_{\Omega \setminus \Gamma_s} (\boldsymbol{\sigma}_s \cdot \boldsymbol{\varepsilon}(\dot{\mathbf{U}}_s) + \rho \ddot{\mathbf{u}}_s \cdot \dot{\mathbf{U}}_s) \, d\mathbf{x} - \mathcal{W}_s(\dot{\mathbf{U}}_s) - \mathcal{W}'_s(\mathbf{u}_s) \right) ds \quad (\text{A.5})$$

where the total energy is defined by

$$\mathcal{H}_t = \mathcal{E}^*(\mathbf{u}_t^*, l_t) + \mathcal{S}(l_t) + \mathcal{K}^*(\mathbf{u}_t^*, \dot{\mathbf{u}}_t^*, l_t, \dot{l}_t) - \mathcal{W}_t^*(\mathbf{u}_t^*, l_t). \quad (\text{A.6})$$

In the first-order stability principle (A.4), the notation  $\mathcal{A}'(\mathbf{u}^*, l)(\mathbf{v}^* - \mathbf{u}^*, s - l)$  denotes the Gâteaux derivative of the action functional with respect to the displacement variation  $\mathbf{w}^* = \mathbf{v}^* - \mathbf{u}^*$  and crack advance  $\delta l = s - l$ . Recall that the transported displacement  $\mathbf{u}_t^*$  is defined on the initial configuration  $\Omega \setminus \Gamma_0$  which is fixed during the (virtual) crack increment, thanks to the introduction of the diffeomorphism  $\phi$ . The displacement variation  $\mathbf{w}^*$  is thus independent from that of the crack  $\delta l$ , and induces automatically a variation  $\mathbf{w}$  in the current material configuration via a pushforward operation  $\mathbf{w} \circ \phi = \mathbf{w}^*$ .

## Equivalence with the Classical Formulations

We will show in this section that the variational approach to dynamic fracture summarized by Definition A.1 is equivalent to the usual elastodynamic equation in the uncracked bulk and Griffith's law of crack evolution (1.10). However, it should be noted that the variational formulation is more general. To achieve this goal, we will carefully evaluate the derivative of the action functional with respect to arbitrary displacement variation  $\mathbf{w}^* = \mathbf{v}^* - \mathbf{u}^*$  and crack advance  $\delta l = s - l$ . Lengthy calculations are detailed in Appendix B, and only the main results are presented here.

By firstly evaluating the action variation corresponding to zero virtual crack advance  $\delta l = s - l = 0$  and using the fact that  $\mathbf{v}_t^* - \mathbf{u}_t^* = \mathbf{w}_t^* \in C_0$  is a vector space, one obtains by virtue of the regularity hypotheses

$$\begin{aligned} \mathcal{A}'(\mathbf{u}^*, l)(\mathbf{w}^*, 0) &= \int_I \left( \int_{\Omega \setminus \Gamma_t} (\rho \ddot{\mathbf{u}}_t - \operatorname{div} \boldsymbol{\sigma}_t - \mathbf{f}_t) \cdot \mathbf{w}_t \, d\mathbf{x} + \int_{\partial\Omega_F} (\boldsymbol{\sigma}_t \mathbf{n} - \mathbf{F}_t) \cdot \mathbf{w}_t \, ds \right. \\ &\quad \left. + \int_{\Gamma_t} \boldsymbol{\sigma}_t \mathbf{n} \cdot \mathbf{w}_t \, ds \right) dt \\ &= 0 \text{ for all } \mathbf{w}_t^* \in C_0 \end{aligned} \quad (\text{A.7})$$

from which the classical wave equation is deduced

$$\rho \ddot{\mathbf{u}}_t - \operatorname{div} \boldsymbol{\sigma}_t = \mathbf{f}_t \quad \text{in } \Omega \setminus \Gamma_t, \quad \boldsymbol{\sigma}_t \mathbf{n} = \mathbf{F}_t \quad \text{on } \partial\Omega_F \quad \text{and} \quad \boldsymbol{\sigma}_t \mathbf{n} = \mathbf{0} \quad \text{on } \Gamma_t. \quad (\text{A.8})$$

We then evaluate the action derivative with zero virtual displacement variation  $\mathbf{w}^* = \mathbf{0}$ , leading to

$$\mathcal{A}'(\mathbf{u}^*, l)(\mathbf{0}, \delta l) = \int_I (G_c - G_t) \delta l_t \, dt \geq 0 \text{ for all } \delta l_t \geq 0 \text{ with } t \in (0, T) \quad (\text{A.9})$$

where the dynamic energy release rate  $G_t$  to be compared with the fracture toughness  $G_c$  reads

$$G_t = \int_{\Omega \setminus \Gamma_t} \left( (\kappa(\dot{\mathbf{u}}_t) - \psi(\varepsilon(\mathbf{u}_t))) \operatorname{div} \boldsymbol{\theta}_t + \boldsymbol{\sigma}_t \cdot (\nabla \mathbf{u}_t \nabla \boldsymbol{\theta}_t) + \operatorname{div}(\mathbf{f}_t \otimes \boldsymbol{\theta}_t) \cdot \mathbf{u}_t + \rho \ddot{\mathbf{u}}_t \cdot \nabla \mathbf{u}_t \boldsymbol{\theta}_t + \rho \dot{\mathbf{u}}_t \cdot \nabla \dot{\mathbf{u}}_t \boldsymbol{\theta}_t \right) \mathrm{d}\mathbf{x}. \quad (\text{A.10})$$

From (A.9), we retrieve the desired crack stability condition which states that the dynamic energy release rate must be smaller or equal to the material fracture toughness. The consistency condition

$$(G_t - G_c)\dot{l}_t = 0$$

can then be derived thanks to the energy balance principle (A.5) and detailed calculations in Appendix B. The combination of these two conditions along with the irreversibility condition leads to the desired Griffith's law of crack propagation (1.10).

Note that we retrieve the static energy release rate (Destuynder & Djaoua, 1981) by setting the velocity  $\dot{\mathbf{u}}_t$  and the acceleration  $\ddot{\mathbf{u}}_t$  in (A.10) to zero. A similar formula for  $G_t$  is obtained in (Attigui & Petit, 1996) by constructing an *ad-hoc* field  $0 \leq \|\boldsymbol{\theta}_t\| \leq 1$  which transforms surface (line) integrals to volume (surface) integrals. Here the dynamic energy release rate  $G_t$  is identified by calculating the variation of the space-time action integral (A.3) with respect to crack increment *evolution*. Using the Euler-Lagrange equation

$$\mathcal{A}'(\mathbf{u}^*, l)(\mathbf{0}, \delta l) = \int_I \left( \frac{\partial \mathcal{L}_t}{\partial l_t} - \frac{\mathrm{d}}{\mathrm{d}t} \frac{\partial \mathcal{L}_t}{\partial \dot{l}_t} \right) \cdot \delta l_t \mathrm{d}t$$

and the fact that the Lagrangian depends on the crack velocity  $\dot{l}_t$  solely via the kinetic energy  $\mathcal{K}^*$ , we find the same expression for the dynamic energy release rate  $G_t$  as indicated in (Freund, 1990, p. 423)

$$G_t = \frac{\partial(\mathcal{K}^* + \mathcal{W}_t^* - \mathcal{E}^*)}{\partial l_t} - \frac{\mathrm{d}}{\mathrm{d}t} \frac{\partial \mathcal{K}^*}{\partial \dot{l}_t}.$$

Contrary to the quasi-static regime, this quantity  $G_t$  doesn't possess the physical meaning of the derivative of the Lagrangian with respect to crack extension due to the presence of the term  $(\mathrm{d}/\mathrm{d}t)(\partial \mathcal{K}^* / \partial \dot{l}_t)$ , as has been already noted in (Nishioka & Atluri, 1983).

Although  $\boldsymbol{\theta}_t$  enters into the definition of  $G_t$  in (A.10), the dynamic energy release rate is independent of the exact virtual perturbation used to establish the bijection (2.49), owing to the following

**Proposition A.2.** *The dynamic energy release rate  $G_t$  is equivalent to the classical dynamic  $J$ -integral in the form of a path integral (1.8). As a corollary, the dynamic energy release rate (A.10) is independent of the virtual perturbation.*

*Proof.* For theoretic analysis purpose a specific integration path  $C_r$  is used in (1.8). The symbol  $\mathbf{n}$  is assumed to be the normal pointing out of the ball  $B_r(\mathbf{P}_t)$  with  $C_r = \partial B_r(\mathbf{P}_t)$  its boundary. To removing any singularities near the crack tip  $\mathbf{P}_t$ , we will partition the cracked domain  $\Omega \setminus \Gamma_t$  into the part  $\tilde{B}_r = B_r(\mathbf{P}_t) \setminus \Gamma_t$  included in the ball  $B_r(\mathbf{P}_t)$ , and the part  $\Omega_r = \Omega \setminus (\Gamma_t \cup B_r(\mathbf{P}_t))$  outside the ball, see Figure A.1. Using the following identity in  $\Omega_r$

$$\begin{aligned} \operatorname{div} \left( (\kappa(\dot{\mathbf{u}}_t) + \mathbf{f}_t \cdot \mathbf{u}_t - \psi(\varepsilon(\mathbf{u}_t))) \boldsymbol{\theta}_t \right) &= \rho \dot{\mathbf{u}}_t \cdot \nabla \dot{\mathbf{u}}_t \boldsymbol{\theta}_t + \nabla \mathbf{f}_t \boldsymbol{\theta}_t \cdot \mathbf{u}_t + \mathbf{f}_t \cdot \nabla \mathbf{u}_t \boldsymbol{\theta}_t \\ &\quad - \boldsymbol{\sigma}_t \cdot \varepsilon(\nabla \mathbf{u}_t) \boldsymbol{\theta}_t + (\kappa(\dot{\mathbf{u}}_t) + \mathbf{f}_t \cdot \mathbf{u}_t - \psi(\varepsilon(\mathbf{u}_t))) \operatorname{div} \boldsymbol{\theta}_t \end{aligned} \quad (\text{A.11})$$

and performing an integration by parts

$$\int_{\Omega_r} \boldsymbol{\sigma}_t \cdot (\nabla \mathbf{u}_t \nabla \boldsymbol{\theta}_t) \mathrm{d}\mathbf{x} = - \int_{C_r} (\nabla \mathbf{u}_t^\top \boldsymbol{\sigma}_t) \mathbf{n} \cdot \boldsymbol{\theta}_t \mathrm{d}\mathbf{x} - \int_{\Omega_r} (\operatorname{div} \boldsymbol{\sigma}_t \cdot \nabla \mathbf{u}_t \boldsymbol{\theta}_t + \boldsymbol{\sigma}_t \cdot \nabla^2 \mathbf{u}_t \boldsymbol{\theta}_t) \mathrm{d}\mathbf{x}, \quad (\text{A.12})$$

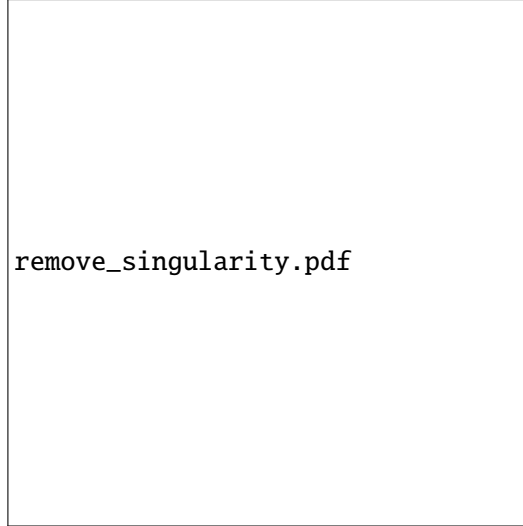


Figure A.1 – Partition of the cracked domain  $\Omega \setminus \Gamma_t$  using a  $\mathbf{P}_t$ -centered ball  $B_r(\mathbf{P}_t)$  of radius  $r$

the dynamic energy release rate  $G_t$  reads

$$\begin{aligned}
 G_t &= \int_{\tilde{B}_r} (\dots) d\mathbf{x} + \int_{\Omega_r} \left( \operatorname{div} \left( \left( \kappa(\dot{\mathbf{u}}_t) + \mathbf{f}_t \cdot \mathbf{u}_t - \psi(\boldsymbol{\varepsilon}(\mathbf{u}_t)) \right) \boldsymbol{\theta}_t \right) - (\operatorname{div} \boldsymbol{\sigma}_t + \mathbf{f}_t - \rho \ddot{\mathbf{u}}_t) \cdot \nabla \mathbf{u}_t \boldsymbol{\theta}_t \right) d\mathbf{x} \\
 &\quad - \int_{C_r} (\nabla \mathbf{u}_t^\top \boldsymbol{\sigma}_t) \mathbf{n} \cdot \boldsymbol{\theta}_t ds \\
 &= \int_{\tilde{B}_r} (\dots) d\mathbf{x} - \int_{C_r} \left( \left( \kappa(\dot{\mathbf{u}}_t) + \mathbf{f}_t \cdot \mathbf{u}_t - \psi(\boldsymbol{\varepsilon}(\mathbf{u}_t)) \right) (\boldsymbol{\theta}_t \cdot \mathbf{n}) + (\nabla \mathbf{u}_t^\top \boldsymbol{\sigma}_t) \mathbf{n} \cdot \boldsymbol{\theta}_t \right) ds \\
 &= \int_{\tilde{B}_r} (\dots) d\mathbf{x} + \int_{C_r} \mathbf{E}_t \mathbf{n} \cdot \boldsymbol{\theta}_t ds - \int_{C_r} (\mathbf{f}_t \cdot \mathbf{u}_t) (\boldsymbol{\theta}_t \cdot \mathbf{n}) ds
 \end{aligned}$$

where the second equality follows from dynamic equilibrium (A.8). On the last line  $\mathbf{E}_t$  denotes the dynamic Eshelby tensor (Maugin, 1994)

$$\mathbf{E}_t = \left( \psi(\boldsymbol{\varepsilon}(\mathbf{u}_t)) - \kappa(\dot{\mathbf{u}}_t) \right) \mathbb{I} - \nabla \mathbf{u}_t^\top \boldsymbol{\sigma}_t. \quad (\text{A.13})$$

The last term involving the body force density  $\mathbf{f}_t$  will have a vanishing contribution as  $r \rightarrow 0$ , since  $\mathbf{f}_t$  is supposed to be regular and asymptotically  $\mathbf{u}_t$  is of order  $O(r^{1/2})$  in linear elastic fracture mechanics.

To solve the contradiction of having the Lagrangian density in (A.13) and the Hamiltonian density in (1.8), contributions from the integral on  $\tilde{B}_r$  must be considered, see (Maugin, 1994). By classical singularity analysis and the steady state condition  $\dot{\mathbf{q}}_t \approx -\nabla \mathbf{q}_t \dot{l}_t \boldsymbol{\tau}_t$  verified for all (tensorial) fields  $\mathbf{q}$  near the crack tip (Freund, 1990), the first two terms of  $G_t$  in (A.10) are of order  $O(r^{-1})$  and hence have a vanishing contribution when integrated with the area element  $r dr d\theta$  on  $\tilde{B}_r$  as  $r$  tends to zero. Similarly the term involving the body force density  $\mathbf{f}_t$  is not singular enough to contribute. However the last two terms  $\rho \ddot{\mathbf{u}}_t \cdot \nabla \mathbf{u}_t \boldsymbol{\theta}_t + \rho \dot{\mathbf{u}}_t \cdot \nabla \dot{\mathbf{u}}_t \boldsymbol{\theta}_t$  are integrable (Nishioka & Atluri, 1983) and will yield a finite value in the limit. Using the real velocity field  $\dot{\mathbf{u}}_t$  in the steady state condition and the fact that  $\boldsymbol{\theta}_t \rightarrow \boldsymbol{\tau}_t$  when  $r$  becomes small due to continuity, we have

$$\rho \ddot{\mathbf{u}}_t \cdot \nabla \mathbf{u}_t \boldsymbol{\theta}_t = \rho \dot{\mathbf{u}}_t \cdot \nabla \dot{\mathbf{u}}_t \boldsymbol{\theta}_t \quad \text{as } r \rightarrow 0.$$

Then an integration by parts in  $\tilde{B}_r$  gives (noting that  $\boldsymbol{\theta}_t \cdot \mathbf{n} = 0$  on  $\Gamma_t$ )

$$\int_{\tilde{B}_r} \rho \dot{\mathbf{u}}_t \cdot \nabla \dot{\mathbf{u}}_t \boldsymbol{\theta}_t d\mathbf{x} = \int_{C_r} \rho (\dot{\mathbf{u}}_t \cdot \dot{\mathbf{u}}_t) (\boldsymbol{\theta}_t \cdot \mathbf{n}) ds - \int_{\tilde{B}_r} \rho \dot{\mathbf{u}}_t \cdot \nabla \dot{\mathbf{u}}_t \boldsymbol{\theta}_t d\mathbf{x} - \int_{\tilde{B}_r} \rho \dot{\mathbf{u}}_t \cdot \dot{\mathbf{u}}_t \operatorname{div} \boldsymbol{\theta}_t d\mathbf{x} \quad (\text{A.14})$$

from which the contribution from the last two terms in (A.10) can be deduced

$$\begin{aligned} \lim_{r \rightarrow 0} \int_{\tilde{B}_r} (\rho \ddot{\mathbf{u}}_t \cdot \nabla \mathbf{u}_t \boldsymbol{\theta}_t + \rho \dot{\mathbf{u}}_t \cdot \nabla \dot{\mathbf{u}}_t \boldsymbol{\theta}_t) d\mathbf{x} &= \lim_{r \rightarrow 0} \int_{\tilde{B}_r} 2\rho \dot{\mathbf{u}}_t \cdot \nabla \dot{\mathbf{u}}_t \boldsymbol{\theta}_t d\mathbf{x} = \lim_{r \rightarrow 0} \int_{C_r} \rho (\dot{\mathbf{u}}_t \cdot \dot{\mathbf{u}}_t) (\boldsymbol{\theta}_t \cdot \mathbf{n}) ds \\ &= \lim_{r \rightarrow 0} \int_{C_r} 2\kappa (\dot{\mathbf{u}}_t) \boldsymbol{\theta}_t \cdot \mathbf{n} ds \end{aligned}$$

where the last term in (A.14) vanishes in the limit  $r \rightarrow 0$ . We obtain hence

$$G_t = \lim_{r \rightarrow 0} \int_{C_r} (\mathbf{E}_t + 2\kappa(\dot{\mathbf{u}}_t)\mathbb{I})\mathbf{n} \cdot \boldsymbol{\theta}_t ds = \lim_{r \rightarrow 0} \int_{C_r} \mathbf{J}_t \mathbf{n} \cdot \boldsymbol{\tau}_t ds. \quad (\text{A.15})$$

which completes the proof.  $\square$

*Remark.* Compared to the classical  $J$ -integral, the advantage of the dynamic energy release rate in the form of (A.10) resides in its direct usage for numerical computations with finite elements, since it involves an integral in the cells.

*Remark* (Generalization to curved or kinked crack paths). Let us recall that the crack  $l \mapsto \gamma(l)$  is supposed to follow a pre-defined straight path in this contribution. It can be generalized to arbitrary but smooth enough *pre-defined* curved paths without much technical difficulties. It suffices to carefully construct a virtual perturbation  $\boldsymbol{\theta}^*$  verifying Definition 2.2, and define the bijection  $\boldsymbol{\phi}_t(\mathbf{x})$  as a solution to a particular Cauchy evolution problem

$$\begin{cases} \boldsymbol{\phi}_0(\mathbf{x}) = \mathbf{x}, \\ \frac{d}{dt} \boldsymbol{\phi}_t(\mathbf{x}) = \boldsymbol{\theta}^*(\boldsymbol{\phi}_t(\mathbf{x})) \text{ for } t > 0, \end{cases}$$

see (Khludnev et al., 2010) for a mathematical analysis of this problem.. The obtained *scalar* crack equation of motion will be formally the same as (1.10), which predicts the crack length  $l_t$  as a function of time along the this path. Note however that crack propagation direction should be at least continuous in time (curved path) so that the shape derivative method embodied by the diffeomorphism  $\boldsymbol{\phi}$  makes sense. In the presence of a crack kinking associated with a temporal discontinuity of the crack tangent (cf. Figure 1.4), the shape derivative methods should be adapted to capture the topology change due to the kinking (Hintermüller & Kovtunenkov, 2011).

When the crack path is unknown, an interesting attempt is to include the crack tangent angle into the action integral (A.3) and evaluate the variation induced by arbitrary crack direction change. Remark that the propagation criterion derived in (Adda-Bedia et al., 1999; Oleaga, 2001) corresponds in fact to a vectorial extension of the scalar propagation law (1.10)

$$\lim_{r \rightarrow 0} \int_{C_r} \mathbf{J}_t \mathbf{n} ds = G_c \boldsymbol{\tau}_t$$

and the component perpendicular to the crack propagation direction  $\boldsymbol{\tau}_t$  determines the crack path.



# B

## Detailed Calculations

### Calculation of the First-Order Action Variation

We will carefully explore the first-order stability principle (A.4) by calculating the action variation with respect to arbitrary displacement and crack variations. The following easily established identities

$$\begin{aligned}\frac{d}{dl_t} \det \nabla \phi(\mathbf{x}^*) &= \det \nabla \phi(\mathbf{x}^*) \operatorname{tr}(\nabla \theta^*(\mathbf{x}^*) \nabla \phi(\mathbf{x}^*)^{-1}) = \operatorname{div} \theta_t(\mathbf{x}) \det \nabla \phi(\mathbf{x}^*), \\ \frac{d}{dl_t} \nabla \phi(\mathbf{x}^*)^{-1} &= -\nabla \phi(\mathbf{x}^*)^{-1} \nabla \theta^*(\mathbf{x}^*) \nabla \phi(\mathbf{x}^*)^{-1} = -\nabla \phi(\mathbf{x}^*)^{-1} \nabla \theta_t(\mathbf{x}).\end{aligned}$$

will be used for all subsequent calculations.

The classical wave equation can be obtained by calculating the action variation with zero crack advance  $\delta l = 0$

$$\begin{aligned}\mathcal{A}'(\mathbf{u}^*, l)(\mathbf{w}^*, 0) &= \int_I dt \int_{\Omega \setminus \Gamma_0} \left( A_0 \left( \frac{1}{2} \nabla \mathbf{u}_t^* \nabla \phi^{-1} + \frac{1}{2} \nabla \phi^{-\top} (\nabla \mathbf{u}_t^*)^\top \right) \cdot \left( \frac{1}{2} \nabla \mathbf{w}_t^* \nabla \phi^{-1} + \frac{1}{2} \nabla \phi^{-\top} (\nabla \mathbf{w}_t^*)^\top \right) \det \nabla \phi \right. \\ &\quad \left. - \rho (\dot{\mathbf{u}}_t^* - \dot{l}_t \nabla \mathbf{u}_t^* \nabla \phi^{-1} \theta^*) \cdot (\dot{\mathbf{w}}_t^* - \dot{l}_t \nabla \mathbf{w}_t^* \nabla \phi^{-1} \theta^*) \det \nabla \phi \right) d\mathbf{x}^* - \mathcal{W}_t^*(\mathbf{w}_t^*),\end{aligned}$$

which gives

$$\begin{aligned}\mathcal{A}'(\mathbf{u}^*, l)(\mathbf{w}^*, 0) &= \int_I dt \int_{\Omega \setminus \Gamma_t} (\sigma_t \cdot \varepsilon(\mathbf{w}_t) + \rho \dot{l}_t \dot{\mathbf{u}}_t \cdot \nabla \mathbf{w}_t \theta_t) d\mathbf{x} - \mathcal{W}_t(\mathbf{w}_t) \\ &\quad + \underbrace{\int_I dt \int_{\Omega \setminus \Gamma_0} \rho \frac{d}{dt} ((\dot{\mathbf{u}}_t^* - \nabla \mathbf{u}_t^* \nabla \phi^{-1} \dot{l}_t \theta^*) \det \nabla \phi) \cdot \mathbf{w}_t^* d\mathbf{x}^*}_R\end{aligned}\quad (\text{B.1})$$

where  $\mathbf{w}$  denotes the pushforward of  $\mathbf{w}^*$  to the current cracked configuration via (2.50).

To proceed, we observe that the real acceleration  $\ddot{\mathbf{u}}_t$  can be obtained by differentiating (2.52)

$$\ddot{\mathbf{u}}_t(\mathbf{x}) = -\nabla \dot{\mathbf{u}}_t(\mathbf{x}) \dot{l}_t \theta^*(\mathbf{x}^*) + \frac{d}{dt} \left( \dot{\mathbf{u}}_t^*(\mathbf{x}^*) - \nabla \mathbf{u}_t^*(\mathbf{x}^*) \nabla \phi(\mathbf{x}^*)^{-1} \dot{l}_t \theta^*(\mathbf{x}^*) \right) \quad (\text{B.2})$$

where  $\nabla \dot{\mathbf{u}}_t$  is the (Eulerian) velocity gradient. Using (B.2), the last term above can be written

$$\begin{aligned}R &= \int_I dt \int_{\Omega \setminus \Gamma_0} (\rho (\ddot{\mathbf{u}}_t \circ \phi + (\nabla \dot{\mathbf{u}}_t \circ \phi) \dot{l}_t \theta^*) \cdot \mathbf{w}_t^* \det \nabla \phi \\ &\quad + \rho \dot{l}_t (\dot{\mathbf{u}}_t^* - \nabla \mathbf{u}_t^* \nabla \phi^{-1} \dot{l}_t \theta^*) \cdot \mathbf{w}_t^* \operatorname{tr}(\nabla \phi^{-1} \nabla \theta^*) \det \nabla \phi) d\mathbf{x}^*,\end{aligned}$$



which leads to

$$\begin{aligned} R &= \int_I dt \int_{\Omega \setminus \Gamma_t} (\rho \ddot{\mathbf{u}}_t \cdot \mathbf{w}_t + \rho \dot{l}_t \nabla \dot{\mathbf{u}}_t \boldsymbol{\theta}_t \cdot \mathbf{w}_t + \rho \dot{l}_t \dot{\mathbf{u}}_t \cdot \mathbf{w}_t \operatorname{div} \boldsymbol{\theta}_t) d\mathbf{x} \\ &= \int_I dt \int_{\Omega \setminus \Gamma_t} (\rho \ddot{\mathbf{u}}_t \cdot \mathbf{w}_t - \rho \dot{l}_t \dot{\mathbf{u}}_t \cdot \nabla \mathbf{w}_t \boldsymbol{\theta}_t) d\mathbf{x}, \end{aligned} \quad (\text{B.3})$$

where an integration by parts in  $\Omega \setminus \Gamma_t$  has been used on establishing the last equality. Regrouping (B.1) and (B.3), we obtain thus the spatially weak dynamic equilibrium

$$\mathcal{A}'(\mathbf{u}^*, l)(\mathbf{w}^*, 0) = \int_I dt \int_{\Omega \setminus \Gamma_t} (\boldsymbol{\sigma}_t \cdot \boldsymbol{\varepsilon}(\mathbf{w}_t) + \rho \ddot{\mathbf{u}}_t \cdot \mathbf{w}_t) d\mathbf{x} - \mathcal{W}_t(\mathbf{w}_t). \quad (\text{B.4})$$

An integration by parts then gives the desired wave equation (A.7) for the displacement.

We then evaluate the action variation with respect to arbitrary crack increment  $\delta l$  but zero displacement variation

$$\begin{aligned} \mathcal{A}'(\mathbf{u}^*, l)(\mathbf{0}, \delta l) &= \int_I G_c \cdot \delta l_t dt \\ &\quad + \int_I \delta l_t dt \int_{\Omega \setminus \Gamma_t} \left( (\psi(\boldsymbol{\varepsilon}(\mathbf{u}_t)) - \kappa(\dot{\mathbf{u}}_t)) \operatorname{div} \boldsymbol{\theta}_t - \boldsymbol{\sigma}_t \cdot (\nabla \mathbf{u}_t \nabla \boldsymbol{\theta}_t) - \operatorname{div}(\mathbf{f}_t \otimes \boldsymbol{\theta}_t) \cdot \mathbf{u}_t \right) d\mathbf{x} \\ &\quad - \underbrace{\int_I dt \int_{\Omega \setminus \Gamma_0} (\rho(\dot{\mathbf{u}}_t^* - \dot{l}_t \nabla \mathbf{u}_t^* \nabla \boldsymbol{\phi}^{-1} \boldsymbol{\theta}^*) \cdot (-\nabla \mathbf{u}_t^* \nabla \boldsymbol{\phi}^{-1} \boldsymbol{\theta}^* \cdot \dot{\delta l}_t + \dot{l}_t \nabla \mathbf{u}_t^* \nabla \boldsymbol{\phi}^{-1} \nabla \boldsymbol{\theta}^* \nabla \boldsymbol{\phi}^{-1} \boldsymbol{\theta}^* \cdot \delta l_t) \det \nabla \boldsymbol{\phi}) d\mathbf{x}^*}_{R}. \end{aligned} \quad (\text{B.5})$$

The last term can be written using integration by parts in the time domain

$$\begin{aligned} R &= \int_I \delta l_t dt \int_{\Omega \setminus \Gamma_0} \rho \frac{d}{dt} ((\dot{\mathbf{u}}_t^* - \dot{l}_t \nabla \mathbf{u}_t^* \nabla \boldsymbol{\phi}^{-1} \boldsymbol{\theta}^*) \cdot (\nabla \mathbf{u}_t^* \nabla \boldsymbol{\phi}^{-1} \boldsymbol{\theta}^*) \det \nabla \boldsymbol{\phi}) d\mathbf{x}^* \\ &\quad + \int_I \delta l_t dt \int_{\Omega \setminus \Gamma_t} \rho \dot{l}_t \dot{\mathbf{u}}_t \cdot \nabla \mathbf{u}_t \nabla \boldsymbol{\theta}_t \boldsymbol{\theta}_t d\mathbf{x}, \end{aligned}$$

which gives

$$\begin{aligned} R &= \int_I \delta l_t dt \int_{\Omega \setminus \Gamma_0} (\rho(\ddot{\mathbf{u}}_t \circ \boldsymbol{\phi} + (\nabla \dot{\mathbf{u}}_t \circ \boldsymbol{\phi}) \dot{l}_t \boldsymbol{\theta}^*) \cdot (\nabla \mathbf{u}_t^* \nabla \boldsymbol{\phi}^{-1} \boldsymbol{\theta}^*) \det \nabla \boldsymbol{\phi} \\ &\quad + \rho(\dot{\mathbf{u}}_t^* - \dot{l}_t \nabla \mathbf{u}_t^* \nabla \boldsymbol{\phi}^{-1} \boldsymbol{\theta}^*) \cdot (\nabla \dot{\mathbf{u}}_t^* \nabla \boldsymbol{\phi}^{-1} \boldsymbol{\theta}^* - \dot{l}_t \nabla \mathbf{u}_t^* \nabla \boldsymbol{\phi}^{-1} \nabla \boldsymbol{\theta}^* \nabla \boldsymbol{\phi}^{-1} \boldsymbol{\theta}^*) \det \nabla \boldsymbol{\phi}) d\mathbf{x}^* \\ &\quad + \int_I \delta l_t dt \int_{\Omega \setminus \Gamma_t} (\rho \dot{l}_t \dot{\mathbf{u}}_t \cdot \nabla \mathbf{u}_t \boldsymbol{\theta}_t \operatorname{div} \boldsymbol{\theta}_t + \rho \dot{l}_t \dot{\mathbf{u}}_t \cdot \nabla \mathbf{u}_t \nabla \boldsymbol{\theta}_t \boldsymbol{\theta}_t) d\mathbf{x}. \end{aligned}$$

We obtain thus

$$\begin{aligned} R &= \int_I \delta l_t dt \int_{\Omega \setminus \Gamma_t} (\rho \ddot{\mathbf{u}}_t \cdot \nabla \mathbf{u}_t \boldsymbol{\theta}_t + \rho \dot{l}_t \nabla \dot{\mathbf{u}}_t \boldsymbol{\theta}_t \cdot \nabla \mathbf{u}_t \boldsymbol{\theta}_t + \rho \dot{l}_t \dot{\mathbf{u}}_t \cdot \nabla \mathbf{u}_t \boldsymbol{\theta}_t \operatorname{div} \boldsymbol{\theta}_t) d\mathbf{x} \\ &\quad + \int_I \delta l_t dt \int_{\Omega \setminus \Gamma_0} \rho(\dot{\mathbf{u}}_t^* - \dot{l}_t \nabla \mathbf{u}_t^* \nabla \boldsymbol{\phi}^{-1} \boldsymbol{\theta}^*) \cdot (\nabla \dot{\mathbf{u}}_t^* \nabla \boldsymbol{\phi}^{-1} \boldsymbol{\theta}^*) \det \nabla \boldsymbol{\phi} d\mathbf{x}^*. \end{aligned}$$

Differentiating (2.51) to obtain the material time derivative of the deformation gradient  $(d/dt)(\nabla \mathbf{u}_t)$

$$\frac{d}{dt}(\nabla \mathbf{u}_t(\mathbf{x})) = \nabla \dot{\mathbf{u}}_t^*(\mathbf{x}^*) \nabla \boldsymbol{\phi}(\mathbf{x}^*)^{-1} - \dot{l}_t \nabla \mathbf{u}_t(\mathbf{x}) \nabla \boldsymbol{\theta}_t(\mathbf{x}),$$

and with its definition

$$\frac{d}{dt}(\nabla \mathbf{u}_t(\mathbf{x})) = \nabla \dot{\mathbf{u}}_t(\mathbf{x}) + \nabla^2 \mathbf{u}_t(\mathbf{x}) \dot{l}_t \boldsymbol{\theta}^*(\mathbf{x}^*)$$

where  $\nabla^2 \mathbf{u}_t$  is the second gradient of the displacement field (a third-order tensor), we obtain

$$R = \int_I \delta l_t dt \int_{\Omega \setminus \Gamma_t} (\rho \ddot{\mathbf{u}}_t \cdot \nabla \mathbf{u}_t \boldsymbol{\theta}_t + \rho \dot{l}_t \nabla \dot{\mathbf{u}}_t \boldsymbol{\theta}_t \cdot \nabla \mathbf{u}_t \boldsymbol{\theta}_t + \rho \dot{\mathbf{u}}_t \cdot \nabla \dot{\mathbf{u}}_t \boldsymbol{\theta}_t + \rho \dot{l}_t \dot{\mathbf{u}}_t \cdot (\nabla^2 \mathbf{u}_t \boldsymbol{\theta}_t) \boldsymbol{\theta}_t + \rho \dot{l}_t \dot{\mathbf{u}}_t \cdot \nabla \mathbf{u}_t \nabla \boldsymbol{\theta}_t \boldsymbol{\theta}_t + \rho \dot{l}_t \dot{\mathbf{u}}_t \cdot \nabla \mathbf{u}_t \boldsymbol{\theta}_t \operatorname{div} \boldsymbol{\theta}_t) d\mathbf{x}.$$

Using an integration by parts in the domain  $\Omega \setminus \Gamma_t$  knowing that  $\boldsymbol{\theta}_t = \mathbf{0}$  on  $\partial\Omega$  and  $\boldsymbol{\theta}_t \cdot \mathbf{n} = 0$  on  $\Gamma_t$  by definition

$$\int_{\Omega \setminus \Gamma_t} \rho \dot{l}_t \dot{\mathbf{u}}_t \cdot \nabla \mathbf{u}_t \nabla \boldsymbol{\theta}_t \boldsymbol{\theta}_t d\mathbf{x} = - \int_{\Omega \setminus \Gamma_t} (\rho \dot{l}_t \dot{\mathbf{u}}_t \cdot \nabla \mathbf{u}_t \boldsymbol{\theta}_t \operatorname{div} \boldsymbol{\theta}_t + \rho \dot{l}_t \nabla \dot{\mathbf{u}}_t \boldsymbol{\theta}_t \cdot \nabla \mathbf{u}_t \boldsymbol{\theta}_t + \rho \dot{l}_t \dot{\mathbf{u}}_t \cdot (\nabla^2 \mathbf{u}_t \boldsymbol{\theta}_t) \boldsymbol{\theta}_t) d\mathbf{x},$$

we get finally

$$R = \int_I \delta l_t dt \int_{\Omega \setminus \Gamma_t} (\rho \ddot{\mathbf{u}}_t \cdot \nabla \mathbf{u}_t \boldsymbol{\theta}_t + \rho \dot{\mathbf{u}}_t \cdot \nabla \dot{\mathbf{u}}_t \boldsymbol{\theta}_t) d\mathbf{x}$$

which permits with (B.5) to deduce the desired equations (A.9) and (A.10).

## Local Energy Balance Condition

In this section we will derive the equivalent local condition of the global energy balance (A.5), which gives the desired Griffith's law of motion (1.10) when combined with the local stability condition (A.9). The Lagrangian defined in (A.3) is explicitly dependent on time solely through the external work potential (2.59). Its total derivative can thus be given by

$$\frac{d\mathcal{L}}{dt} = \frac{\partial \mathcal{L}}{\partial \mathbf{u}_t^*} \dot{\mathbf{u}}_t^* + \frac{\partial \mathcal{L}}{\partial \ddot{\mathbf{u}}_t^*} \ddot{\mathbf{u}}_t^* + \frac{\partial \mathcal{L}}{\partial \dot{l}_t} \dot{l}_t + \frac{\partial \mathcal{L}}{\partial \ddot{l}_t} \ddot{l}_t + \frac{\partial \mathcal{L}}{\partial t}. \quad (\text{B.6})$$

Using the weak dynamic equilibrium (B.4) and the fact that  $\dot{\mathbf{u}}_t^* - \dot{\mathbf{U}}_t \in C_0$ , we have

$$\frac{\partial \mathcal{L}}{\partial \mathbf{u}_t^*} (\dot{\mathbf{u}}_t^* - \dot{\mathbf{U}}_t) - \frac{d}{dt} \frac{\partial \mathcal{L}}{\partial \ddot{\mathbf{u}}_t^*} (\dot{\mathbf{u}}_t^* - \dot{\mathbf{U}}_t) = \mathbf{0}. \quad (\text{B.7})$$

Plugging (B.7) into (B.6), we obtain

$$\frac{d\mathcal{L}}{dt} = \frac{d}{dt} \left( \frac{\partial \mathcal{L}}{\partial \ddot{\mathbf{u}}_t^*} \dot{\mathbf{u}}_t^* \right) + \frac{\partial \mathcal{L}}{\partial \mathbf{u}_t^*} \dot{\mathbf{U}}_t - \frac{d}{dt} \frac{\partial \mathcal{L}}{\partial \ddot{\mathbf{u}}_t^*} \dot{\mathbf{U}}_t + \frac{\partial \mathcal{L}}{\partial \dot{l}_t} \dot{l}_t + \frac{\partial \mathcal{L}}{\partial \ddot{l}_t} \ddot{l}_t + \frac{\partial \mathcal{L}}{\partial t}. \quad (\text{B.8})$$

With all necessary temporal regularity, we note that the energy balance condition (A.5) can be equivalently written as

$$\frac{d\mathcal{H}}{dt} = \frac{d}{dt} (\mathcal{L} + 2\mathcal{K}) = \frac{d}{dt} \left( \mathcal{L} - \frac{\partial \mathcal{L}}{\partial \ddot{\mathbf{u}}_t^*} \dot{\mathbf{u}}_t^* - \frac{\partial \mathcal{L}}{\partial \dot{l}_t} \dot{l}_t \right) = \frac{\partial \mathcal{L}}{\partial \mathbf{u}_t^*} \dot{\mathbf{U}}_t - \frac{d}{dt} \frac{\partial \mathcal{L}}{\partial \ddot{\mathbf{u}}_t^*} \dot{\mathbf{U}}_t + \frac{\partial \mathcal{L}}{\partial t}. \quad (\text{B.9})$$

Comparing (B.8) and (B.9), we obtain the desired local energy balance condition

$$\left( \frac{\partial \mathcal{L}}{\partial \dot{l}_t} - \frac{d}{dt} \frac{\partial \mathcal{L}}{\partial \ddot{l}_t} \right) \cdot \dot{l}_t = 0.$$



# Bibliography

- Abraham, F. F., Brodbeck, D., Rafey, R. A., & Rudge, W. E. (1994). Instability dynamics of fracture: a computer simulation investigation. *Physical Review Letters*, 73(2), 272. (Cited on page 5).
- Adda-Bedia, M., & Arias, R. (2003). Brittle fracture dynamics with arbitrary paths I. Kinking of a dynamic crack in general antiplane loading. *Journal of the Mechanics and Physics of Solids*, 51(7), 1287–1304. doi:10.1016/S0022-5096(03)00022-X. (Cited on page 10)
- Adda-Bedia, M., Arias, R., Amar, M. B., & Lund, F. (1999). Generalized Griffith criterion for dynamic fracture and the stability of crack motion at high velocities. *Physical Review E*, 60(2), 2366–2376. (Cited on pages 6, 161 and 165).
- Adhikary, S. D., Li, B., & Fujikake, K. (2012). Dynamic behavior of reinforced concrete beams under varying rates of concentrated loading. *International Journal of Impact Engineering*, 47, 24–38. (Cited on pages 144 and 149).
- Alessi, R., Marigo, J.-J., & Vidoli, S. (2015). Gradient damage models coupled with plasticity: Variational formulation and main properties. *Mechanics of Materials*, 80, 351–367. (Cited on pages 30, 31, 144, 152 and 155).
- Alfano, G., Rosati, L., & Valoroso, N. (2000). A numerical strategy for finite element analysis of no-tension materials. *International Journal for Numerical Methods in Engineering*, 48(3), 317–350. (Cited on pages 41 and 42).
- Ambati, M., Gerasimov, T., & de Lorenzis, L. (2015). A review on phase-field models of brittle fracture and a new fast hybrid formulation. *Computational Mechanics*, 55(2), 383–405. (Cited on page 45).
- Ambrosio, L., & Tortorelli, V. M. (1990). Approximation of functional depending on jumps by elliptic functional via Gamma-convergence. *Communications on Pure and Applied Mathematics*, 43(8), 999–1036. doi:10.1002/cpa.3160430805. (Cited on page 14)
- Amor, H. (2008). *Approche variationnelle des lois de Griffith et de Paris via des modeles non-locaux d'endommagement : Etude theorique et mise en oeuvre numerique* (Doctoral dissertation, Université Paris 13). (Cited on page 36).
- Amor, H., Marigo, J.-J., & Maurini, C. (2009). Regularized formulation of the variational brittle fracture with unilateral contact: Numerical experiments. *Journal of the Mechanics and Physics of Solids*, 57(8), 1209–1229. doi:10.1016/j.jmps.2009.04.011. (Cited on pages 12, 18, 20, 21, 36, 37, 41, 43, 45, 105, 113, 127, 130 and 135)
- Attigui, M., & Petit, C. (1996). Numerical path independent integral in dynamic fracture mechanics. In *ECF 11 – Mechanisms and Mechanics of Damage and Failure*. (Cited on page 163).
- Balay, S., Abhyankar, S., Adams, M., Brown, J., Brune, P., Buschelman, K., . . . Zhang, H. (2015). *PETSc Users Manual* (technical report Number ANL-95/11 - Revision 3.6). Argonne National Laboratory. Accessed on 1 May 2016. (Cited on pages 22, 74 and 76).
- Ballarini, R., & Royer-Carfagni, G. (2016). Closed-Path J-Integral Analysis of Bridged and Phase-Field Cracks. *Journal of Applied Mechanics*, 83(6), 061008. (Cited on pages 57 and 64).
- Barenblatt, G. I. (1962). The Mathematical Theory of Equilibrium Cracks in Brittle Fracture. *Advances in Applied Mechanics*. *Advances in Applied Mechanics*, 7, 55–129. doi:10.1016/S0065-2156(08)70121-2. (Cited on pages 6 and 10)
- Batra, G., Bedford, A., & Drumheller, D. S. (1986). Applications of Hamilton's principle to continua with singular surfaces. *Archive for Rational Mechanics and Analysis*, 93(3), 223–251. doi:10.1007/BF00281499. (Cited on page 35)
- Bazant, Z. P., & Belytschko, T. B. (1985). Wave propagation in a strain-softening bar: Exact solution. *Journal of Engineering Mechanics*, 111(3), 381–389. (Cited on pages 19 and 81).
- Beaurain, J. (2011). *Recherche de solutions bifurquées et étude de leur stabilité dans les problèmes d'endommagement* (Doctoral dissertation, Université Pierre et Marie Curie). (Cited on page 74).
- Benallal, A., Billardon, R., & Geymonat, G. (1993). Bifurcation and Localization in Rate-Independent Materials. Some General Considerations. In Q. Nguyen (Editor), *Bifurcation and Stability of Dissipative Systems* (Volume 327, Pages 1–44). International Centre for Mechanical Sciences. Springer Vienna. (Cited on page 19).

- Benallal, A., & Marigo, J.-J. (2007). Bifurcation and stability issues in gradient theories with softening. *Modelling and Simulation in Materials Science and Engineering*, 15(1), S283. (Cited on page 20).
- Benson, S. J., McInnes, L. C., & Moré, J. J. (2001). GPCG: A Case Study in the Performance and Scalability of Optimization Algorithms. *ACM Transactions on Mathematical Software*, 27(3), 361–376. doi:10.1145/502800.502805. (Cited on page 75)
- Borden, M. J., Verhoosel, C. V., Scott, M. A., Hughes, T. J., & Landis, C. M. (2012). A phase-field description of dynamic brittle fracture. *Computer Methods in Applied Mechanics and Engineering*, 217–220, 77–95. doi:10.1016/j.cma.2012.01.008. (Cited on pages 6, 23, 36, 37, 41, 72, 73, 111, 115, 123 and 126)
- Bouchbinder, E., Goldman, T., & Fineberg, J. (2014). The dynamics of rapid fracture: instabilities, nonlinearities and length scales. *Reports on Progress in Physics*, 77(4), 046501. (Cited on page 11).
- Boué, T. G., Cohen, G., & Fineberg, J. (2015). Origin of the microbranching instability in rapid cracks. *Physical Review Letters*, 114(5), 054301. (Cited on pages 122 and 159).
- Bourdin, B., Francfort, G. A., & Marigo, J.-J. (2000). Numerical experiments in revisited brittle fracture. *Journal of the Mechanics and Physics of Solids*, 48(4), 797–826. (Cited on pages 12, 14, 15, 19, 22, 28, 36, 37 and 41).
- Bourdin, B., Francfort, G. A., & Marigo, J.-J. (2008). The Variational Approach to Fracture. *Journal of Elasticity*, 91(1-3), 5–148. (Cited on pages 6, 12, 13, 15, 17, 67, 68, 95, 102, 105 and 126).
- Bourdin, B., Larsen, C. J., & Richardson, C. L. (2011). A time-discrete model for dynamic fracture based on crack regularization. *International Journal of Fracture*, 168(2), 133–143. (Cited on pages 16, 17, 21, 37, 72, 74, 94, 95 and 105).
- Bourdin, B., Marigo, J.-J., Maurini, C., & Sicsic, P. (2014). Morphogenesis and propagation of complex cracks induced by thermal shocks. *Physical Review Letters*, 112(1), 014301. (Cited on pages 20 and 27).
- Braides, A. (1998). *Approximation of free-discontinuity problems*. Springer Science & Business Media. (Cited on page 14).
- Braides, A. (2002). *Gamma-convergence for Beginners*. Oxford University Press Oxford. (Cited on pages 14, 19 and 20).
- Cazes, F., Coret, M., Combescure, A., & Gravouil, A. (2009). A thermodynamic method for the construction of a cohesive law from a nonlocal damage model. *International Journal of Solids and Structures*, 46(6), 1476–1490. (Cited on pages 6 and 157).
- CEA, & EC. (2015). *EUROPLEXUS: A Computer Program for the Finite Element Simulation of Fluid-Structure Systems under Transient Dynamic Loading. User's Manual*. Commissariat à l'énergie atomique and European Commission. (Cited on pages v, x, 73, 75, 112 and 155).
- Chambolle, A., Francfort, G. A., & Marigo, J.-J. (2009). When and how do cracks propagate? *Journal of the Mechanics and Physics of Solids*, 57(9), 1614–1622. doi:10.1016/j.jmps.2009.05.009. (Cited on pages 10, 13, 14, 108 and 158)
- Charlotte, M., Francfort, G. A., Marigo, J.-J., & Truskinovsky, L. (2000). Revisiting brittle fracture as an energy minimization problem: comparison of Griffith and Barenblatt surface energy models. In *Symposium on continuous damage and fracture*. (Cited on page 14).
- Cherepanov, G. P. (1967). The propagation of cracks in a continuous medium. *Journal of Applied Mathematics and Mechanics*, 31(3), 503–512. (Cited on page 8).
- Cherepanov, G. P. (1989). A remark on the dynamic invariant or path-independent integral. *International Journal of Solids and Structures*, 25(11), 1267–1269. doi:10.1016/0020-7683(89)90090-5. (Cited on page 7)
- Ciarlet, P. G. (1993). *Mathematical elasticity: Three-dimensional elasticity*. Elsevier. (Cited on page 38).
- Ciarlet, P. G., & Nečas, J. (1987). Injectivity and self-contact in nonlinear elasticity. *Archive for Rational Mechanics and Analysis*, 97(3), 171–188. (Cited on pages 21 and 45).
- Clayton, J. D., & Knap, J. (2014). A geometrically nonlinear phase field theory of brittle fracture. *International Journal of Fracture*, 189(2), 139–148. doi:10.1007/s10704-014-9965-1. (Cited on page 38)
- Comi, C. (1999). Computational modelling of gradient-enhanced damage in quasi-brittle materials. *Mechanics of Cohesive-Frictional Materials*, 4(1), 17–36. (Cited on pages 6 and 19).
- Comi, C. (2001). A non-local model with tension and compression damage mechanisms. *European Journal of Mechanics - A/Solids*, 20(1), 1–22. doi:10.1016/S0997-7538(00)01111-6. (Cited on page 19)
- Comi, C., Mariani, S., & Perego, U. (2007). An extended FE strategy for transition from continuum damage to mode I cohesive crack propagation. *International Journal for Numerical and Analytical Methods in Geomechanics*, 31(2), 213–238. doi:10.1002/nag.537. (Cited on page 157)
- Conti, S., Focardi, M., & Iurlano, F. (2015). Phase field approximation of cohesive fracture models. *Annales de l'Institut Henri Poincaré (C) Non Linear Analysis*. doi:10.1016/j.anihpc.2015.02.001. (Cited on page 14)

- Cuvilliez, S., Feyel, F., Lorentz, E., & Michel-Ponnelle, S. (2012). A finite element approach coupling a continuous gradient damage model and a cohesive zone model within the framework of quasi-brittle failure. *Computer Methods in Applied Mechanics and Engineering*, 237-240, 244–259. doi:[10.1016/j.cma.2012.04.019](https://doi.org/10.1016/j.cma.2012.04.019). (Cited on pages [6](#) and [157](#))
- Dally, T., & Weinberg, K. (2015). The phase-field approach as a tool for experimental validations in fracture mechanics. *Continuum Mechanics and Thermodynamics*, 1–10. (Cited on page [23](#)).
- de Borst, R., Remmers, J. J. C., Needleman, A., & Abellan, M.-A. (2004). Discrete vs smeared crack models for concrete fracture: bridging the gap. *International Journal for Numerical and Analytical Methods in Geomechanics*, 28(7-8), 583–607. doi:[10.1002/nag.374](https://doi.org/10.1002/nag.374). (Cited on pages [6](#) and [19](#))
- de Vree, J. H. P., Brekelmans, W. A. M., & van Gils, M. A. J. (1995). Comparison of nonlocal approaches in continuum damage mechanics. *Computers & Structures*, 55(4), 581–588. (Cited on page [19](#)).
- Del Piero, G. (1989). Constitutive equation and compatibility of the external loads for linear elastic masonry-like materials. *Meccanica*, 24(3), 150–162. doi:[10.1007/BF01559418](https://doi.org/10.1007/BF01559418). (Cited on page [41](#))
- Destuynder, P., & Djaoua, M. (1981). Sur une interprétation mathématique de l'intégrale de Rice en théorie de la rupture fragile. *Mathematical Methods in the Applied Sciences*, 3(1), 70–87. (Cited on pages [47](#), [49](#), [158](#) and [163](#)).
- Destuynder, P., Djaoua, M., & Lescure, S. (1983). Quelques remarques sur la mécanique de la rupture élastique. *Journal de Mécanique Théorique et Appliquée*, 2(1), 113–135. (Cited on page [96](#)).
- Dumouchel, P.-E., Marigo, J.-J., & Charlotte, M. (2008). Dynamic fracture: an example of convergence towards a discontinuous quasistatic solution. *Continuum Mechanics and Thermodynamics*, 20(1), 1–19. doi:[10.1007/s00161-008-0071-3](https://doi.org/10.1007/s00161-008-0071-3). (Cited on pages [95](#), [103](#), [105](#) and [106](#))
- Elices, M., Guinea, G., Gómez, J., & Planas, J. (2002). The cohesive zone model: advantages, limitations and challenges. *Engineering Fracture Mechanics*, 69(2), 137–163. doi:[10.1016/S0013-7944\(01\)00083-2](https://doi.org/10.1016/S0013-7944(01)00083-2). (Cited on page [10](#))
- Erdogan, F., & Sih, G. C. (1963). On the crack extension in plates under plane loading and transverse shear. *Journal of Basic Engineering*, 85(4), 519–525. (Cited on page [10](#)).
- Eshelby, J. D. (1970). Energy Relations and the Energy-Momentum Tensor in Continuum Mechanics. In M. Kanninen, W. F. Adler, A. R. Rosenfeld, & R. I. Jaffee (Editors), *Inelastic behaviour of solids* (Pages 77–114). McGraw-Hill. (Cited on page [11](#)).
- Eshelby, J. D. (1975). The elastic energy-momentum tensor. *Journal of Elasticity*, 5(3-4), 321–335. (Cited on page [6](#)).
- Fineberg, J., & Bouchbinder, E. (2015). Recent developments in dynamic fracture: some perspectives. *International Journal of Fracture*, 1–25. doi:[10.1007/s10704-015-0038-x](https://doi.org/10.1007/s10704-015-0038-x). (Cited on page [11](#))
- Fineberg, J., Gross, S. P., Marder, M., & Swinney, H. L. (1992). Instability in the propagation of fast cracks. *Physical Review B*, 45(10), 5146–5154. doi:[10.1103/PhysRevB.45.5146](https://doi.org/10.1103/PhysRevB.45.5146). (Cited on page [119](#))
- Fineberg, J., & Marder, M. (1999). Instability in dynamic fracture. *Physics Reports*, 313(1), 1–108. (Cited on pages [5](#), [11](#), [116](#), [119](#) and [126](#)).
- Francfort, G. A., & Marigo, J.-J. (1998). Revisiting brittle fracture as an energy minimization problem. *Journal of the Mechanics and Physics of Solids*, 46(8), 1319–1342. (Cited on pages [x](#), [6](#), [9](#), [12](#) and [13](#)).
- Freddi, F., & Royer-Carfagni, G. (2010). Regularized variational theories of fracture: A unified approach. *Journal of the Mechanics and Physics of Solids*, 58(8), 1154–1174. doi:[10.1016/j.jmps.2010.02.010](https://doi.org/10.1016/j.jmps.2010.02.010). (Cited on pages [20](#), [21](#), [39](#), [41](#), [42](#), [43](#), [45](#), [46](#), [77](#), [123](#), [125](#), [127](#), [128](#), [130](#), [132](#), [135](#), [136](#), [138](#), [139](#), [144](#), [151](#) and [157](#))
- Freund, L. B. (1972). Energy flux into the tip of an extending crack in an elastic solid. *Journal of Elasticity*, 2(4), 341–349. doi:[10.1007/BF00045718](https://doi.org/10.1007/BF00045718). (Cited on page [8](#))
- Freund, L. B. (1990). *Dynamic Fracture Mechanics*. doi:[10.1017/CBO9780511546761](https://doi.org/10.1017/CBO9780511546761). (Cited on pages [6](#), [8](#), [9](#), [163](#) and [164](#))
- Gol'Dstein, R. V., & Salganik, R. L. (1974). Brittle fracture of solids with arbitrary cracks. *International Journal of Fracture*, 10(4), 507–523. (Cited on pages [10](#) and [11](#)).
- Gray, C. G., & Taylor, E. F. (2007). When action is not least. *American Journal of Physics*, 75(5), 434–458. (Cited on page [30](#)).
- Grégoire, D., Maigre, H., Réthoré, J., & Combescure, A. (2007). Dynamic crack propagation under mixed-mode loading – Comparison between experiments and X-FEM simulations. *International Journal of Solids and Structures*, 44(20), 6517–6534. doi:[10.1016/j.ijsolstr.2007.02.044](https://doi.org/10.1016/j.ijsolstr.2007.02.044). (Cited on pages [10](#) and [130](#))
- Griffith, A. A. (1921). The phenomena of rupture and flow in solids. *Philosophical transactions of the Royal Society of London*, 221, 163–198. (Cited on pages [4](#), [6](#) and [10](#)).
- Guilbaud, D. (2015). Damage plastic model for concrete failure under impulsive loadings. In *COMPLAS XIII: Proceedings of the XIII International Conference on Computational Plasticity: Fundamentals and Applications* (Pages 1031–1042). CIMNE. (Cited on pages [144](#), [146](#), [149](#) and [152](#)).



- Gurtin, M. E. (1964). Variational principles for linear elastodynamics. *Archive for Rational Mechanics and Analysis*, 16(1), 34–50. (Cited on page 30).
- Haboussa, D., Grégoire, D., Elguedj, T., Maigre, H., & Combescure, A. (2011). X-FEM analysis of the effects of holes or other cracks on dynamic crack propagations. *International Journal for Numerical Methods in Engineering*, 86(4-5), 618–636. (Cited on pages 9, 10, 130, 131 and 132).
- Hakim, V., & Karma, A. (2005). Crack path prediction in anisotropic brittle materials. *Physical Review Letters*, 95(23), 235501. (Cited on pages 107 and 108).
- Hakim, V., & Karma, A. (2009). Laws of crack motion and phase-field models of fracture. *Journal of the Mechanics and Physics of Solids*, 57(2), 342–368. doi:10.1016/j.jmps.2008.10.012. (Cited on pages 6, 22, 35, 37, 57, 58, 64 and 107)
- Halphen, B., & Nguyen, Q. S. (1975). Sur les matériaux standard généralisés. *Journal de Mécanique*, 14, 39–63. (Cited on page 18).
- Hamilton, W. R. (1834). On a general method in dynamics. *Philosophical transactions of the Royal Society of London*, 124, 247–308. (Cited on page 30).
- Hentz, S. (2003). *Modélisation d'une structure en béton armé soumise à un choc par la méthode des éléments discrets sphériques* (Doctoral dissertation, Université Joseph Fourier Grenoble). (Cited on page 152).
- Hentz, S., Donzé, F. V., & Daudeville, L. (2004). Discrete element modelling of concrete submitted to dynamic loading at high strain rates. *Computers & Structures*, 82(29), 2509–2524. (Cited on page 5).
- Hesch, C., & Weinberg, K. (2014). Thermodynamically consistent algorithms for a finite-deformation phase-field approach to fracture. *International Journal for Numerical Methods in Engineering*, 99(12), 906–924. (Cited on pages 38 and 41).
- Hintermüller, M., & Kovtunen, V. A. (2011). From shape variation to topological changes in constrained minimization: a velocity method-based concept. *Optimization Methods and Software*, 26(4-5), 513–532. (Cited on pages 158 and 165).
- Hofacker, M., & Miehe, C. (2013). A phase field model of dynamic fracture: Robust field updates for the analysis of complex crack patterns. *International Journal for Numerical Methods in Engineering*, 93(3), 276–301. doi:10.1002/nme.4387. (Cited on page 36)
- Hofacker, M., & Miehe, C. (2012). Continuum phase field modeling of dynamic fracture: variational principles and staggered FE implementation. *International Journal of Fracture*, 178(1-2), 113–129. (Cited on pages 6, 23, 36, 41, 72, 123 and 127).
- Hossain, M. Z., Hsueh, C.-J., Bourdin, B., & Bhattacharya, K. (2014). Effective toughness of heterogeneous media. *Journal of the Mechanics and Physics of Solids*, 71, 15–32. doi:10.1016/j.jmps.2014.06.002. (Cited on pages 23, 95, 96 and 126)
- Hughes, T. J. (1987). *The Finite Element Method: Linear Static and Dynamic Finite Element Analysis*. Englewood Cliffs, New Jersey: Prentice-Hall. (Cited on pages 68 and 85).
- Hughes, T. J., & Hulbert, G. M. (1988). Space-time finite element methods for elastodynamics: Formulations and error estimates. *Computer Methods in Applied Mechanics and Engineering*, 66(3), 339–363. doi:10.1016/0045-7825(88)90006-0. (Cited on pages 67 and 155)
- Hussain, M. A., Pu, S. L., & Underwood, J. (1974). Strain energy release rate for a crack under combined mode I and mode II. In *Fracture Analysis: Proceedings of the 1973 National Symposium on Fracture Mechanics, Part II*. ASTM International. (Cited on page 10).
- Irwin, G. (1957). Analysis of Stresses and Strains Near the End of a Crack Traversing a Plate. *Journal of Applied Mechanics*, 24, 361–364. (Cited on page 8).
- Jirasek, M. (1998). Nonlocal models for damage and fracture: comparison of approaches. *International Journal of Solids and Structures*, 35(31-32), 4133–4145. (Cited on page 19).
- Kachanov, L. M. (1958). Time of the rupture process under creep conditions. *Isv. Akad. Nauk. SSR. Otd Tekh. Nauk*, 8, 26–31. (Cited on page 18).
- Kalthoff, J. F. (2000). Modes of dynamic shear failure in solids. *International Journal of Fracture*, 101(1-2), 1–31. doi:10.1023/A:1007647800529. (Cited on pages 2 and 122)
- Kanninen, M. F., & Popelar, C. H. (1985). *Advanced Fracture Mechanics*. Oxford: Oxford University Press. (Cited on page 9).
- Karma, A., Kessler, D. A., & Levine, H. (2001). Phase-Field Model of Mode III Dynamic Fracture. *Phys. Rev. Lett.* 87(4), 045501. doi:10.1103/PhysRevLett.87.045501. (Cited on pages 6, 22, 35 and 37)
- Katzav, E., Adda-Bedia, M., & Arias, R. (2007). Theory of dynamic crack branching in brittle materials. *International Journal of Fracture*, 143(3), 245–271. doi:10.1007/s10704-007-9061-x. (Cited on pages 10, 11 and 119)
- Khludnev, A., Sokołowski, J., & Szulc, K. (2010). Shape and topological sensitivity analysis in domains with cracks. *Applications of Mathematics*, 55(6), 433–469. (Cited on pages 47, 49 and 165).

- Klinsmann, M., Rosato, D., Kamlah, M., & McMeeking, R. M. (2015). An assessment of the phase field formulation for crack growth. *Computer Methods in Applied Mechanics and Engineering*, 294, 313–330. (Cited on pages 23, 36, 41 and 96).
- Kuhn, C., & Müller, R. (2010). A continuum phase field model for fracture. *Engineering Fracture Mechanics*, 77(18), 3625–3634. (Cited on page 37).
- Kupfer, H. B., & Gerstle, K. H. (1973). Behavior of concrete under biaxial stresses. *Journal of the Engineering Mechanics Division*, 99(4), 853–866. (Cited on page 21).
- Lancioni, G., & Royer-Carfagni, G. (2009). The Variational Approach to Fracture Mechanics. A Practical Application to the French Panthéon in Paris. *Journal of Elasticity*, 95(1-2), 1–30. doi:10.1007/s10659-009-9189-1. (Cited on pages 20, 36, 41, 45 and 127)
- Larsen, C. J. (2010). Models for dynamic fracture based on Griffith's criterion. In *IUTAM Symposium on Variational Concepts with Applications to the Mechanics of Materials* (Pages 131–140). (Cited on pages 6, 12 and 16).
- Larsen, C. J., Ortner, C., & Süli, E. (2010). Existence of Solutions to a Regularized Model of Dynamic Fracture. *Mathematical Models and Methods in Applied Sciences*, 20(7), 1021–1048. (Cited on pages 72 and 74).
- Lazzaroni, G., Bargellini, R., Dumouchel, P.-E., & Marigo, J.-J. (2012). On the role of kinetic energy during unstable propagation in a heterogeneous peeling test. *International Journal of Fracture*, 175(2), 127–150. doi:10.1007/s10704-012-9708-0. (Cited on page 105)
- Le, D. T., Maurini, C., Marigo, J.-J., & Vidoli, S. (2015). Strain-gradient vs. damage-gradient regularizations of damage models. In *Fourth International Conference on Computational Modeling of Fracture and Failure of Materials and Structures (CFRAC)*, Cachan, France. (Cited on page 19).
- Lee, S.-K., Song, Y.-C., & Han, S.-H. (2004). Biaxial behavior of plain concrete of nuclear containment building. *Nuclear Engineering and Design*, 227(2), 143–153. doi:10.1016/j.nucengdes.2003.09.001. (Cited on page 21)
- Lemaitre, J., & Chaboche, J.-L. (1978). Aspect phénoménologique de la rupture par endommagement. *Journal de Mécanique Appliquée*, 2(3), 317–65. (Cited on page 18).
- León Baldelli, A. A., Babadjian, J.-F., Bourdin, B., Henao, D., & Maurini, C. (2014). A variational model for fracture and debonding of thin films under in-plane loadings. *Journal of the Mechanics and Physics of Solids*, 70, 320–348. (Cited on page 20).
- Li, T. (2015). FEniCS Dynamic Gradient Damage. <https://bitbucket.org/litany/dynamic-gradient-damage>. Accessed on 1 May 2016. (Cited on pages v, x, 75, 83 and 156).
- Livne, A., Ben-David, O., & Fineberg, J. (2007). Oscillations in Rapid Fracture. *Physical Review Letters*, 98(12), 124301. doi:10.1103/PhysRevLett.98.124301. (Cited on page 94)
- Logg, A., Mardal, K.-A., & Wells, G. (Editors). (2012). *Automated Solution of Differential Equations by the Finite Element Method: The FEniCS Book*. doi:10.1007/978-3-642-23099-8. (Cited on pages 75 and 156)
- Lorentz, E., & Kazymyrenko, K. (2014). Application of a nonlocal damage law to model concrete fracture. *Computational Modelling of Concrete Structures*, 209–217. (Cited on page 39).
- Lorentz, E., & Andrieux, S. (1999). A variational formulation for nonlocal damage models. *International Journal of Plasticity*, 15(2), 119–138. doi:10.1016/S0749-6419(98)00057-6. (Cited on pages 6 and 18)
- Lorentz, E., & Andrieux, S. (2003). Analysis of non-local models through energetic formulations. *International Journal of Solids and Structures*, 40(12), 2905–2936. doi:10.1016/S0020-7683(03)00110-0. (Cited on pages 6 and 19)
- Lorentz, E., & Benallal, A. (2005). Gradient constitutive relations: numerical aspects and application to gradient damage. *Computer Methods in Applied Mechanics and Engineering*, 194(50-52), 5191–5220. doi:10.1016/j.cma.2004.12.016. (Cited on pages 18 and 19)
- Lorentz, E., Cuvilliez, S., & Kazymyrenko, K. (2011). Convergence of a gradient damage model toward a cohesive zone model. *Comptes Rendus Mécanique*, 339(1), 20–26. doi:10.1016/j.crme.2010.10.010. (Cited on pages 23, 144 and 152)
- Lorentz, E., Cuvilliez, S., & Kazymyrenko, K. (2012). Modelling large crack propagation: from gradient damage to cohesive zone models. *International Journal of Fracture*, 178(1-2), 85–95. (Cited on pages 23, 27 and 30).
- Lorentz, E., & Godard, V. (2011). Gradient damage models: Toward full-scale computations. *Computer Methods in Applied Mechanics and Engineering*, 200(21-22), 1927–1944. doi:10.1016/j.cma.2010.06.025. (Cited on pages 70, 111, 141 and 160)
- Marder, M., & Gross, S. (1995). Origin of crack tip instabilities. *Journal of the Mechanics and Physics of Solids*, 43(1), 1–48. doi:10.1016/0022-5096(94)00060-1. (Cited on page 5)
- Marigo, J.-J. (2002). From Clausius-Duhem and Drucker-Ilyushin inequalities to standard materials. In *Continuum Thermomechanics: The Art and Science of Modelling Material Behaviour* (Pages 289–300). Gérard A. Maugin, Raymonde Drouot and François Sidoroff. (Cited on pages 18 and 27).



- Marigo, J.-J. (2010). Initiation of Cracks in Griffith's Theory: An Argument of Continuity in Favor of Global Minimization. *Journal of Nonlinear Science*, 20(6), 831–868. doi:[10.1007/s00332-010-9074-x](https://doi.org/10.1007/s00332-010-9074-x). (Cited on pages 10 and 14)
- Maso, G. D., & Lazzaroni, G. (2010). Quasistatic crack growth in finite elasticity with non-interpenetration. *Annales de l'Institut Henri Poincaré (C) Non Linear Analysis*, 27(1), 257–290. doi:[10.1016/j.anihpc.2009.09.006](https://doi.org/10.1016/j.anihpc.2009.09.006). (Cited on page 21)
- Maugin, G. (1994). On the  $J$ -integral and energy-release rates in dynamical fracture. *Acta Mechanica*, 105(1-4), 33–47. doi:[10.1007/BF01183940](https://doi.org/10.1007/BF01183940). (Cited on pages 6 and 164)
- Maurini, C., Bourdin, B., Gauthier, G., & Lazarus, V. (2013). Crack patterns obtained by unidirectional drying of a colloidal suspension in a capillary tube: experiments and numerical simulations using a two-dimensional variational approach. *International Journal of Fracture*, 184(1-2), 75–91. doi:[10.1007/s10704-013-9824-5](https://doi.org/10.1007/s10704-013-9824-5). (Cited on page 20)
- May, S., Vignollet, J., & de Borst, R. (2015). A numerical assessment of phase-field models for brittle and cohesive fracture:  $\Gamma$ -convergence and stress oscillations. *European Journal of Mechanics - A/Solids*, 52, 72–84. doi:[10.1016/j.euromechsol.2015.02.002](https://doi.org/10.1016/j.euromechsol.2015.02.002). (Cited on pages 36, 41 and 126)
- Mesgarnejad, A., Bourdin, B., & Khonsari, M. M. (2013). A variational approach to the fracture of brittle thin films subject to out-of-plane loading. *Journal of the Mechanics and Physics of Solids*, 61(11), 2360–2379. doi:[10.1016/j.jmps.2013.05.001](https://doi.org/10.1016/j.jmps.2013.05.001). (Cited on page 20)
- Mesgarnejad, A., Bourdin, B., & Khonsari, M. M. (2015). Validation simulations for the variational approach to fracture. *Computer Methods in Applied Mechanics and Engineering*, 290, 420–437. doi:[10.1016/j.cma.2014.10.052](https://doi.org/10.1016/j.cma.2014.10.052). (Cited on pages 23 and 27)
- Miehe, C., Hofacker, M., Schänzel, L.-M., & Aldakheel, F. (2015). Phase field modeling of fracture in multi-physics problems. Part II. Coupled brittle-to-ductile failure criteria and crack propagation in thermo-elastic-plastic solids. *Computer Methods in Applied Mechanics and Engineering*, 294, 486–522. doi:[10.1016/j.cma.2014.11.017](https://doi.org/10.1016/j.cma.2014.11.017). (Cited on pages 38 and 127)
- Miehe, C., Hofacker, M., & Welschinger, F. (2010). A phase field model for rate-independent crack propagation: Robust algorithmic implementation based on operator splits. *Computer Methods in Applied Mechanics and Engineering*, 199(45-48), 2765–2778. doi:[10.1016/j.cma.2010.04.011](https://doi.org/10.1016/j.cma.2010.04.011). (Cited on pages 14, 22, 35, 36, 41, 43, 44, 45, 64, 77, 122, 125, 127, 129, 130 and 156)
- Miehe, C., & Schänzel, L.-M. (2014). Phase field modeling of fracture in rubbery polymers. Part I: Finite elasticity coupled with brittle failure. *Journal of the Mechanics and Physics of Solids*, 65, 93–113. (Cited on page 38).
- Miehe, C., Schänzel, L.-M., & Ulmer, H. (2015). Phase field modeling of fracture in multi-physics problems. Part I. Balance of crack surface and failure criteria for brittle crack propagation in thermo-elastic solids. *Computer Methods in Applied Mechanics and Engineering*, 294, 449–485. doi:[10.1016/j.cma.2014.11.016](https://doi.org/10.1016/j.cma.2014.11.016). (Cited on pages 38 and 39)
- Miehe, C., Welschinger, F., & Hofacker, M. (2010). Thermodynamically consistent phase-field models of fracture: Variational principles and multi-field FE implementations. *International Journal for Numerical Methods in Engineering*, 83(10), 1273–1311. doi:[10.1002/nme.2861](https://doi.org/10.1002/nme.2861). (Cited on pages 6, 22, 35, 36 and 64)
- Mielke, A. (2005). Evolution of rate-independent systems. *Evolutionary equations*, 2, 461–559. (Cited on pages 6 and 17).
- Moës, N., Stolz, C., Bernard, P.-E., & Chevaugeon, N. (2011). A level set based model for damage growth: The thick level set approach. *International Journal for Numerical Methods in Engineering*, 86(3), 358–380. doi:[10.1002/nme.3069](https://doi.org/10.1002/nme.3069). (Cited on page 6)
- Moës, N., Dolbow, J., & Belytschko, T. (1999). A finite element method for crack growth without remeshing. *International Journal for Numerical Methods in Engineering*, 46(1), 131–150. doi:[10.1002/\(SICI\)1097-0207\(19990910\)46:1<131::AID-NME726>3.0.CO;2-J](https://doi.org/10.1002/(SICI)1097-0207(19990910)46:1<131::AID-NME726>3.0.CO;2-J). (Cited on page 12)
- Moré, J., & Toraldo, G. (1991). On the Solution of Large Quadratic Programming Problems with Bound Constraints. *SIAM Journal on Optimization*, 1(1), 93–113. (Cited on page 75).
- Moreau, J.-J. (1962). Décomposition orthogonale d'un espace hilbertien selon deux cônes mutuellement polaires. *Comptes Rendus de l'Académie des Sciences*, 255, 238–240. (Cited on page 40).
- Moreau, K., Moës, N., Picart, D., & Stainier, L. (2015). Explicit dynamics with a non-local damage model using the thick level set approach. *International Journal for Numerical Methods in Engineering*, 102(3-4), 808–838. doi:[10.1002/nme.4824](https://doi.org/10.1002/nme.4824). (Cited on pages 6, 21 and 126)
- Mott, N. F. (1947). Brittle fracture in mild steel plates. *Engineering*, 165, 16–18. (Cited on page 4).
- Mumford, D., & Shah, J. (1989). Optimal approximations by piecewise smooth functions and associated variational problems. *Communications on Pure and Applied Mathematics*, 42(5), 577–685. doi:[10.1002/cpa.3160420503](https://doi.org/10.1002/cpa.3160420503). (Cited on page 14)

- Nakamura, T., Shih, C., & Freund, L. (1985). Computational methods based on an energy integral in dynamic fracture. *International Journal of Fracture*, 27(3-4), 229–243. doi:10.1007/BF00017970. (Cited on pages 7 and 8)
- Negri, M. (1999). The anisotropy introduced by the mesh in the finite element approximation of the Mumford-Shah functional. *Numerical Functional Analysis and Optimization*, 20(9-10), 957–982. (Cited on pages 67 and 111).
- Negri, M. (2010). A comparative analysis on variational models for quasi-static brittle crack propagation. *Advances in Calculus of Variations*, 3(2), 149–212. (Cited on pages 12 and 14).
- Nguyen, Q. S. (2000). *Stability and Nonlinear Solid Mechanics*. John Wiley & Sons, Ltd. (Cited on pages 14 and 20).
- Nishioka, T., & Atluri, S. N. (1983). Path-independent integrals, energy release rates, and general solutions of near-tip fields in mixed-mode dynamic fracture mechanics. *Engineering Fracture Mechanics*, 18(1), 1–22. (Cited on pages 163 and 164).
- Oleaga, G. E. (2001). Remarks on a basic law for dynamic crack propagation. *Journal of the Mechanics and Physics of Solids*, 49(10), 2273–2306. (Cited on page 165).
- Ortiz, M. (1985). A constitutive theory for the inelastic behavior of concrete. *Mechanics of Materials*, 4(1), 67–93. (Cited on page 40).
- Ožbolt, J., Bede, N., Sharma, A., & Mayer, U. (2015). Dynamic fracture of concrete L-specimen: Experimental and numerical study. *Engineering Fracture Mechanics*, 148, 27–41. doi:10.1016/j.engfracmech.2015.09.002. (Cited on pages 138, 139, 141, 142 and 160)
- Ožbolt, J., & Sharma, A. (2011). Numerical simulation of reinforced concrete beams with different shear reinforcements under dynamic impact loads. *International Journal of Impact Engineering*, 38(12), 940–950. (Cited on pages 144, 146 and 149).
- Peerlings, R. H. J., de Borst, R., Brekelmans, W. A. M., & Geers, M. G. D. (1998). Gradient-enhanced damage modelling of concrete fracture. *Mechanics of Cohesive-frictional Materials*, 3(4), 323–342. (Cited on page 19).
- Peerlings, R. H. J., de Borst, R., Brekelmans, W. A. M., & de Vree, J. H. P. (1996). Gradient enhanced damage for quasi-brittle materials. *International Journal for Numerical Methods in Engineering*, 39(19), 3391. (Cited on page 19).
- Peerlings, R. H. J., Geers, M. G. D., de Borst, R., & Brekelmans, W. A. M. (2001). A critical comparison of nonlocal and gradient-enhanced softening continua. *International Journal of Solids and Structure*, 38(44), 7723–7746. (Cited on pages 6 and 19).
- Pham, K. H., & Ravi-Chandar, K. (2016). On the growth of cracks under mixed-mode I + III loading. *International Journal of Fracture*, 199(1), 105–134. doi:10.1007/s10704-016-0098-6. (Cited on page 10)
- Pham, K. (2010). *Construction et analyse de modèles d'endommagement à gradient* (Doctoral dissertation, Université Pierre et Marie Curie). (Cited on page 105).
- Pham, K., Amor, H., Marigo, J.-J., & Maurini, C. (2011). Gradient damage models and their use to approximate brittle fracture. *International Journal of Damage Mechanics*, 20(4), 618–652. (Cited on pages 6, 14, 17, 18, 19, 20, 22, 26, 27, 29, 34, 35, 37, 45, 67, 69, 72 and 105).
- Pham, K., & Marigo, J.-J. (2010a). Approche variationnelle de l'endommagement : I. Les concepts fondamentaux. *Comptes Rendus Mécanique*, 338(4), 191–198. (Cited on pages 17 and 18).
- Pham, K., & Marigo, J.-J. (2010b). Approche variationnelle de l'endommagement : II. Les modèles à gradient. *Comptes Rendus Mécanique*, 338(4), 199–206. (Cited on pages x, 6, 17, 21, 25, 26 and 34).
- Pham, K., & Marigo, J.-J. (2013). From the onset of damage to rupture: construction of responses with damage localization for a general class of gradient damage models. *Continuum Mechanics and Thermodynamics*, 25(2-4), 147–171. (Cited on pages 18, 20 and 27).
- Pham, K., Marigo, J.-J., & Maurini, C. (2011). The issues of the uniqueness and the stability of the homogeneous response in uniaxial tests with gradient damage models. *Journal of the Mechanics and Physics of Solids*, 59(6), 1163–1190. (Cited on pages 18, 20 and 27).
- Piero, G. D., Lancioni, G., & March, R. (2007). A variational model for fracture mechanics: Numerical experiments. *Journal of the Mechanics and Physics of Solids*, 55(12), 2513–2537. doi:10.1016/j.jmps.2007.04.011. (Cited on pages 21, 38, 41, 70 and 130)
- Ravi-Chandar, K. (1998). Dynamic fracture of nominally brittle materials. *International Journal of Fracture*, 90(1-2), 83–102. (Cited on page 119).
- Ravi-Chandar, K., & Knauss, W. G. (1984a). An experimental investigation into dynamic fracture: I. Crack initiation and arrest. *International Journal of Fracture*, 25(4), 247–262. (Cited on page 5).
- Ravi-Chandar, K., & Knauss, W. G. (1984b). An experimental investigation into dynamic fracture: II. Microstructural aspects. *International Journal of Fracture*, 26(1), 65–80. (Cited on pages 5, 11 and 116).

- Ravi-Chandar, K., & Knauss, W. G. (1984c). An experimental investigation into dynamic fracture: III. On steady-state crack propagation and crack branching. *International Journal of Fracture*, 26(2), 141–154. (Cited on pages 4, 5, 10, 11 and 116).
- Ravi-Chandar, K., & Knauss, W. G. (1984d). An experimental investigation into dynamic fracture: IV. On the interaction of stress waves with propagating cracks. *International Journal of Fracture*, 26(3), 189–200. (Cited on page 3).
- Réthoré, J., Gravouil, A., & Combescure, A. (2005). An energy-conserving scheme for dynamic crack growth using the eXtended finite element method. *International Journal for Numerical Methods in Engineering*, 63(5), 631–659. doi:10.1002/nme.1283. (Cited on page 9)
- Rice, J. R. (1968). A path independent integral and the approximate analysis of strain concentration by notches and cracks. *Journal of Applied Mechanics*, 35(2), 379–386. (Cited on page 8).
- Rocco, C., Guinea, G. V., Planas, J., & Elices, M. (1999). Size effect and boundary conditions in the Brazilian test: Experimental verification. *Materials and Structures*, 32(3), 210–217. (Cited on pages 132 and 137).
- Royer, D., & Clorennec, D. (2007). An improved approximation for the Rayleigh wave equation. *Ultrasonics*, 46(1), 23–24. doi:10.1016/j.ultras.2006.09.006. (Cited on pages 8 and 9)
- Ruiz, G., Ortiz, M., & Pandolfi, A. (2000). Three-dimensional finite-element simulation of the dynamic Brazilian tests on concrete cylinders. *International Journal for Numerical Methods in Engineering*, 48, 963–994. (Cited on pages 132, 134 and 137).
- Sacco, E. (1990). Modellazione e calcolo di strutture in materiale non resistente a trazione. *Rendiconti di Matematica dell'Accademia dei Lincei*, 1(3), 235–258. (Cited on page 42).
- Schardin, H. (1959). Velocity effects in fracture. In B. L. Averbach, D. K. Felbeck, G. T. Hahn, & D. A. Thomas (Editors), *Fracture* (Pages 297–330). Wiley, New York. (Cited on pages 5, 127 and 160).
- Scherzinger, W. M., & Dohrmann, C. R. (2008). A robust algorithm for finding the eigenvalues and eigenvectors of  $3 \times 3$  symmetric matrices. *Computer Methods in Applied Mechanics and Engineering*, 197(45–48), 4007–4015. doi:10.1016/j.cma.2008.03.031. (Cited on page 77)
- Schlüter, A., Kuhn, C., Müller, R., & Gross, D. (2016). An investigation of intersonic fracture using a phase field model. *Archive of Applied Mechanics*, 86(1), 321–333. doi:10.1007/s00419-015-1114-4. (Cited on page 23)
- Schlüter, A., Willenbücher, A., Kuhn, C., & Müller, R. (2014). Phase field approximation of dynamic brittle fracture. *Computational Mechanics*, 54(5), 1141–1161. doi:10.1007/s00466-014-1045-x. (Cited on pages 23, 36, 37, 69, 72 and 111)
- Sharon, E., & Fineberg, J. (1996). Microbranching instability and the dynamic fracture of brittle materials. *Physical Review B*, 54(10), 7128–7139. doi:10.1103/PhysRevB.54.7128. (Cited on pages 5, 116, 117 and 119)
- Sharon, E., & Fineberg, J. (1999). Confirming the continuum theory of dynamic brittle fracture for fast cracks. *Nature*, 397(6717), 333–335. (Cited on pages 11 and 119).
- Sharon, E., Gross, S. P., & Fineberg, J. (1995). Local Crack Branching as a Mechanism for Instability in Dynamic Fracture. *Physical Review Letters*, 74(25), 5096. doi:10.1103/PhysRevLett.74.5096. (Cited on page 5)
- Sharon, E., Gross, S. P., & Fineberg, J. (1996). Energy dissipation in dynamic fracture. *Physical Review Letters*, 76(12), 2117. (Cited on pages 5, 11 and 116).
- Sicsic, P., & Marigo, J.-J. (2013). From Gradient Damage Laws to Griffith's Theory of Crack Propagation. *Journal of Elasticity*, 113(1), 55–74. (Cited on pages 18, 20, 22, 23, 27, 34, 39, 47, 50, 57, 58, 59, 60, 61, 93 and 158).
- Sicsic, P., Marigo, J.-J., & Maurini, C. (2014). Initiation of a periodic array of cracks in the thermal shock problem: A gradient damage modeling. *Journal of the Mechanics and Physics of Solids*, 63, 256–284. (Cited on pages 18 and 20).
- Silling, S. A., & Lehoucq, R. B. (2010). Peridynamic Theory of Solid Mechanics. *Advances in Applied Mechanics*, 44, 73–168. (Cited on pages 6 and 19).
- Simone, A., Askes, H., Peerlings, R. H. J., & Sluys, L. J. (2003). Interpolation requirements for implicit gradient-enhanced continuum damage models. *Communications in Numerical Methods in Engineering*, 19(7), 563–572. (Cited on page 68).
- Song, J.-H., Wang, H., & Belytschko, T. (2008). A comparative study on finite element methods for dynamic fracture. *Computational Mechanics*, 42(2), 239–250. doi:10.1007/s00466-007-0210-x. (Cited on page 6)
- Spatscheck, R., Brener, E., & Karma, A. (2011). Phase-Field Modeling of Crack Propagation. *Philosophical Magazine*, 91(1), 75–95. (Cited on page 22).
- Sternberg, E. (1960). On the integration of the equations of motion in the classical theory of elasticity. *Archive for Rational Mechanics and Analysis*, 6(1), 34–50. (Cited on page 7).

- Stolarska, M., Chopp, D. L., Moës, N., & Belytschko, T. (2001). Modelling crack growth by level sets in the extended finite element method. *International Journal for Numerical Methods in Engineering*, 51(8), 943–960. doi:[10.1002/nme.201](https://doi.org/10.1002/nme.201). (Cited on page 12)
- Strobl, M., & Seelig, T. (2015). A novel treatment of crack boundary conditions in phase field models of fracture. *PAMM*, 15(1), 155–156. doi:[10.1002/pamm.201510068](https://doi.org/10.1002/pamm.201510068). (Cited on page 126)
- Versieux, H. (2016). A relation between a dynamic fracture model and quasi-static evolution. *ESAIM: M2AN*, 50(1), 77–91. (Cited on page 100).
- Vignollet, J., May, S., de Borst, R., & Verhoosel, C. V. (2014). Phase-field models for brittle and cohesive fracture. *Meccanica*, 49(11), 2587–2601. doi:[10.1007/s11012-013-9862-0](https://doi.org/10.1007/s11012-013-9862-0). (Cited on pages 115 and 126)
- Xiao, H., Bruhns, O. T., & Meyers, A. (1997). Logarithmic strain, logarithmic spin and logarithmic rate. *Acta Mechanica*, 124(1-4), 89–105. (Cited on pages 38 and 74).
- Xiao, H., & Chen, L. (2002). Hencky’s elasticity model and linear stress-strain relations in isotropic finite hyperelasticity. *Acta Mechanica*, 157(1-4), 51–60. doi:[10.1007/BF01182154](https://doi.org/10.1007/BF01182154). (Cited on page 38)
- Yoffe, E. H. (1951). LXXV. The moving Griffith crack. *The London, Edinburgh, and Dublin Philosophical Magazine and Journal of Science*, 42(330), 739–750. (Cited on page 10).

SMEMAG.pdf

**Titre :** Analyse de la rupture dynamique fragile via les modèles d'endommagement à gradient : principes variationnels et simulations numériques

**Mots clés :** rupture dynamique fragile, modèles d'endommagement à gradient, champ de phase, méthodes variationnelles, implémentation numérique

**Résumé :** Une bonne tenue mécanique des structures du génie civil en béton armé sous chargements dynamiques sévères est primordiale pour la sécurité et nécessite une évaluation précise de leur comportement en présence de propagation dynamique de fissures. Dans ce travail, on se focalise sur la modélisation constitutive du béton assimilé à un matériau élastique-fragile endommageable. La localisation des déformations sera régie par un modèle d'endommagement à gradient où un champ scalaire réalise une description régularisée des phénomènes de rupture dynamique. La contribution de cette étude est à la fois théorique et numérique. On propose une formulation variationnelle des modèles d'endommagement à gradient en dynamique. Une définition rigoureuse de plusieurs taux de restitution d'énergie dans le modèle d'endommagement est donnée et on démontre que la propagation dynamique de fissures est régie par un critère de Griffith généralisé. On décrit ensuite une implémentation numérique efficace basée sur une discrétisation par éléments finis standards en espace et la méthode de Newmark en temps dans un cadre de calcul parallèle. Les résultats de simulation de plusieurs problèmes modèles sont discutés d'un point de vue numérique et physique. Les lois constitutives d'endommagement et les formulations d'asymétrie en traction et compression sont comparées par rapport à leur aptitude à modéliser la rupture fragile. Les propriétés spécifiques du modèle d'endommagement à gradient en dynamique sont analysées pour différentes phases de l'évolution de fissures : nucléation, initiation, propagation, arrêt, branchement et bifurcation. Des comparaisons avec les résultats expérimentaux sont aussi réalisées afin de valider le modèle et proposer des axes d'amélioration.

**Title:** Gradient-damage modeling of dynamic brittle fracture: variational principles and numerical simulations

**Keywords:** dynamic brittle fracture, gradient damage models, phase-field, variational methods, numerical implementation

**Abstract:** In civil engineering, mechanical integrity of the reinforced concrete structures under severe transient dynamic loading conditions is of paramount importance for safety and calls for an accurate assessment of structural behaviors in the presence of dynamic crack propagation. In this work, we focus on the constitutive modeling of concrete regarded as an elastic-damage brittle material. The strain localization evolution is governed by a gradient-damage approach where a scalar field achieves a smeared description of

dynamic fracture phenomena. The contribution of the present work is both theoretical and numerical. We propose a variationally consistent formulation of dynamic gradient damage models. A formal definition of several energy release rate concepts in the gradient damage model is given and we show that the dynamic crack tip equation of motion is governed by a generalized Griffith criterion. We then give an efficient numerical implementation of the model based on a standard finite-element spatial discretization and the Newmark time-stepping methods in a parallel computing framework. Simulation results of several problems are discussed both from a computational and physical point of view. Different damage constitutive laws and tension-compression asymmetry formulations are compared with respect to their aptitude to approximate brittle fracture. Specific properties of the dynamic gradient damage model are investigated for different phases of the crack evolution: nucleation, initiation, propagation, arrest, kinking and branching. Comparisons with experimental results are also performed in order to validate the model and indicate its further improvement.